

IAEA-TECDOC-684

Corrosion of zirconium alloys in nuclear power plants



INTERNATIONAL ATOMIC ENERGY AGENCY

IAEA

The IAEA does not normally maintain stocks of reports in this series.
However, microfiche copies of these reports can be obtained from

INIS Clearinghouse
International Atomic Energy Agency
Wagramerstrasse 5
P.O. Box 100
A-1400 Vienna, Austria

Orders should be accompanied by prepayment of Austrian Schillings 100,—
in the form of a cheque or in the form of IAEA microfiche service coupons
which may be ordered separately from the INIS Clearinghouse.

CORROSION OF ZIRCONIUM ALLOYS IN NUCLEAR POWER PLANTS
IAEA, VIENNA, 1993
IAEA-TECDOC-684
ISSN 1011-4289

Printed by the IAEA in Austria
January 1993

FOREWORD

Current trends towards extended burnup, increased outlet temperatures and plant life extension in nuclear power facilities require the solution of a large number of problems related to the reliability of the materials used, especially in key components such as fuel cladding. In particular, the corrosion of metals and alloys under irradiation poses special problems for the nuclear industry. At present, the ability to predict the long term behaviour of materials in a radiation environment is rather limited due mainly to a lack of knowledge of detailed mechanisms.

For zirconium alloys, it is clear that there is a need for more feedback between experiments on the factors influencing in-reactor corrosion, experiments designed to reveal micromechanistic processes and attempts to model the overall behaviour of fuel cladding in the reactor core.

To improve our understanding of corrosion mechanisms under irradiation of zirconium alloys, to collect information systematically and to identify areas where further experimentation is needed, in 1989 the IAEA initiated a special project with the participation of experts from Canada, France, Japan, USA and the former USSR.

This technical document is the result of two years of joint investigations. In view of the rapidly evolving mechanistic understanding of the phenomena in this field, the document presents a series of snapshots of current ideas in specific areas of study that are relevant to the whole problem. Any attempt to present an agreed upon micromechanistic hypothesis that explains the overall phenomena must await further detailed investigations. Throughout the text, the authors have endeavoured to indicate critical gaps in our basic knowledge. It is hoped that this will stimulate experimental studies in just those areas where further data are most urgently required.

The IAEA wishes to express its thanks to all the authors of the report. The IAEA staff member responsible for this publication was A. Nechaev of the Division of Nuclear Fuel Cycle and Waste Management.

EDITORIAL NOTE

In preparing this material for the press, staff of the International Atomic Energy Agency have mounted and paginated the original manuscripts and given some attention to presentation.

The views expressed do not necessarily reflect those of the governments of the Member States or organizations under whose auspices the manuscripts were produced.

The use in this book of particular designations of countries or territories does not imply any judgement by the publisher, the IAEA, as to the legal status of such countries or territories, of their authorities and institutions or of the delimitation of their boundaries.

The mention of specific companies or of their products or brand names does not imply any endorsement or recommendation on the part of the IAEA.

CONTENTS

1. INTRODUCTION	7
2. CORROSION MECHANISM IN THE ABSENCE OF IRRADIATION	9
2.1. Uniform oxide formation	9
2.1.1. Introduction	9
2.1.2. Oxidation kinetics	13
2.1.3. The mechanism of pretransition oxide growth	22
2.1.4. Mechanism of oxide breakdown	27
2.1.5. Post-transition growth	31
2.2. Non-uniform (nodular) oxide formation	33
2.2.1. Nodular oxide formation	34
2.2.2. Mechanism of nodule formation	36
2.2.3. Simulating nodular corrosion in high temperature water	38
2.3. Hydrogen absorption	38
2.3.1. Absorption of hydrogen gas	39
2.3.2. Hydrogen uptake during oxidation	47
2.3.3. Hydrogen absorption via metallic contacts	54
3. RADIATION EFFECTS ON THE CORROSION OF ZIRCONIUM ALLOYS	57
3.1. Influence of radiation on zirconium alloy corrosion phenomena	57
3.1.1. Radiation type, intensity, spectral shift, duration	57
3.1.2. Coolant chemistry	58
3.1.3. Alloy composition	58
3.1.4. Metallurgical condition	58
3.1.5. Surface condition	58
3.1.6. Temperature	59
3.1.7. Dissimilar metal effects	59
3.1.8. Heat flux	59
3.2. Effects of alloy composition	59
3.3. Uniform oxidation of zirconium alloys under irradiation	60
3.3.1. Oxidation in irradiated low-oxygen coolants	62
3.3.1.1. Oxidation and hydriding of fuel cladding	62
3.3.1.2. Oxidation and hydriding of reactor pressure tubes	64
3.3.1.3. Oxidation and hydriding in test reactor loops	66
3.3.1.4. Thick-film effects in low-oxygen coolants	67
3.3.2. Oxidation in irradiated oxygenated coolants	68
3.3.2.1. Oxidation and hydriding of fuel cladding	68
3.3.2.2. Oxidation and hydriding of pressure tubes	68
3.3.2.3. Oxidation and hydriding in test reactor loops	69
3.4. Localized oxidation and hydriding	70
3.4.1. Nodular oxide formation	70
3.4.2. Alloy element segregation	71
3.4.3. Dissimilar metal effects	71
3.4.4. Other localized effects	71
3.5. Significance of radiation effects to zirconium alloy behaviour in service	72

4.	FACTORS AFFECTING IRRADIATION CORROSION	73
4.1.	Irradiation damage	73
4.1.1.	Fast neutron damage in metals	73
4.1.2.	Displacement damage in other structures	74
4.1.3.	Effect of irradiation on microstructures	76
4.2.	Local radiation chemistry	82
4.2.1.	Radiolysis in the bulk water	82
4.2.2.	Radiolysis near metal surfaces or in the pores surrounded by metal oxides ..	88
4.2.3.	“Thick oxide film effects”	90
4.3.	Crud deposition and heat transfer effects	92
4.3.1.	PWR crud deposition	92
4.3.2.	WWER crud deposition	109
4.3.3.	BWR crud deposition	109
4.3.4.	Effects of heat transfer	111
4.4.	Metallurgical and chemical variables	116
4.4.1.	Fabrication variables	116
4.4.2.	Behaviour of alloying additions	119
4.4.3.	Electrochemical effects	121
4.4.4.	Effects of surface treatment of zirconium alloy components	125
5.	PRESENT STATUS OF THE MECHANISTIC UNDERSTANDING OF THE EFFECTS OF IRRADIATION	129
5.1.	Current understanding of the out-reactor oxidation mechanism	129
5.1.1.	Mobile species	129
5.1.2.	Evolution of oxide morphology	131
5.1.3.	The development and nature of oxide porosity	139
5.1.4.	Oxide barrier layers	142
5.1.5.	Effect of some variables on the oxide structure	144
5.2.	Empirical correlations of effects of irradiation	147
5.2.1.	Development of irradiation corrosion models	149
5.2.2.	Micromechanisms for in-reactor corrosion	156
5.2.3.	Present status of mechanistic studies	157
5.2.4.	Recommendations for future work	157
6.	CONCLUSIONS	159
	APPENDIX	161
	REFERENCES	163
	CONTRIBUTORS TO DRAFTING AND REVIEW	177

1. INTRODUCTION

Failures in the basic materials used in nuclear power plants continue to be costly and insidious, despite increasing industry vigilance to catch failures before they degrade safety. For instance, the overall costs to the US industry from materials problems could amount to as much as US \$10 billion¹ annually. Moreover, estimates indicate that the cost of a pipe failure in a nuclear plant is one hundred times greater than the cost of a similar failure in a coal-fired plant [1].

So the problem exists and is demanding more attention from utilities and regulators. According to a recent study on "Materials Science & Engineering for the 1990s": "Resumption of commercialization of nuclear power will require solving many problems related to reliability of materials for reactors... Particular requirements are (1) a non-destructive measure of the condition of materials (surface and bulk) that is preferably on-line and continuous and (2) a physically based mechanistic model of material behaviour in the environment"[1].

In the context of the last conclusion corrosion of metals and alloys under irradiation has to be particularly emphasized. Despite the many years of experience and investigations in this field there is no common agreement on either the importance or precise mechanisms of irradiation effects. Consequently, there is a lack of capacity for prediction of long-term materials behaviour in radiation environment. At the same time, the modern trends in nuclear power development (extended burnup, increased outlet temperature, increased lithium concentration, plant life extension, radiation control, etc.) urgently require an answer to the question: are the existing materials capable of guaranteeing a high level of reliability in improved schemes of fuel utilization, or under improved plant operation conditions, or under extension of the nuclear power plant operation over the design lifetime [2,3]? As was stated at the IAEA meeting on fundamental aspects of corrosion of Zr-based alloys in water reactor environment (Portland, USA, 1989), "clarification of irradiation effects is the item of topmost importance".

Zirconium alloys have been established as vital materials in water reactor technology, functioning as fuel cladding, pressure tubes, fuel channels (boxes) and fuel spacer grid materials. Performance of the zirconium alloys in service has generally been satisfactory, but there have been occasional problems, including fuel cladding and pressure tube degradation and failure. However, a major motivation for this review of zirconium alloy oxidation and hydriding behaviour under irradiation involves the anticipated need for the continuing satisfactory performance of the zirconium alloys over the next several decades. An element of this expected service is the potential for more severe operating requirements, notably a major trend toward longer residence of some fuel types in reactor to achieve higher burnups; also some trends to higher pH in PWR coolants and hydrogen additions to BWR coolants. Anticipating that from time to time reactor operators may want to make other service modifications or may be faced with interpretation of unexpected phenomena, it seems important to develop an improved understanding of the phenomena that have emerged in some thirty years of zirconium alloy utilization. While the basic trends in corrosion behaviour seem to be largely consistent, the development of a mechanistic understanding that provides a sound basis for interpretation and prediction remains only fragmentary. This review intends to summarize briefly the key phenomena, the status of the mechanistic understanding, and to identify the gaps in our understanding and establish a basis for future

¹ 1 billion = 10⁹.

initiatives to advance this understanding of radiation effects on zirconium alloy corrosion.

An important need is to anticipate the consequences of actions before they cause serious degradation of zirconium alloy reactor components. This strongly suggests the value of the systematic consideration of the consequences of changes in reactor operation on fuel cladding and other zirconium alloy components. Sometimes operational considerations are in conflict. For example, increasing lithium contents in PWR coolants to minimize crud transport at some point begins to jeopardize the oxidation resistance of zirconium alloys. Early recognition of the problems and selection of a suitable compromise can avoid a period of expensive retrenchment.

This review includes only information available in the open literature. The sources of data include:

- oxidation and hydriding data from fuel cladding, non-fueled reactor components, and irradiated unfueled specimens;
- relevant data from unirradiated specimens, from specimens exposed in-reactor but out-of-core, and also from specimens tested in laboratory loops and autoclaves operated with thermal and water chemistry parameters similar to those in-flux;
- supporting data on water radiolysis and radiation damage.

Much of the existing oxidation and hydriding data base has been developed from examination of irradiated zirconium alloy materials (specimens, pressure tubes, BWR channels, spacer materials, water tubes) that operated at low heat transfer rates. To the extent that these data can be shown to correlate with phenomena on fuel cladding, operating under elevated heat transfer conditions, they expand the basis for interpreting observations on fuel cladding. Conversely, the fuel cladding results offer potential contributions to an integrated data base that is applicable over a wide range of heat transfer conditions. At the same time, it is important to identify and understand oxidation and hydriding phenomena that result uniquely from heat transfer effects.

Some alloy systems seem to be pressed to near their operational limits for reactor service in some regimes. A better understanding of alloy element and impurity effects may allow operational improvements without major initiatives to qualify completely different alloy systems. Nuclear reactor operating regimes include a range of water chemistries, including hydrogenated, low oxygen (e.g. PWR, WWER), marginally low oxygen (e.g. PHWR), and oxygenated conditions (e.g. BWR, RBMK). Some phenomena and oxidation kinetics are unique to some regimes. In some cases radiation is clearly involved in the oxidation kinetics. In other cases, effects of heat transfer, coolant species (e.g. Li^+) and radiation remain a matter of controversy.

These are some examples of the need for a more fundamental understanding of zirconium alloy behaviour, with the opportunity for practical applications. Thus, there are important practical stimuli and much scope for further understanding of the effects of irradiation on Zr-alloys (and other materials used in nuclear installations) by careful experimentation. Moreover, these studies will need to address the effect of irradiation on all components of heterogeneous systems: the metal, the oxide and the environment, and especially those processes recurring at the interphases between these components.

The present review is aimed at providing specialists with some systematic information on the subject and with important considerations on the key items for further experimentation.

2. CORROSION MECHANISM IN THE ABSENCE OF IRRADIATION

2.1. UNIFORM OXIDE FORMATION

2.1.1. Introduction

Because of the thermodynamics of the Zr.O system (Fig.2.1), not all the oxygen that reacts forms oxide, some dissolves in the matrix [4]. Figures 2.2 and 2.3 are merely examples from among the many microhardness plots available from the literature.

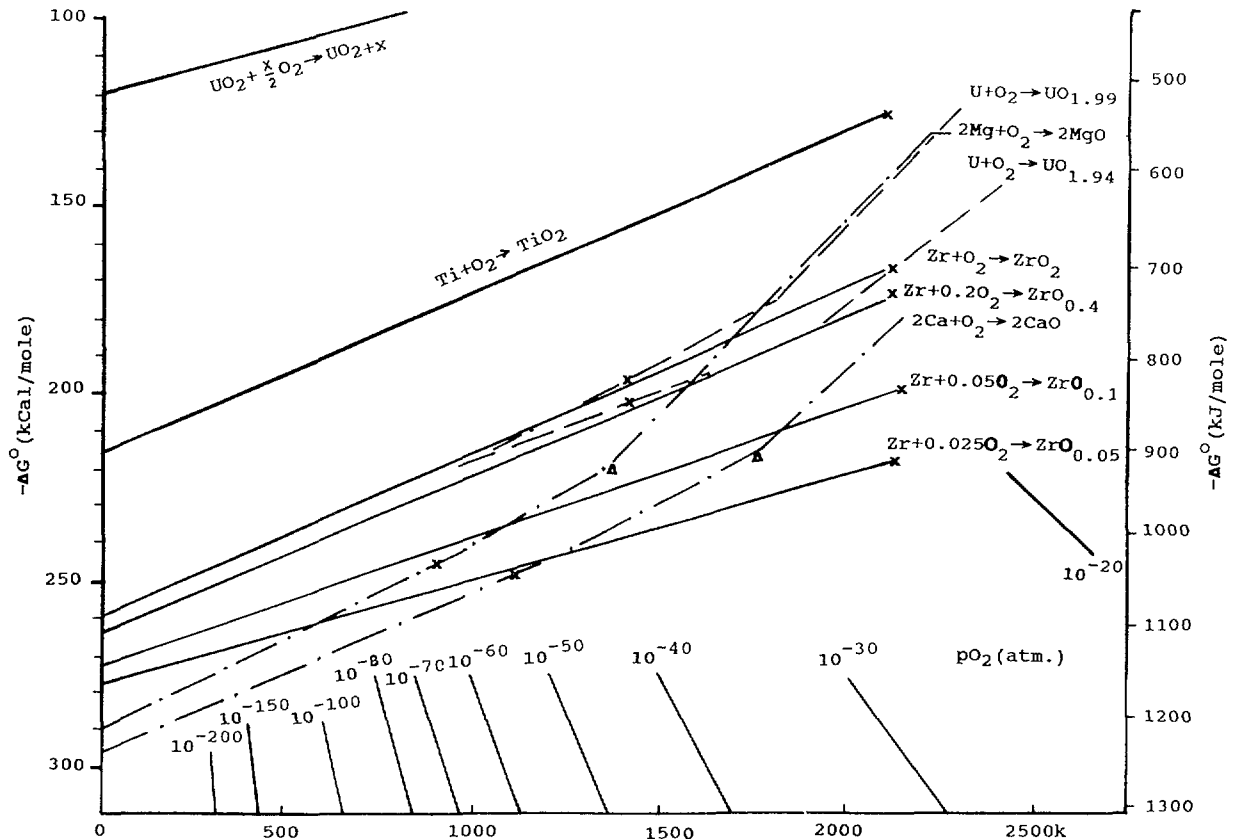
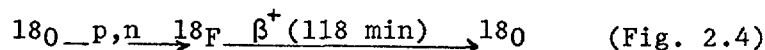


FIG. 2.1. Darken and Gurry plot of thermodynamics of Zr/O and other relevant systems [4].

The fraction dissolving depends on the balance between the kinetics of oxidation and the kinetics of dissolution [5]. Thus, since the dissolution process seems to vary much less from alloy to alloy than the oxidation process, rapidly oxidizing alloys should have shallower diffusion zones than slowly oxidizing alloys at all temperatures, although the ability to measure these diffusion zones at low temperatures is very limited. Any discontinuity in the oxidation kinetics will result either in growth or diminution of the oxygen diffusion zone.

The fraction of oxygen dissolving is not well known, or accepted, even at high temperatures where it is highest because the activation energy for dissolution is higher than the activation energy for oxide growth (Table 2.1) [5]. At low temperatures neither the fraction dissolved nor its distribution is well known. Dissolution is known to be localized at $\leq \sim 600^\circ\text{C}$ but the extent of this localization is not well known. Preferential dissolution along grain boundaries has been demonstrated at $\sim 600^\circ\text{C}$ by the nuclear reaction:



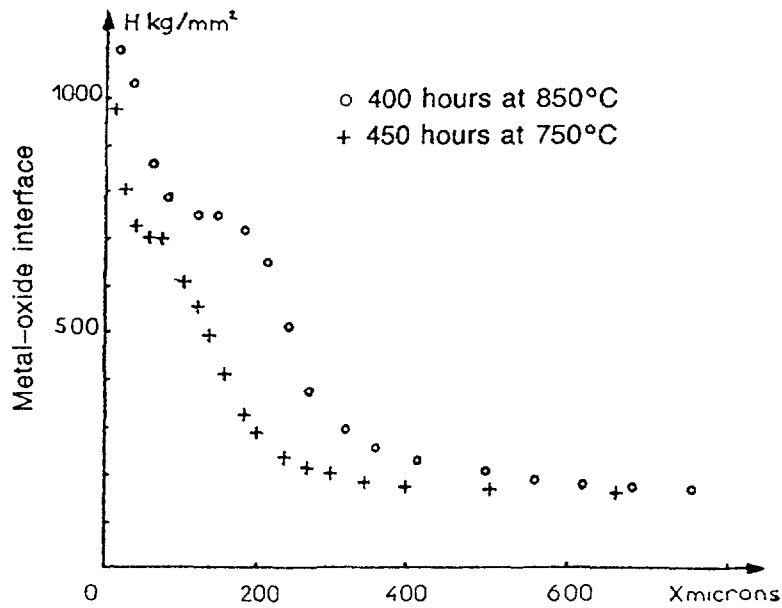


FIG. 2.2. Variation in the microhardness as a function of the depth of penetration of oxygen in zirconium (50 g load) [5].

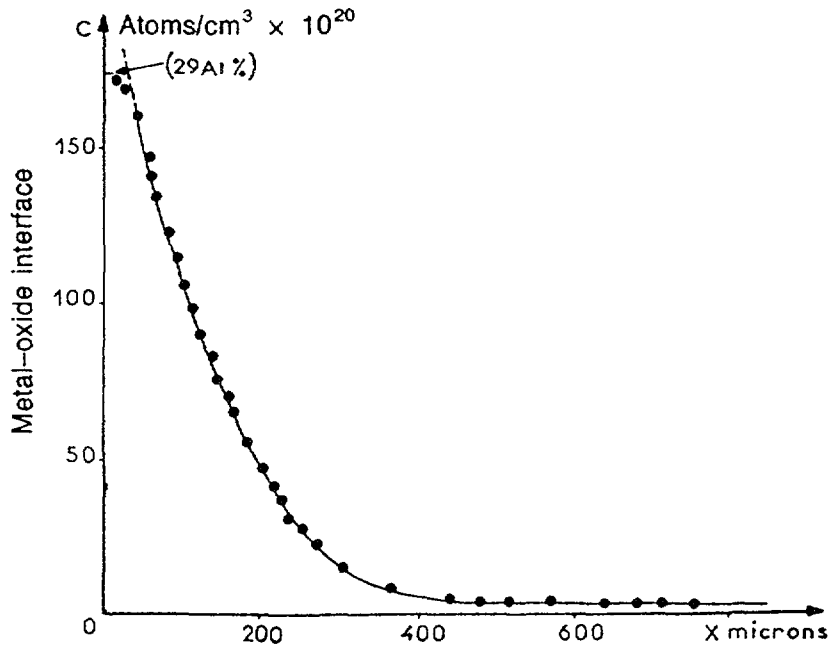


FIG. 2.3. Curve for the penetration of oxygen, established using the $^{16}\text{O}(d,p)^{17}\text{O}^*$ nuclear reaction with $E_d = 900$ keV, and compared with a calculated curve (error function complement) for a zirconium specimen oxidized at 850°C for 400 h [5].

but at lower temperatures local sites on the grain boundaries seem to be active sites for dissolution (Fig. 2.5) [6].

The difference between the total O_2 reacting (accurately known) and the amount dissolving (not well known) causes problems with calibrating other physical methods for establishing the oxide thickness (e.g. impedance, interferometry) so that errors in such calibrations at low temperature (300–400°C) may be equal to the range of values for the fraction of oxygen dissolving (0–10%) and add to the difficulties caused by variations in the local oxide growth from grain to grain (Fig. 2.6) [7];

TABLE 2.1. FRACTION OF REACTED OXYGEN IN SOLUTION IN ZIRCONIUM
(References refer to the original table in Ref. [5])

Temp. (°C)	Time (hr)	Total O ₂ (mg/dm ²)	Fraction in metal	Ref.	Temp. (°C)	Time (hr)	Total O ₂ (mg/dm ²)	Fraction in metal	Ref.	
400	6	2.26	0.084	95	800	0.1	~85 ^a	0.247	23	
	644	~20	≥0.05	42		1.0	~190 ^a	0.342	23	
450	6	5.91	0.085	95		6.41	235	0.306	96	
	6	5.12	0.082	95		10	~430 ^a	0.465	23	
500	6	11.2	0.071	95		20	~850 ^a	0.264	23	
	300	~77	0.10 ± 0.02	42		22.9	415	0.39	96	
	356	~78	0.11	42		50	~4200 ^a	0.054	23	
	409	~80	0.13 ± 0.02	42		78.75	700	0.407	96	
	450	~95	0.07	42		840	7.0	460	0.35	50
	500	~97	0.12 ± 0.02	42			40.0	860	0.49	50
	550	~105	0.10	42	113.0		1300	0.555	50	
	550	6	25.4	0.087	95		234.0	11710	0.635	50
316		~146	0.19	42	435.0		2190	0.635	50	
341		~152	0.14 ± 0.03	42	601.5		2450	0.65	50	
371		~154	0.13	42	850	6	~306	0.51	42	
402		~145	0.16 ± 0.05	42		6	371	0.394	96	
435		~166	0.23	42		16	~543	0.42	42	
457		~165	0.19	42		24	~800	0.57	42	
486		~161	0.17 ± 0.03	42		24	671	0.556	96	
				48		~1050	0.56 ± 0.05	42		
600	6	44.9	0.085	95	900	0.1	~150 ^a	0.40	23	
	100	~160	0.22	42		1.0	~410 ^a	0.44	23	
	125	~172	0.17 ± 0.03	42		5.0	~3300 ^a	0.066	23	
	150	~194	0.22	42	910	0.75	200	0.58	50	
	186	~196	0.18 ± 0.05	42		4.0	550	0.45	50	
	209	~226	0.21	42		17.0	900	0.58	50	
	259	~232	0.18	42		63.7	1470	0.58	50	
	668	40.66	173	0.139		96	146.0	2080	0.675	50
	92.55	263	0.175	96	975	4.0	840	0.47	50	
700	0.2	~60 ^a	0.185	23		16.7	1350	0.67	50	
	2.0	~130 ^a	0.246	23		63.7	2350	0.72	50	
	2.75	66	0.091	96		237.5	4240	0.765	50	
	16.41	150	0.167	96		1000	0.1	~630 ^a	0.27	23
	20	~280 ^a	0.358	23			1.0	~1800 ^a	0.28	23
	100	~500 ^a	0.46	23	3.0		~3000 ^a	0.29	23	
447	676	0.494	96	7.0	~7000 ^a		0.14	23		
750	7.5	187	0.251	96	1100		0.1	~1500 ^a	0.20	23
	23.1	315	0.315	96			1.0	~4600 ^a	0.20	23
	96	~590	0.37 ± 0.04	42		4.0	~9500 ^a	0.18	23	

^aSpecimens oxidized in air, all others in oxygen.

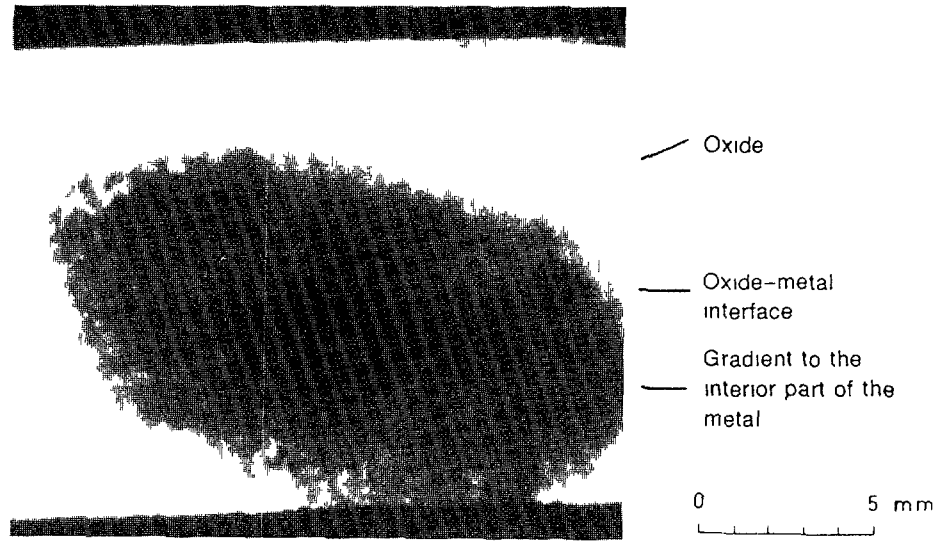


FIG. 2.4. Oxygen distribution in the region between the oxide-metal interface and the metal interior (darkest part) of zirconium, oxidized in oxygen-18 at 600°C for 2.7×10^5 s [6].

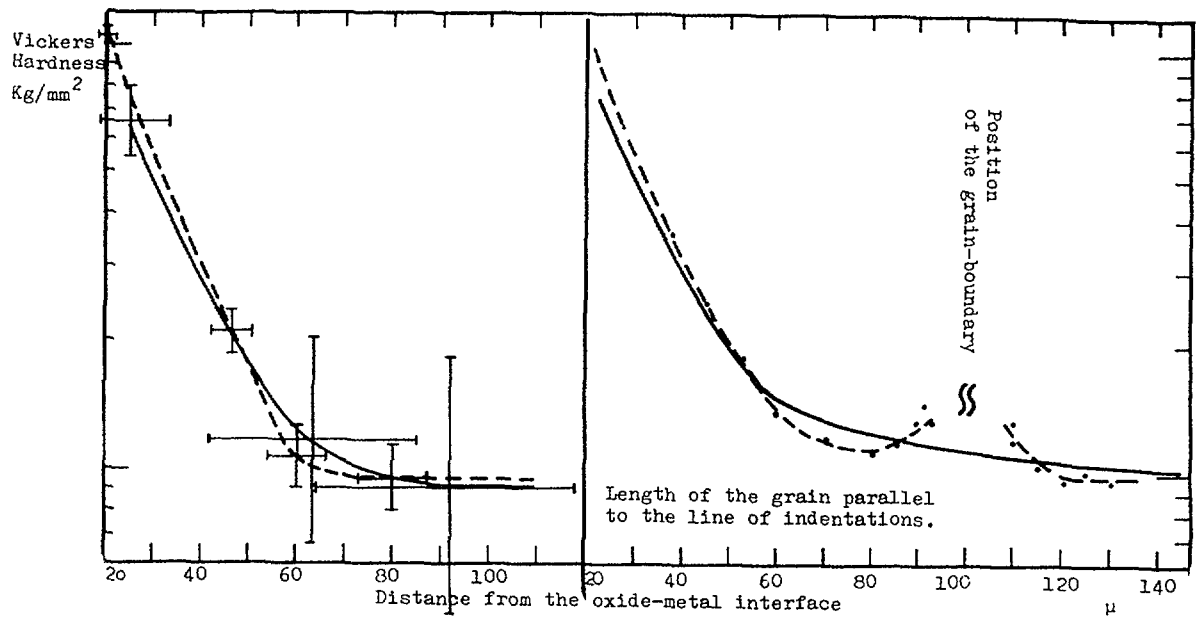


FIG. 2.5a. Size of indentations of microhardness tests, using loads of 15 g - - - and 130 g ——. The specimen was oxidized at 600°C for 1.8×10^6 s [6].

FIG. 2.5b. Microhardness tests in the neighbourhood of a grain boundary, using loads of 15 g - - - and 130 g ——. The size of the crystal grain is small compared to the depth of penetration of oxygen [6].

variations in the oxide thickness at grain boundaries (Fig. 2.7) and variations over an individual grain surface (Fig.2.8) so as to render accurate knowledge of oxide growth kinetics impossible, based on present evidence [8].

The oxide growth kinetics are usually derived from the weight gain kinetics (the amount of O_2 reacting), assuming that all the oxide formed remains on the specimen, converted directly to an oxide thickness (assumed to be uniform) using the theoretical density of ZrO_2 (not known to be accurate). This conversion, in the light of the above, can only be approximate (1 μm oxide \sim 15 mg/dm² oxygen weight gain). The only

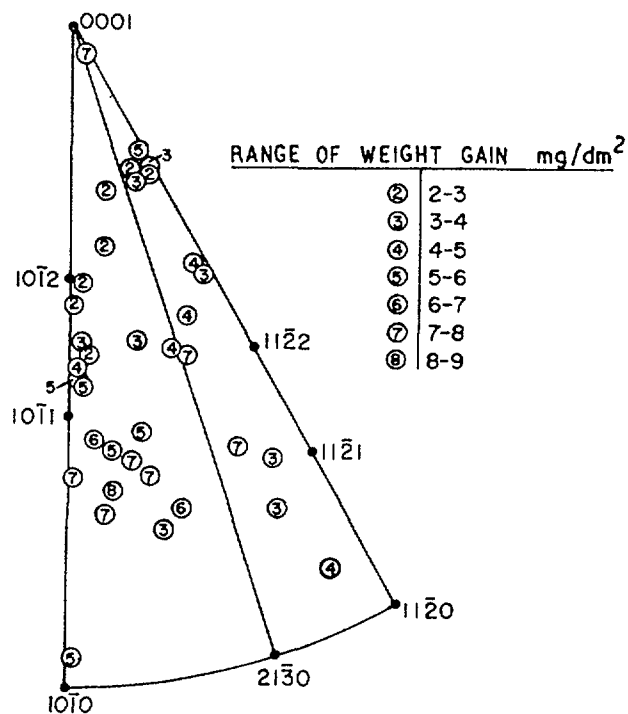


FIG. 2.6. Relation between weight gain on single crystals of Van Arkel zirconium (After 1 min in steam at 500°C, 1 atmosphere) and surface orientation [7].

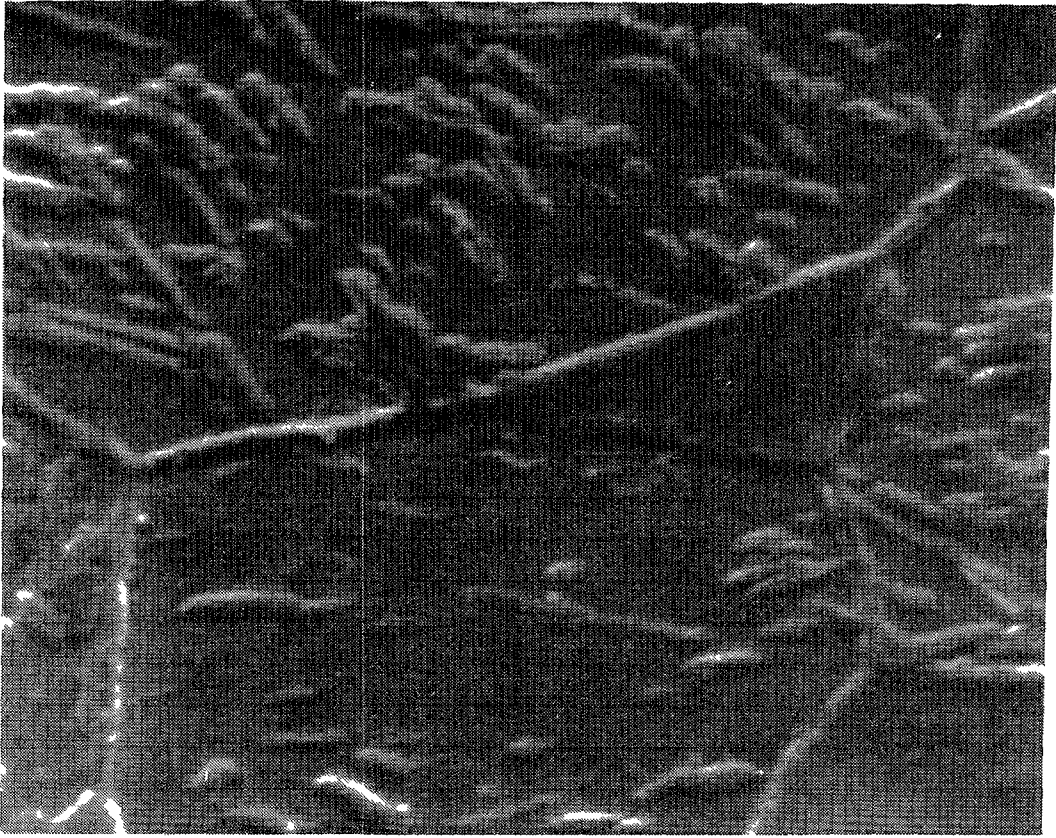
merit that such an approach has is that if used in a standardized manner it permits a comparison of the kinetic behaviour of different alloys. The dissolution of oxygen in the metal is thought (but not known) to be insensitive to alloying variability.

2.1.2. Oxidation kinetics

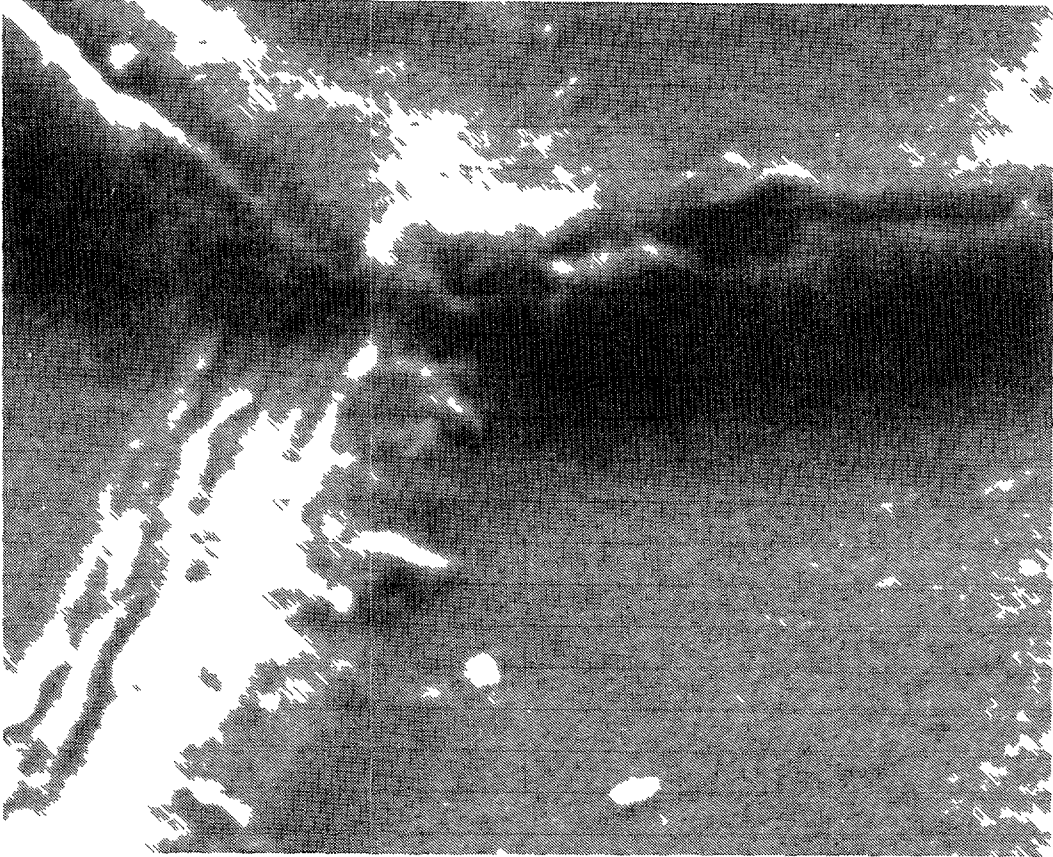
For the present discussion we will accept the fiction that the above conversion of weight gain to oxide thickness gives the oxide growth kinetics but we reemphasize the following caveats:

- Oxide films are assumed, but not known, to have the theoretical ZrO_2 density.
- No correction has been made for local dissolution of oxygen in the metal.
- Unless ΔO (rather than ΔW) is quoted the experimental results have not been corrected for the hydrogen absorbed, if the reaction was with H_2O .
- It is assumed that no loss of oxide occurs by any process (e.g. spalling, dissolution), and that all the weight change measured is from the oxygen reacted (e.g. no carbon from CO_2 , or other species are weighed).

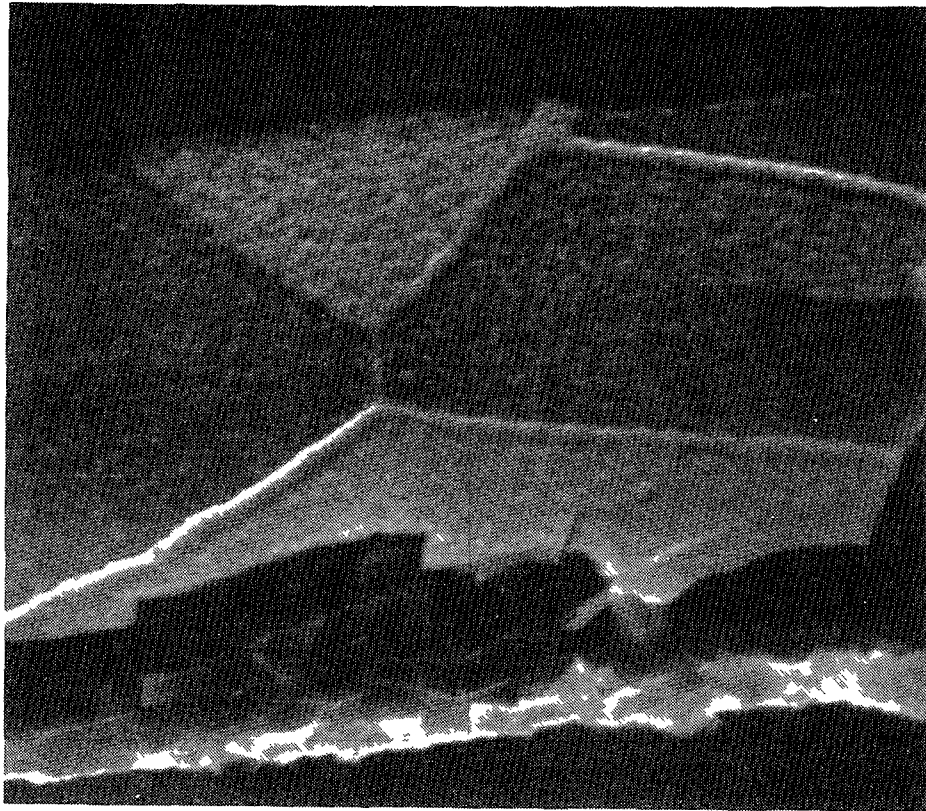
The weight gain kinetics for zirconium and its alloys usually fall into two periods, colloquially referred to as pre and post-transition (Fig.2.9) [9,10]. The initial, pre-transition period is characterized by a decreasing rate of weight gain which is usually closer to a cubic or a quartic growth kinetic curve than to the parabolic kinetics predicted by the Wagner/Hauffe theory. It is believed that the departures from parabolic kinetics arise because the diffusion process controlling oxide



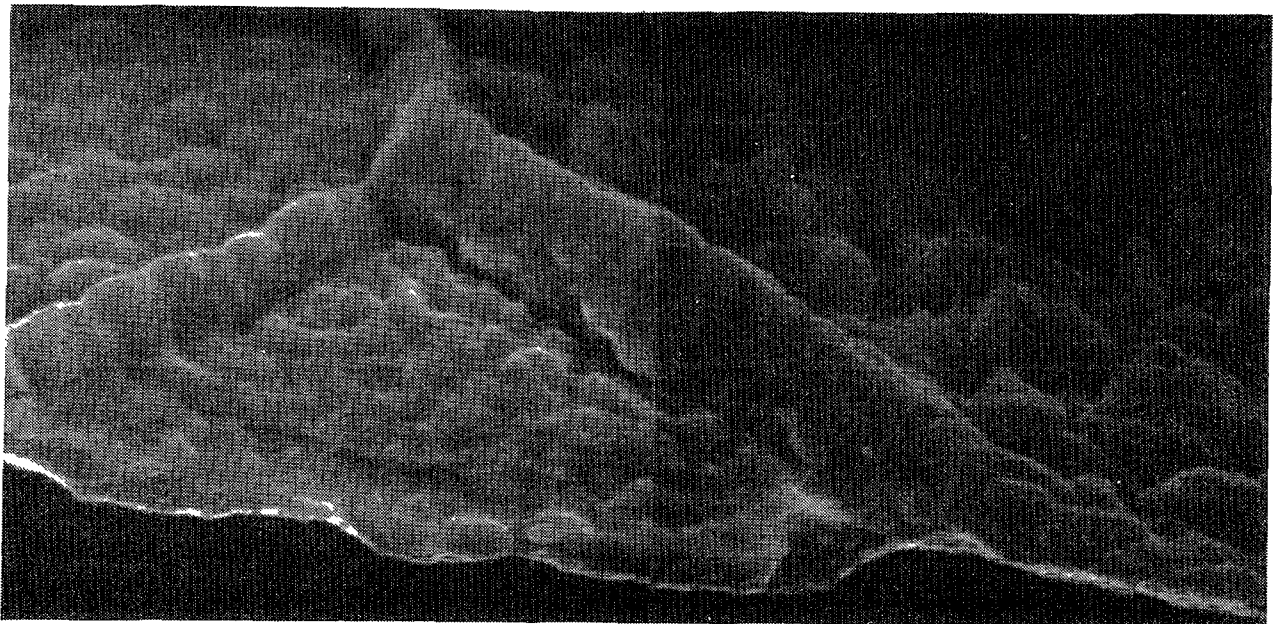
(a)



(b)



(c)



(d)

FIG. 2.7. Oxide ridges at grain boundaries, (a, b) outside surface, (c, d) oxide-metal interface.

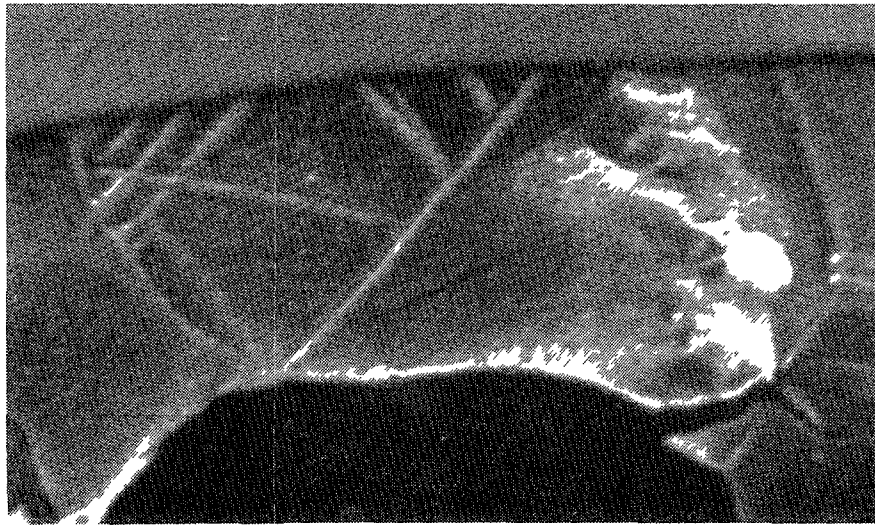


FIG. 2.8. Development of a rough oxide-metal interface. The centre of the central grain is still showing a relatively planar interface, whereas roughening of the interface has spread over the rest of the interface. The straight ridges of thicker oxide are at twins and the curved ones along grain boundaries. Mean oxide thickness: $0.4 \mu\text{m}$ ($2000\times$).

growth is not a homogeneous one occurring in a uniform solid (as required by this theory) but is heavily localized at crystallite boundaries within the oxide [11,12]. Electron microscopy shows that the oxide is microcrystalline (Fig. 2.10) and that the mean crystallite size increases initially as the oxide thickens [13]. Details of this phenomenon are not completely agreed upon. Differences of opinion as to whether some initial crystallite orientations grow at the expense of others, or whether successive layers of crystallites initiate and grow to different extents remain to be resolved. The oxide forms under compression because of the high Pilling-Bedworth ratio (the ratio of the oxide volume to the volume of metal from which it formed) of ~ 1.56 , which depends on the value used for the density of the oxide film.

On massive specimens this volume change must be accommodated normal to the free surface, by a combination of crystallographic and deformation processes that have yet to be explored completely. It is observed that the crystallographic and morphological texture that develops in the oxide is always perpendicular to the oxide/metal interface; that it is not dependent on metal orientation; and that those oxide orientations that develop predominantly in the texture [14] are just those orientations that are needed to minimise the compressive stresses in the plane of the surface (Fig. 2.11). The epitaxial relations observed [15] for very thin oxide films on the $(11\bar{2}0)$ face of zirconium are a mixture of:-

$$\begin{aligned} (100) [001]_m // (0001) [11\bar{2}0] \text{ and} \\ (100) [010]_m // (0001) [11\bar{2}0] \end{aligned}$$

while the minimum stress in the oxide is obtained for [16] $(101)[101]_m // (10\bar{1}0) [11\bar{2}0]$. As the oxide thickens reflections of the form 104 become the most prominent on $(11\bar{2}0)$ and 104 , 102 or 101 are also the strongest on other orientations of the substrate [14]. However, it is evident that no unique epitaxial relationship exists for thermal oxide films on zirconium [15]. This suggests that the increase in crystallite size and the texture that develops are driven by the compressive stresses produced by oxide growth.

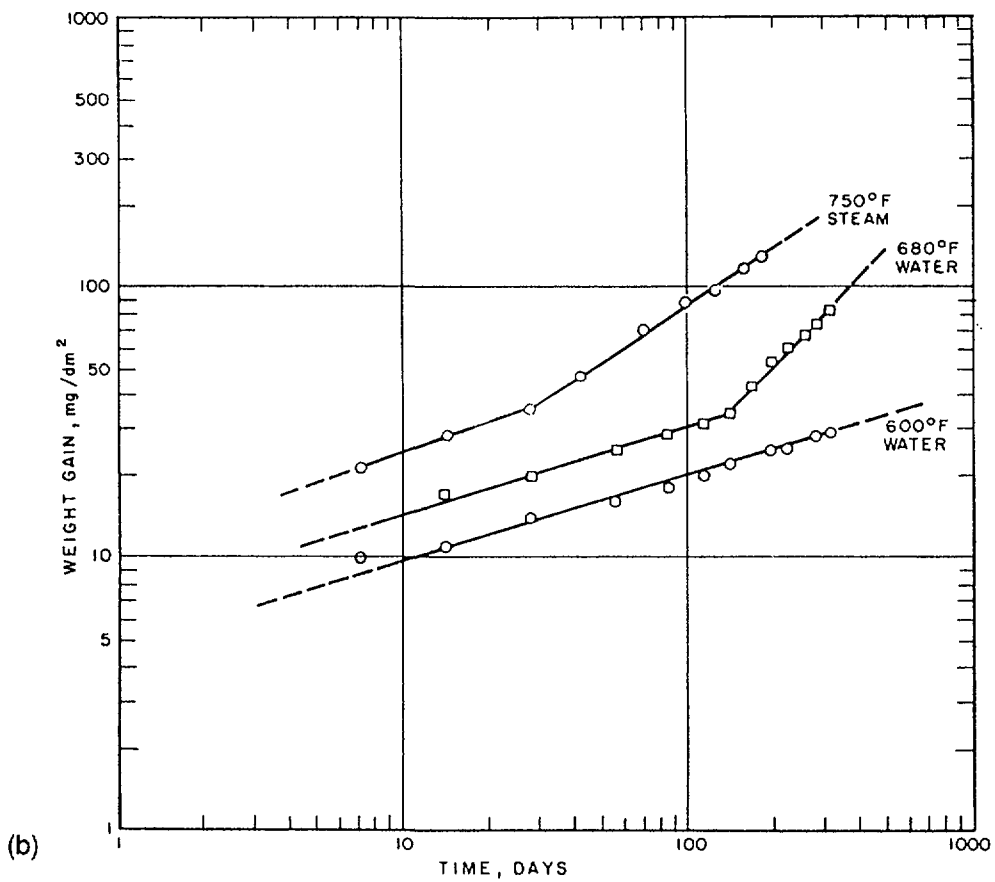
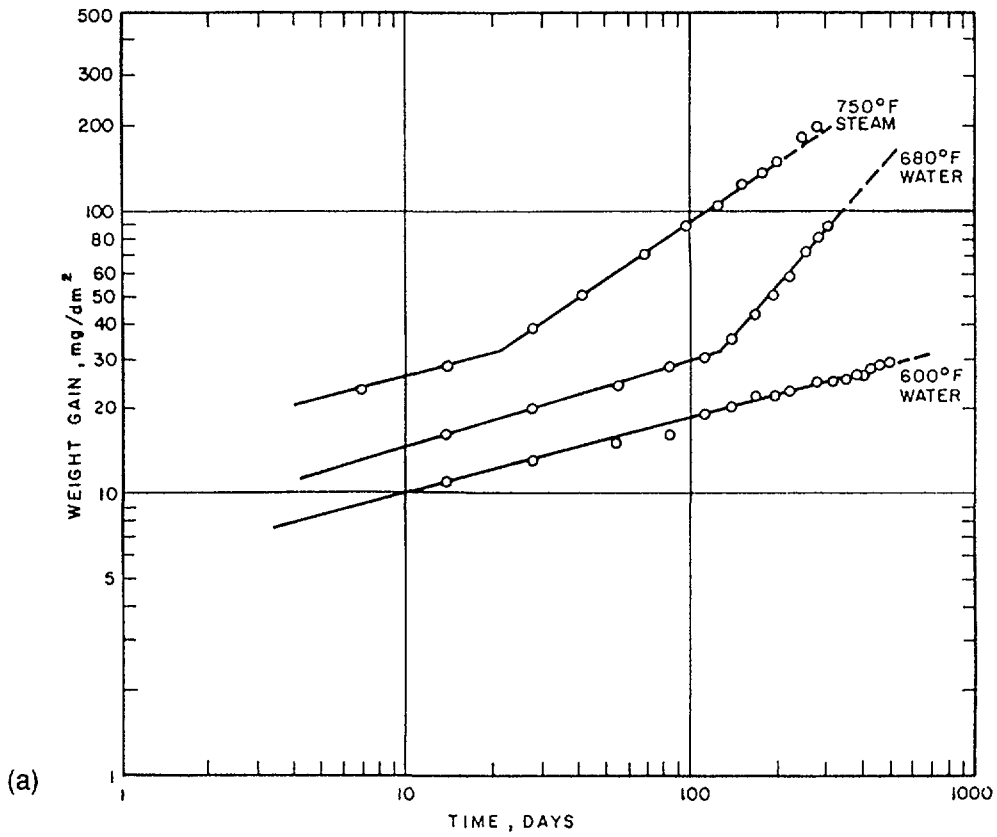


FIG. 2.9. Typical plots of corrosion data for the Zircaloys [10]:
 (a) corrosion of beta-quenched Zircaloy-4;
 (b) corrosion of beta-quenched Zircaloy-2.

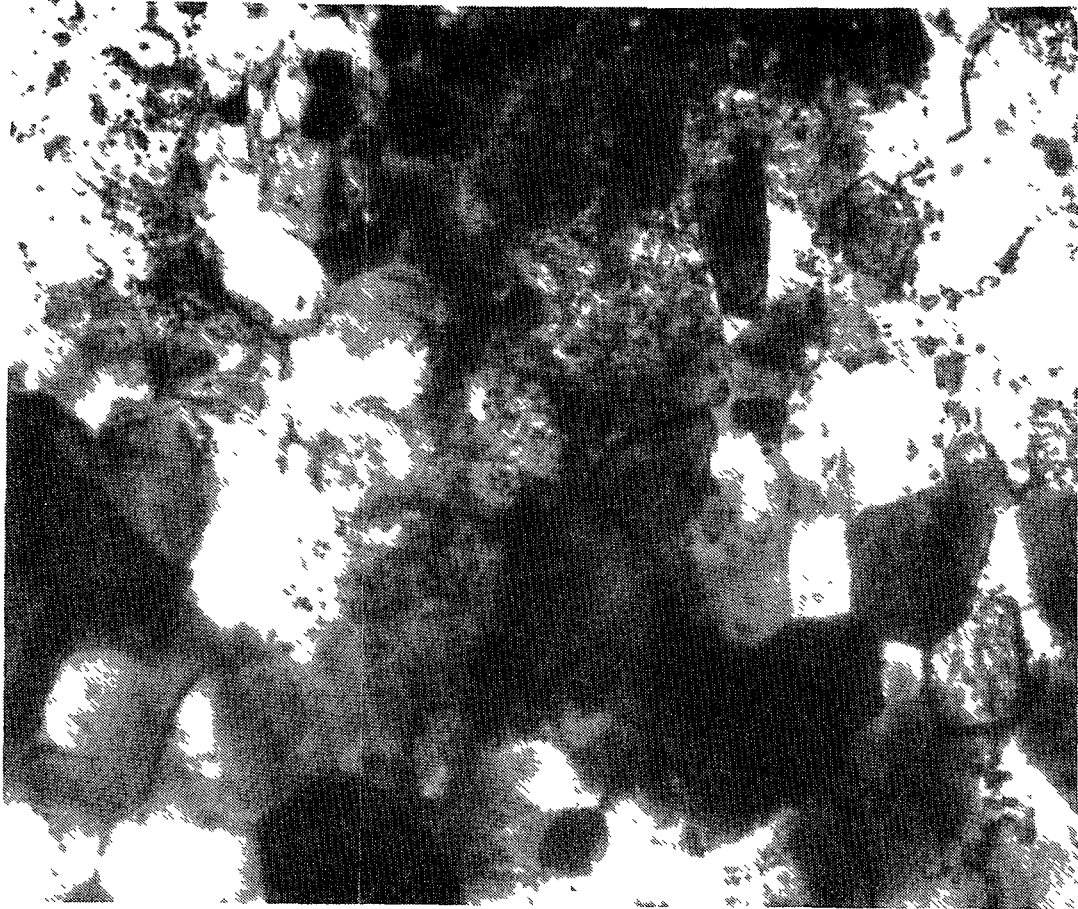


FIG. 2.10a. Transmission electron micrograph showing the structure of the oxide phase adjacent to the oxide-metal interface (bright field).

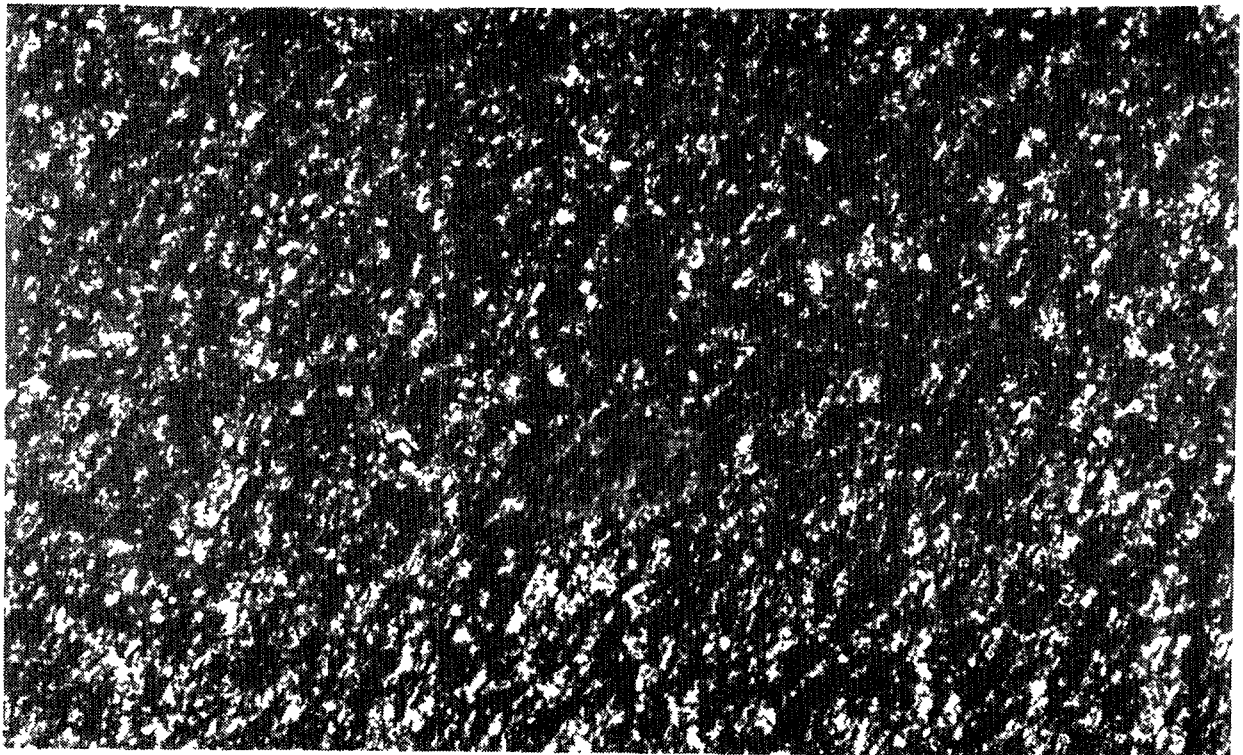


FIG. 2.10b. Crystallite morphology in a thin zirconia film formed at 300°C in oxygen on zirconium (dark field).

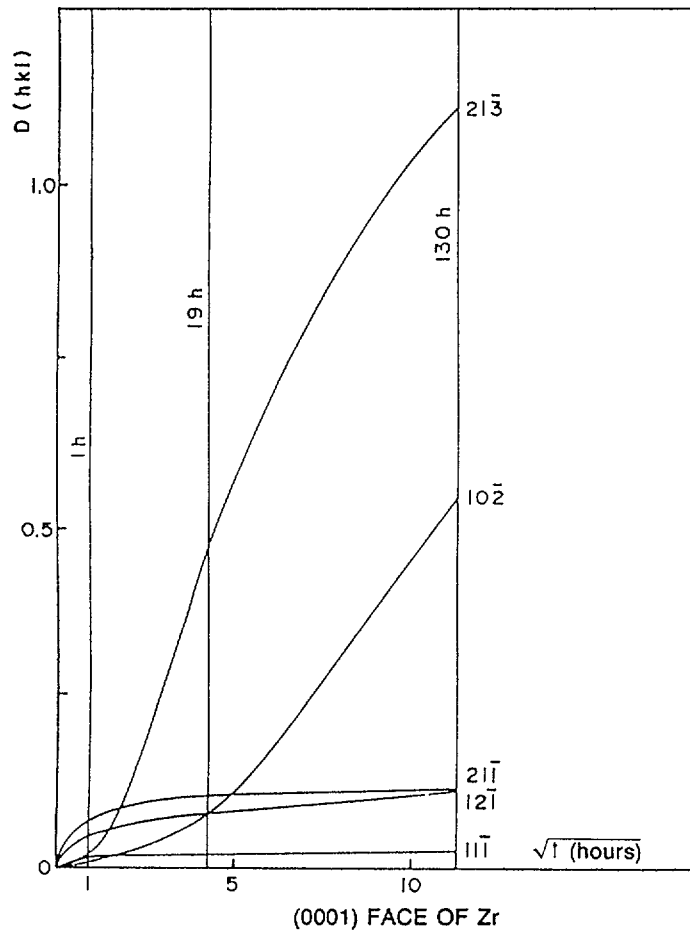


FIG. 2.11. Variation of the values of $D_{(hkl)}$ observed on the (0001) face of a zirconium single crystal during oxidation [14].

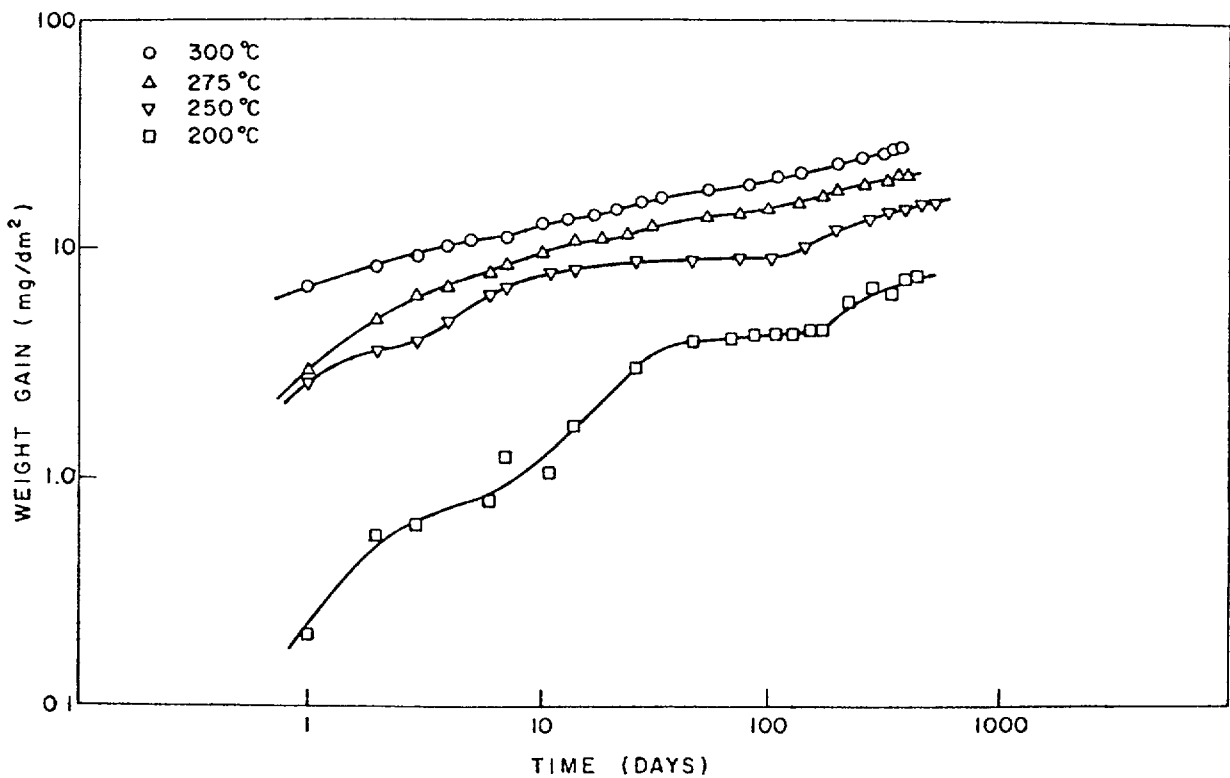


FIG. 2.12. Oxidation of Zircaloy-2 (Ac) in water at 200–300°C [18].

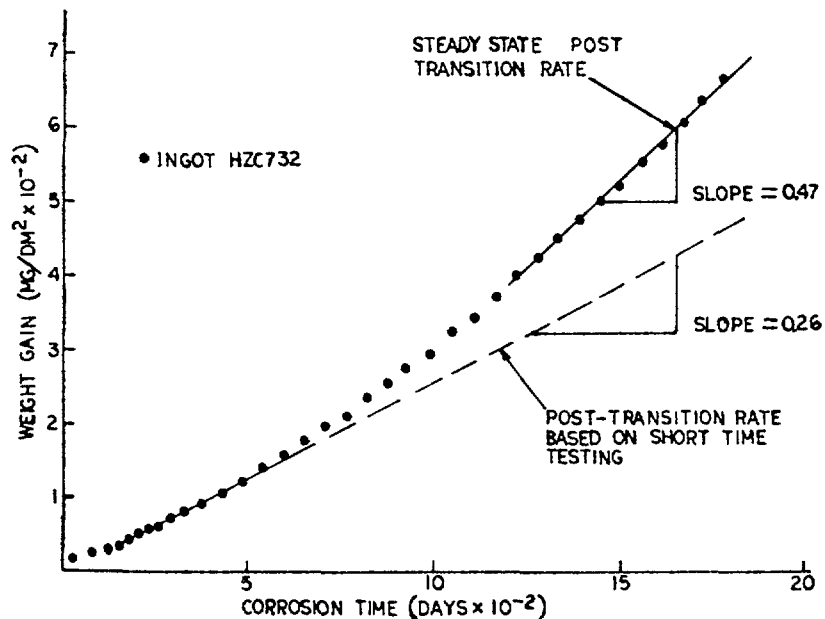


FIG. 2.13. Corrosion weight gain of Zircaloy-4 in water at 633 K [19].

An opposing argument has been made that the compressive stresses influence the diffusion of oxygen directly through an effect on the anion vacancy volume [17]. However, this mechanism does not seem to be able to predict the development of the oxide texture, and is difficult to formulate for a system where lattice diffusion is a minor contributor to the oxygen ion flux. Such effects might represent a further contribution to the low exponents in the rate law, but are difficult to assess in a system where crystallite boundary diffusion predominates.

Although approximating to a cubic or quartic growth curve, the kinetics of pre-transition oxide growth are more complicated than suggested by the single rate law [18]. At least one well defined inflection in the thin oxide film region (0.5 - 0.7 μm) separates the pretransition period into two distinct periods (Fig.2.12). The causes of this change in kinetics and the nature of the early growth have been investigated and explanations suggested [5], but for present purposes these variations can be ignored since under irradiation in-reactor we will always be concerned with thicker oxides than this.

When the oxide reaches a thickness of about 2 μm , the oxidation rate increases to a post-transition linear rate [9,10]. This linear rate may also increase slowly [19] with increasing thickness over long periods of time (Fig. 2.13), but this latter effect is not well established at present. At relatively high temperatures ($\geq 400^\circ\text{C}$) and when measurements are taken continuously with a microbalance (or similar technique), and thereby at low pressure, the change in kinetics to the post-transition linear rate is smooth [20] and no sudden discontinuities are observed (Fig. 2.14). At lower temperatures, high pressures, and when the weighings are done discontinuously (as in all autoclave testing), the post-transition period is initiated by a sudden increase in rate and is followed by a series of oxidation cycles [21], not unlike the initial pretransition period in size and duration (Fig. 2.15). These cycles eventually disappear and an effectively linear post-transition rate becomes evident.

The transition process is indicative of the generation of porosity in the previously impervious oxide film. There seem to be at least two different types of flaw generated at this time; the first are vertical

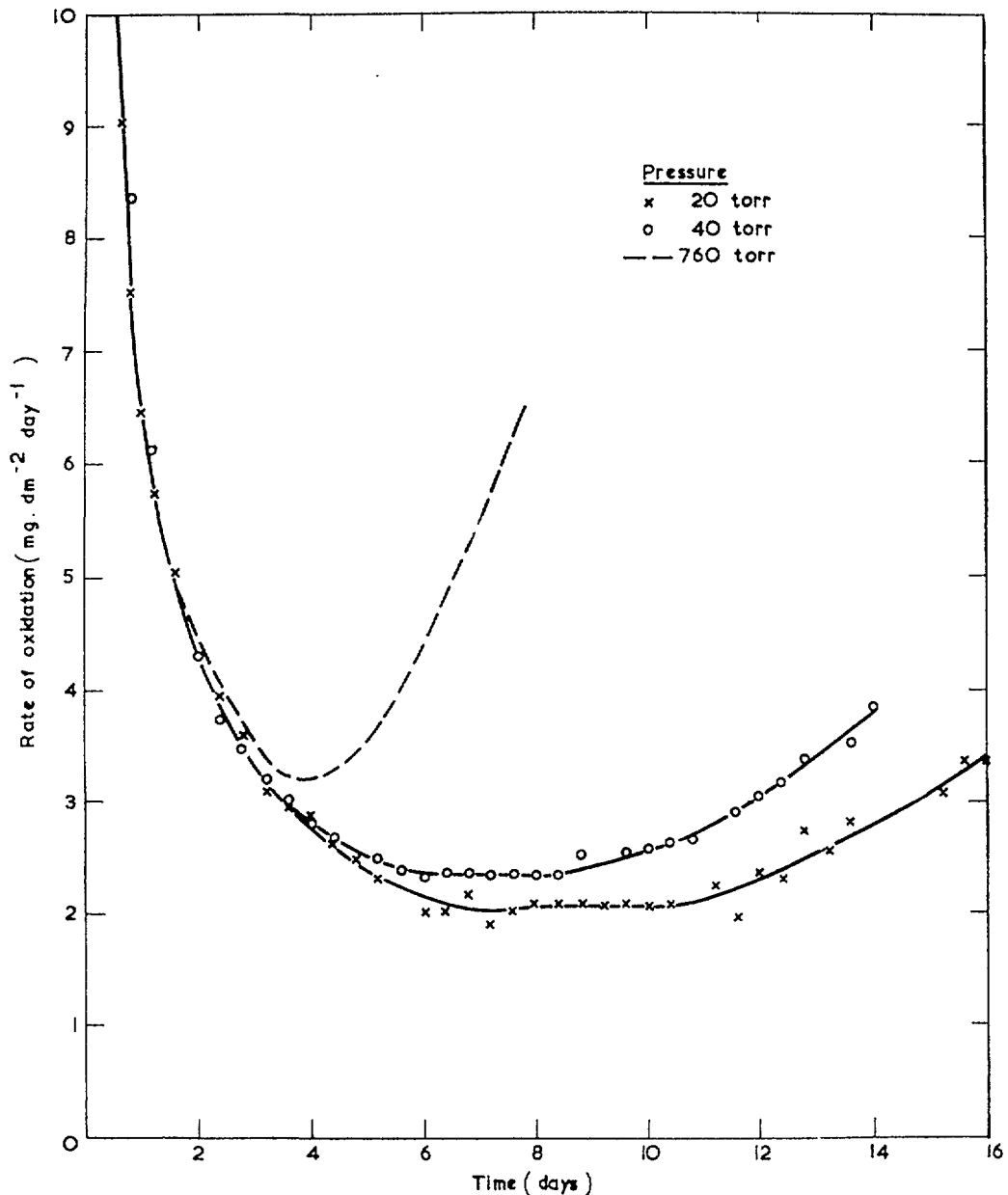


FIG. 2.14. Reaction of Zircaloy-2 with water vapour at 450°C; effect of pressure on the propagation of cubic/linear' transition [20].

cracks that can pass most of the way through the oxide but are usually infrequent except at corners or edges. The second are fine pores (probably at crystallite boundaries) that form a network within the oxide [5,22]. The question of whether lateral cracks also form at this time, or whether these are artefacts of the metallographic technique has been argued extensively [23,24], and at present no unequivocal evidence for their presence is available. Vertical cracks seem to be more prominent in circumstances that encourage cyclic post-transition kinetics and relatively absent when smooth transition curves are observed.

There are two aspects of the cyclic post-transition behaviour that require discussion at this point. The first which will be discussed now is the practical problem of whether or not the cycles are caused, or at least accentuated, by the thermal cycles necessitated by the discontinuous weighing technique; the second, which will be discussed later, is the mechanistic question of whether the cycles do or do not represent the growth of successive layers of pre-transition barrier layer oxide following

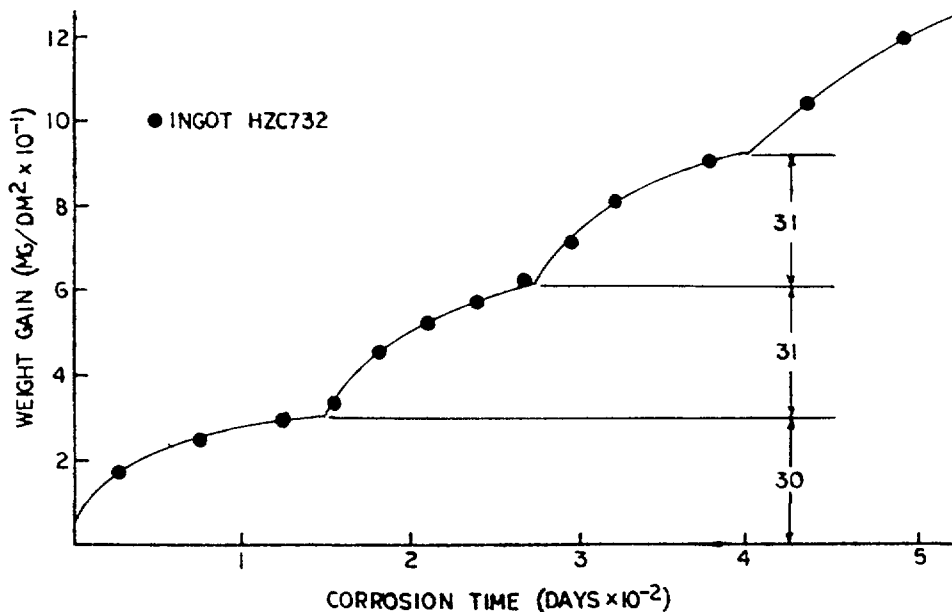


FIG. 2.15. Short-time corrosion weight gain of Zircaloy-4 in water at 633 K [19].

a sudden breakdown of the original impervious oxide by some degenerative process.

The influence of thermal cycling on the kinetics of oxidation has never been fully investigated. Several early studies examined the effect of frequent thermal cycles during the pre-transition period [25] and found no effect (Fig. 2.16). None of these studies was extended up to the normal transition in the oxidation kinetics so that a definitive answer cannot be given. Unfortunately, because most continuous measurement techniques function only at low pressure, and the long times to transition at low temperatures encourage these techniques to be used primarily at high temperatures, there is almost no overlap in temperature and pressure between data sets obtained by continuous or discontinuous techniques. In the interests of establishing the true kinetics at low temperature and high pressure a technique for continuously measuring oxide thickness under such conditions is needed. If such a technique were available, then the effects of deliberately introduced thermal cycles could be investigated. This question is not by any means trivial, since attempts to correlate the effects of irradiation with laboratory data are often made by comparing oxidation kinetics obtained in laboratory autoclaves (with repeated thermal cycling) with data measured on fuel cladding, or other components, at the end of individual reactor cycles that may (in the ideal case) represent exposures of one to two years without a thermal cycle. As a first approach to establishing whether or not such comparisons are valid, a series of autoclave tests running for 1 year, without thermal cycling, should be used to obtain data on identical material to that on which the kinetics have already been established using frequent (14 or 28 day) thermal cycles.

2.1.3. The mechanism of pretransition oxide growth

A comprehensive model for the growth of pretransition oxide films requires the following information:

- (a) A full description of oxide film structure and the evolution of the crystallite size, size distribution and texture; phase composition; the nature of the reasons for the restricted selection of monoclinic crystallite orientations (e.g. does that imply that at temperature the

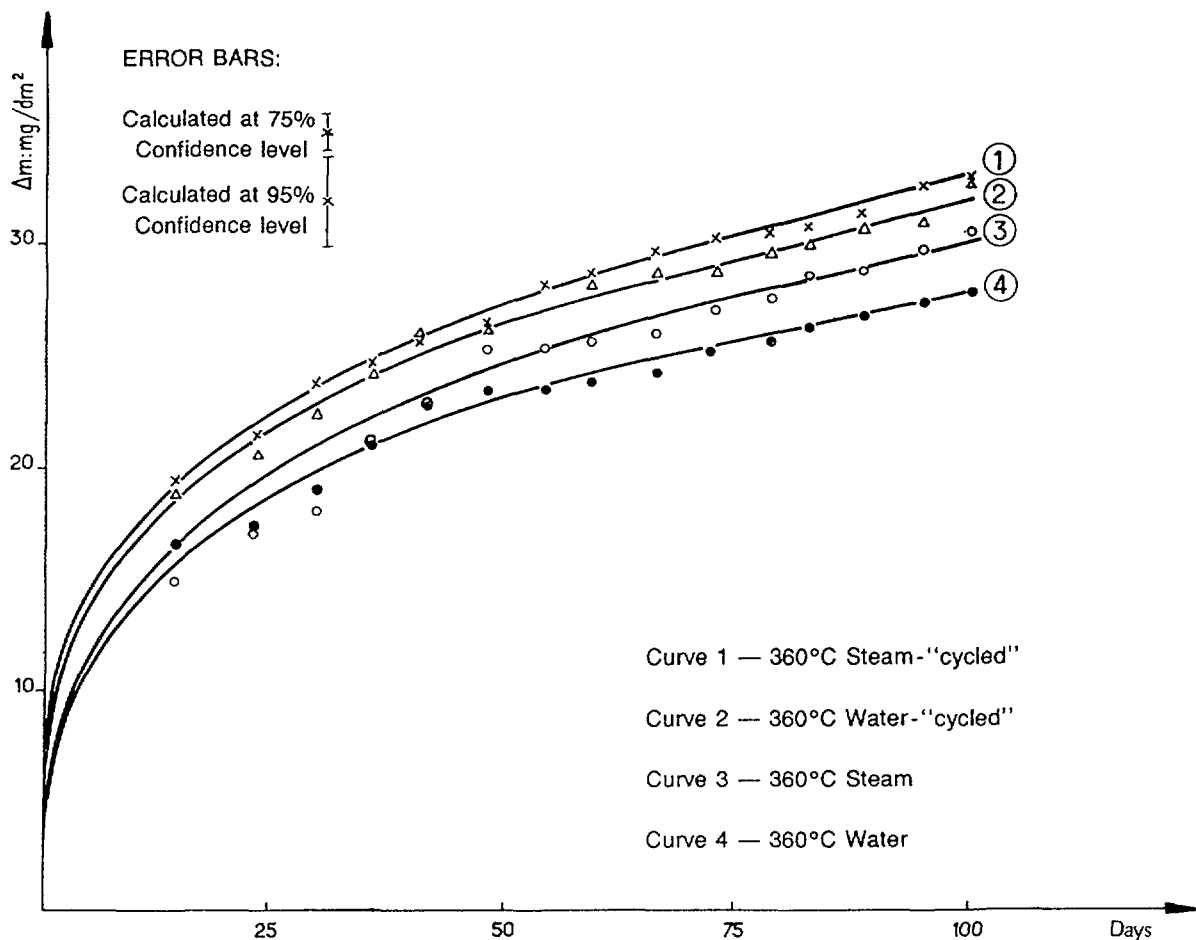


FIG. 2.16. Influence of thermal cycling on the corrosion resistance of Zircaloy-2 [25].

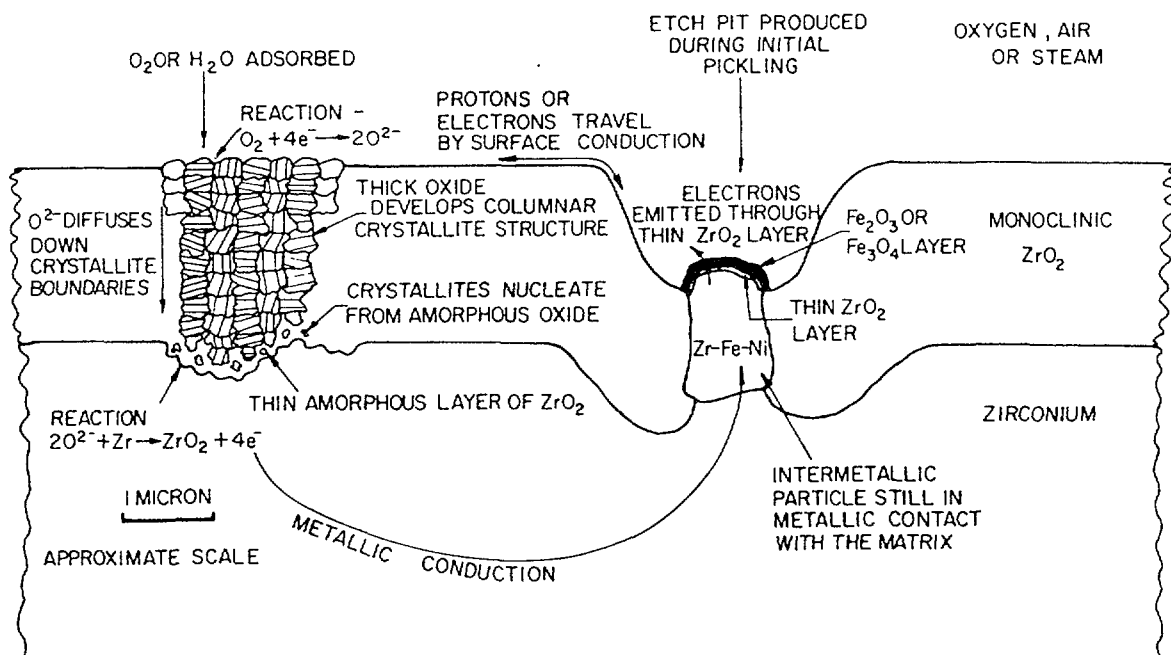


FIG. 2.17. Schematic diagram of oxide film on Zircaloy-2 and the processes occurring in it during oxidation [5].

crystallites were tetragonal or cubic and stabilised by the compressive stresses); knowledge of all the diffusing species (O^{2-} , OH^- , H^- , Zr^{4+} , etc.) and their diffusion kinetics in the lattice and at crystallite boundaries. Figure 2.17 is a simplified attempt to represent a pre-transition oxide film [5].

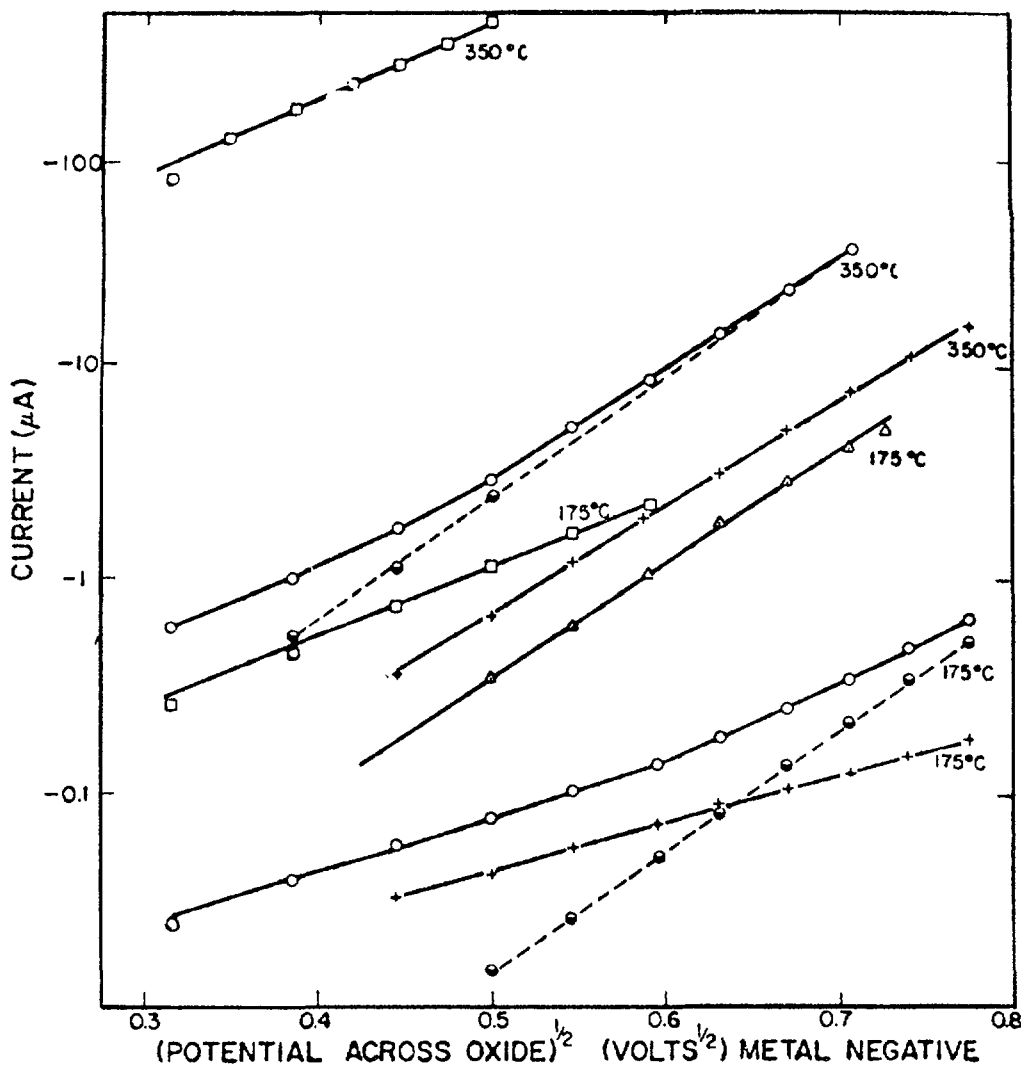


FIG. 2.18. $\log I$ versus $V^{1/2}$ (Schottky) plots for forward electronic (metal negative) characteristics of: +, Zircaloy-2 oxidized in steam (800 psi) at 350°C to a weight-gain of 19 mg/dm²; o, Zircaloy-2 oxidized in dry air at 350°C to a weight-gain of 19 mg/dm²; o, as before but with prior subtraction of an ohmic component of $4 \times 10^6 \Omega$ at 175°C and $3.2 \times 10^5 \Omega$ at 350°C; □, Zircaloy-2 oxidized in air at 350°C to a weight-gain of 19 mg/dm² and then coated with magnetite ($\sim 100 \text{ \AA}$) in 300°C water containing $Fe(OH)_2$; Δ, an anodic ZrO_2 film (300 Å) on crystal-bar zirconium coated with Fe_3O_4 . Specimen area: 8.5 cm² [27].

(b) The nature of the electrical properties of the oxide. Since ZrO_2 is intrinsically an insulator, dopants have a big effect on conductivity. Localized doping, or localized regions of high conductivity for other reasons, are particularly important (Fig. 2.18) [26,27]. Evidence shows that the intermetallics represent such regions in the Zircaloys and unalloyed zirconium (which usually contains Zr_2Fe or Zr_3Fe precipitates), but not in Zr-2.5 Nb which is generally free of them in the cold-worked condition if the Fe impurity concentration is low [5]. In the latter alloy the transition metal impurities dissolve preferentially in the β -Zr phase.

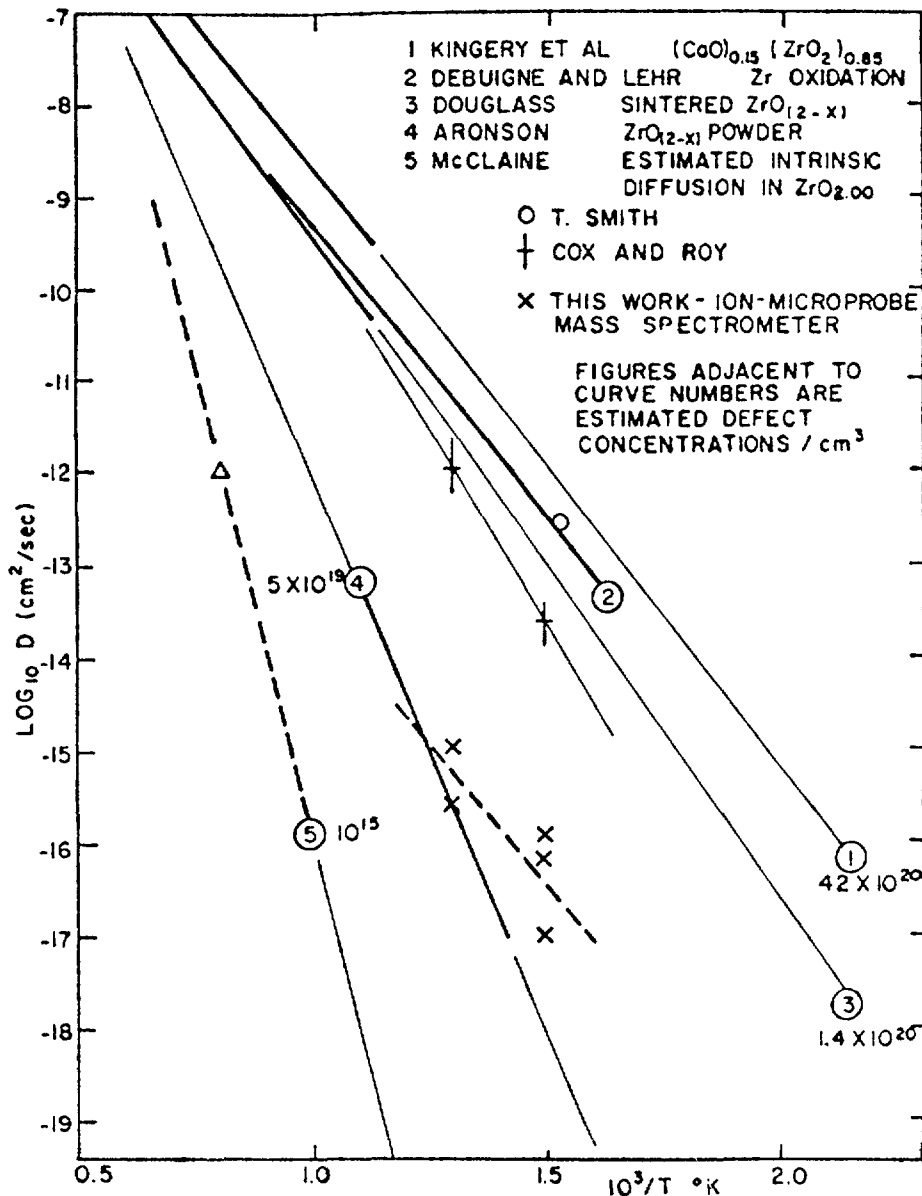


FIG. 2.19. Diffusion coefficients for oxygen in zirconia (references refer to the original figure in Ref. [12]).

(c) Correlations of oxidation kinetics with O_2 diffusion in ZrO_2 fit best with crystallite boundary diffusion [11,12] which is many orders of magnitude higher than that for lattice diffusion at normal reactor temperatures (Fig. 2.19); but the details of this process, rather than average values over large areas are needed because of the localised thickness variations that develop at the oxide-metal interface.

(d) Electrochemical studies show that high fields persist across the oxide (Fig. 2.20), and that this electronic resistivity is a significant component of the overall oxidation resistance [28]. However, a detailed understanding of local conduction effects remains absent for oxides in high temperature water, and is especially important under irradiation.

(e) In order to describe the overall oxidation process we must concentrate on the closed circuit electrochemical aspects. The electronic current flows at local sites (intermetallics) in the Zircalloys; the surface current of electrons or protons represents an electrochemical potential variation across the surface. Thus, the surface potential is expected to

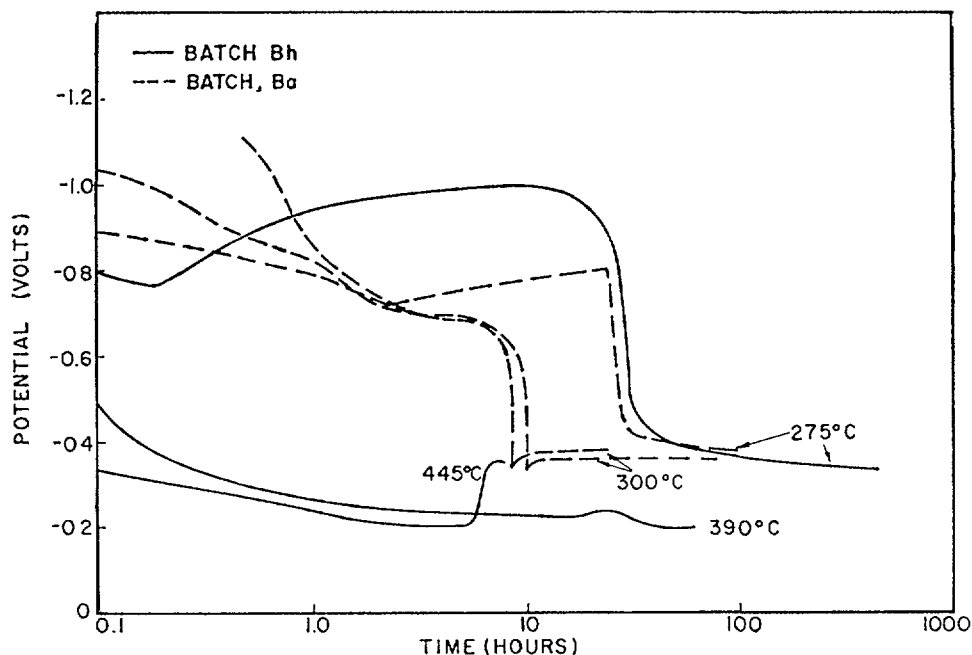


FIG. 2.20. Potential versus time curves for Zircaloy-2 in fused salt (Bh and Ba refer to the designations of two batches of Zircaloy-2) [28].

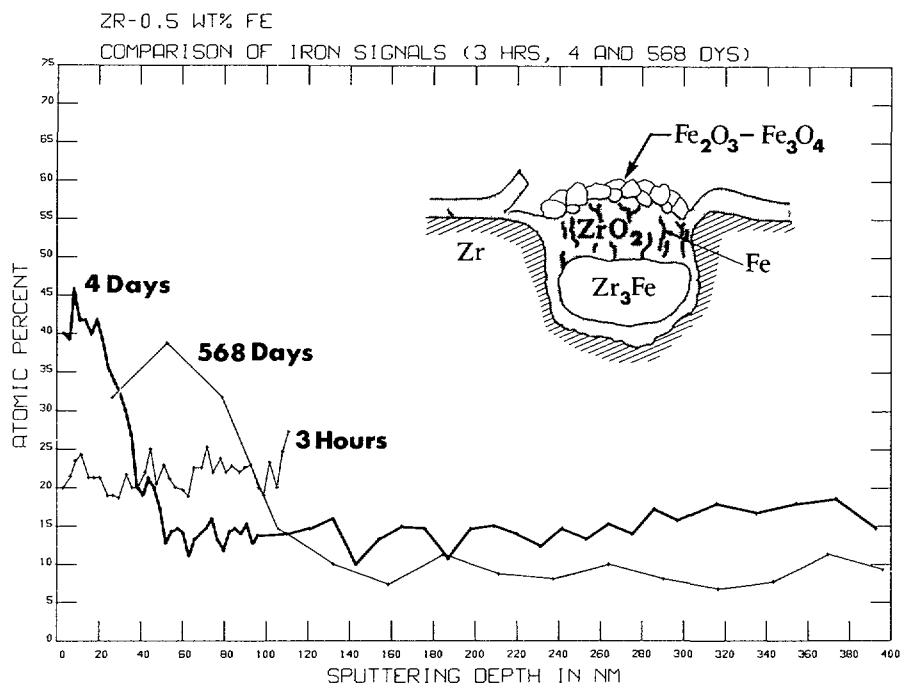


FIG. 2.21. Iron profile, for three different lengths of oxidation at 573 K, within the oxide film formed on a Zr_3Fe precipitate [29].

be very position dependent. Little or no evidence on this is available even at low temperatures.

(f) For alloys other than the Zircaloys we must make individual studies e.g. Zr-Nb has few intermetallics, and evidence suggests that electronic conduction is relatively homogeneous. Thus, surface potential variation may be much smaller than for the Zircaloys.

(g) The evolution of the oxide structure and the incorporation of alloying elements in pretransition oxides are not well known - Electron

microscopy gives good data in the very thin film region of oxide evolution. Ion milling of thick films is possible with difficulty but at intermediate thicknesses (0.5 - 4 μm) the films are not well characterized. Similarly, the distribution and location of impurities and alloying elements across the oxide [29] are known for thick films from Auger Electron Spectroscopy (Fig. 2.21) but evidence on pretransition oxides is slender and not always believable. Whether the alloying additions and impurities occupy substitutional or interstitial positions in the oxide and their effective valence in barrier type oxide films, is virtually unknown for all species. A start on such measurements has been made for Fe in ZrO_2 by Mossbauer Spectroscopy [30].

The gaps in our knowledge of the oxidation process in the absence of irradiation are still tremendous and most mechanistic discussion, as a result, can only be qualitative. The state of even this qualitative understanding has hardly advanced in the last fifteen years.

2.1.4. Mechanism of oxide breakdown

The fact that there is an acceleration in the oxidation rate at the transition point in Zircalloys implies an effective reduction of the protective fraction of the total oxide film. The processes causing this thinning are the source of some contention. Clearly cracking of the oxide occurs as crack networks are seen by electron-microscopical replica techniques (Fig. 2.22). However, at high temperature ($\sim 500^\circ\text{C}$) and low pressure a rate transition occurs but visible cracks are few and far between (Fig. 2.23). This has led to the suggestion that a network of fine pores was involved in the transition process under these conditions [5]. The onset of these breakdown processes occurs by a process of local nucleation followed by spreading across the surface. Edges, support holes, punched-in identification numbers and a "random" distribution of other surface sites provide the initiation points [40]. During transition a spotty appearance that is superficially similar to nodular corrosion often appears. However, during the normal rate transition there is little difference in oxide thickness between white spots and the surrounding black oxide [40].

Porosimetry with mercury filling the pores (Fig. 2.24) under pressure was able to measure the effective diameter of these pores (if they were assumed to be straight cylinders), and impedance measurements, particularly measurements with mercury and aqueous electrolytes gave an indication of the depth of penetration. This has suggested that the pores approached close to, if not right up to, the metal/oxide interface, leaving no thickness of barrier oxide that is significantly thicker on average than the normal air formed oxide (2-5 nm) [22,31]. By contrast, post transition oxides formed in high temperature water (300-360 $^\circ\text{C}$), often showed a dense network of cracks. Thus, in general the smooth kinetic transition seen in high temperature/low pressure conditions can be ascribed to the development of a network of fine pores, while the discontinuous cyclic kinetics seen in the low temperature/high pressure conditions may be ascribed to local cracking of the oxide. The question of whether the fine-pore development occurs also in this instance is still argued, although the porosimetry strongly suggests that it does. Porosimetry also suggests that there is no post-breakdown reformation of a significant thickness of barrier oxide as suggested by Kass [32]. The cyclic nature of the kinetics may, therefore, mark the successive formation of the networks of grosser cracks, with further growth of porous oxide at the metal-oxide interface between these episodes of cracking.



FIG. 2.22. Zircaloy-2 surface after oxidation in steam at 350°C (billet Z8006, 192 days at 350°C, weight gain 40 mg/dm²) (6000×) - specimen surface was uniformly covered with cracks at about this frequency [5].

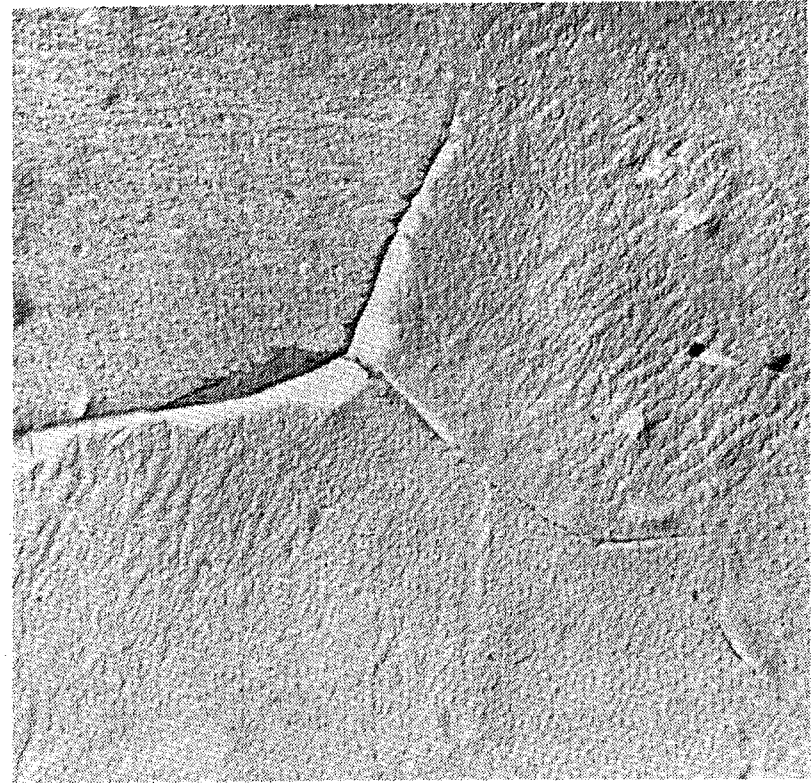


FIG. 2.23. Zircaloy-2 surface after oxidation in steam at 500°C (billet Z105, 12 days at 500°C, weight gain 360 mg/dm²) (16 000×) - only a few small cracks like this were seen on the whole surface [5].

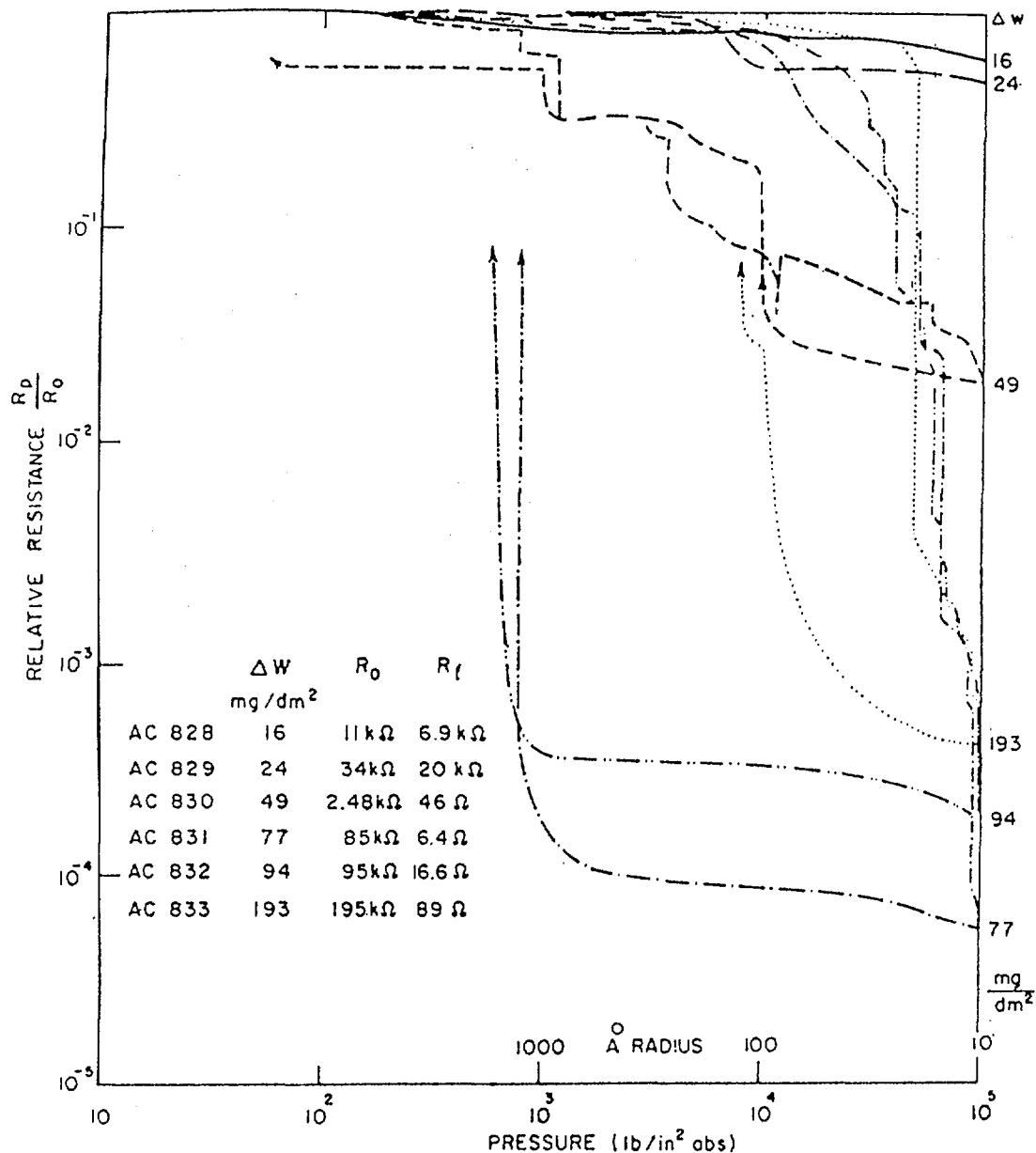


FIG. 2.24. Development of porosity in oxide films formed in 400°C steam. Note appearance of porosity prior to normally accepted weight gain at transition (~30 mg/dm²) [22].

The argument that these pores or cracks only progress a fraction of the way through the oxide has been made both on mechanical grounds, and on the basis of impedance measurements in aqueous solution. The high compressive stresses in the oxide film at the oxide-metal interface decline monotonically towards the surface of the oxide because fresh oxide layers are formed by inward migration of oxygen alone. A crack or pore initiating at the surface (because this region has gone into tension) should penetrate only to the level where the net stress in the oxide is zero (neutral axis) after redistribution of the stresses in the oxide. The mechanical argument cannot explain the apparently deep penetration of the porosity. The impedance measurements in aqueous electrolytes are less definitive than those made in mercury because of the high double layer impedance in series with the oxide (even for air formed oxides). This renders the technique insensitive to small pores progressing close to oxide/metal interface, even if aqueous solutions are able to enter them. Penetration by the electrolyte will not necessarily occur if the experiment is not done under

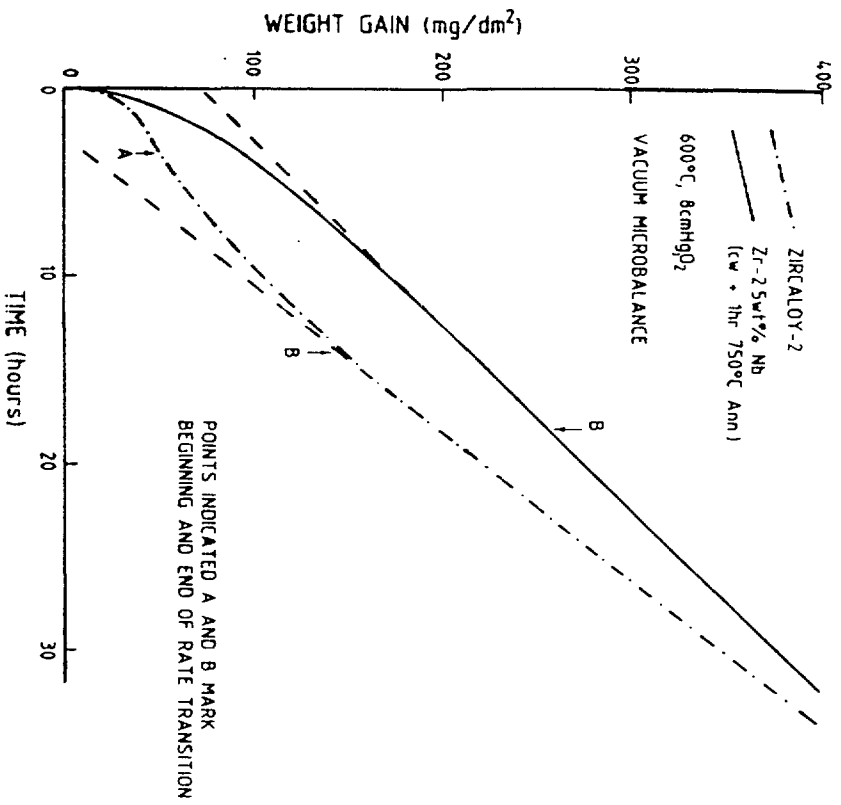


FIG. 2.25. Oxidation kinetics of Zircaloy-2 and Zr-2.5 Nb on linear co-ordinates obtained by continuous weighing [36].

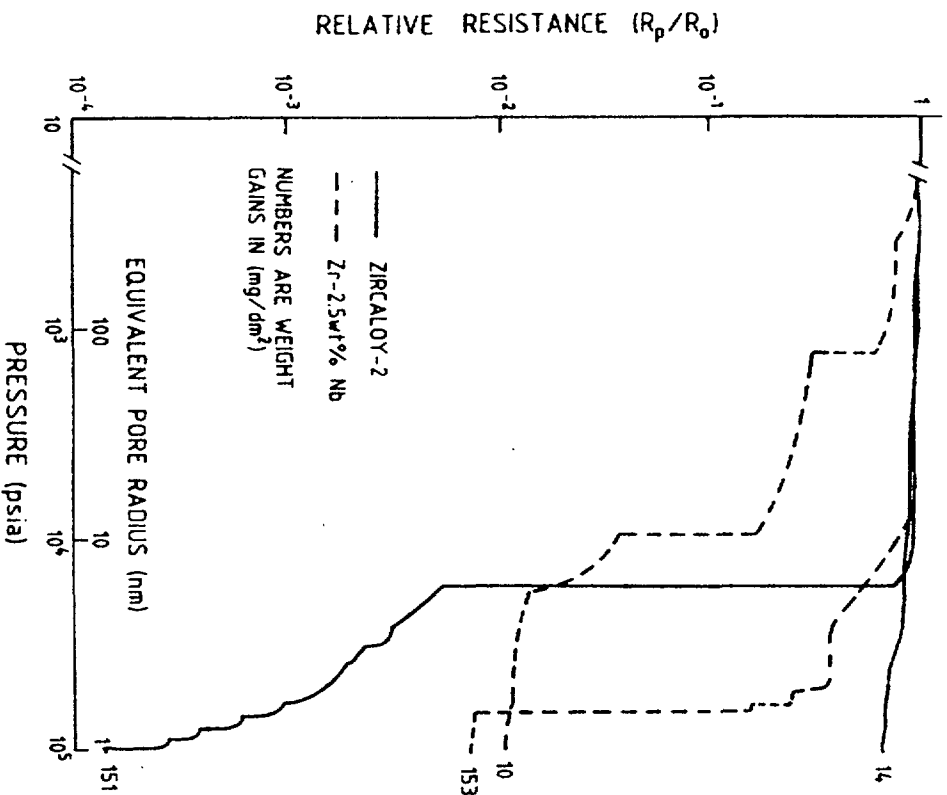


FIG. 2.26. Comparison of porosimeter results on oxide films on Zircaloy-2 and Zr-2.5 Nb [36].

vacuum, because of the compression of the air in the pores by the rising electrolyte level.

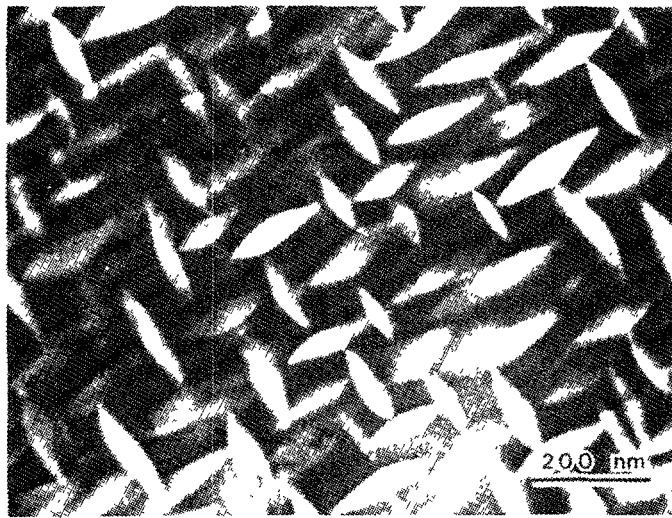
In the case of the other alloys the kinetics of the rate transition do not necessarily follow this form. For instance, the Zr-2.5 Nb alloy often shows a traditional parabolic form of kinetics where no well defined increase in oxidation rate occurs (Fig. 2.25) [33]. This is generally explained as the development of porosity from the start of oxidation, that ultimately reaches an equilibrium (linear rate) when the rate of development of porosity and of new barrier oxide become equal. This view is confirmed by porosimetry and impedance measurements that show similar, (but perhaps a bit smaller) pore sizes than in the Zircalloys, with much thicker barrier oxide layers for Zr-2.5 Nb (Fig. 2.26) [33].

The mechanisms by which the various defects form in the oxide are still generally unclear. The stress gradient through the oxide, that results from its formation exclusively by oxygen migration, will result in the surface layer eventually going into tension. On such an hypothesis, the outer layer would crack once it went into tension and the crack would propagate to the position of zero stress in the oxide (neutral axis), but should not propagate to the oxide/metal interface (even after the stresses in the oxide are redistributed). Another hypothesis for generating small microcracks in the oxide derives from the observation that those monoclinic ZrO_2 crystallites forming on the surface are just the restricted range of orientations that could be expected if the oxide were formed initially as cubic or tetragonal ZrO_2 and transformed subsequently to monoclinic ZrO_2 [13,34]. On this hypothesis the oxide film would be a form of partially stabilised zirconia (PSZ), with a significant percentage of tetragonal ZrO_2 maintained by the high compressive stresses. As any given tetragonal crystallite moves out in the oxide (by formation of fresh oxide below it) this stress would decrease, and would eventually become too small to stabilize tetragonal ZrO_2 . The crystallite would then undergo the martensitic transformation, leading to a twinned structure that seems to generate microcracks in commercial ceramics (Fig. 2.27) [35].

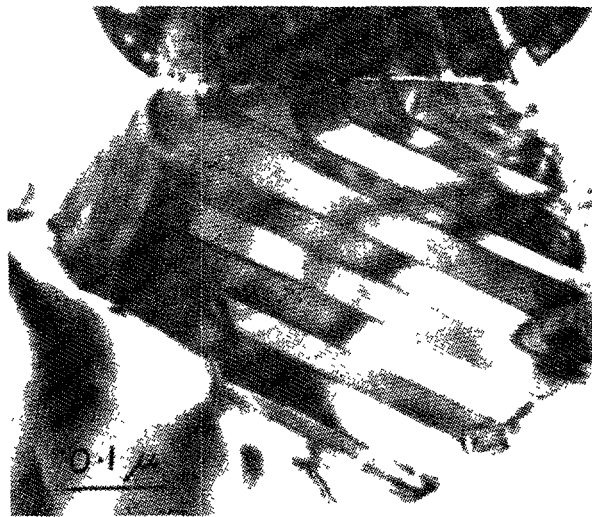
Such cracks could then interlink to form the fine pores, or act as nuclei for grosser cracks. In this instance, although such microcracking should initiate at or near the oxide/environment interface, it should progress to the point in the oxide where the compressive stress in the oxide equalled that necessary for the stability of tetragonal ZrO_2 . This would predict much deeper cracking than the simple mechanical hypothesis, and would result in a barrier layer thickness dependent on the matrix strength (since the maximum stress achievable in the oxide is influenced by the creep strength of the substrate). If the stress decreases approximately linearly with distance through the oxide from the oxide/metal interface to the oxide/environment interface then, for a high strength alloy such as Zr-2.5 Nb the position at which the tetragonal/monoclinic transformation of the ZrO_2 occurred would be further from the oxide/metal interface in this instance than for an alloy with a weaker matrix. This could explain the thicker barrier layer in oxides on Zr-2.5 Nb, than on the Zircalloys [36], however, unfortunately no direct evidence for such a transformation occurring in the oxide film has been found.

2.1.5. Post-transition growth

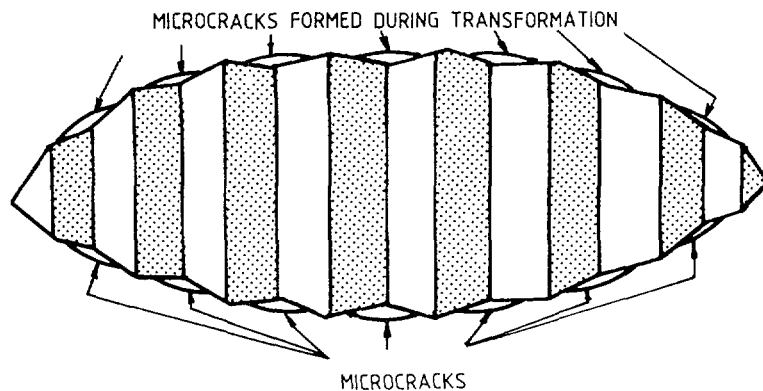
Once the post-transition oxide film develops an equilibrium pore and crack structure the oxidation rate becomes effectively linear. As has been pointed out the cyclic nature of the kinetics after transition probably represents cycles of formation of grosser cracks in the oxide. There is no



(a)



(b)



(c)

FIG. 2.27. Partially stabilized zirconia containing $t\text{-ZrO}_2$ particles (a), transformed ZrO_2 particle in Al_2O_3 (b) and mechanism of microcrack formation during twinning on transformation (c) [35].

unequivocal evidence to support a reformation of a thick barrier layer at any time during these cycles [22,31,32].

In-reactor, where a further increment of irradiation induced creep and growth may be present [37], a further hypothesis, by which creep of the substrate induced cracking at or near the oxide/metal interface may be possible. Such cracks would then propagate outwards until they reached the surface. Localised creep of the substrate may also occur at the

oxide-metal interface during out-reactor corrosion as part of the processes that accommodate the volume change during oxide formation. If so, then a similar crack nucleation process could occur.

The distinction between these various hypothesis may be possible with a careful combination of electron microscopy and impedance techniques, although the relaxation of stresses during the preparation of E.M. foils may induce cracks that were not there to begin with. In thick oxides, cracks penetrating only to the approximate position of the neutral axis can often be seen metallographically, but are normally too few to explain the overall oxidation behaviour, although they do seem to cause regions of locally thick oxide. If small pores are developing from the interlinking of microcracks produced by either of the other two hypotheses, then a distinction might be made if we could establish whether pores start to develop at the oxide/environment interface or the oxide/metal interface. Impedance techniques using a variety of contacts on the outer surface (including immersion techniques) and analysis of the frequency spectrum may be able to resolve this, even if the pores cannot be seen in electron microscope replicas. Such measurements in bulk PSZ claim to be able to distinguish bulk from grain boundary diffusion (for example) [38]. In high temperature water the potential for dissolution processes to enlarge these pores, or to cause them in the first place (as seems to occur in concentrated LiOH solutions) must also be considered [39].

2.2. NON-UNIFORM (NODULAR) OXIDE FORMATION

This phenomenon is particularly relevant to nodular corrosion under BWR water chemistry conditions. Unfortunately no out-reactor simulation of this has yet been achieved in high temperature water in the laboratory, although many causes of white-oxide-spot formation have been investigated in the past [40]. These can be summarized as:

- Formation at carbide particles
- Formation at large intermetallics
- Formation at gas-void stringers
- Formation with impurities (e.g. F⁻) in the water
- Formation at hydrides.

None of these seems to be capable of explaining the BWR observations. However, nodule formation in 500°C high pressure steam seems capable of giving good correlations with observed material lot variability in-reactor [41]. Variations on the 500°C steam test in the form of either a dual temperature test (simulating preoxidation) [42] or a higher temperature 520°C test (claimed to give better discrimination of batches) [43] are now being recommended. Whatever the precise test conditions used, β or ($\alpha + \beta$)-quenched material gives the best resistance to the high temperature test.

Despite this there are clearly aspects of the in-reactor behaviour that are not normally present in the steam test (e.g. electrochemical and galvanic effects), so one is left wondering how close is the scientific comparability of the two phenomena. The experiments of Urquhart and Vermilyea in 500°C steam with applied potentials [44] suggest the importance of such effects but do not necessarily cause the same phenomenon since the currents were not controlled in these tests. Thus, local ohmic heating (such as causes the breakdown of anodic oxide films) cannot be eliminated as a possible cause of their observations.

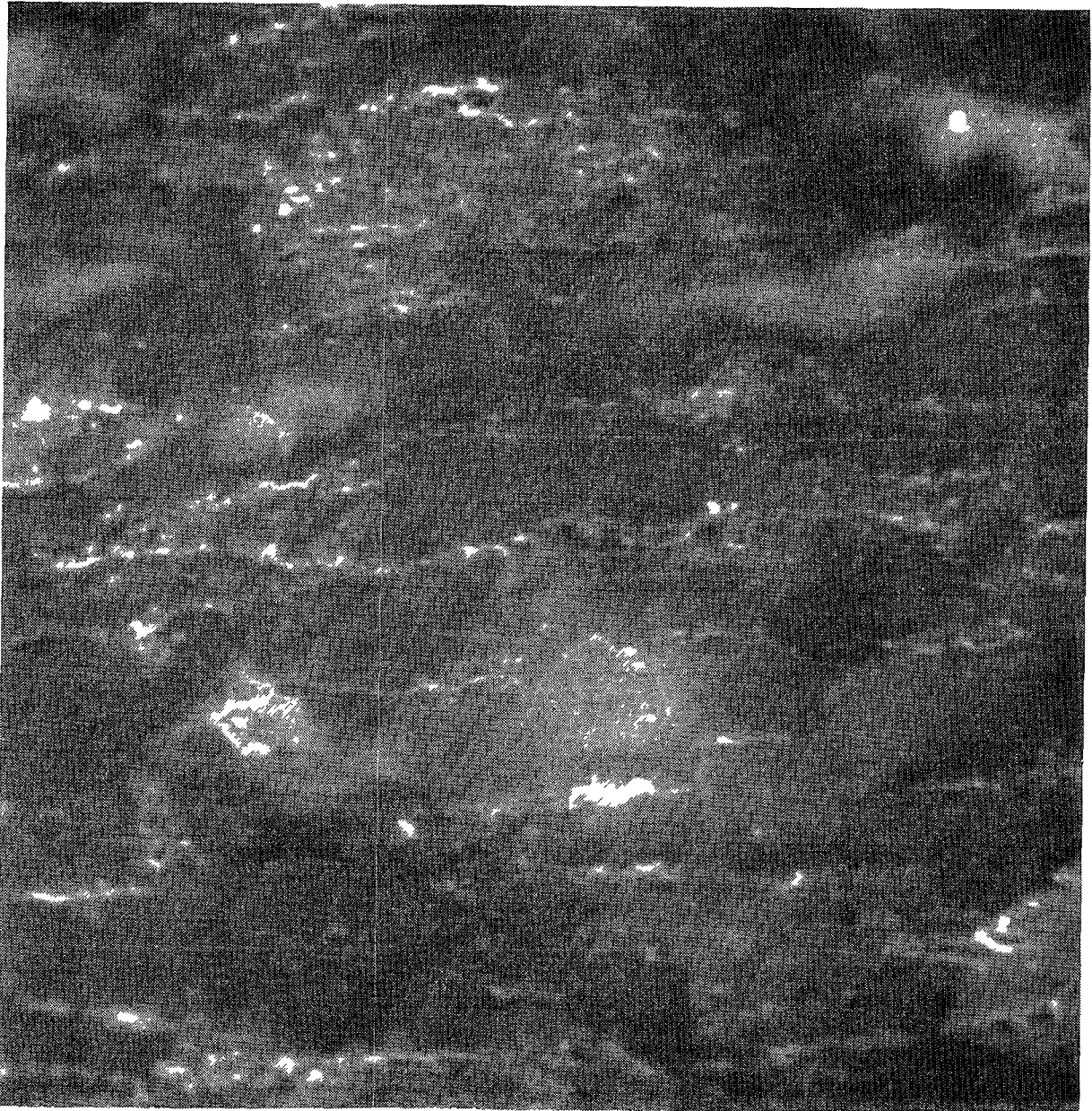


FIG. 2.28. Local white-oxide formation along intermetallic stringers in Zircaloy-2 after 14 day, 400°C steam test (2000×).

2.2.1. Nodular oxide formation

There is not much definite knowledge of the mechanism of nodular oxide formation in 500°C steam. The work that has been done suffers from a number of limitations. Thus, virtually all of the experimentation that purports to demonstrate that nodules initiate in precipitate free areas of surface has been performed on samples heat treated to generate very large grains, and to displace virtually all the intermetallics to the grain boundaries [45,47]. Such material would of course not have passed the standard 400°C steam test, and would have shown white oxide spots (nodules) after prolonged corrosion in 400°C steam. The rest of the work has been done on non-Zircaloy materials (e.g. unalloyed zirconium) that are relatively intermetallic free, and that are also traditionally expected to fail a 400°C steam test and develop white oxide "spots". An example of such effects can be seen in the laser glazing studies of Sabol et al [48], where depletion of the alloying elements in the surface degraded the

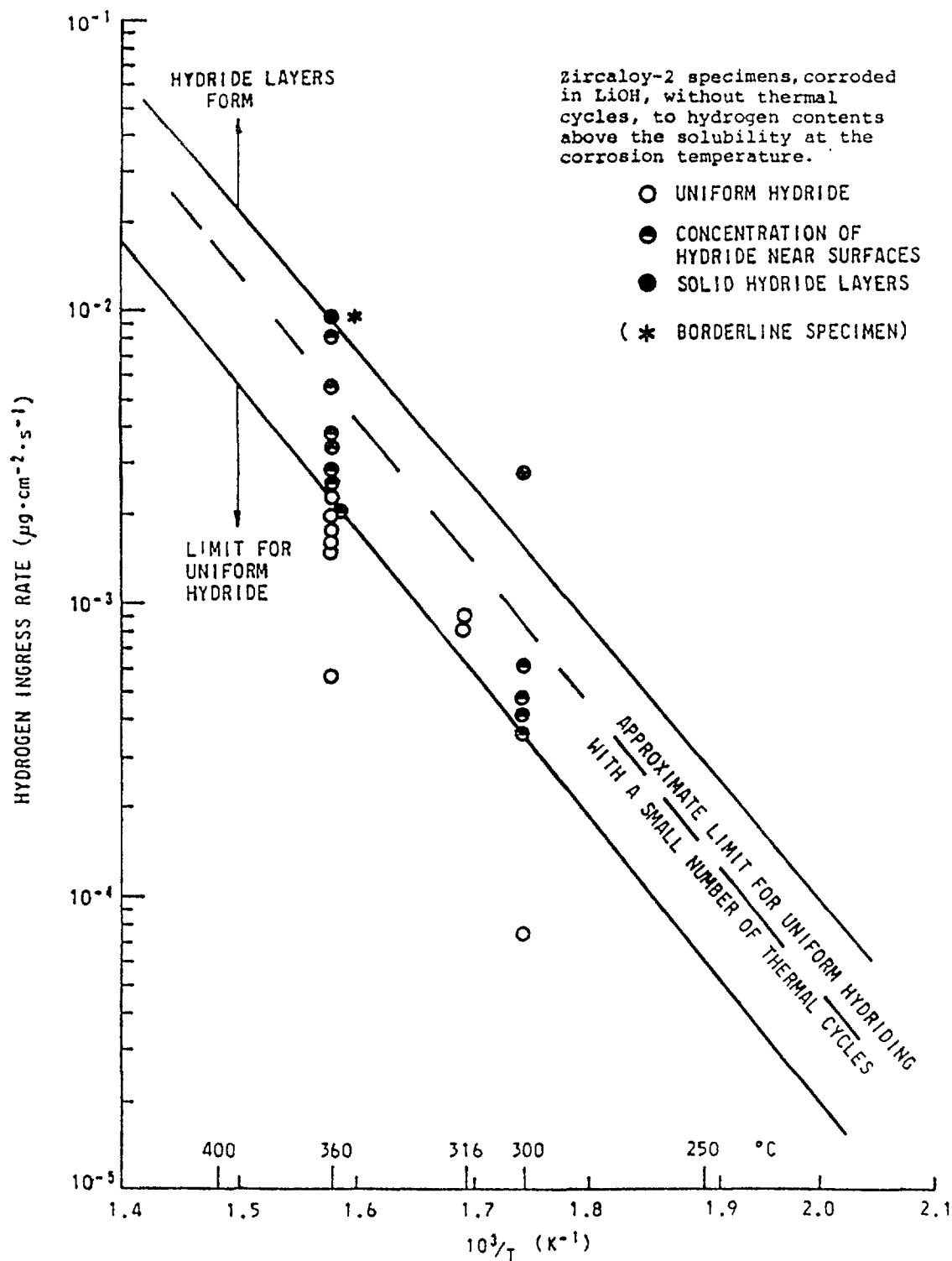
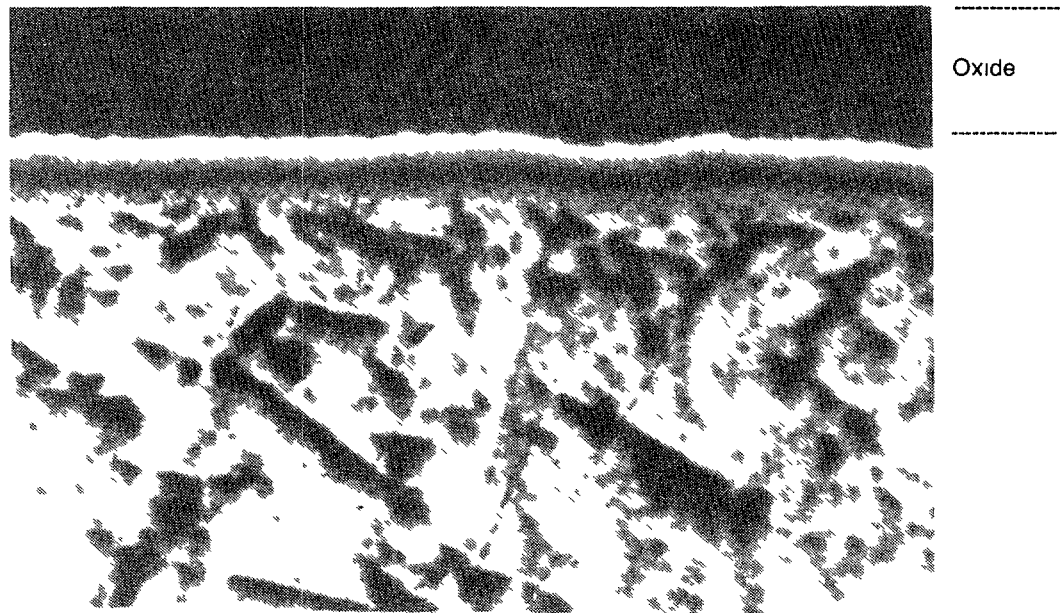


FIG. 2.29. Critical hydrogen fluxes for surface hydride layer formation (from Chemistry & Materials Division, CRNL, Progress Report, January–March 1979, AECL-6538).

corrosion resistance. Thus, use of this evidence requires us to accept that all nodules will form away from intermetallics because it has long been known that some poorly heat treated materials nucleate nodules at such locations. In support of this the work of Demars, Givord and Armand is often quoted [49]. However, only one of their heat treatments (an $\alpha+\beta$ treatment with no further α anneal) gave nodules that formed within the grains. After even short subsequent low temperature anneals the white spots on this material were located at the sites of the heavily segregated intermetallics. Figure 2.28 gives an example of such nucleation of white



Autoradiograph in situ; exp. 20 min (500×)

FIG. 2.30. Redistribution of tritium at the oxide-metal interface (portion of the oxidized sample annealed in argon at 800°C for two hours, air cooled) [52].

Note: absence of tritium in the metal zone adjacent to the oxide due to the high oxygen level there and tritium enrichment in the metal zone with low oxygen content.

spots at an early stage of growth. These would develop with prolonged exposure in 400°C steam (or 300°C water) but would not give a highly regular nodule outline even after long exposures.

Similarly, the work that purports to show hydride precipitation at the metal-oxide interface as the cause of nodule nucleation suffers from severe problems [50]. At the experimental temperature none of the specimens appears to contain enough hydrogen for the solubility to have been exceeded. Thus, the evidence for clusters of local hydride precipitates after quenching such specimens from 500°C appears more probably to be a result of the local rapid ingress of hydrogen following nodule nucleation rather than a cause of it. In support of this, evidence that a critical hydrogen ingress rate must be exceeded locally before solid hydride layers can be formed near the oxide/metal interface can be found in the literature (Fig. 2.29). The generally more severe nodular corrosion of Zircaloy-4 compared with Zircaloy-2, despite the lower hydrogen uptake rates of Zircaloy-4 directly contradicts such a mechanism. A further difficulty that confronts the hypothesis that nodules nucleate at interfacial hydrides is the observation that, in the Zircaloys, hydrogen and hydrides are effectively excluded from a thin layer at the oxide/metal interface where high concentrations of dissolved oxygen result from diffusion of this species into the metal (Fig. 2.30) [51,52]. Nevertheless, the implication of hydrogen in the process cannot be dismissed, as nodular oxidation does not occur in high pressure oxygen at 500°C, and it may be that hydrogen liberated within the oxide is the critical factor as suggested by several authors [53,54].

2.2.2. Mechanism of nodule formation

The studies in 500°C steam have concentrated on the variables associated with the metallurgical structure of the cladding. However, although this variability between cladding batches is one of the obvious

features of the in-reactor phenomenon, as is shown by the dependence of nodular corrosion on second phase precipitate size and distribution [55], there are clearly other factors that control the incidence of nodule formation. The same batches of cladding can behave quite differently in different reactors. The other factors that are important in BWRs are:

(a) Galvanic effects resulting from contact with or proximity to stainless steels or nickel alloys. This effect was shown most clearly in SGHWR with the mixed-grid experiment in which alternate grids at the bottom of a fuel bundle were either Zircaloy or stainless steel [56]. Nodular corrosion occurred predominantly at the stainless steel grids, and was distributed symmetrically about them, whereas the small numbers of nodules seen at Zircaloy grids were generally downstream of the grids. The effect is also evident in examples of control blade handle "shadows" appearing on the adjacent fuel channel [57], and the common observation of spots of thick oxide around points of contact of the cladding with Inconel springs in an otherwise Zircaloy grid. A further manifestation of this phenomenon is the evidence for ridges of thick oxide on the SGHWR Zircaloy-2 pressure tubes adjacent to the stainless steel grids on the fuel bundles [58], and the same observation on the Zr-2.5 Nb pressure tubes in RBMK reactors [59].

(b) Effects of impurities, such as copper in the reactor water are shown by the evidence that copper in the water is one of the primary factors leading to CILC failures (Crud Induced Localised Corrosion, an advanced form of nodular corrosion) [60,61], and by the general reduction in the frequency of nodules on otherwise similar batches of cladding when the copper alloy condenser tubes in a reactor are replaced by titanium tubes. In the grosser forms of nodular attack (CILC failures) it is evident that other factors are important as well. The Ca, Mg and Si content of the water may be critical in forming the hard impervious crud layers that are thought to participate in CILC failures. This aspect of the problem was certainly thought to be critical in the early-life CILC failures in SGHWR [60]. The presence of a hard, free-standing crud layer that can support a steam-filled crack between it and the oxide; or the formation of such steam-filled cracks within the oxide are essential to the final failure stages. Measurements of the thermal conductivity of high Cu crud [60] showed that it was higher than that of ZrO_2 , and so unless such layers are excessively thick, the temperature rise across them (in the absence of a steam-filled crack in the system) will be insufficient to cause the high temperatures at the Zr/ ZrO_2 interface that are needed to get the high corrosion rates and hydrogen migration that are observed.

(c) Effects of radiolytic species in the water are clearly important since the phenomenon of nodular corrosion is not evident in reactors without the presence of dissolved oxygen in the water [62]. This may arise from oxygen added with the feedwater or more usually from radiolytic production. The presence of boiling in the system is important only to the extent that it causes partitioning of the species (e.g. oxygen and hydrogen) into the steam phase, thus changing the concentrations in the water phase. The direct reaction of radiolytic species with the metal surface is unable to account for the oxidation rates observed unless unreasonably long diffusion distances, and hence long lifetimes for the species are assumed. Thus, the actual quantities of radiolytic species produced are thought to be less important than shifts in the equivalent redox potential of the irradiated water, and hence in the surface electrochemical potential of the Zircaloy that results during irradiation.

(d) The local power and flux spectra appear also to be important, as the differences reported between Gd-rods and UO_2 -rods [61] cannot be

understood on the basis of local power or flux, since the Gd-rods are operating at lower power than the UO₂-rods in the critical early irradiation period when nodules are initiating. There are also differences in the radiation spectrum seen by the cladding on Gd-rods compared with UO₂-rods. This may be an important aspect of the difference, since a fuel pin can be likened to a large self-powered flux detector, and the net flux of charged particles from the zirconium oxide into the water will represent a polarisation current that can change the local surface potential of the cladding. This could also explain the differences seen between nodular corrosion over plena (e.g. those in the high flux regions of segmented rods) and the lower nodular coverage seen on adjacent fuelled regions [61]. The absence of a direct correlation with either local power or heat flux is illustrated further by the common observation that nodular corrosion is often more severe on the unfuelled Zircaloy-4 channels than on the fuel cladding contained in them, although in this instance material differences must be regarded as a large part of the overall effect.

2.2.3. Simulating nodular corrosion in high temperature water

In-reactor the important factors in the extent of nodular corrosion for a given metallurgical condition of the alloy include the following:

- fast neutron irradiation
- the radiolysis of the water and stripping of H₂ and O₂ into the steam phase during boiling to leave an excess of O₂ that originates primarily in the feedwater. Radiation effects in the downcomer introduce important differences from plant to plant [62]
- the presence of specific impurities in the water (e.g. Cu)
- the influence of galvanic contacts with stainless steel or Inconel
- modifications of the redox potential of the system, such as results from adding H₂ to the water.

While not all of these factors could be effectively simulated in the laboratory (e.g. fast neutrons), many could be. No attempt is known of autoclave testing in which the H₂O₂ ratio in the water, the polarization of the specimen, and the presence of reducible species such as Cu²⁺ were used as independent variables.

Preliminary tests [63] show that Cu²⁺ is preferentially reduced to Cu⁰ at room temperature at a few intermetallic sites in normal stress-relieved cladding by galvanic coupling to platinum, but that no such sites are sufficiently cathodic to cause this effect with β-quenched cladding.

2.3. HYDROGEN ABSORPTION

There are still many unknown factors in the mechanisms of hydrogen absorption by zirconium alloys. Not least of these is the shortage of good values for the diffusion of hydrogen either in the ZrO₂ lattice or in crystallite boundaries. Since early experiments purporting to measure this have usually been essays in the study of the breakdown of the oxide, one might expect our knowledge of this process to be more complete. However, because the fact that oxide breakdown was occurring was ignored, and

because of the difficulties in characterising these breakdowns we actually know no more about breakdown processes than we do about diffusion in coherent oxide films.

Zirconium alloys are normally protected against hydrogen ingress by the surface oxide film, which presents a good barrier both to ingress, and to the egress of hydrogen already in the metal. However, laboratory work has shown that, under conditions of straining at a notch, this oxide film offers little protection, and zirconium alloys are susceptible to rapid cracking (up to 10^{-5} m/s) in hydrogen [64,65]. These experiments revealed only small differences in the crack velocities of the same alloys which show surprisingly large differences in crack velocity under DHC conditions with only internal hydrogen [66]. There are three fundamentally different processes by which hydrogen isotopes can enter a fabricated zirconium alloy component. The first, and most trivial mechanistically, is by diffusion into the zirconium alloy via a direct metallurgical contact with another metal having a high diffusivity for hydrogen, and a higher fugacity of hydrogen than the zirconium. The other two ingress routes operate through the surface oxide film. The first of these occurs when zirconium is exposed in a hydrogen atmosphere containing insufficient oxidising species to maintain the protective nature of the oxide, while the second occurs as part of the normal oxidation process in aqueous media. These three processes will be dealt with individually.

2.3.1. Absorption of hydrogen gas

All zirconium components, unless held at high temperature in a good vacuum, carry a ZrO_2 film on their surfaces. In air at room temperature, the thickness of this oxide is limited by electron tunneling to 2-5 nm. Thickening of this oxide can proceed by a variety of processes. By increasing the electric field across the oxide further oxygen ion transport through the air-formed film can be initiated either at room temperature or above. This same process will proceed by thermal activation if the temperature is raised in the presence of an oxidant. Such an oxide film is normally a very good barrier against reaction with hydrogen gas and, provided sufficient oxidant is present in the environment, may remain so indefinitely. "Sufficient" in this context was established by Shannon [67] to be that required to maintain the normal oxidation rate at the temperature concerned (Fig. 2.31); the "normal" oxidation rate being that obtained at environmental pressures sufficiently high for the pressure dependence of the oxidation rate to approach zero [68].

These observations led to the postulate that, for any conditions of temperature, pressure and oxidant, there should be a critical hydrogen/oxidant ratio above which the oxide film would remain protective, and gross reaction with hydrogen would be prevented [69]. There could still be a slow absorption of hydrogen by reaction with the oxidant if this were a hydrogen containing molecule. Several investigators [69,70] have established these critical ratios, for a limited range of environments, and they are generally observed to be in the range 10^2 - 10^6 (Table 2.2). The results were quite variable, and may show a change with temperature. In the range of 300-400°C the tendency is for the ratio to decrease. Thus, very small concentrations of oxidizing species in hydrogen gas are sufficient to prevent direct surface reaction with hydrogen at reactor operating temperatures. This effect was borne out in experiments on cracking in hydrogen gas where small oxygen additions were sufficient to inhibit crack growth [65]. However, it is notable (by comparing the total pressure and the critical ratio in Table 2.2) that more oxygen appeared to be necessary to ensure passivation of strained metal at the crack tip, than appears to be the case for reaction on a smooth surface.

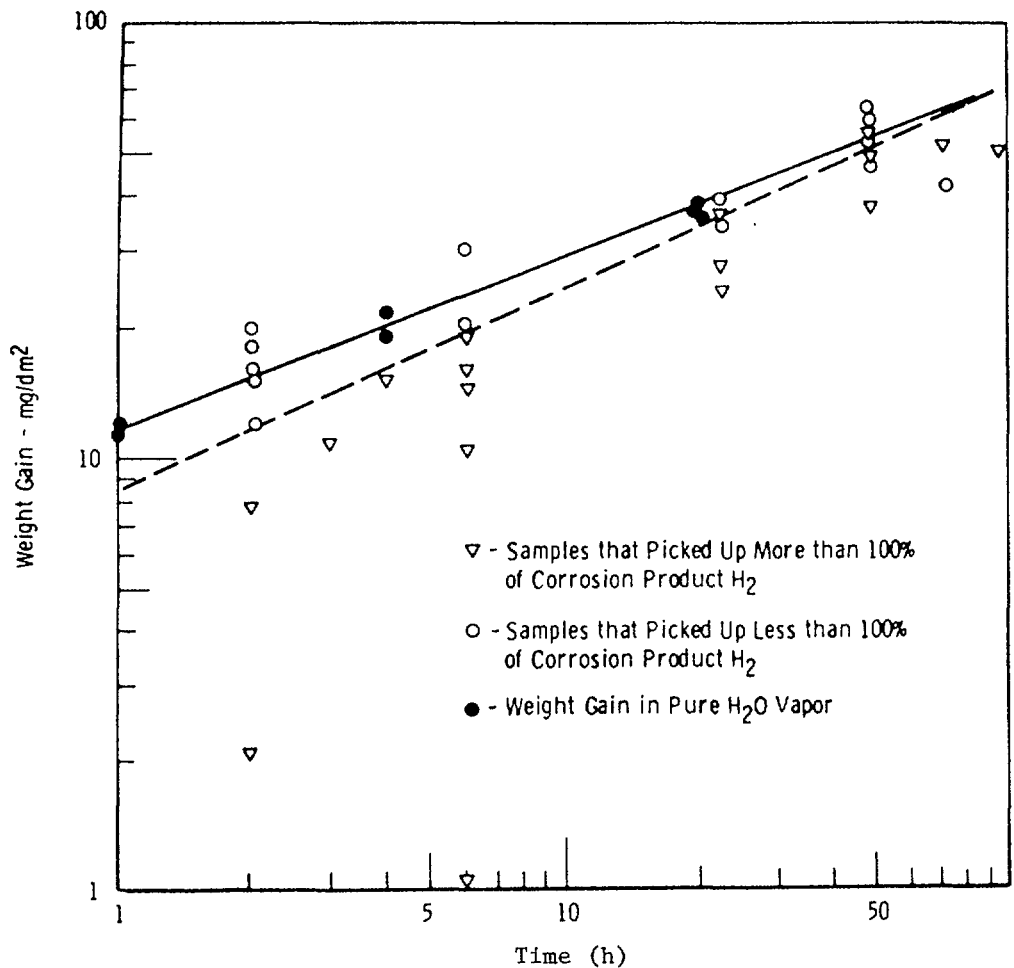


FIG. 2.31. Plot showing influence of oxidation rate during exposure to H_2/H_2O mixtures at $400^\circ C$ on hydrogen uptake [67].

TABLE 2.2. CRITICAL H_2 /OXIDANT RATIOS FOR DIRECT HYDRIDING
(References refer to the original table in Ref. [245])

Material	Temperature ($^\circ C$)	H_2 Pressure (atm)	Critical Ratio	Author	Ref.
Zircaloy-2	343	6.5×10^{-2} -1.0	10^6 - 10^8	Boyle & Kisiel	9
"	400	1.3×10^{-2}	10^2	Shannon	7
"	320	1.0	10^5	Gibby	BNWL-150 (1965)
"	300	1.0	10^5	} Une	10
"	400	1.0	10^2		
"	25	0.1	10^2 - 10^3	} Coleman & Cox	5
Zr-2.5% Nb	25	0.1	10^2 - 10^3		

If insufficient oxidising species are present to prevent the oxide film from slowly dissolving in the zirconium matrix, then, after an incubation time required for dissolution in the metal to lead to "breakdown" of the surface oxide [70-73], a rapid direct reaction with hydrogen gas ensues (Fig. 2.32). The progress of the oxide "breakdown" process can be monitored, during the incubation period, by measuring the electrical resistivity (Fig. 2.33) of the oxide film [67]. The resistivity of the oxide declines rapidly with time, as a result of the increasing hypostoichiometry of the oxide, and hydriding commences once the resistivity declines below a critical level. The hypostoichiometry changes because the rate of dissolution of oxygen atoms from the oxide into the metal now exceeds the rate at which replacement oxygen atoms can be acquired from the environment. In addition to the increasing electronic conductivity associated with this process, an increase in the number of anion vacancies will result.

As a result of these observations, investigators studying the rate of reaction of hydrogen with oxidized zirconium surfaces have been tempted to postulate that hydrogen is migrating via these anion vacancies as interstitial H_2 [74,75]. From their experiments they have then calculated diffusivities for hydrogen in the ZrO_2 lattice. However, there is no unambiguous evidence from these experiments to support an argument that hydrogen is migrating via the ZrO_2 lattice at all. The diffusivities which they calculate are very high for such a lattice diffusion process, and lie in a range more typical of surface diffusivities. Experiments of this type give permeation rates 10^7 (or more) times those measured by effusion experiments using tritium [76-78]. From these, a diffusion coefficient for tritium in the surface layer (arbitrarily defined as the first 5 μm) of $10^{-20} m^2/s$ at $300^\circ C$ was estimated [77]. At the start of such an experiment the T_2 concentration in the alloy is known, and is assumed to be zero at the oxide/environment interface. The diffusion of tritium in any suboxide zone of metal is assumed to be fast compared with that in the oxide, so that the calculated numbers are relevant to diffusion in the oxide. This is in good agreement with a value of $3 \times 10^{-19} m^2/s$ which can be calculated from the autoradiographs in ref. [52] for $400-500^\circ C$.

There is some circumstantial evidence that hydrogen entering the metal under these conditions does not pass through the oxide lattice. Tritium autoradiography [52] has shown that, when a specimen preoxidized in O_2 or air was exposed to T_2 gas, tritium appeared in the metal core but the oxide film remained essentially free of tritium (Fig. 2.34). Other experiments showed that tritium, built into the oxide film during reaction with T_2O , remained fixed once the specimen was cooled and did not migrate into the metal, or exchange with the hydrogen in the environment, over periods of years [76]. This again suggests that the diffusivity in the oxide is orders of magnitude less than that calculated from the reaction rate experiments [74,75]. Conversely, tritium absorbed in porous oxide films, by exposure to T_2O , exchanged rapidly with hydrogen in the environment and vanished in periods of, at most, a few days [76]. Thus, at the very most, any tritium which was present in the oxide on the specimens heated in T_2 gas had exchanged with the laboratory environment, and vanished, by the time the autoradiograph was exposed. This indicates strongly that the T_2 , which entered the metal in these experiments, did so via pores or cracks in the oxide and not by diffusion through the bulk of the oxide lattice. Autoradiographs of similar specimens preoxidized in oxygen and then exposed to T_2O showed tritium both in the metal and in the oxide (Fig. 2.35). This shows the fundamental difference between reaction with T_2 and T_2O .

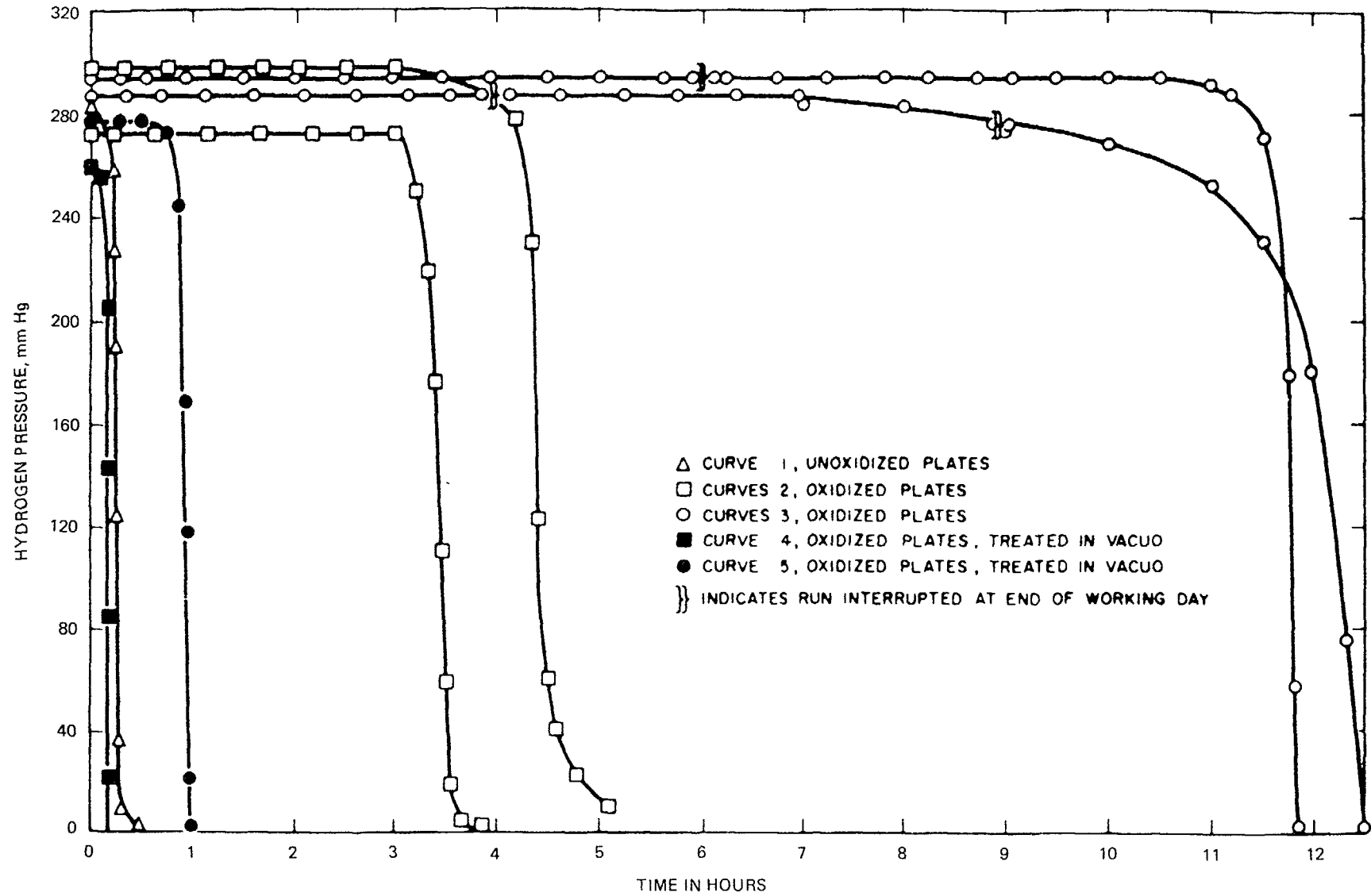


FIG. 2.32. Incubation times for absorption of hydrogen gas by zirconium at 400°C [71].

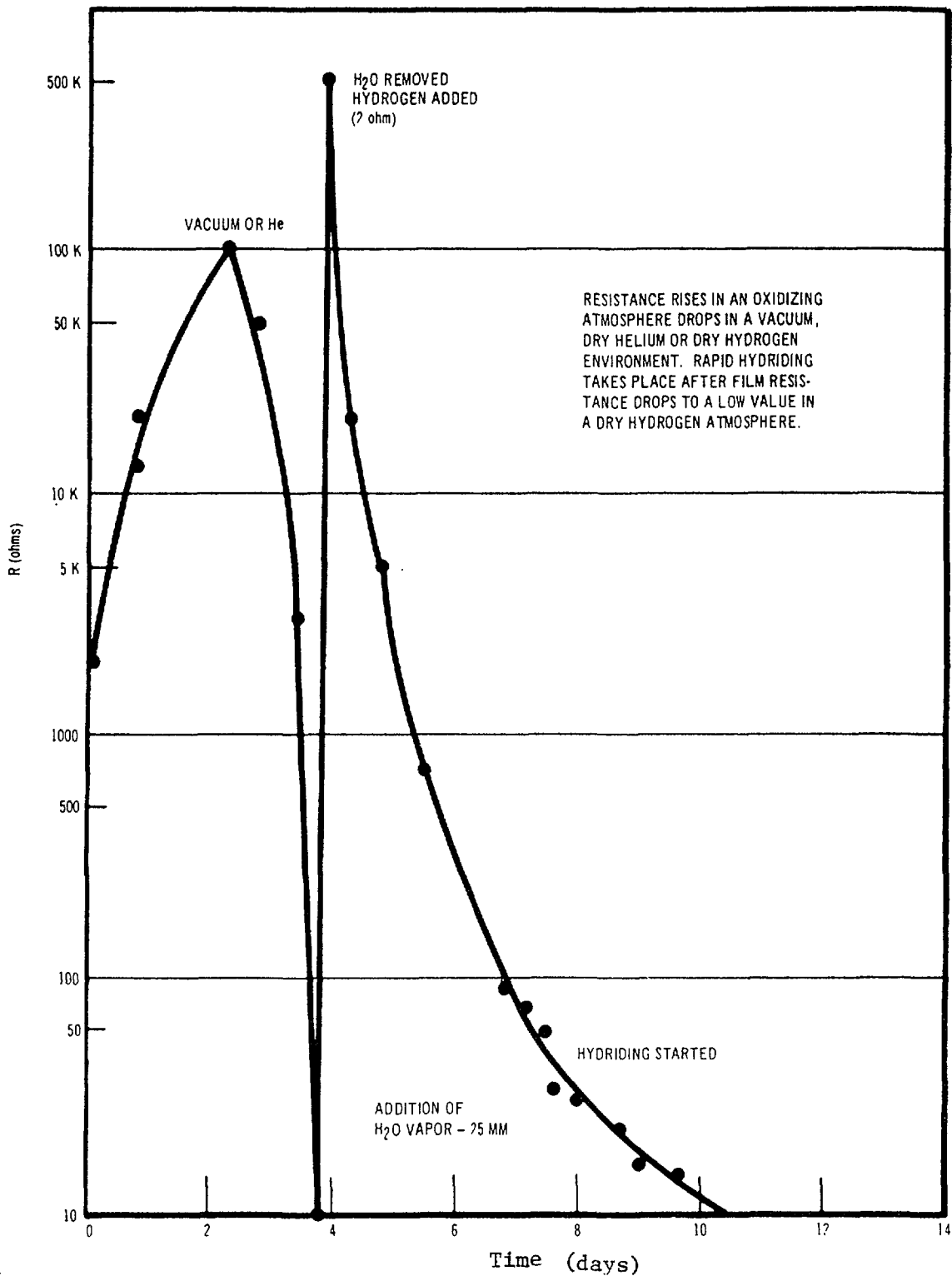


FIG. 2.33. Plot of electrical resistance for Zircaloy-2 exposed to gaseous environments at 450°C [67].

The experiments of Shannon and others gave no direct clues to the microscopic nature of the "breakdown process" in the oxide film, other than for the accompanying changes in conductivity and stoichiometry. The implicit assumption that these would be homogeneous changes is carried by the deductions subsequently made. Electron microscope studies [79,80] of the oxide films formed on zirconium, of similar purity to that used in the hydrogen diffusivity studies, showed that the oxide films formed in a far from uniform and parallel-sided manner. Ridges of thick oxide form

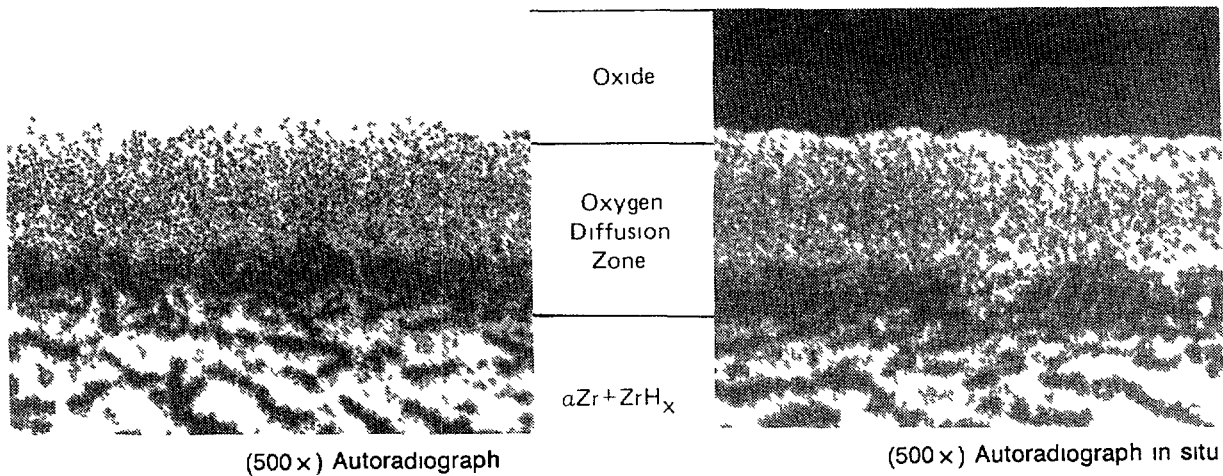


FIG 2.34. Autoradiograph showing lack of tritium absorption by a thick oxide film formed in O_2 when subsequently exposed to T_2 (oxidized in O_2 at $600^\circ C$ for 66.5 h to weight gain of 6.84 mg/dm^2 , exposed to T_2 gas at $800^\circ C$ for 16.5 h) [52]

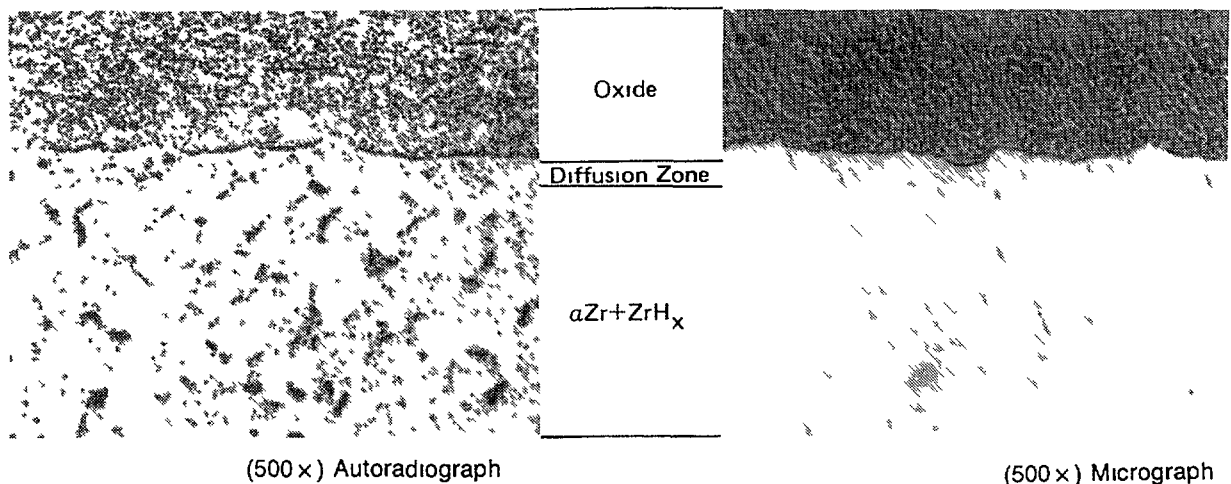


FIG 2.35. Autoradiograph showing tritium incorporated in a thick oxide film formed in O_2 when subsequently exposed to T_2O (oxidized in O_2 at $600^\circ C$ for 66.5 h to weight gain of 727 mg/dm^2 , exposed in T_2O vapour at $400^\circ C$ for 72 h, additional weight gain 5 mg/dm^2) [52]

preferentially along many grain boundaries, and big variations in the oxide thickness occur from grain to grain (Fig. 2.7a). Many of these features have also been recognized from optical microscopy [81]. However, the lines of cracks (Fig. 2.7b) which form in the oxide along these ridges, and along grain boundaries separating grains which grow thick and thin oxide films [79-82], are less easily seen in the optical microscope. These cracks are encouraged by the curvature in the oxide/environment interface introduced by the local variation in oxide thickness and the high Pilling-Bedworth ratio of ~ 1.5 . These factors cause the outer surface of the oxide to go into tension, whereas oxide films formed as a planar layer on a smooth surface remain in compression at the same point in time.

However, even in regions where cracks form in the outer part of the oxide, the inner layers of the oxide will remain in compression because the new layers of oxide form at the oxide-metal interface by inward diffusion of oxygen. Thus, there will probably always be a thin layer of protective oxide at the bottom of these cracks. This argument is supported by the observation that cracks are visible in the oxide surface formed during oxidation, and yet these oxide films continue to present excellent barriers

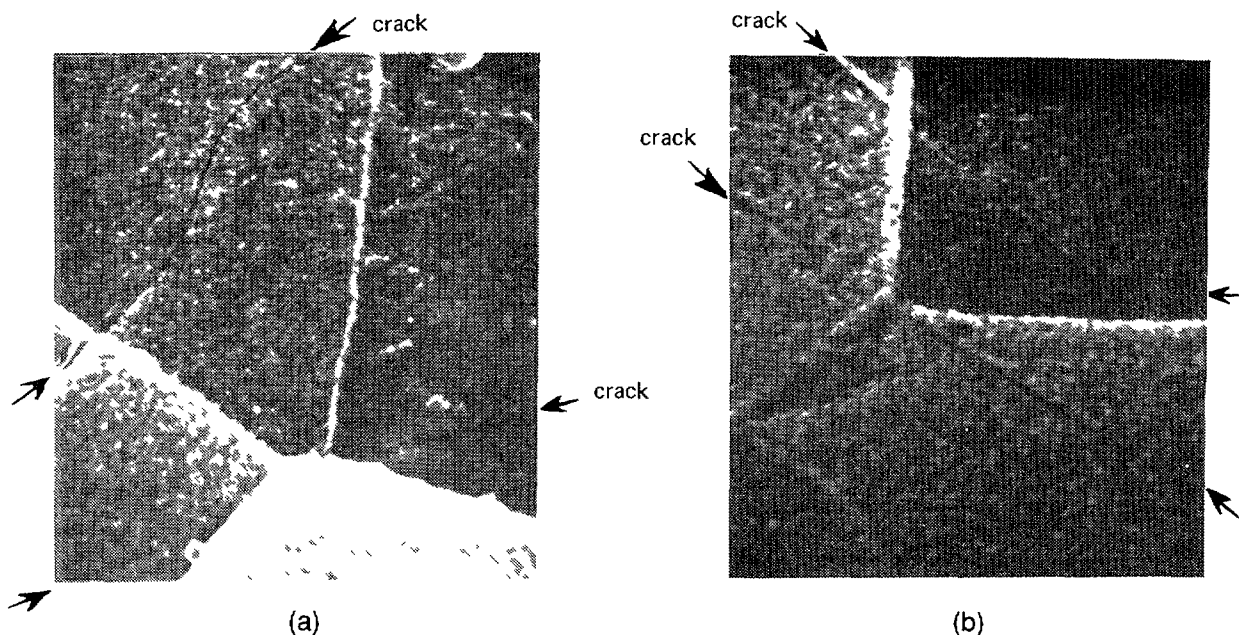


FIG. 2.36. Oxide-metal interface of stripped oxide films showing cracks induced by the stripping (3000 \times). These cracks do not follow oxide ridges [245].

to the ingress of hydrogen. Hence, such cracks are not the routes by which hydrogen enters the metal, although they may help to initiate, or become part of such a route during the "breakdown" process. That these cracks do not penetrate to the oxide/metal interface is shown in SEM studies of stripped oxide films. Examination of the oxide/metal interfaces [8,82] clearly showed the ridges of thick oxide along grain boundaries (Fig. 2.7d), and the variations in oxide thickness from grain to grain (Fig. 2.7c), but did not reveal any signs of cracks penetrating through to the interface at these locations. In instances when the stripping process induced cracking of the oxide, these cracks generally cut across oxide ridges at grain boundaries (Fig. 2.36), suggesting that these sites were not even regions of weakness in the oxide. Only occasionally have cracks running parallel to, and within, the oxide ridges been seen at the oxide-metal interface. Some other route, which allows direct access of hydrogen to the oxide/metal interface, must develop during the incubation period, therefore.

When a specimen, with an oxide film such as those above, is heated in an environment (vacuum or H_2) containing insufficient oxidant to maintain the normal growth of the oxide, the rate of oxygen dissolution in the metal will exceed the rate of formation of new oxide. Under these conditions, the oxide film will slowly dissolve in the metal. This process has been observed (Fig. 2.37) by following the thinning of interference-coloured oxide films in the optical microscope [83,84]. On the scale of resolution of this instrument the dissolution process appears to be uniform, provided that the metal core has not become saturated in oxygen [6,84]. However, autoradiography of ^{18}F reveals the oxygen distribution by way of the $^{18}O(p,n)^{18}F$ reaction [6] and shows that preferential diffusion of oxygen along zirconium grain boundaries occurs.

When the dissolution of oxide films is studied by electron microscopy, examination of the oxide/metal interfaces shows that the thinning of the oxide is not uniform. Because of the preferential diffusion of oxygen along the grain boundaries in zirconium, the dissolution of the oxide ridges at these sites occurs preferentially and

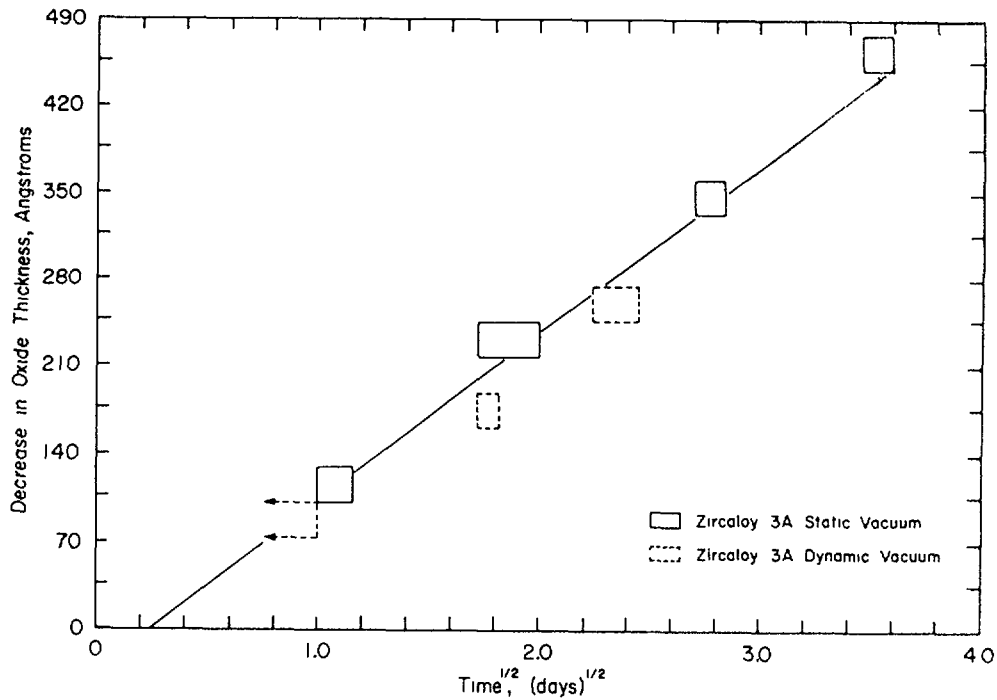


FIG. 2.37. Decrease in thickness of interference-colour oxide films as a function of annealing time in vacuo at 400°C [83].

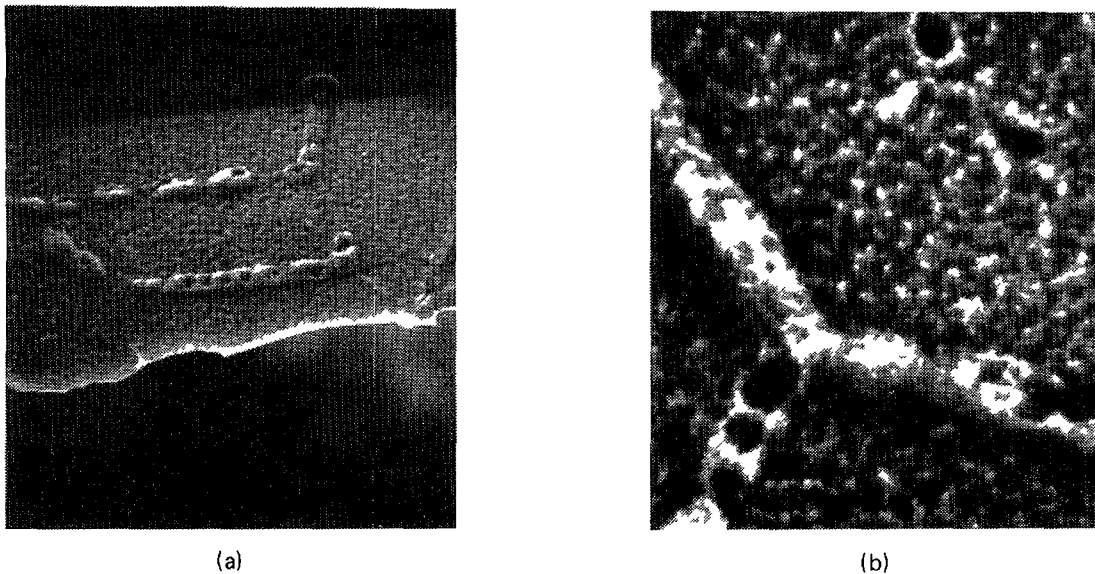


FIG. 2.38. Oxide-metal interface of specimen after vacuum annealing at 500°C. Note breakup of oxide ridges and formation of pores; (a) 1000 \times , (b) 3000 \times [245].

inhomogeneously (Fig. 2.38). This irregular dissolution of the grain boundary ridges leads to the formation of large pores in the oxide. These pores are thought to pass right through the oxide film because similar rows of pores have been seen when oxide films on specimens exposed to low oxygen partial pressure environments were viewed from the outside by a replica technique (Fig. 2.39). These pores also occur in the oxide away from the prior metal grain boundaries, perhaps because of enhanced local oxygen diffusion at incoherent twins, or dislocation pile-ups.

The uniform dissolution of the bulk of the oxide, seen in the interference colour studies [83,84], is probably the process which leads to

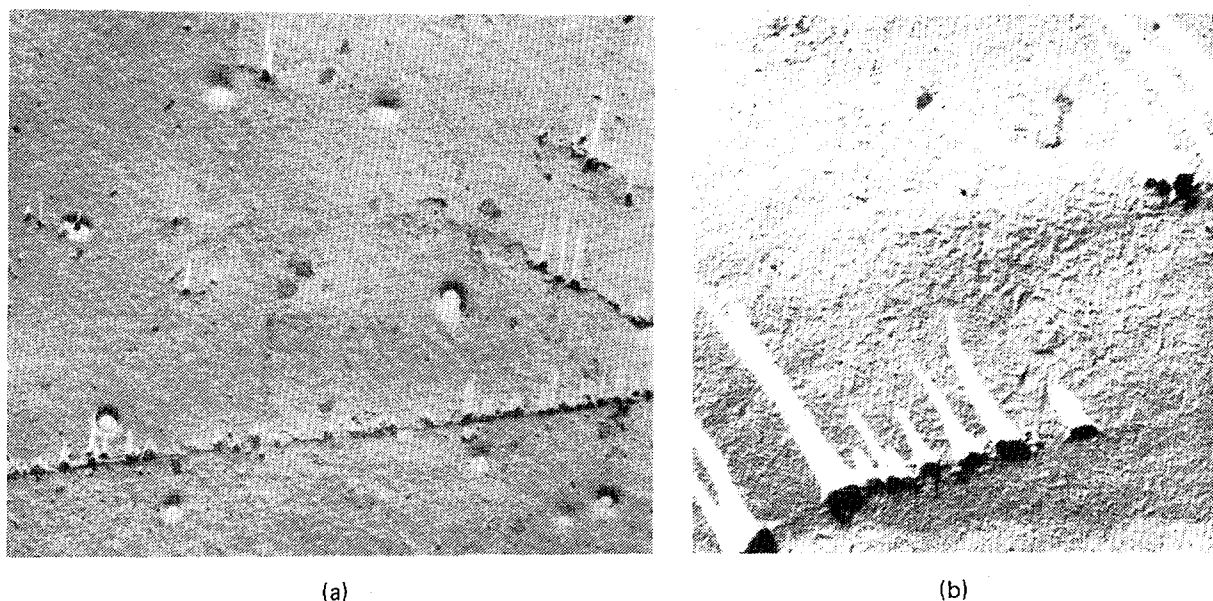


FIG. 2.39. Replica of zirconium oxide surface of specimen heated in a low oxygen environment (He), showing a similar array of pores to those seen in Fig. 2.38. Diameter at surface is smaller than at oxide-metal interface; (a) 4000 \times , (b) 10 000 \times [245].

the observed drop in oxide resistivity [67,70]. However, the preferential dissolution of the oxide at grain boundaries, and other sites, which leads to the formation of arrays of pores at these locations, is probably the process which terminates the incubation period, and leads to the rapid direct reaction of hydrogen with the metal. Since these pores appear to pass right through the oxide, there will be no oxide diffusion barrier to prevent such a reaction at these sites. Thus, none of the investigations which purported to measure the diffusivity of hydrogen in ZrO_2 by exposing preoxidized specimens in hydrogen gas will have measured such a quantity, and alternative techniques for measuring the hydrogen diffusion coefficient in ZrO_2 must be applied.

2.3.2. Hydrogen uptake during oxidation

Direct reaction of gaseous hydrogen with the zirconium at the bottoms of pores is not a possible route for hydrogen ingress during normal oxidation because there will always be at least a thin barrier layer of oxide at the oxide/metal interface. Even when oxide films become porous, in the post-transition region of oxidation kinetics, the pores which develop will not penetrate up to the oxide/metal interface, although they may approach quite close to it, because there will always be enough oxidant available to maintain at least a thin barrier layer at the bottom of the pore.

Oxidation studies using T_2/H_2O mixtures [76] have shown that, during normal oxidation, no T_2 enters the metal (Table 2.3) until the thermally-induced exchange reaction has progressed to the point where a measurable fraction of HTO has been formed. Thus, the hydrogen isotopes which enter the metal do so as an integral part of the reaction of the zirconium with water molecules, and not by reaction with any dissolved hydrogen in the water. Studies have shown that this situation persists (Fig. 2.40) until hydrogen overpressures in the system of tens of MPa are present [85].

During the reaction of zirconium alloys with water the hydrogen is liberated, initially, as an adsorbed hydrogen atom on the oxide surface,

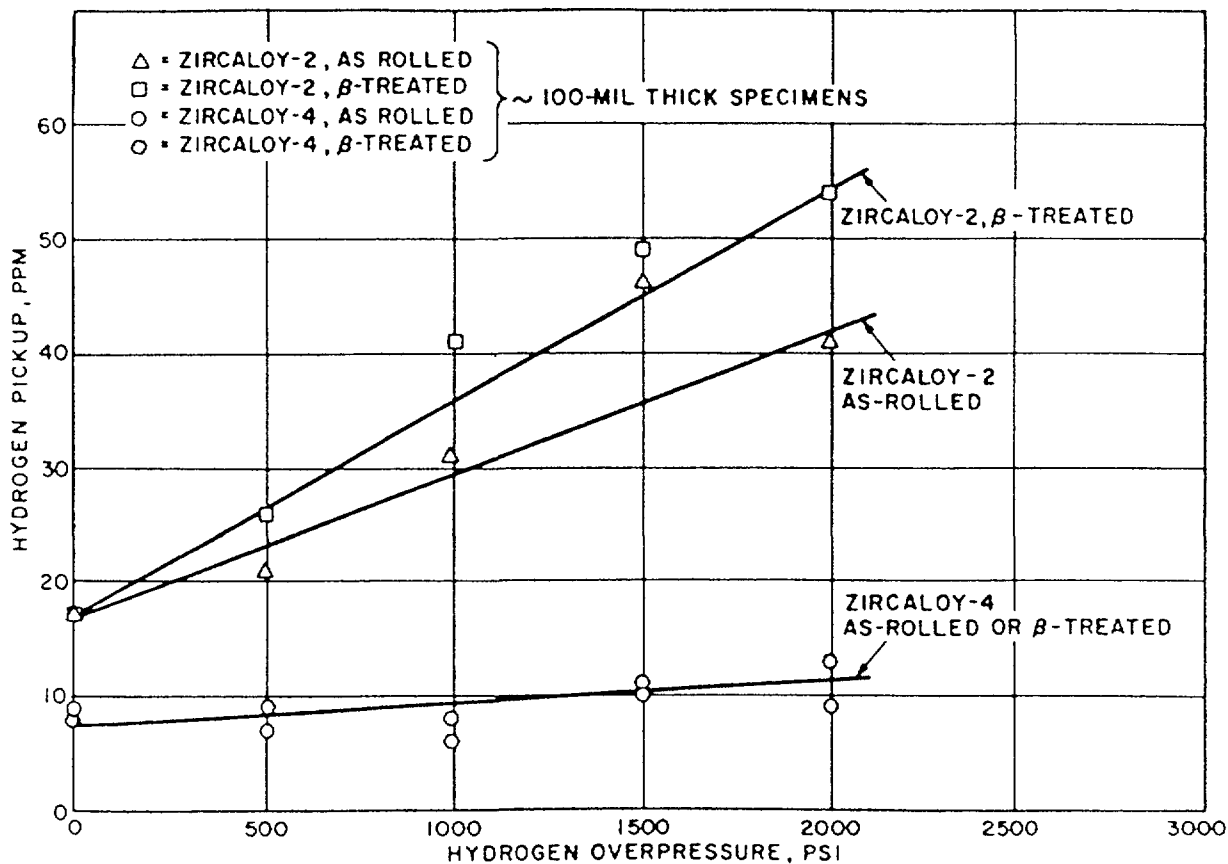


FIG. 2.40. Hydrogen pickup by Zircaloy-2 and Zircaloy-4 as a function of hydrogen overpressure after 14 day exposure in 343°C water [85].

TABLE 2.3. OXIDATION IN T₂/H₂O MIXTURES

Sample	Temp. (°C)	Time (h)	Wt. Gain (mg/dm ²)	Hydrogen Absorption		
				ppm	% Theor.	Observations
GR40 Zr-2.5 wt% Nb (1)	400	66.0	15.5	14	21.2	No significant tritium uptake.
GR41 Zr-2.5 wt% Nb (2)	400	113.0	14.5	13	23.4	Small amount of tritium in oxide and metal.
GR42 Zircaloy-2 (3)	500	24.5	24.5	39	23.0	No tritium detected in oxide or metal.

(1) Heated at 1000°C in vac. for 1 h and quenched.

(2) Heated at 880°C in vac. for 72 h and quenched, reheated at 500°C for 6 h. The large amount of isothermal α -phase present in this sample probably results from oxygen absorption during the long anneal at 880°C.

(3) Preoxidized in O₂ at 500°C for 24 h; $\Delta w = 28.2$ mg/dm².

when a proton is discharged by an electron emerging through the oxide film. The site at which this occurs depends on the morphology of the oxide film (Fig. 2.17). Thus, for alloys of the Zircaloy type, which contain additions of Fe, Cr and Ni (to a total of ~0.3 wt%) in the form of a distribution of second-phase particles, the electron current flows primarily at sites where intermetallics partially, or completely, short-circuit the oxide [86]. In alloys containing no, or few, such intermetallic particles of the transition metals (e.g. Zr-2.5 Nb) the electron current flows homogeneously through the bulk of the oxide [86].

The hydrogen atoms released by the discharge of the protons (either locally at intermetallics, or uniformly over the surface) then either recombine, and are evolved as hydrogen gas, or diffuse into the metal. In order to get into the metal they must diffuse through whatever barrier layer of ZrO_2 is present at or near the site of proton discharge. There is little direct knowledge of the precise species that diffuse in ZrO_2 . The possibilities are OH^- diffusion, H^+ hopping from anion to anion, diffusion of interstitial hydrogen atoms or hydride ions, and probably other processes. It is the competition between the rates of the recombination/evolution and diffusion processes which determines the proportion of the corrosion-hydrogen which enters the metal. Any local situation which affects the relative probabilities of recombination or ingress into the metal will, therefore, affect the hydrogen uptake percentage. Despite the importance of this step in the reaction no measurements of hydrogen recombination rates on either pure or doped zirconia surfaces are known.

The presence of alloying additions, such as nickel, which are thought to decrease the rate of the recombination reaction, or even, under some conditions, to directly dissociate molecular hydrogen dissolved in the water [85], could then lead to high percentage uptakes for the corrosion hydrogen by allowing a greater opportunity for the hydrogen atoms to diffuse into the metal. It was for this reason that nickel was eliminated from the alloy in the development of Zircaloy-4 from Zircaloy-2 [87]. It is also notable that the hydrogen uptake percentage shown by Zircaloy-4 in water is virtually independent of the hydrogen overpressure (Fig. 2.40), unlike that of Zircaloy-2 [85], thus adding further weight to the argument that the presence of nickel can lead to the direct dissociation and ingress of hydrogen dissolved in the water, when this is present to excess.

The presence of dissolved oxygen, or other oxidizing species (e.g. nitric acid), is able to speed up the removal of the discharged protons from the ZrO_2 surface and hence reduce the percentage hydrogen uptake (Fig. 2.41). The precise mechanism by which this is achieved, whether by direct reaction of oxygen dissolved in the water with hydrogen atoms on the surface, or by the substitution of the reduction of oxygen by the electrons for the reduction of protons (as the cathodic reaction), has not been identified. The presence of dissolved hydrogen in the water, as we have seen above, has virtually no effect on alloys without nickel containing precipitates, and only a small effect on Zircaloy-2, until very large concentrations are present. Once the oxide film becomes porous, in the post-transition oxidation region, the hydrogen apparently finds it more difficult to evolve at the oxide surface, for there is a general tendency for percentage uptakes to increase [88]. This effect is thought to be a combination of the reduced diffusion distance through the thin barrier layer of ZrO_2 in the porous oxide, coupled with the increased difficulty involved in diffusing out of the porous oxide when recombination no longer occurs on the oxide surface. These effects are smaller at temperatures typical of reactor operation than at higher temperatures (Fig. 2.42).

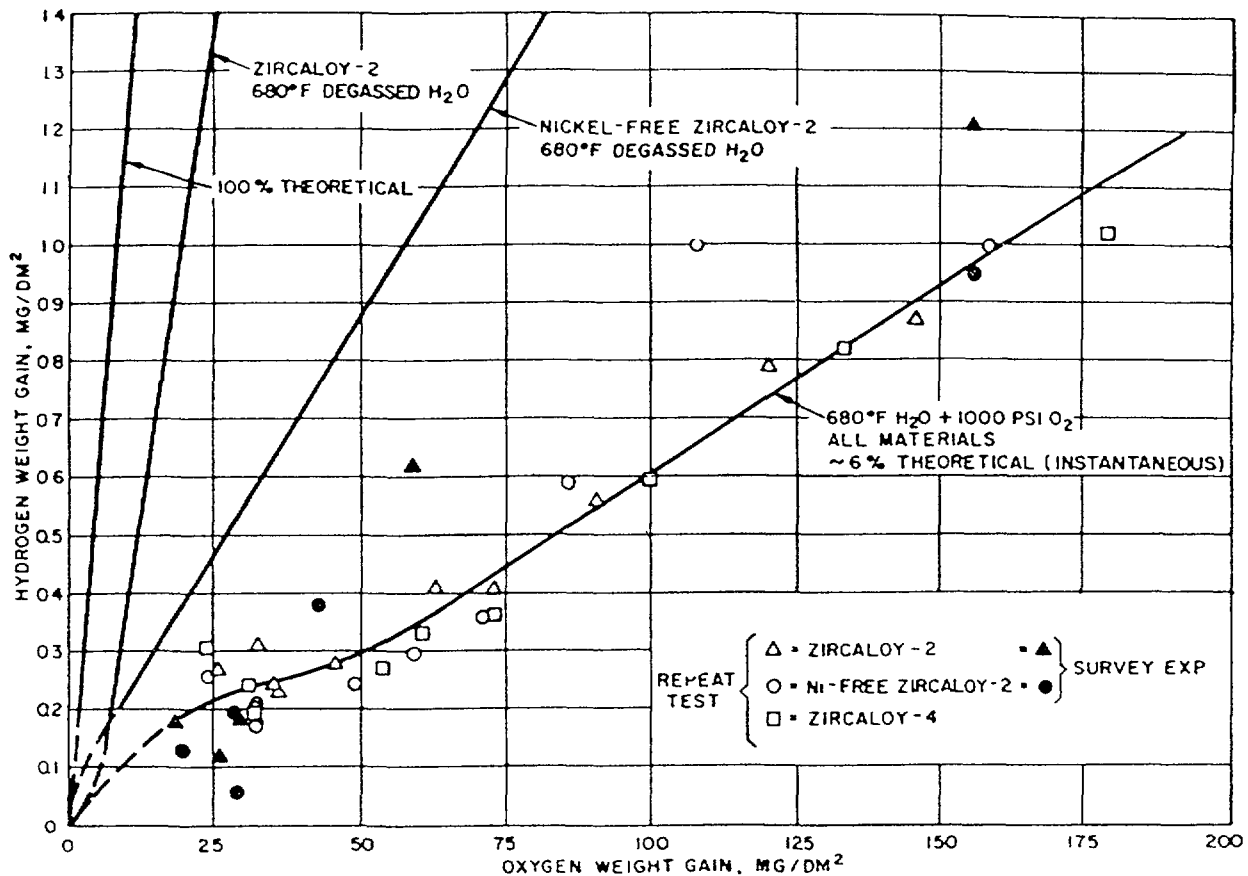


FIG. 2.41. Effect of oxygen content of water on hydrogen uptake by Zircaloys in 360°C water [85].

The strong correlation (Fig. 2.43) of hydrogen uptake percentages with the nature of the elements in the intermetallic precipitates [5], coupled with the observations of localized electron conduction at these sites, leads to the inference that the hydrogen entering the metal does so via some specific property of the oxide formed over these intermetallics. The nature of these oxide films [89] is only now being elucidated so the understanding of this aspect of the uptake mechanism may change rapidly in the near future. However, preliminary results suggest that elements like Fe and Ni may remain in the zero oxidation state in the oxide on an intermetallic. The state of agglomeration of these atoms has not yet been established, but the possibility of continuous filaments of metal (stringers) within these oxides cannot yet be ruled out. Such stringers could account for both the high local electrical conductivity and the easy ingress of hydrogen at these sites.

Although it is thought that, in alloys containing large numbers of intermetallic particles large enough to partially, or completely short-circuit the oxide, the hydrogen from the corrosion reaction enters the metal at these sites, it is known from tritium autoradiography that the uniform oxide between the intermetallics contains a significant (Fig. 2.44), but unknown, concentration of hydrogen [52]. That the quantity of tritium in such oxides appears to be roughly proportional to oxide thickness (Fig. 2.45), for interference-coloured oxides, suggests a relatively constant concentration of tritium in these oxides, with little concentration gradient through them. Attempts to measure this concentration using only infra-red spectroscopy techniques [90] were unsuccessful, but indicated that the concentration of OH⁻ in ZrO₂ films was probably <5%. Application of modern Fourier Transform Infra-Red (FTIR) techniques to this problem has now been made, and suggests an even lower

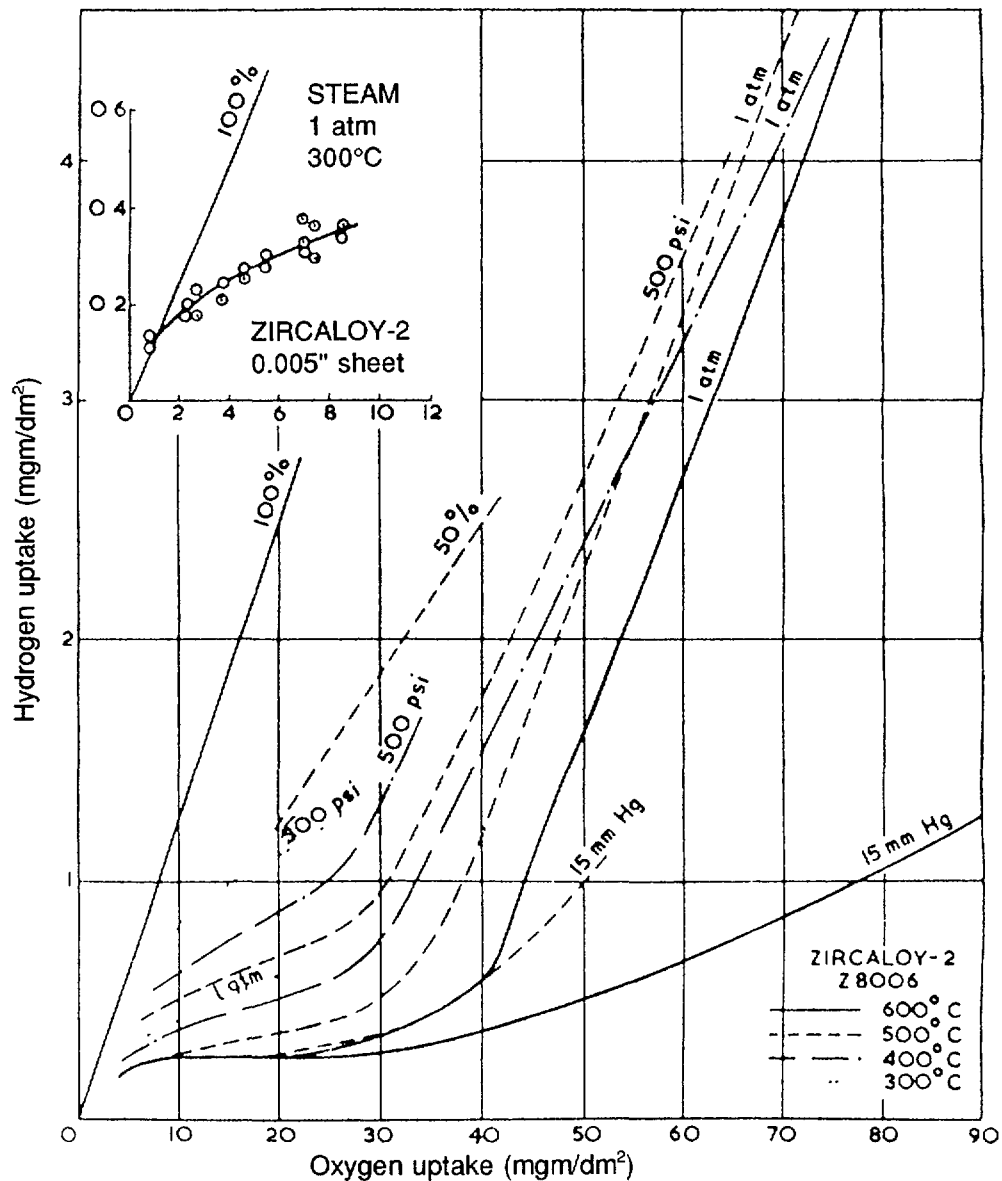


FIG. 2.42. Change in hydrogen uptake rate with oxide film thickness for Zircaloy-2 [88].

level of OH^- in the oxide, although SIMS measurements indicate high concentrations of hydrogen to be present [91]. Thus, perhaps the hydrogen in the oxide film is not present as OH^- .

Despite the known presence of hydrogen in the uniform oxide film there is little knowledge of its mobility. The long-term stability of autoradiographic specimens against exchange of the tritium with laboratory water vapour suggests that the mobility is low, but does not permit the calculation of other than an upper bound for the mobility. If, as observed, the tritium content of an $0.5 \mu\text{m}$ oxide film remains apparently unchanged after one year at room temperature, the permeability of tritium through these films must have been much less than $\sim 10^{-19} \text{ mol}\cdot\text{m}^{-2}\cdot\text{s}^{-1}$ at room temperature. This is very much lower than the value extrapolated from the elevated temperature tests [74,79], which we have already argued represents surface diffusion down pores (Fig. 2.46).

Recent work by nuclear reaction techniques [92] on ZrO_2 films formed in 400°C air and by SIMS on oxides formed [93] in-reactor, shows

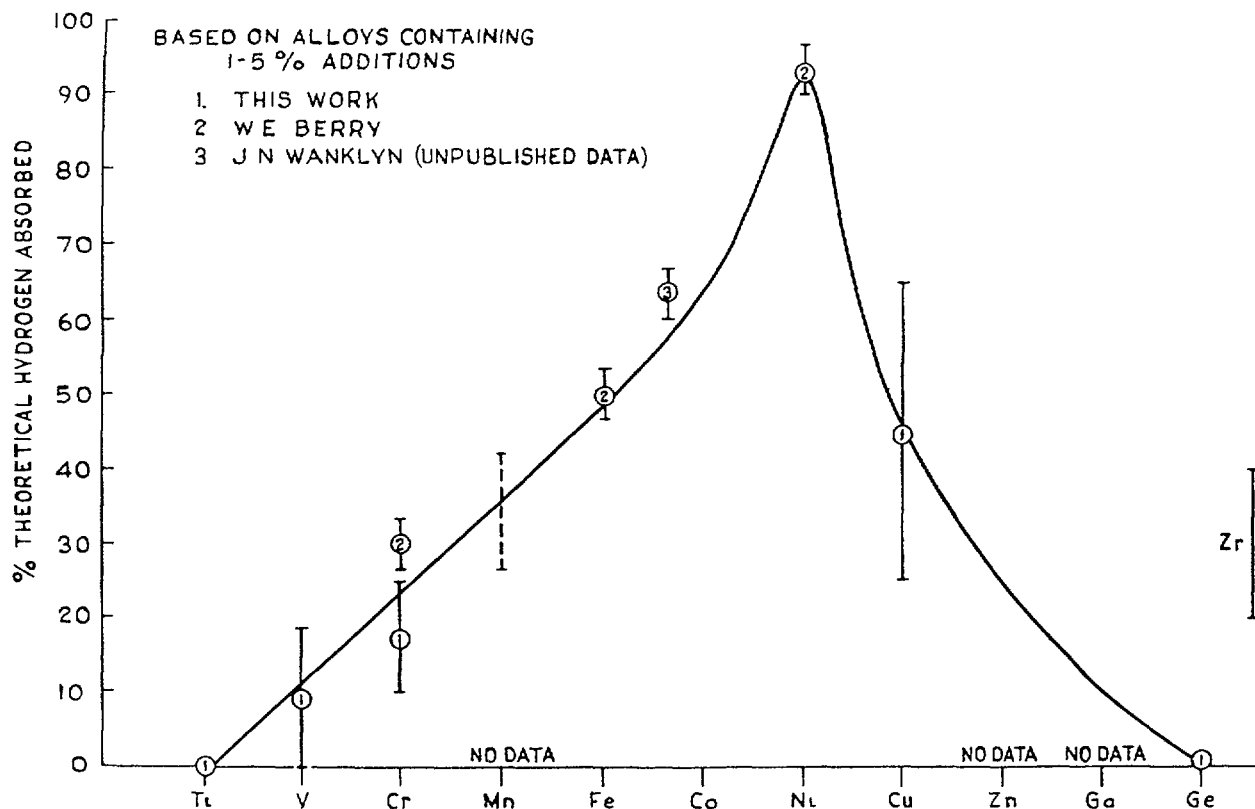


FIG. 2.43. Effect of alloying elements in intermetallic form on hydrogen uptake percentage (references refer to the original figure in Ref. [88]).

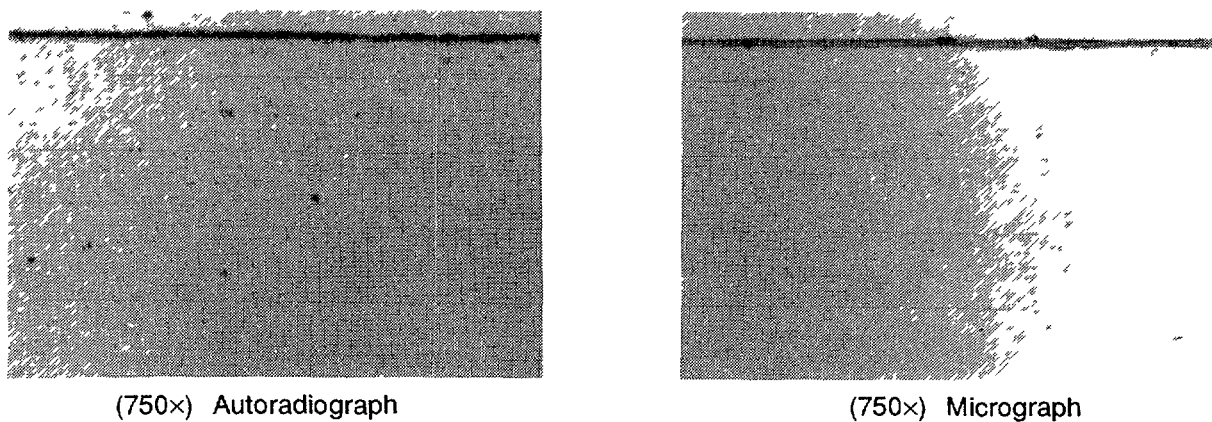
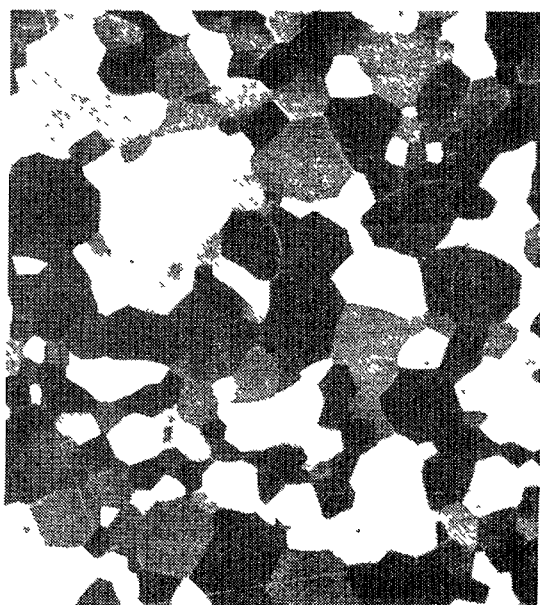


FIG. 2.44. Autoradiograph showing uniform tritium content in thin zirconia film formed in T_2O for long enough to saturate oxide (oxidized in O_2 at $400^\circ C$ for 66.5 h to weight gain of 12.7 mg/dm^2 , oxidation continued in T_2O at $400^\circ C$ for 48 h to total weight gain of 114.4 mg/dm^2). Compare with non-uniform distribution in Fig. 2.35 [52].

that the hydrogen in the ZrO_2 is tightly bonded and relatively immobile. Values for the diffusivity from these experiments are in good agreement with the above, being in the region of $10^{-20} \text{ m}^2 \cdot \text{s}^{-1}$.

Thus, we arrive at a picture whereby hydrogen uptake in alloys containing intermetallics of Fe, Cr and Ni is controlled by release of the hydrogen atoms at the sites of these particles, and migration of them via the same intermetallics, perhaps by way of stringers of metallic Fe or Ni in the oxide, into the metal. In alloys containing few such particles (e.g. Zr-2.5 Nb) the hydrogen must migrate more uniformly through the



(175×) Autoradiograph



(175×) Micrograph

FIG. 2.45. Surface autoradiograph showing tritium content proportional to oxide thickness. Note that the darkness of the interference colour oxides in the micrograph is not proportional to thickness because of colour response of black and white film (oxidized in T_2O at $400^\circ C$ to weight gain of 1.9 mg/dm^2) [52].

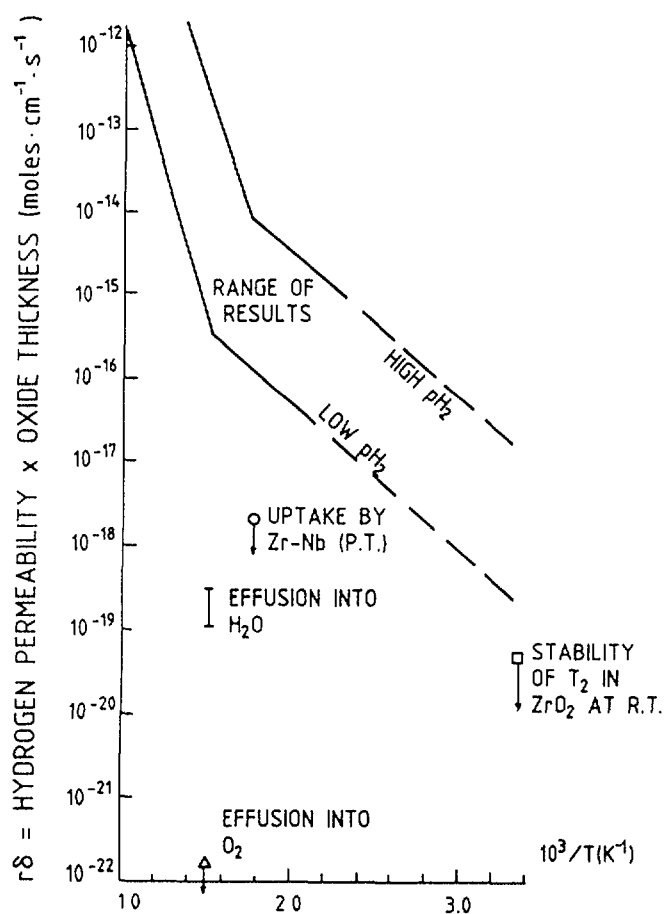


FIG. 2.46. Comparison of permeability data of T. Smith with other estimates of hydrogen in ZrO_2 films [245].

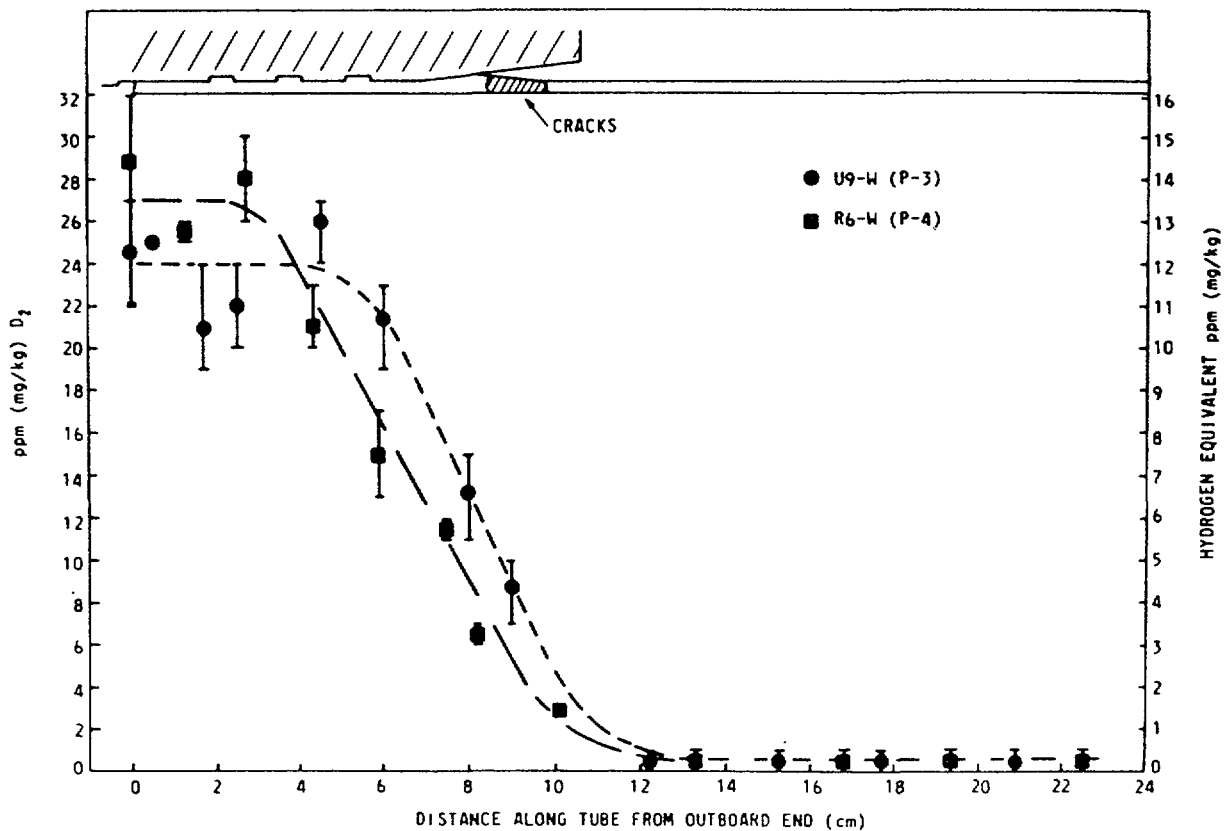


FIG. 2.47. Increase in deuterium concentration at the inlet ends of Zr-2.5 Nb alloy pressure tubes in the Pickering reactors [94].

oxide, which has a low diffusivity for hydrogen. This difference in mechanism can account for the large differences in the observed deuterium uptake rates in Zircaloy-2 and Zr-2.5 Nb alloy pressure tubes [33]. If we assume that the very low rates of uptake by Zr-2.5 Nb are entirely controlled by diffusion through the oxide film, then we can use these rates to calculate an upper bound for the permeability of ZrO_2 . This gives us a value of $\sim 10^{-18} \text{ mol}\cdot\text{m}^{-2}\cdot\text{s}^{-1}$ for the permeability at 290°C . This is in the same range as the results from effusion into steam [76], especially if the actual barrier layer oxide thickness is quite thin (i.e. if the oxide is post-transition). Without a knowledge of the hydrogen concentrations in these oxides, it is not possible to estimate a true diffusion coefficient, but the permeabilities estimated above are not inconsistent with the very low diffusion coefficients in the surface layer measured by the workers at North Carolina State University [77,78], University of Toronto [92] and Ontario Hydro [93].

2.3.3. Hydrogen absorption via metallic contacts

Although hydrogen absorption through a metallic contact may be the most trivial of the three mechanisms mechanistically, it nevertheless has important practical aspects as it may be one route for ingress of excess deuterium into the ends of pressure tubes (Fig. 2.47) from the 403 SS end fitting [94]. The zirconium alloy pressure tube is in good metallic contact with the end-fitting steel in the three grooves of the rolled joint. The factors which control ingress by such a route should, therefore, be considered.

When a galvanic couple between a zirconium alloy and a nickel or iron alloy is exposed to high temperature water the zirconium alloy becomes

TABLE 2.4. COMPARISON OF H UPTAKE BY ZIRCONIUM ALLOY/METAL COUPLES WITH PHYSICAL PROPERTIES OF THE COUPLED METAL
(References refer to the original table in Ref. [245])

Metal	Exchange current density for H ₂ (1) (log i ₀)	Diffusion coeff. of H ₂ at 400°C (cm ² .s ⁻¹)	Enthalpy of solution of H ₂ (kcal/mol)	Permeability to ³ H at 400°C (cm ³ (STP)mm.h ⁻¹ .cm ⁻² atm ^{-1/2})	Hydrogen uptake	
					Ref. [97] (2)	Ref. [98] (3)
Cu	-6.70	9.0 x 10 ⁻⁶ (4)	+0.47 (4)	3.6 x 10 ⁻⁴ (5)	-	13
Fe	-5.93	1.5 x 10 ⁻⁴ (4)	+0.28 (4)	1.5 x 10 ⁻¹ (6)	-	-
Inconel	-5.46	8.0 x 10 ⁻⁷ (7)	-	5.4 x 10 ⁻³ (7)	152	-
304 S/S	-5.37	3.0 x 10 ⁻⁷ (8)	-	3.5 x 10 ⁻³ (6)	-	380
403 S/S	-	5.8 x 10 ⁻⁵ (9)	-	4.6 x 10 ⁻² (9)	-	1380
Ni	-5.17	5.0 x 10 ⁻⁶ (4)	+0.16 (4)	3.0 x 10 ⁻² (6)	-	3780
Pt	-3.73	5.1 x 10 ⁻³ (4)	+0.75 (4)	1.1 x 10 ⁻³ (6)	354	>10000(9)

(1) Comprehensive Treatise of Electrochemistry, Vol.2, Eds. Bockris, Conway, Yeager & White, Plenum, NY, 1981.

(2) mg/kg H₂ in Zircaloy-2 after 60 d coupled to metal in 300°C water under irradiation.

(3) Peak H₂ concentration at centre of Zr-2.5 wt% Nb tube after 10 days in pH10 LiOH with 1.1 MPa H₂ overpressure.

(4) J. Völkl and G. Alefeld, Chapter 5, Diffusion in Solids, Recent Developments, Eds. Nowick and Burton, Ac. Press, New York, 1975.

(5) G.R. Caskey et al., Corrosion, 1976, 32 (9).

(6) R.W. Webb, Permeation of H through Metals, NAA-SR-10462 (1965).

(7) W.M. Robertson, Met. Trans. A, 1977, 8A.

(8) M.R. Louthan and R.G. Derrick, Corr. Sci., 1975, 15,

(9) V.F. Urbanic [98].

anodic and the transition metal alloy cathodic. The cathodic part of the oxidation process then occurs on the transition metal and protons are discharged there and may be absorbed by the transition metal. The effective surface areas of the two parts of the couple will be determined by the conductivity of the water, and in high purity water only small areas adjacent to the point of contact should be effective, although under irradiation this limitation may be relaxed by the effect of irradiation on the conductivity of the electrolyte [95,96]. The distance from the points of closest approach of the two metals in the water and the point of metallurgical contact will be important for the hydrogen migration, but not for the oxidation. This is evident in the instance of localized oxidation opposite a platinum implant [95,96], where the electrical contact was distant from the point of closest approach of the platinum implant and the facing zirconium surface. In this instance, accelerated oxidation but no excess hydriding occurred, whereas adjacent to the platinum implant both accelerated oxidation and enhanced hydrogen contents were observed.

In the case of the Inconel to Zircaloy bonds [95,97], where the interface between the Inconel and the Zircaloy-2 was exposed to the water, and diffusion distances for both hydrogen and electrons were short, both excess oxidation and excess hydriding were observed adjacent to the bond. No enhanced hydrogen uptake was observed in Zircaloy/Zircaloy crevices [96,97], but enhanced oxidation, perhaps from enhanced radiolysis, was seen. Although it might be expected that the diffusivity of hydrogen in the transition metal would affect the rate of migration into the zirconium alloy via the metallurgical bond there is no evidence for comparison (say) between Inconel and stainless steel. However, where high temperature water is in contact with zirconium alloy/transition metal bonds close to or at the interface between them the rate of the cathodic reaction on the transition metal may be more important than the hydrogen diffusivity in it. In this circumstance, the higher nickel content of Inconel than of stainless steel and the specific effects of nickel with regard to the hydrogen recombination reaction may mean higher excess hydrogen absorption for zirconium alloy/Inconel bonds than for zirconium alloy/stainless steel bonds. This seems to be borne out by the results of Urbanic's [98] experiments on Zr-2.5 Nb tubes with plugs of various metals inserted in them. If these results are compared with some properties of the various metals (Table 2.4) it would appear that the exchange current density for the hydrogen evolution reaction is more important than the hydrogen permeability in determining the uptake by zirconium alloys. However, there is insufficient evidence at present to reach a firm conclusion about the important factors determining the rate of excess hydrogen uptake in zirconium alloys metallurgically bonded to transition metals; the indications are that we should look at the efficiency of the coupled metal as a cathode, rather than its diffusion properties.

3. RADIATION EFFECTS ON THE CORROSION OF ZIRCONIUM ALLOYS

From the wide use of zirconium alloys as components in nuclear reactors has come clear evidence that reactor radiation is a major corrosion parameter. The evidence emerges from comparisons of zirconium alloy corrosion behavior in different reactor types, for example, BWRs versus PWRs, and in corresponding reactor loop chemistries. Also, oxidation rates differ with location (including varying temperature and radiation levels) along components such as fuel rods and reactor pressure tubes. In most respects, oxidation effects on power reactor components are paralleled by oxidation behavior on specimens exposed to radiation in reactor loops. Factors that influence zirconium alloy oxidation under irradiation include: radiation type, intensity and fluence, coolant chemistry, alloy composition, metallurgical condition, surface condition, temperature, and proximity to dissimilar metals. This section provides an overview of zirconium alloy oxidation and hydriding behaviour under irradiation. Details of the interaction of the factors indicated above are treated in other sections of the report.

3.1. INFLUENCE OF RADIATION ON ZIRCONIUM ALLOY CORROSION PHENOMENA

Systematic evaluation of radiation effects on zirconium alloy corrosion reveals the following general characteristics:

- Small radiation effects on specimens and reactor and fuel assembly components in low-oxygen aqueous coolants (e.g., PWR, PHWR, WWER, reactor loops), in lower fluence regimes;
- Strong evidence for accelerated radiation-induced oxidation on non-heat-transfer specimens and components in low-oxygen aqueous coolants at higher fluences;
- Controversy about radiation effects on fuel cladding in low-oxygen coolants, due to the complexity of separating heat transfer, LiOH concentration, and radiation effects;
- Accelerated uniform oxidation on specimens and reactor and fuel assembly components in oxygenated aqueous coolants;
- Accelerated nodular oxidation on fuel cladding and fuel assembly components exposed to oxygenated coolants; less prevalent nodular oxidation on specimens in loops with oxygenated coolants (early thick oxide formation may obscure nodule formation), except for loops operated under boiling conditions;
- Localized oxidation from a variety of causes, including: (a) dissimilar metal effects; (b) alloy element segregations for some alloys; (c) spacer effects on LWR fuel rods; and (d) stress or strain effects in cladding.

There are a number of factors that influence corrosion behavior under irradiation. Such factors include radiation type, coolant chemistry, alloy composition, etc., and are discussed in the following.

3.1.1. Radiation type, intensity, spectral shift, duration

Reactor fluxes are composites of many energetic species. There have been relatively few definitive investigations that isolate effects of individual species. Investigations outside the reactor need to account for important environmental factors (temperature, redox conditions, etc.) over

periods that allow irradiations to reach definite levels. The leading attempts to isolate radiation species have involved gammas, electrons, protons, and deuterons. The early results to date tend to rule out substantial effects of gammas or high-energy electrons, and point to neutrons as the most significant flux component in zirconium oxidation phenomena under irradiation. However, behaviour of gadolinia/uranium rods suggest that the influence of specific radiation species is not fully resolved (e.g., possible influence of beta flux). Variations in flux due to fuel shuffling and to perturbations near control rods need to be accounted for in the interpretation of radiation effects on zirconium alloy cladding and on certain components.

3.1.2. Coolant chemistry

The major environmental influence of dissolved oxygen was outlined above. Other coolant-borne species (e.g., copper, iron, nickel, etc.) deposit as metal oxides (crud) on fuel rod surfaces and have, in selected cases, appeared to contribute to accelerated oxidation on both BWR and PWR cladding. Effects of pH, impurities (Cl, F, etc.), Li concentration, and radiolytic species need to be accounted for. While pH does not appear to be a major variable over typical ranges in reactor coolants, zirconium alloy oxidation can be markedly influenced by LiOH that is used for pH control, if conditions facilitate concentration of lithium in the oxide. However, there is evidence that normal PWR conditions do not result in such markedly elevated lithium concentrations.

3.1.3. Alloy composition

Only a few alloys have come to prominence in nuclear service. The criterion of low neutron capture cross section limits the range of alloy additions. The performance of the leading alloys has generally been within the ranges of acceptable parameters. However, initiatives are underway to identify alloys that will better tolerate trends to more severe operating requirements. Section 3.2 addresses effects of specific alloy compositions.

3.1.4. Metallurgical condition

Effects of metallurgical condition on fuel rod oxidation and hydriding have been a major consideration because welds assure that multiple metallurgical conditions exist in each fuel rod. Early investigations suggested that the alpha and beta (fast cooled) conditions for the Zircalloys had similar corrosion characteristics. On the other hand, Zircaloy heat treated in the alpha plus beta region or slow-cooled through the region had inferior oxidation resistance (also demonstrated for Ozhennite). The beta treatment became prominent when it was recognized that it mitigates nodular attack on the Zircalloys, both in high-temperature autoclaves and in oxygenated reactor environments. However, cladding generally receives certain finishing treatments after the beta anneal. The annealed and cold-worked condition for Zr-2.5 Nb had relatively high oxidation rates under irradiation in oxygenated conditions, compared to the quenched, cold-worked, and aged condition. The differences in oxidation rate were smaller for the two Zr-2.5 Nb conditions for irradiations in a low oxygen coolant.

3.1.5. Surface condition

Zirconium alloys have been exposed in several surface conditions, both in service and in reactor-loop investigations. Early reactor and fuel assembly components were autoclaved. Gradually, the autoclave treatments

were eliminated, first for PWR cladding, more recently for BWR cladding. Some cladding saw service in the as-pickled surface condition, but the standard treatment for BWR and PWR cladding is now the belt-ground condition. Pressure tubes continue to be autoclaved. In terms of reactor performance, all of the surface treatments appear to have been satisfactory. However, loop studies demonstrated marked differences in corrosion behavior under irradiation for various surface treatments.

3.1.6. Temperature

Radiation effects on zirconium alloy oxidation and hydriding have been investigated extensively in the range of water reactor operation (approximately 240 to 330°C). In this range, radiation effects have been characterized, varying as indicated earlier, from almost no effect to accelerations of oxidation of up to two orders of magnitude, depending on environment, radiation level, and other factors summarized in this chapter. Of fundamental significance are steam-phase studies suggesting that radiation enhancements disappear as temperatures approach 400°C. At low temperatures, results appear to fit an extrapolation from power reactor temperatures with a low temperature coefficient.

3.1.7. Dissimilar metal effects

Early fuel assembly spacer grid materials included stainless steel and Inconel. While the zirconium alloy corrosion behavior in contact with these materials was generally satisfactory, there was evidence that the adjacent metals caused locally enhanced oxidation on the zirconium alloys, including oxide thickening near Inconel spring contacts and thicker nodules adjacent to stainless steel spacers in the SGHWR. Tests in the ETR G-7 loop revealed localized accelerated oxidation on two types of dissimilar metal couples: Zircaloy/Inconel and Zircaloy/platinum (also Zr-2.5 Nb/platinum). In a low-oxygen coolant, local oxide thickening occurred on Zircaloy where the bimetal interface with Inconel was exposed to water. Accelerated hydriding also occurred, with the Inconel appearing to act as a "window" for hydrogen entry to the Zircaloy. Welded Zircaloy/platinum couples developed local hydriding in the Zircaloy adjacent to the weld. The weld metal developed subsurface stringer-like oxide, similar to laboratory experience. Also, a "shine" effect produced accelerated local oxidation on zirconium alloy specimens adjacent to the platinum inserts.

3.1.8. Heat flux

As indicated earlier, heat flux becomes an important consideration when corrosion on heat transfer surfaces subject to radiation is interpreted. Often in question are the relative effects of radiation, thermal effects, and species that may have concentrated in the oxides as a result of heat transfer.

The following discussion addresses phenomena and characteristics of uniform and localized oxidation of zirconium alloys under irradiation. Associated hydriding phenomena are summarized also .

3.2. EFFECTS OF ALLOY COMPOSITION

Table 3.1 indicates zirconium alloys that have been subjected to reactor service and/or reactor loop evaluations, including common and less common alloys. Three areas are addressed in Table 3.1: fuel cladding, pressure tubes, and loop studies. Other service applications include BWR

TABLE 3.1. SUMMARY OF ZIRCONIUM ALLOYS EVALUATED UNDER IRRADIATION

Alloy	Fuel Cladding	Pressure Tubes	Loop Studies ^(f)
1. Zircaloy-2	✓	✓	✓
2. Low Ni Zircaloy-2	(a)	(a)	✓
3. Zircaloy-4	✓	(a)	✓
4. Zr-1.2 Cr-0.08 Fe	(a)	--	✓
5. Zr-1.2 Cu-0.28 Fe	--	--	✓
6. Zr-3 Nb-1 Sn	(a)	--	✓
7. Zr-0.2 Sn-0.1 Fe-0.1 Ni-0.1 Nb ^(b)		--	
8. Zr-2.5 Nb	(a)	✓	✓
9. Crystal bar zirconium	--	--	✓
10. Zr-1 Nb	✓	--	✓
11. Zr-3.5 Sn-0.8 Mo-0.8 Nb ^(c)	--	(a)	✓
12. Zr-0.52 Nb-0.03 Fe-0.06 Sn-0.49 Cr-0.13 O ^(d)	--	--	✓
13. Zr-1.0 Nb-1.0 Sn-0.1 Fe ^(e)	(a)	--	--

(a) Demonstration basis.

(b) Designated Ozhemnite-0.5 [99].

(c) Designated Excel [100].

(d) Designated Scanuk-4 [101].

(e) Designated ZIRLO [102].

(f) Does not include all alloys tested in loops.

and WVER 440 fuel channels and fuel assembly spacer materials, involving the same alloys indicated for fuel cladding and pressure tube applications. Table 3.2 compares the oxidation and hydriding characteristics for the principal alloy types.

Alloys differ in their responses to the chemical and radiation environments. These effects will be addressed in subsequent sections.

3.3. UNIFORM OXIDATION OF ZIRCONIUM ALLOYS UNDER IRRADIATION

Uniform oxidation, as defined here, generally denotes growth of oxides that do not vary widely in thickness across relatively large areas. However, some localized phenomena will be cited that do not involve marked differences in oxide thickness. On the other hand, oxides regarded here as uniform often vary gradually in thickness from one location to another on a given reactor material, for example, along the length of a fuel rod or a reactor pressure tube.

TABLE 3.2. ALLOY CHARACTERISTICS UNDER IRRADIATION

<u>Alloy</u>	<u>Oxidation Rate</u>	<u>Hydriding Rate</u>
1. Zircaloy-2	Intermediate rates	Intermediate rates
2. Low Ni Zircaloy-2	Similar to other Zircaloys	Like Zircaloy-4
3. Zircaloy-4	Like Zircaloy-2 in PWRs, but higher oxidation in BWRs	Generally less than Zircaloy-2
4. Zr-1.2 Cr-0.08 Fe	Like Zircaloys but susceptible to alloy segregation	Similar to Zircaloy-2 except when alloy segregation evident
5. Zr-1.2 Cu-0.28 Fe	Much higher than Zircaloys	Much higher than Zircaloys
6. Zr-3 Nb-1 Sn	Mildly lower than Zircaloys	Mildly lower than Zircaloy-4
7. Ozhennite-0.5	Similar to Zircaloys ^(a)	Higher than Zircaloy-2 ^(a)
8. Zr-2.5 Nb	Generally Lower than Zircaloys	Much lower than Zircaloys
9. Crystal bar zirconium	Higher than Zircaloys	Much higher than Zircaloys
10. Zr-1 Nb	(b)	(b)
11. Zr-3.5 Sn-0.8 Mo-0.8 Nb	Higher than Zircaloys	--
12. Scanuk Alloys	--	--
13. Zr-1.0 Nb-1.0 Sn-0.1 Fe	Lower than Zircaloy	Lower than Zircaloy-4 due to lower oxidation

(a) Loop study reported in Reviews on Coatings and Corrosion, Vol. I, No. 4 (1975) pp. 299-366.

(b) Few direct comparisons to the Zircaloys are available; Reference [103] cites higher oxidation rate on Zr-1 Nb than on Zircaloy-4 fuel cladding; Reference [104] cites relatively high oxide thicknesses on Zr-1 Nb cladding (VK-50 Reactor); cladding in WVER 440 reactors operates with low oxidation and hydriding rates [105].

Defining radiation effects on oxidation requires comparisons on identical materials in similar water chemistries, across a range of radiation levels or relative to unirradiated control materials. Reactor loops with specimen locations over a range of flux levels and outside the flux zone have provided the basis for quantifying radiation effects and for detecting even subtle trends. Radiation effects become evident on reactor

components (e.g., reactor pressure tubes) by comparisons of metallographic sections that represent locations corresponding to a variety of flux levels. Non-destructive techniques (principally eddy current) are also sufficiently advanced to permit oxide thickness measurements on reactor components and fuel rods to precisions better than $\pm 5 \mu\text{m}$.

Oxidation studies on zirconium alloy specimens and reactor components with negligible heat transfer provide a basis to isolate radiation effects. Evaluations on heat transfer surfaces, principally fuel rods, offer the complexity of simultaneous radiation and thermal effects. Phenomena that are more pronounced under heat transfer (e.g., crud deposition and concentration of species such as lithium) may impose significant influences that are not readily simulated on unheated surfaces.

3.3.1. Oxidation in irradiated low-oxygen coolants

The following zirconium alloy reactor and fuel assembly components are utilized in reactors of the pressurized water type:

- Pressure tubes - PHWR, Hanford N Reactor,
- Fuel cladding - PWR, N Reactor, WWER, PHWR,
- Fuel channels - MZFR, WWER 440, Atucha-1,
- Guide tubes/fuel spacers - PWR.

Data from three sources are presented:

- Oxide thicknesses on Zircaloy-4 PWR fuel cladding, determined by metallography and eddy current (Figure 3.1),
- Oxide thicknesses from pressure tubes, determined by metallography, including Zircaloy-2 (Figures 3.2 and 3.3) and Zr-2.5 Nb (Figure 3.3),
- Oxide weight gains on Zircaloy-2 specimens exposed in a test reactor loop; specimens weighed (Figures 3.4 and 3.5).

Test loop data provide the highest precision in judgments of radiation effects on oxidation. The loop specimens are weighed to $\pm 0.1 \text{ mg}$ and sometimes include identical specimens exposed to the same coolant over a range of neutron fluxes or outside the flux [109].

3.3.1.1. Oxidation and Hydridding of Fuel Cladding

Aqueous corrosion of Zircaloy-4 PWR fuel cladding has been represented by some investigators as showing no radiation enhancement [103]. The metallographic approach to the definition of corrosion rates may have missed the early, relatively subtle, radiation effects detected by weight gains on loop specimens [109,110]. In fact, comparisons of the wide band of corrosion results on fuel cladding with nominal data from unirradiated specimens (Figure 3.1) suggest some radiation enhancement. More recent evidence on PWR fuel cladding at higher exposures suggests an additional radiation effect, above the enhanced oxidation from thermal effects on heat transfer surfaces [106,111]. In lithiated reactor coolants, lithium hydroxide may concentrate within the oxide film and cause accelerated oxidation independent of irradiation effects. However, enhancements of PWR cladding oxidation were attributed to radiation rather than lithium effects [106].

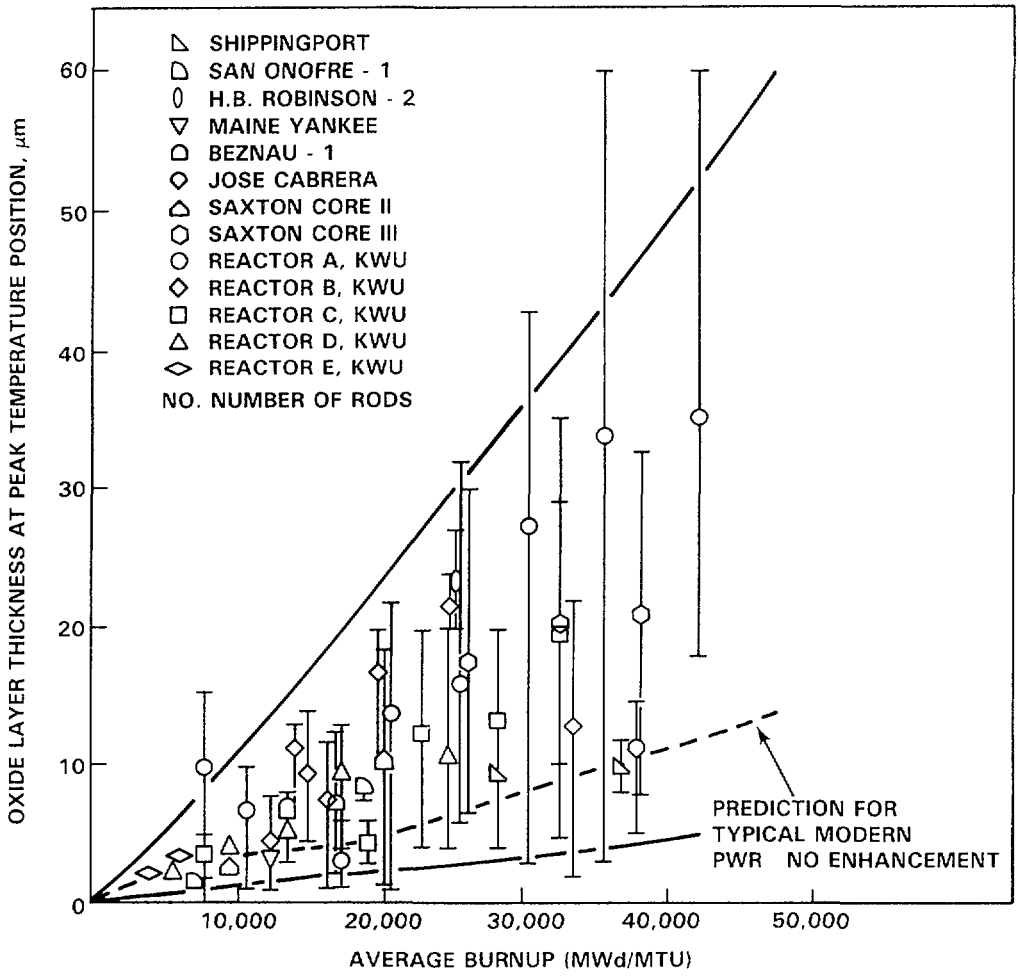


FIG. 3.1. Maximum oxide layer thickness of PWR fuel rods versus burnup [106].

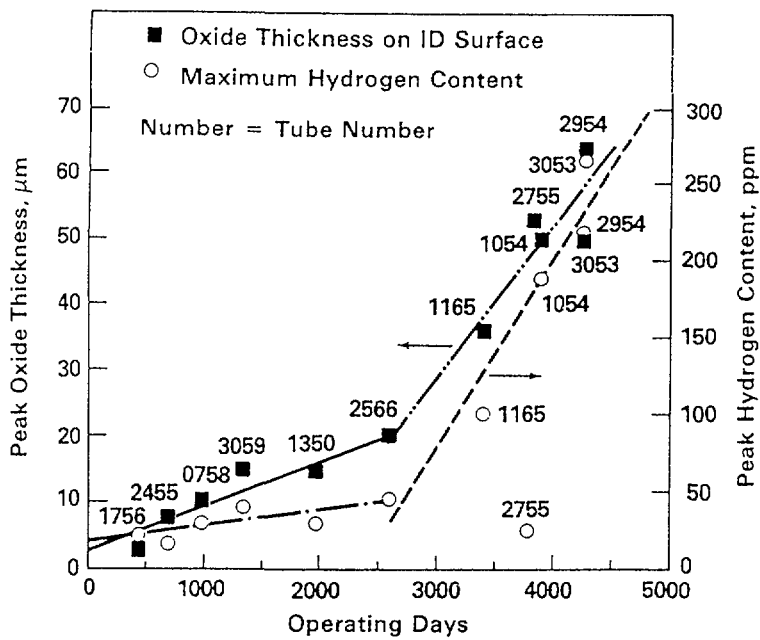


FIG. 3.2. Maximum oxidation and hydrogen content of N-reactor pressure tubes [107].

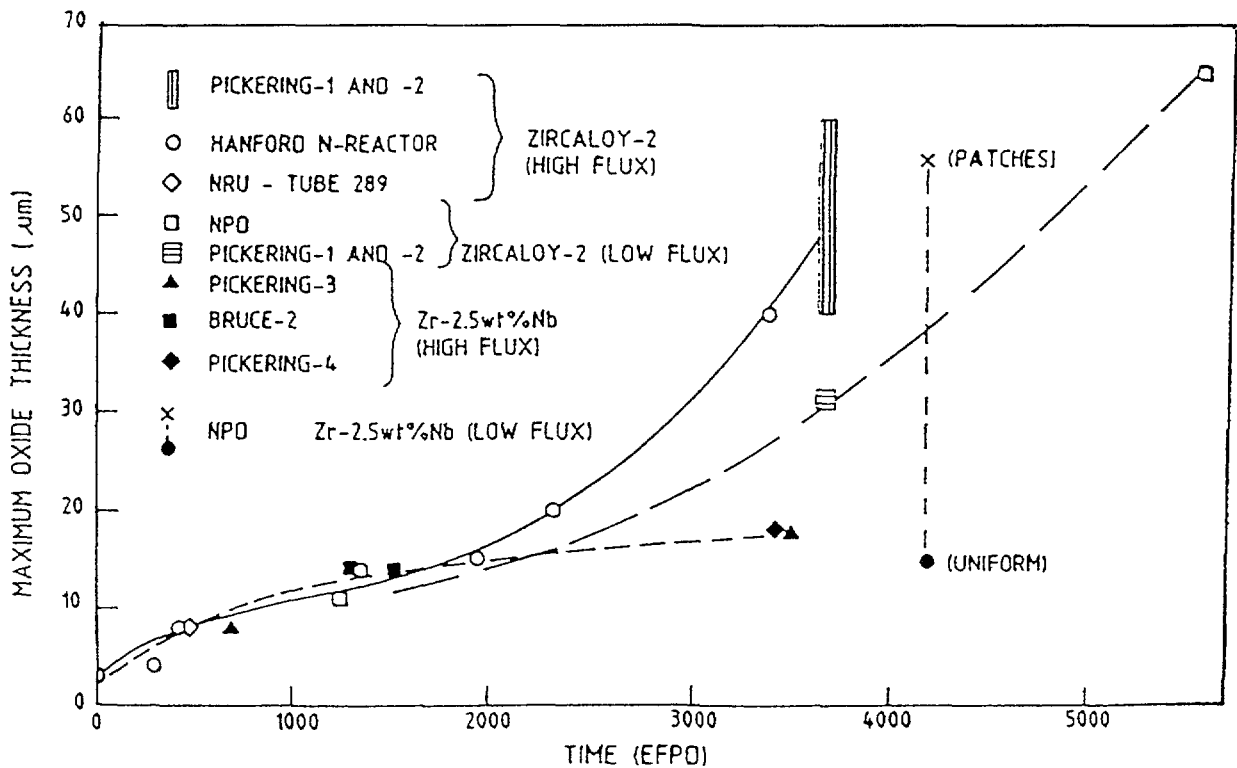


FIG. 3.3. Long term corrosion of cold worked Zircaloy-2 and Zr-2.5 Nb pressure tubes [33, 108].

3.3.1.2. Oxidation and hydriding of reactor pressure tubes

Zircaloy-2 pressure tubes have been examined periodically over the 25 year active life of the Hanford N-Reactor (Figure 3.2); Zircaloy-2 and Zr-2.5 Nb pressure tubes have been examined after extended exposures in CANDU reactors (Figure 3.3). The tube examinations provide a relatively comprehensive evaluation of radiation effects:

- As a function of time for a series of tube examinations,
- As a function of flux and temperature along tube lengths,
- Inside (water-side) versus outside (generally moist helium, nitrogen or CO₂) surface oxidation,
- Azimuthal variations.

Details regarding the above effects are reported elsewhere [33,107,108]; here the focus will be on the major oxidation and associated hydriding results. Figure 3.2 summarizes maximum oxidation and hydriding results on a series of N-Reactor pressure tubes, exposed in ammoniated, low-oxygen coolant. Tubes with lower exposures demonstrate relatively low oxidation rates. The data in Figure 3.2 indicate a transition to a higher rate that is sustained over the subsequent exposures (2500 to 4000 d). The two oxidation trend lines represent least squares analysis of the data. The transition to the higher rate is consistent with thick-film phenomena first observed in test reactor investigations during the late 1960's and early 1970's [109] (see Section 3.4.4). The accelerated oxidation appears on Zircaloy pressure tubes from the Hanford N-Reactor, Pickering-1 and -2, and NPD reactors (Figures 3.2 and 3.3), all operating in generally-nonboiling pressurized water conditions. The Hanford N-Reactor coolant was ammoniated, maintaining relatively high H₂ concentrations (30-40 cc H₂/kg). The PHWRs operate with lithiated water, with D₂ overpressures, at relatively low concentrations (3-10 cc D₂/kg, but frequently lower).

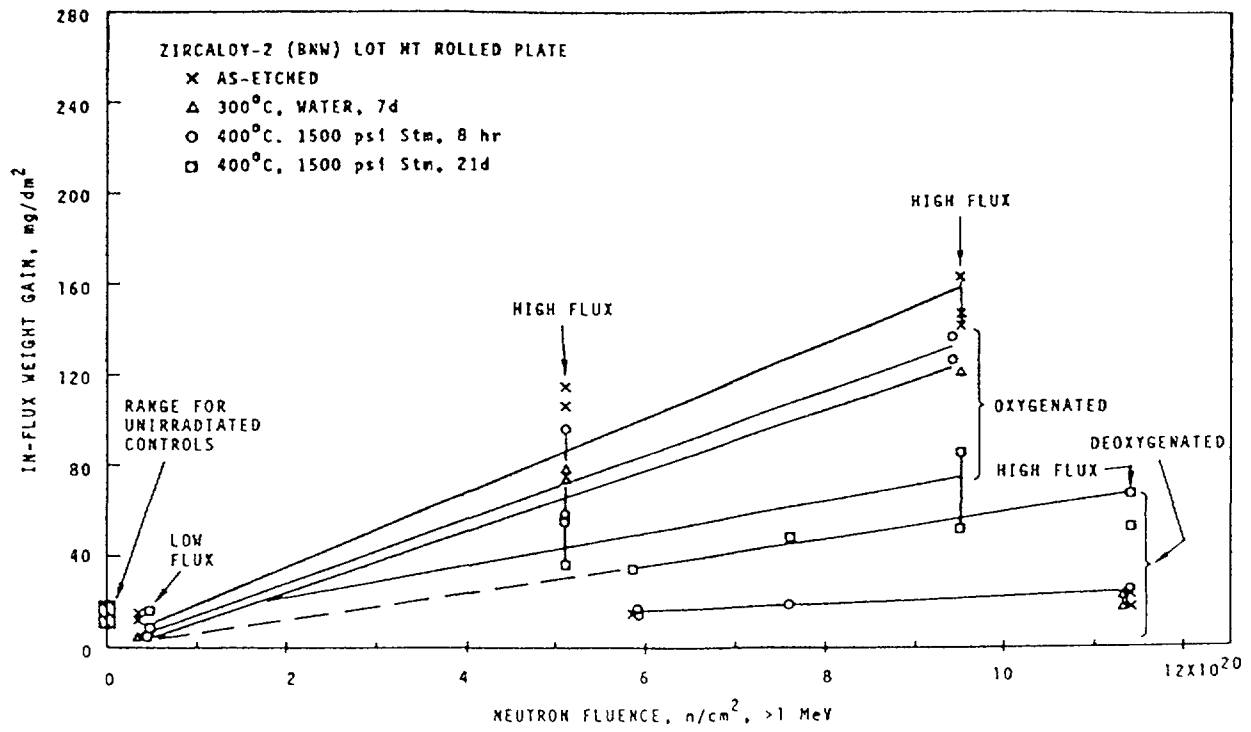


FIG. 3.4. Corrosion of Zircaloy-2, lot HT, as a function of fast neutron fluence in oxygenated and deoxygenated ATR 1D loop coolants (LiOH pH control) [109].

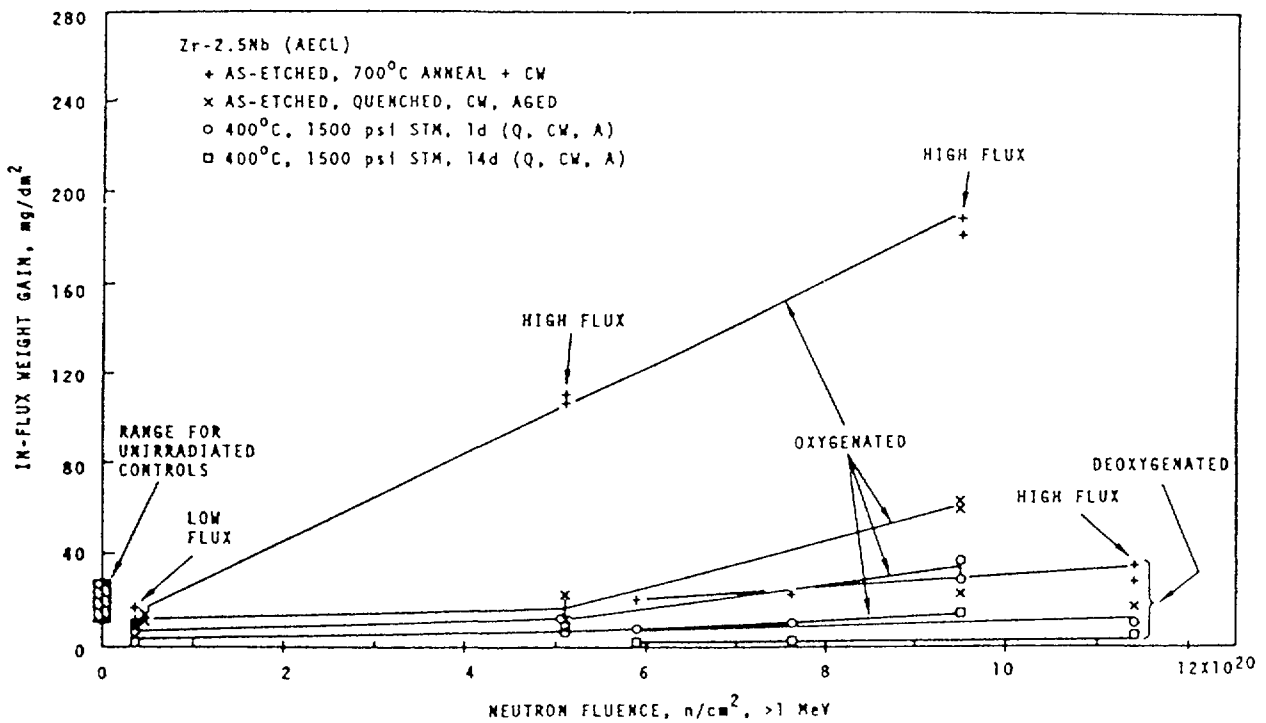


FIG. 3.5. Corrosion of Zr-2.5 Nb alloy as a function of fast neutron fluence in oxygenated and deoxygenated ATR 1D loop coolants (LiOH pH control) [109].

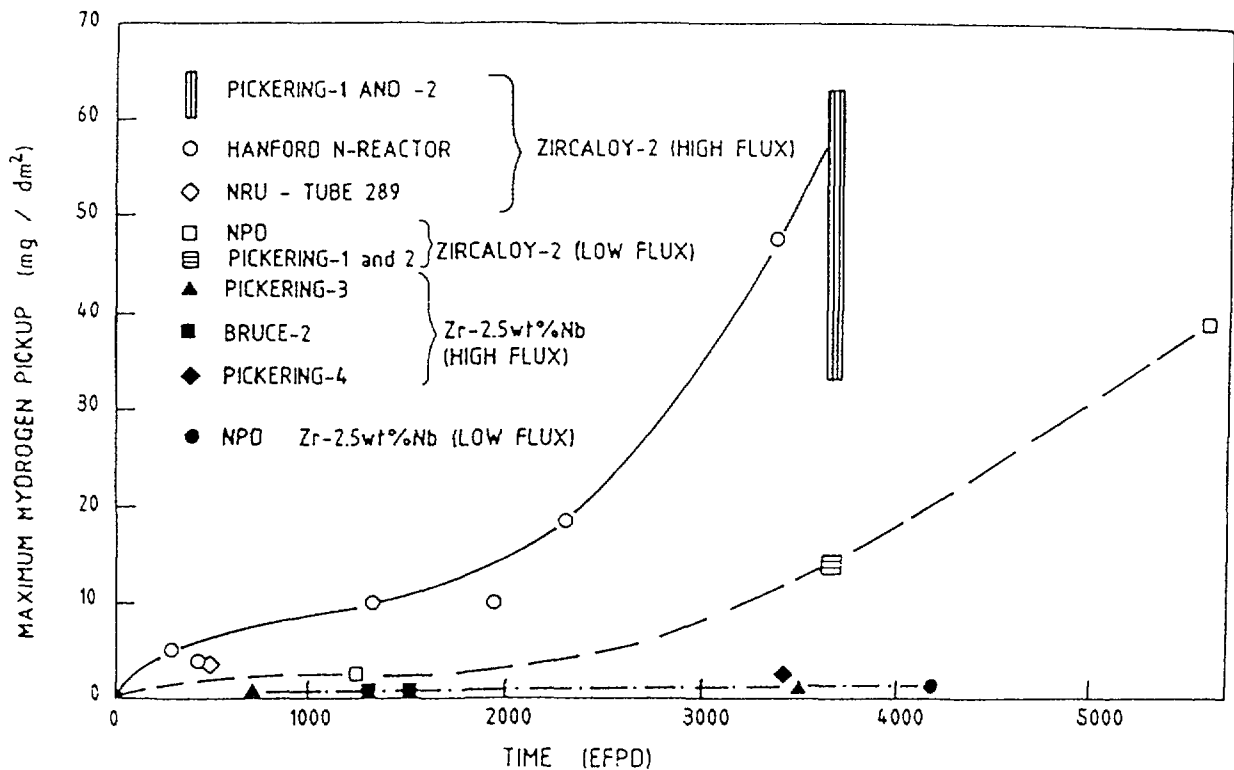


FIG. 3.6. Long term hydriding of cold-worked Zircaloy-2 and Zr-2.5 Nb pressure tubes [33, 108].

The associated hydriding trends largely parallel the oxidation trends for Zircaloy-2 tubes (Figures 3.2, 3.3, and 3.6). Tube 2755 (Figure 3.2) represents an exception to the trend; the tube had the expected oxide thickness, but a hydrogen content an order of magnitude below the trend line. Laboratory investigations confirmed that material from Tube 2755 is more resistant to hydriding than material from similar tubes with in-reactor hydriding histories [112]. Lot-to-lot differences in both oxidation and hydriding were observed for Zircaloy-2 specimens in test reactor investigations [109].

Figures 3.3 and 3.6 compare oxidation and hydriding trends for Zr-2.5 Nb pressure tubes. At exposures shown in Figure 3.3, oxidation on Zr-2.5 Nb tubes has not begun to demonstrate the transition that occurred consistently on Zircaloy-2 materials (Figure 3.2 and Ref. [109]). Hydriding trends for Zr-2.5 Nb tubes are consistently below trends for Zircaloy-2 (Figure 3.6), agreeing with results from test reactor specimens [109,110].

3.3.1.3. Oxidation and hydriding in test reactor loops

An overview of the oxidation of loop specimens as a function of alloy composition is given in Table 3.2, and indicates marked differences in oxidation characteristics.

Figure 3.4 shows the oxidation characteristics as a function of neutron fluence for identical Zircaloy specimens irradiated in both low-oxygen and oxygenated test reactor coolants. Compared to the end-of-life radiation levels on fuel cladding and pressure tubes ($>5 \times 10^{21}$ n.cm⁻², >1 MeV) the radiation exposures presented in Figure 3.4 are relatively low, demonstrating early behavior. Oxidation of specimens exposed as-etched to low-oxygen coolant was only slightly accelerated, compared with unirradiated controls. Oxidation of prefilmed specimens was accelerated, compared with unirradiated controls. Beyond

oxide thicknesses of 12 to 13 μm , Zircaloy-2 specimens exposed to a low-oxygen ETR G-7 loop coolant moved into a regime of highly accelerated oxidation, discussed in the following section.

Figure 3.5 indicates that Zr-2.5 Nb also had low oxidation rates in the low-oxygen test reactor coolant. In fact, oxidation rates were slightly lower than rates on unirradiated controls, in contrast to slight acceleration on Zircaloy-2 specimens. Further examination of the Zr-2.5 Nb behavior suggested that the lower oxidation for irradiated specimens was due to radiation-induced aging of the Zr-2.5 Nb material, that tends to initially improve the oxidation resistance [113].

An overview of hydriding of loop specimens as a function of alloy is also summarized in Table 3.2. Hydriding trends generally parallel oxidation trends, but exceptions have been observed (Figure 3.2 and Ref. [119]), sometimes involving high oxidation rates and low hydriding rates.

3.3.1.4. Thick-film effects in low-oxygen coolants

The upturn in Zircaloy-2 oxidation rates shown in Figure 3.2. represents a trend previously discovered in test reactor exposures in the late 1960s and early 1970s [109]. The test reactor series demonstrated that rapid oxidation rates did not decrease when Zircaloy-2 specimens were transferred from an oxygenated aqueous coolant to a low-oxygen aqueous coolant if the oxide film thickness was 30 μm or greater [106]. If the film thickness was 10 μm or less, the oxidation rate decreased after the oxygenated to low-oxygen transfer [109]. To further clarify the threshold thickness that appeared to define the onset of thick-film behavior, Zircaloy-2 specimens were preoxidized in a laboratory autoclave. Identical Zircaloy-2 specimens were exposed in the ETR G-7 loop with the following surface conditions:

- As-etched,
- Thin oxides (13 to 24 mg/dm^2),
- Thick oxides (192 to 471 mg/dm^2).

Specimens were irradiated to three fluences: 9×10^{19} , 1.0×10^{21} and 1.5×10^{21} $\text{n}\cdot\text{cm}^{-2}$, >1 MeV in a low-oxygen (<0.05 ppm O_2) loop coolant.

The as-etched specimens oxidized at only slightly accelerated rates, compared to unirradiated controls, typical of early Zircaloy behaviour in hydrogenated coolants [109,110]. The specimens exposed with thin prefilms oxidized at mildly accelerated rates. The specimens exposed with initially thick films oxidized at highly accelerated rates. In fact, the oxidation rates on the specimens with the thick prefilm in the low-oxygen coolant were similar to rates on identical specimens exposed in an oxygenated coolant.

The test reactor series on specimens with thick prefilms in low-oxygen water demonstrated that at oxide thicknesses above ~ 12 μm , oxidation rates are highly accelerated. Oxidation characteristics of the thick-film specimens led to the Thick-Film Hypothesis [109]:

"Beyond a threshold oxide thickness (>12 μm for test reactor loop conditions), aqueous radiolysis in oxide cracks and pores controls Zircaloy-2 oxidation rates under irradiation."

This represents only one preliminary view that attempts to explain how oxidation occurs in a hydrogenated coolant at rates that suggest highly oxidizing conditions [109]. Oxidation rates on identical specimens in low-oxygen coolants were similar to rates on specimens irradiated in an oxygenated coolant in the same loop.

3.3.2. Oxidation in irradiated oxygenated coolants

The following zirconium alloy reactor and fuel assembly components are utilized in oxygenated reactor coolants:

- Pressure tubes - SGHWR and RBMK reactor types,
- Fuel cladding - BWR, SGHWR, RBMK reactor types,
- Fuel channels - BWR,
- Fuel Spacers - BWR.

Addressed here are effects of radiation on corrosion of fuel cladding, pressure tubes, and specimens exposed to oxygenated coolants under irradiation.

3.3.2.1. Oxidation and hydriding of fuel cladding

The BWR and SGHWR coolants, without hydrogen additions, typically have dissolved oxygen and hydrogen peroxide contents of a few tenths of a ppm O₂. BWR and SGHWR fuel cladding is subject to accelerated oxidation, promoted by the synergistic effects of dissolved oxygen and radiation. The accelerated oxidation has two components: uniform and nodular. Impurities such as Ca, Mg, Cu, Si and Al also may contribute to the development of nodules. The nodular component is addressed under Localized Phenomena. Figure 3.7a indicates oxidation trends on BWR fuel cladding, including both uniform and nodular components. As with PWR cladding, the oxidation varies markedly along the length of a given rod, reflecting variations in radiation flux and water chemistry. Figure 3.7b shows the nodular oxidation trends from a broad range of BWRs.

Hydrogen pickup fractions tend to be lower in oxygenated than in low-oxygen reactor coolants; in some cases the total oxidation has been higher in oxygenated coolant than at corresponding fluences in low-oxygen environments, so that the total hydrogen uptake frequently has been similar for BWR and PWR cladding. However, in high-exposure regimes, oxidation and hydriding of BWR cladding may be lower than corresponding values for PWR cladding at end-of-life.

3.3.2.2. Oxidation and hydriding of pressure tubes

The SGHWR has 100 Zircaloy-2 pressure tubes and 4 Zircaloy-4 tubes [58]. In the oxygenated SGHWR coolant, the tubes have been subject to nodular or "patch-type" corrosion, similar to the phenomena in other boiling water environments [116]. The most severe oxidation occurs on Zircaloy adjacent to the stainless steel spacer grids. Nodules occur on both fuel cladding and pressure tubes. Maximum nodule thicknesses of 160 μ m have been recorded at fuel burnups of 20 MW.d/kg U.

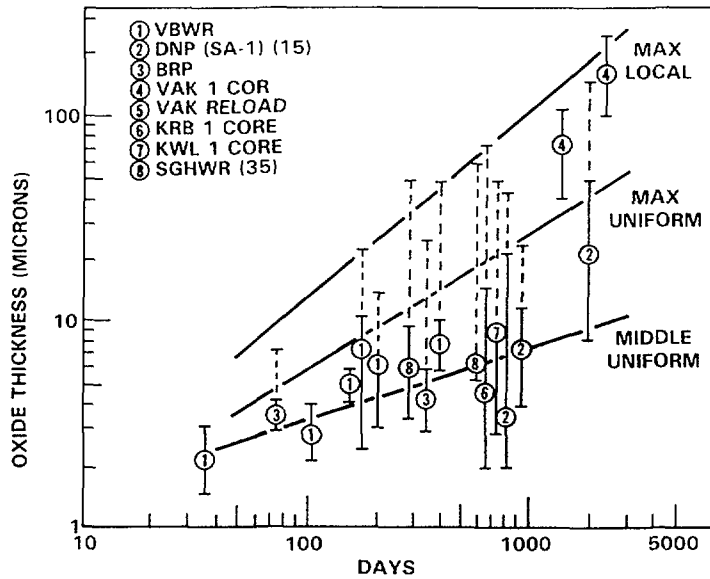


FIG. 3.7a. Uniform and local oxide growth of Zircaloy-2 cladding in BWRs (most data collected by AEG) [114].

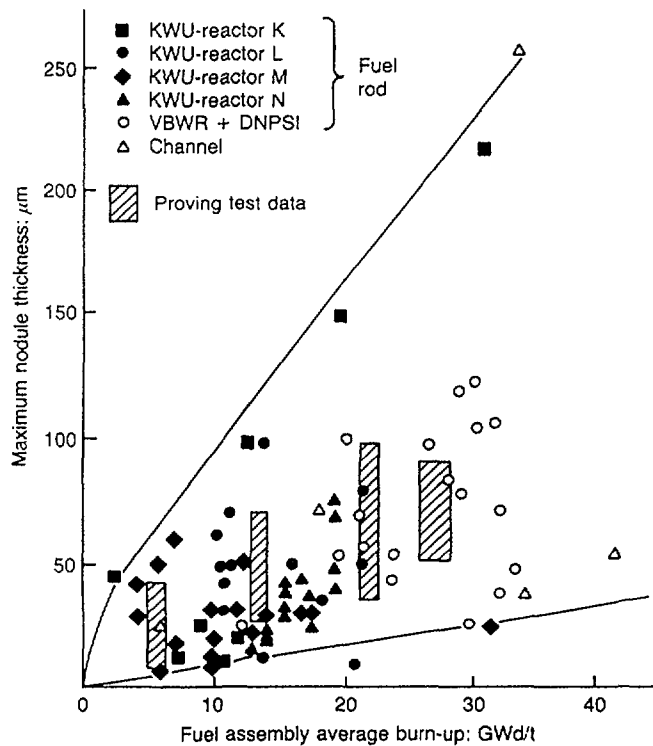


FIG. 3.7b. Nodular oxide growth on Zircaloy cladding in BWRs [115].

3.3.2.3. Oxidation and hydriding in test reactor loops

Figure 3.4 compares the oxidation characteristics of Zircaloy-2 specimens in oxygenated and low-oxygen loop coolants under irradiation. The flux/oxygen interaction results in oxidation rates between one and two orders of magnitude above the rates on corresponding unirradiated specimens.

To illustrate, for Zircaloy-2 Lot CT specimens in the G-7 loop, the in-flux oxidation rate at 280°C and a neutron flux of $1 \times 10^{14} \text{ n.cm}^{-2}$, $>1 \text{ MeV}$, was 3 mdd [109]. The corresponding rate on unirradiated control

specimens was 0.03 mdd, a factor of 100 below the rate under irradiation. Corresponding Lot CT specimens (300°C prefilm) exposed in the low-oxygen G-7 loop coolant oxidized at 0.34 mdd at 1×10^{14} n.cm⁻², an order of magnitude below the rate in the oxygenated environment. The oxidation/fluence relationship is linear for Zircaloy-2 (Figure 3.4) [109] in an oxygenated coolant. A similar relationship also applied to accelerated oxidation on thick-film specimens exposed in the low-oxygen G-7 loop coolant [109].

The accelerated uniform oxidation on loop specimens parallels the accelerated uniform attack on fuel cladding. On the other hand, the incidence of nodular attack on the nonboiling loop specimens seems to be lower than on susceptible Zircaloy materials irradiated in BWRs and in SGHWR. However, some nodules have been observed on loop specimens [109] and others may have coalesced. Nodules occur on Zircaloy in boiling loops [117]. The data in Figure 3.4 for oxygenated conditions demonstrate that specimens with thicker prefilms have higher resistance to the aggressive conditions than specimens initially exposed as-etched or with thinner/prefilms.

Figure 3.5 summarizes the oxidation data for Zr-2.5 Nb exposed in two metallurgical conditions. In the oxygenated coolant, Zr-2.5 Nb specimens in the 700°C anneal plus cold-worked condition oxidized at rates similar to Zircaloy-2. In the quenched, cold worked, aged condition, the Zr-2.5 Nb specimens were initially highly resistant to the oxygenated coolant. In fact, the initial oxidation rates were below rates on unirradiated control specimens (attributed to radiation-induced aging as indicated elsewhere). Mild upturns in oxidation rate occurred for as-etched specimens and for specimens with thin prefilms. Oxidation rates on specimens with thick prefilms remained low over the range of the exposures shown in Figure 3.5.

3.4. LOCALIZED OXIDATION AND HYDRIDING

Several localized oxidation and hydriding phenomena have been observed on irradiated zirconium alloys, including the following:

- Nodular oxide formation,
- Phenomena related to alloy element segregation,
- Dissimilar metal effects.

3.4.1. Nodular oxide formation

Nodular (lenticular or spherical) oxides have been a prevalent phenomenon on high heat transfer surfaces (fuel cladding) and low heat transfer surfaces (fuel spacers, fuel channels) of the Zircaloys. The largely solid oxide nodules nucleate, grow to mature sizes, in some cases coalescing to form thick, uniform oxides [118]. A similar nodular phenomenon was observed on the Zircaloys in autoclaves at elevated temperatures (e.g., 500°C) in high-pressure steam [119]. The nodular attack followed a sequence similar to that observed on BWR and SGHWR materials, but sometimes proceeded beyond coalescence to complete specimen oxidation and disintegration in periods as short as one day at 500°C. A beta heat treatment (e.g., 15 min at 1000°C), combined with rapid cooling, completely suppressed the nodular attack in the 500°C autoclave. Similar heat treatments are now used to suppress the nodular attack on reactor materials.

Zr-2.5 Nb and Ozhennite were resistant to nodular attack in 500°C autoclaving [112], but Ozhennite developed nodules under irradiation [109]. Zr-2.5 Nb seems to also have better resistance than the Zircalloys to nodular attack on reactor materials.

While nodular attack has been a major characteristic of reactors with oxygenated coolants (BWRs, RBMKs, and SGHWR), occasional appearance of nodules on PWR cladding has correlated with uncharacteristic periods of elevated oxygen concentrations in the normally low-oxygen reactor environments. Consequences of the nodular attack have included development of thick spalling oxide on BWR fuel channels and crud-induced localized corrosion (CILC) that has resulted in fuel rod failures in several BWRs.

3.4.2. Alloy element segregation

Phenomena on two of the ETR G-7 loop alloys could be explained by radiation-induced alloy element segregation, involving the Zr-Cr-Fe alloy [109], and subtle evidence for the same in Zr-2.5 Nb.

The Zr-Cr-Fe alloy has shown excellent resistance to nodular attack in autoclaves at 500°C. Under irradiation, local pustules and gray areas corresponded to relatively rapid accelerated attack. The localized effects seemed to be more prevalent on specimens autoclaved (e.g., 400°C, steam) prior to reactor exposure. Electron microprobe scans indicated elevated chromium concentrations in areas of localized attack. Zr-2.5 Nb specimens developed numerous gray halos and small nodules [109]. Local sub-surface lateral cracks in the oxides offered an explanation for the gray halos, but the oxide thickness variations between black and gray oxides were relatively small.

3.4.3. Dissimilar metal effects

Two dissimilar metal couples were investigated in the ETR G-7 loop test series, involving Zircaloy-2/Inconel-600 explosively bonded couples; and Zircaloy-2 and Zr-2.5 Nb coupons with welded platinum inserts [109]. Localized oxidation was observed for both couples, and appeared to involve a radiation effect.

Other dissimilar metal effects on zirconium alloys in reactor service include enhanced oxidation on Zircaloy fuel rods and pressure tubes at locations near to fuel rod spacers that seem to correlate with proximity to stainless steel spacers [119]. Electrochemical effects were invoked as the leading explanation.

3.4.4. Other localized effects

Other localized effects on irradiated loop specimens have been observed, including corner effects, local oxygen barriers, and crevice effects [109]. Localized phenomena also have been observed on fuel cladding, including local oxide thickness variations in the vicinity of fuel spacers on LWR fuel, and sharp contrasts in areas of black and white oxide on fuel rods, seeming to correlate with pellet interfaces or pellet crack structures [117]. There are suggestions that some localized accelerated oxidation on PWR cladding correlates with crud deposits.

3.5. SIGNIFICANCE OF RADIATION EFFECTS TO ZIRCONIUM ALLOY BEHAVIOUR IN SERVICE

Several fuel failure mechanisms have emerged, resulting in substantial numbers of cladding failures, including internal hydriding, fuel densification, through-wall oxidation of PWR fuel, fretting, pellet-cladding interactions, crud-induced localized corrosion (CILC) and a recent problem with distortion of BWR fuel channels. Radiation effects have played a prominent role in several of the mechanisms, but to date radiation-enhanced oxidation has had a major role only in the case of the CILC phenomenon.

Current trends for several fuel types involve increasing fuel burnups and reactor residence times. Some PWRs are operating at temperatures above traditional norms. These trends have revived concerns that increased oxidation and hydriding will press zirconium alloys to operational limits. Oxide thicknesses above 100 μm and hydrogen contents above 500 ppm have been observed on LWR fuel cladding. A combination of accelerated oxidation and hydriding, combined with tube elongation and sagging, resulted in retubing of two Canadian pressurized heavy water reactors (PHWRs).

As indicated earlier, there is controversy regarding the relative roles of thermal and radiation effects on the oxidation and associated hydriding of fuel cladding. Evidence from studies on zirconium alloys at low heat transfer rates indicates that radiation enhancement of oxidation rates is real and sustained in both oxygenated and low-oxygen environments. The onset of major radiation effects appears to correspond to a threshold oxide thickness, particularly for the Zircalloys exposed in low-oxygen coolants.

An improved basis for extrapolation of zirconium alloy oxidation and hydriding behaviour is needed as a function of the following:

- Thermal versus radiation effects,
- Nodular oxidation in oxygenated coolants,
- Alloy composition,
- Lot-to-lot and vendor-to-vendor variations,
- Crud deposition.

The basis needs to involve both an improved basic understanding of the oxidation and hydriding mechanisms and how they are influenced by radiation; in addition the systematic development of improved empirical evaluations that allow future trends to be more accurately gauged and permit the separation of thermal and radiation effects.

4. FACTORS AFFECTING IRRADIATION CORROSION

4.1. IRRADIATION DAMAGE

4.1.1. Fast neutron damage in metals

Any mechanism that could lead to a displacement of an atom from its original stable site should be considered. The mechanisms that could be listed include elastic interaction with transfer of energy high enough for the target atom to escape from its site and, for ionic material, high ionisation processes. In reactors, fast particles include neutrons, primary recoil atoms and Compton electrons created by the gamma rays. Indeed, above 700 keV, Compton electrons will induce the displacement of atoms, but an order of magnitude analysis gives them a negligible contribution to the total irradiation damage.

In the case of metals, most of the structural damage induced during neutron irradiation in power plants is due to elastic scattering by fast neutrons. Usually the experiments reported on the effect of irradiation on microstructure are scaled with the total fluence received by the material. In order to compare material irradiated under various conditions (i.e. various neutron spectra) it is necessary to compute the damage in terms of displacements per atom (dpa).

The number of scattered zirconium atoms for a given fast flux is given by :

$$N = \sigma \phi$$

where σ the elastic scattering cross section,
 ϕ is the fast neutron flux.

The incoming neutron transfers part of its kinetic energy to the target Zr atom by elastic interaction. This will have, for a 1 MeV incident neutron, a maximum recoil energy of :

$$(E_T) \text{ Max} = 40 \text{ keV}$$

and a mean value of :

$$(E_T) \text{ mean} = 20 \text{ keV.}$$

These energies are high enough to displace the target atom that will itself induce a collision cascade of other atoms of the metal by elastic interaction in the so called nuclear stopping regime (i.e. a regime where the loss of energy of the ion in the matter is due to Coulombic interactions with the nuclei of the target). It is mainly controlled by screened Rutherford scattering [120]. Secondary ions will then interact with target atoms until the energy transferred is below the displacement energy. In the case of Zr the value of this energy threshold has been measured to be [121,122]:

$$E_d = 25 \text{ to } 27 \text{ eV.}$$

The number of secondary ions induced by the primary atom can be deduced from hard sphere collision cascade analysis [123]

$$\langle n \rangle = kE_T/2E_d$$

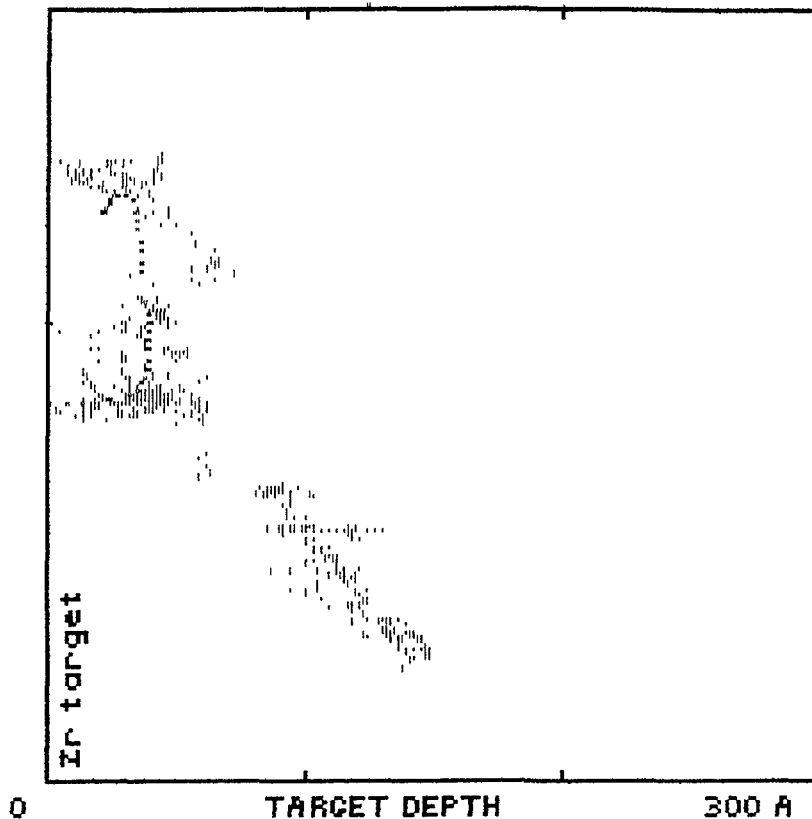


FIG. 4.1.1. Displacement cascade induced by a 20 keV Zr recoil in a Zr matrix. Each point is the final position of an interstitial. Computation was done with the TRIM program [125].

The value of k , an efficiency parameter, is usually taken as being close to:

$$k = 0.8,$$

leading to a typical value of $\langle n \rangle = 300$ displaced atoms after the athermal annealing, in the collision cascade [124]. Fig.4.1.1 gives a typical example of such a displacement cascade for a 20 keV Zr recoil atom in zirconium [125]. The secondary atoms are the displaced or interstitial atoms. Their number, normalized to the number of atoms per volume, leads to the displacements per atom. As the neutron scattering cross section is neutron energy dependent, the relationship between fast flux and damage rate is a function of the neutron flux spectrum. Few complete computations are available on the correspondence between fluence and damage for different types of reactors [126,127]. Typical values of correspondence between fluence ($E > 1$ MeV) and dpa are:

$$d = k \Phi$$

d = damage (dpa)

Φ = fast neutron fluence ($n.m^{-2}$)

$k = 2 \cdot 10^{-25}$ for most power plants.

4.1.2. Displacement damage in other structures

This computation of neutron damage for Zr atoms in a Zr matrix can be extended to other atoms or other structures, in particular for the intermetallic precipitates and the ZrO_2 oxide layer. This is basically possible, if scattering cross sections and displacement energies are available. As is the case for the matrix [128], displacement energies in

intermetallic compounds have rarely been measured [129,130], and results for the oxide are much scarcer. However, even in the case of intermetallic compounds, no significant changes of the displacement energies have been reported when compared with the matrix [130]. Therefore, the extent of the damage can be considered to be the same for any Zr atom, regardless of its original location in the metallic alloy.

Damage in the oxide

In the oxide, the values of the displacement energies have to be measured for both atoms: O and Zr. In the case of another oxide (MgO), the values obtained are more than twice as large in the oxide as in the metallic phase [131]. Therefore, the relationship between neutron flux and damage will be quite different from that in the metal. In the case of UO_2 , displacement energies have been measured using high voltage electron microscopy. A large difference was found for the two types of atoms: 40 eV for U atoms and 20 eV for O atoms. This leads to a very large difference in number of displaced atoms if U or O atoms are taken into account [132].

In the case of an oxide, as reviewed recently [133], the mechanism of radiation damage generation is more complex than in metals. In such materials atomic displacements can be produced either by nuclear interactions, as in metals, or as a consequence of the electronic interactions, generated by charged secondary ions.

In non-metals radiolysis can be more efficient per unit of energy deposited than are knock-on displacements. The electronic losses along fast charged-particle trajectories far outweigh the energy transferred by mechanical collisions. Therefore, most of the incident particle energy is eventually available to generate radiolytic displacements. Moreover, during the electronic stopping process of the secondary knock-on ions, some damage may occur in this ionically bonded material. Indeed, although in this regime the electronic perturbation is relaxed in a very short time in the metal, due to the nature of the free electrons, this will not be the case for ceramics, since the electrons are localized. Recent experiments on superconducting ceramics irradiated with high energy ions showed structural damage during the electronic stopping regime, while nothing was observed in metals [134]. Similarly, the very high sputtering yields of oxides irradiated with energetic ions in the electronic stopping regime can only be explained by the assumption of severe damage induced by this process [135].

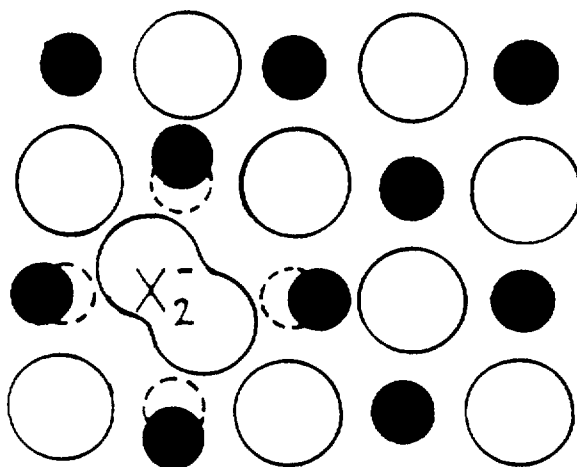


FIG. 4.1.2. Charged defect in an ionic crystal (H center).

During the recombination step after displacement, defect mobility may be appreciably enhanced under irradiation as a consequence not only of the mechanisms operating in the metal (irradiation enhanced diffusion) but also due to the alteration of the electronic states of the defects and to the different mobilities of the defects created, like the F or H centers. Fig. 4.1.2 gives an example of those charged defects in ionic crystals. Long range electrostatic or short range covalent interactions of the defects will influence their aggregation and recombination properties. In the case of ionic materials, direct ionisation due to photons has to be considered. For an irradiation by gamma-rays at an intensity of 10^5 G.h^{-1} , the displacement production rate is of the order of $2 \times 10^{-5} \text{ dpa.h}^{-1}$ [136]. This value, although small compared to the damage induced by neutron or primary recoils, has to be considered when analysing the corrosion behaviour after irradiation during intermediate storage.

4.1.3. Effect of irradiation on microstructures

(a) Zirconia

Few observations are reported on the effect of irradiation upon the structure of bulk zirconia. Y_2O_3 -stabilized zirconia has been irradiated at different temperatures (up to 1025 K) to a fluence of $4.4 \times 10^{25} \text{ n.m}^{-2}$ and a small swelling was observed (about 1.5%) that could be attributed to dislocation loops observed by TEM [137]. An irradiation induced monoclinic to cubic phase transformation of zirconia was obtained at 370 K and a fluence of 10^{24} n.m^{-2} . The irradiation led to a phase transformation from the low temperature stable monoclinic to the high temperature cubic phase. A proposed explanation is based upon the internal stresses developed around the point defects that could stabilize the cubic phase. This irradiation induced cubic phase transformation remained stable up to 1070 K [138]. Subsequent work attributed this phase transformation to fission spikes associated with traces of fissile material contaminating the samples [139].

For the effect of irradiation on the oxide layer, the observations are only performed at a very early stage and up to now, available information on zirconia microstructure only refers to unirradiated material. For instance, the structure of the zirconia layer after autoclave testing was found to be dependent on the structure of the base alloy and on the location examined in the oxide layer. In most of the cases, monoclinic zirconia was observed, but the tetragonal structure was found in the inner oxide layer grown on a beta quenched Zircaloy-4 [140]. For this type of TEM work, care has to be taken to consider a possible change in microstructure due to stress relaxation during thin foil preparation.

Anodic dissolution of the oxide and reprecipitation on the free surface has been observed on specially designed experiments (high UV photon flux), leading to a porous oxide with a high corrosion rate at low temperature [141]. Those conditions, when transposed to power reactors, could give an explanation for local dissolution of the zirconia enhanced by the high electrical field due to an irradiation photocurrent.

In the case of corrosion grown oxide layers, experiments using replicas or thin foils on irradiated or unirradiated Zr alloys, showed that the layer is porous with cylindrical pores of radii in the range of 3-5 nm [36] and that the grain size of the zirconia is very small, of the order of 20-40 nm, with small holes at triple grain boundaries [91].

(b) Zr matrix microstructure

Unless noble gases are intentionally added to zirconium alloys, no bubble formation under irradiation by neutrons is reported [142,143]. This difference in behavior compared with the stainless steels in fast reactors is attributed to a reduced efficiency of edge dislocations as traps for interstitial atoms. Other reasons are given, such as anisotropic diffusion in the hcp lattice or internal residual stresses, following thermomechanical processing, due to the anisotropy in the expansion coefficient and Young's modulus.

As recently reviewed by Griffiths [143], various investigations have been performed on the nature of irradiation defects induced in Zr alloys [144,145]. It is usually reported that after an irradiation to a fluence of 2 to 3 $10^{23} \text{ n}_f \text{ m}^{-2}$, interstitial and vacancy loops are observed. They are of $a/3 \langle 11\bar{2}0 \rangle$ type in planes close to $(10\bar{1}0)$. The ratio between interstitial and vacancy loops is irradiation temperature dependent. Higher irradiation temperatures increase the number of interstitial loops [146,147]. At very high temperature (above the temperature used in power reactors) recovery occurs during irradiation.

For very high fluences in the range of 3 to 8 $\times 10^{25} \text{ n}_f \text{ m}^{-2}$, $\langle c \rangle$ component dislocation loops are observed [148,149]. A strong correlation between the formation of these loops and a significant increase of growth rate was noticed. The growth we refer to is the fuel rod or pressure tube elongation under irradiation due to the formation of interstitial loops on prismatic planes. The strong texture of the cladding tubes or of the pressure tubes leads then to an increase in axial length. Detailed mechanisms are still under discussion [150,151].

The growth may have an effect upon corrosion kinetics: The consequence of growth has to be considered on two different scales:

The corroded cladding may be considered as a composite material for which any dimensional change in the metallic part (cladding growth) will induce tensile stresses in the outer oxide layer.

On a microscopic scale, as the growth of Zr alloys is the result of individual grain geometry changes (shrinkage in $\langle c \rangle$ direction), grain to grain strain incompatibilities will induce high tensile stresses in some specifically oriented grains. According to the various models of growth kinetics, stresses have been computed up to values of 23 MPa [152].

The effect of tensile stresses upon corrosion kinetics has been studied in a limited number of cases [110] and no effect was reported. Changes in irradiation conditions may lead to a renewed interest in this area, since enhanced corrosion kinetics may be expected from those effects.

(c) Effect of irradiation on the second phase precipitates

- Type of precipitates usually present in Zr cladding

Because of the very fine scale of Zr-alloy microstructures, the second phase particles have been analyzed in detail only recently [153-156]. A general review of second phase particles was performed by Charquet [157]. Table 4.1.1, taken from this review, gives a list of these secondary phases. For Zircaloy 4, after a standard heat treatment (stress relieved or recrystallised) the most common precipitate is the Laves phase ZrCr_2 in which some Fe is substituted for Cr. The Fe/Cr ratio is

TABLE 4.1.1. PRECIPITATES FOUND IN INDUSTRIAL ZIRCONIUM ALLOYS (References refer to the original table in Ref. [157])

(A) PRECIPITATES IN ZIRCALOY-2 BASED ON ALLOYING ELEMENTS

Sn 1.2-1.7%, Fe 0.07-0.20%, Cr 0.05-0.15%, Ni 0.03-0.08%

Methods	Heat Treatments	Precipitates		References
		Lattice	Composition	
EM	Alpha Anneal		Fe 5 - 9 % Cr 0 - 2 % Ni 4 - 9 % Sn 1 - 5 % Zr	(1) OSTBERG
TEM (TF) EDXA	600° C - 4 h	bct a = 0.65 nm c = 0.55 nm	Zr, Ni, Fe	(2) VITIKAINEN
TEM (T.F.)	800° C - 2 h	hex ZrCr ₂ lattice: a = 0.501 nm c = 0.822 nm ----- fcc ZrCr ₂ lattice: a = 0.719 nm		(3) KRASEVEC
TEM STEM (T.F. and R.)	700° C - 2 h	hex ZrCr ₂ lattice: a = 0.51 nm c = 0.83 nm ----- tetragonal Zr ₂ Ni a = 0.659 nm c = 0.55 nm	Zr Cr 1,1 Fe 0,9 Zr ₂ Ni _{0.4} Fe _{0.6}	(4) CHEMELLE
TEM (R) EDXA	Beta quench + 750° C - 7 h	hex	Zr Cr _{1,3} Fe 0.7	(5) VERSACI
SEM-TEM EDXA	580° C - 2.5 h	hex ZrCr ₂ lattice: a = 0.508 nm c = 0.828 nm ----- fcc Zr Cr ₂ lattice: a = 0.721 nm ----- orthorhombic a = 0.745 b = 0.582 c = 0.516 ----- hex a = 0.846 nm c = 0.578 nm ----- Sn Metal	Zr Cr ₁ Fe ₁ (Sn Ni) compounds Zr Cr ₁ Fe ₁ Zr Sn Zr ₅ Sn ₃	(6) KUWAE

(B) PRECIPITATES IN ZIRCALOY-4 BASED ON ALLOYING ELEMENTS

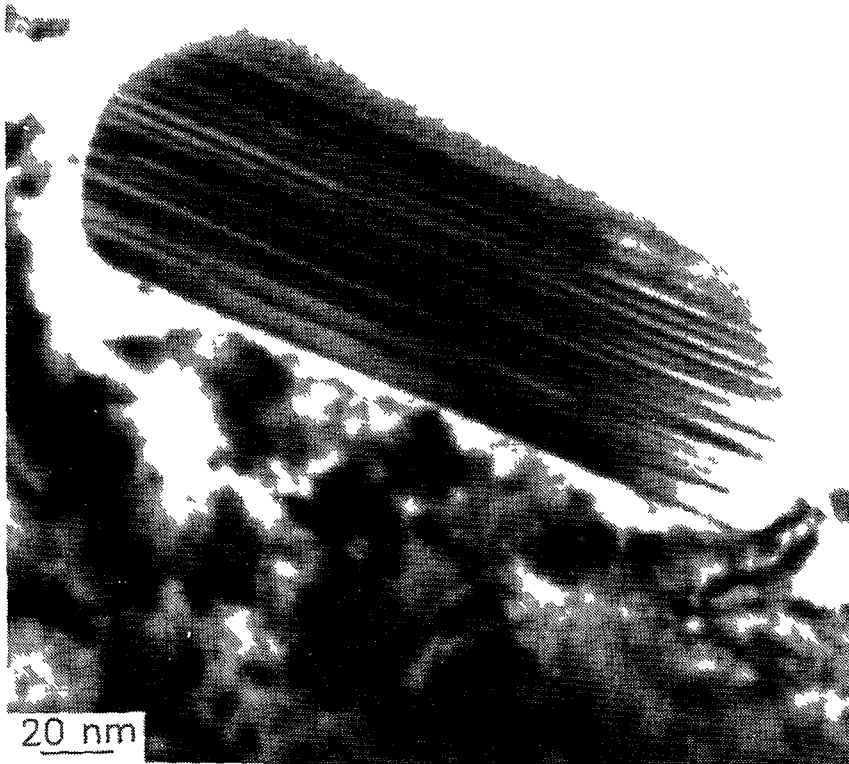
Sn 1.2-1.7%, Fe 0.18-0.24%, Cr 0.07-0.13%

Methods	Heat Treatments	Precipitates		References
		Lattice	Composition	
TEM (TF) EDXA	800° C - 3 h	Hex ZrCr ₂ lattice: a = 0.5079 nm c = 0.8279 nm	Zr Cr 0.6 Fe 1.4	(7) VANDERSANDE
TEM (TF)	Beta quench + 700° C - 6 h	Polytype Structure: hex ZrCr ₂ structure fcc ZrCr ₂ structure		(8) VERSACI
EM - SEM	800° C 23 days 850° C 50 days		ZrCr _{0.7} Fe _{1.3} ZrCr 0.8 Fe 1.2	(9) MEROHI
SEM-EDXA (R and TF)	Many structures		(FeZr)-(FeCrSnZr) (FeSnZr)-FeCrZr	(10) CORTIE
TEM (TF)	Slow cooling from beta	Zr (Cr Fe) ₂ hex Zr (Cr Fe) ₂ fcc		(11) MIQUET
TEM (TF)	Quench from 850° + α anneal		Zr ₃ Fe	(12) GRANGE
TEM (5) EDXA	700° C - 6 h	Hex	Zr Cr 0.7 Fe 1.3	(5) VERSACI
SEM-EDXA TEM (TF and R)	1600° C 2 h α + β quench	Hex Tetragonal fcc Zr Cr ₂ phase tetragonal	Zr Cr 0.6 Fe 1.4 Sn metal	(6) KUWAE

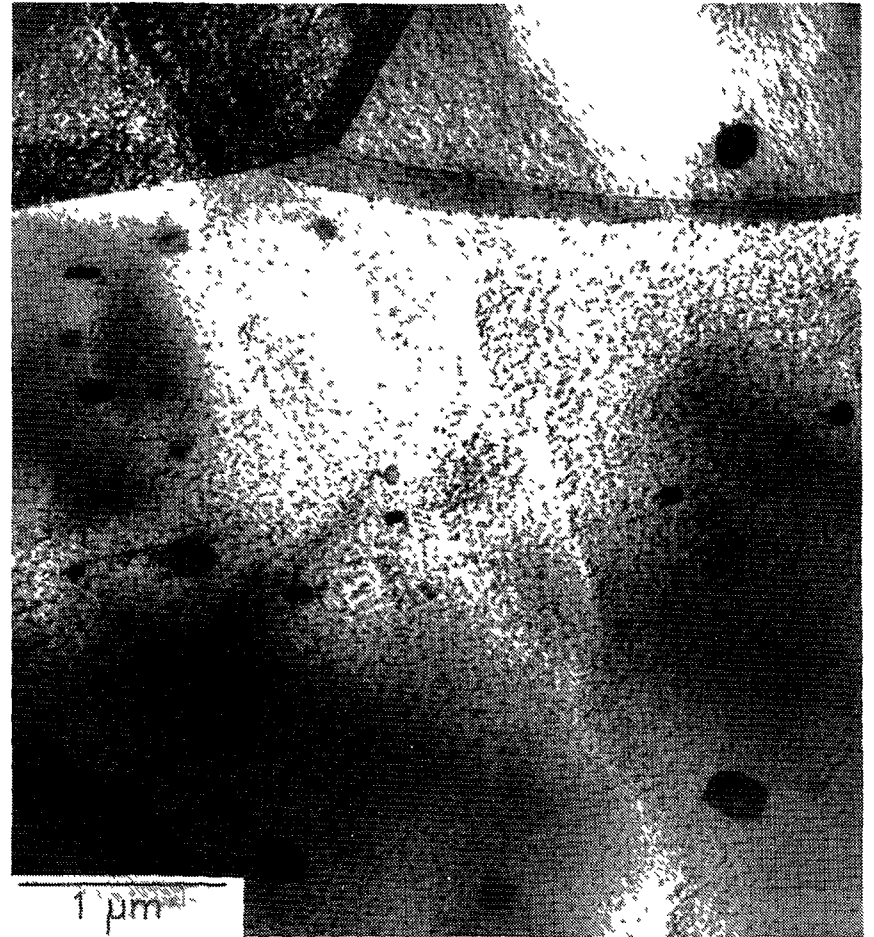
(C) PRECIPITATES IN ZIRCALOYS BASED ON IMPURITIES ELEMENTS

Usual specifications are C < 270 ppm, Si < 120 ppm, P < 20 ppm

Phases	ppm content	Lattice	References
ZrC	C > 140 - 160	fcc a = 0.47 nm	(13)(14)(15)
Zr ₃ Si	Si = 85	Tetragonal a=1.1nm c=0.22 nm	(16)
Zr ₂ Si ₂	Si 26 - 263	a = 0.543 nm	(15)
Zr ₃ P	P < 50 to 153	fcc a = 0.525 - 0.529	(15) (17)
Zr PO.5-1	P = 160	orthorhombic a = 1.67 b = 2.76 c = 0.36	(18)
Zr ₃ P	P = 160	Tetragonal a = 1.08 c = 0.53	(18)



(a)



(b)

FIG. 4.1.3. $Zr(Fe,Cr)_2$ precipitate in recrystallized Zircaloy-4.

dependent upon the temperature of the final heat treatment and is usually found to be in the range of 1 to 2. These precipitates usually have a hexagonal crystal structure but an fcc structure has been reported after fast cooling rates. A typical appearance of such a precipitate in recrystallized Zircaloy-4 is shown in Fig. 4.1.3 . After a beta quench heat treatment the orthorhombic Zr_3Fe can be observed at the inter-plate boundaries of the original beta structure.

In Zircaloy 2, the main types of precipitate are variations around the tetragonal Zr_2Ni and hexagonal $ZrCr_2$ phases. In those alloys the Fe/Cr ratio is usually below 1. All these precipitates for Zircaloy-2 and -4 have been listed in detail in a recent review in connection with the corrosion behaviour [158]. Other impurity induced precipitates include ZrC , Zr_3Si , $ZrSi_2$, ZrP and Zr_3P [157].

For zirconium-niobium alloys, the solubility limit of Nb in Zr is about 0.6 wt% at 500°C but high temperatures lead to the complete dissolution of Nb in the stabilized beta phase and, depending on the thermal treatment, either "single phase" or "two phase" alloys can be obtained for a Nb content > 1.5 wt%. Thermal treatments in the $\alpha+\beta$ region will lead to a more complex structure, since the Zr rich β phase will decompose into $\alpha + \omega$ during the cooling process.

- Effect of irradiation on precipitates

Even if the role played by the precipitates in the behaviour of the fuel is recognized (e.g. in the case of stress corrosion cracking [159] or corrosion behaviour [160]), it is clear that the effect of irradiation on the precipitates themselves has not been analyzed in detail until recently. The first reports [161,162] show that after irradiation an amorphous transformation can be observed in the second phase precipitates of Zircaloy-2 and -4. Depending on the irradiation temperature, the relative stability of the amorphous transformation can be expressed as follows: at low temperatures (<80°C) both Zr_2Ni and $ZrCr_2$ types of precipitates are amorphous at low fluences (below $5 \times 10^{24} n.m^{-2}$). At intermediate temperatures (250°C) a progressive amorphous transformation is observed in $ZrCr_2$ precipitates (the transformation starts from the matrix - precipitate interface), while Zr_2Ni precipitates remain stable in their crystalline form. Fig. 4.1.4 shows the appearance of this amorphous transformation in a recrystallized Zircaloy-4 cladding tube irradiated up to 8 dpa in a power plant. At high temperatures ($T > 400^\circ C$) no amorphous transformation has been reported in any precipitates under the conditions of neutron irradiation used. Reductions of the Fe and Cr contents in the irradiated amorphous particles are reported.

Following those first observations, detailed analysis of the evolution of precipitate microstructures under irradiation was performed following two main directions:

- Detailed analysis of the amorphous transformation with chemical analysis using a STEM equipped with EDAX [163,164].

- Experimental work under simulated irradiation.

(i) In the first case, the new observations lead to the conclusion that the amorphous transformation and precipitate re-resolution are, in many instances, not directly linked: the amorphous transformation is induced by the irradiation only, while the Fe, Cr and Ni re-resolution in the matrix are due to irradiation enhanced diffusion and thermal activation. In the case

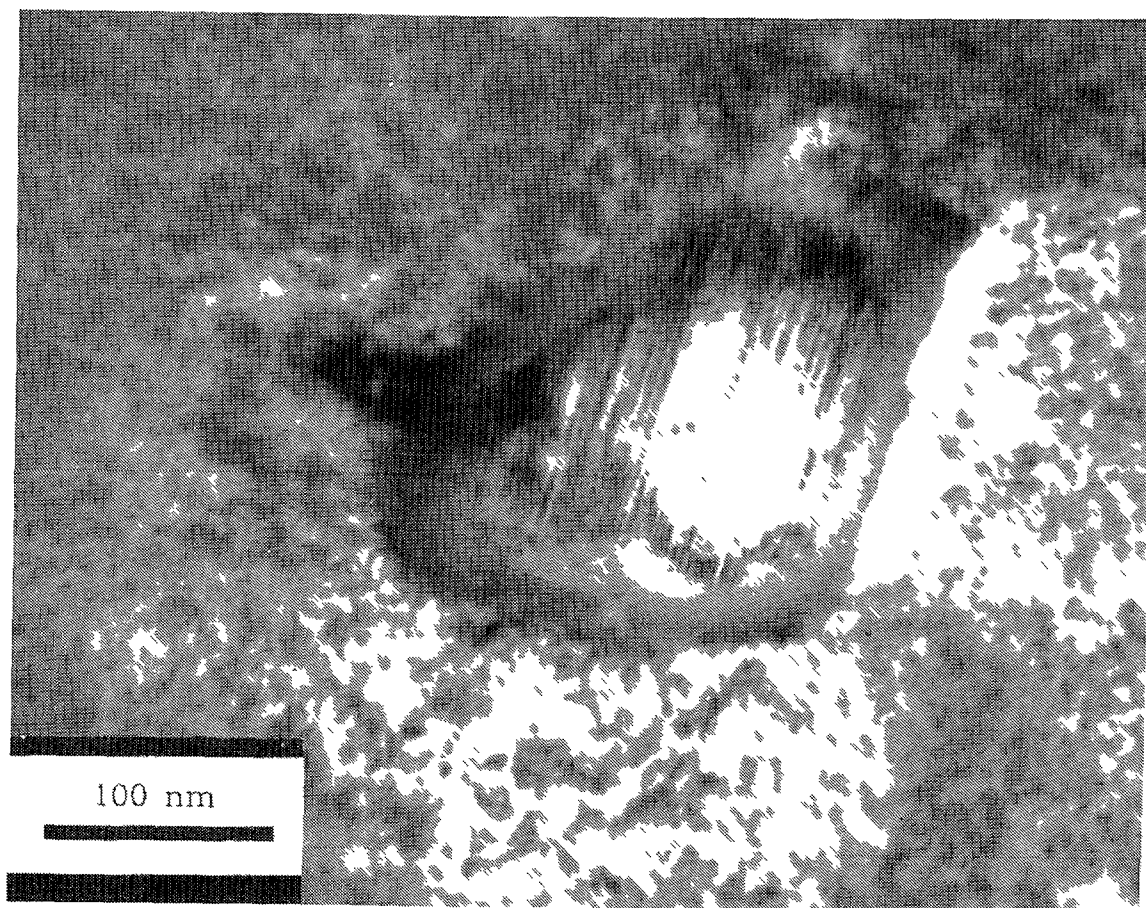


FIG. 4.1.4. Partially amorphous precipitate after irradiation in a power plant up to 8 dpa.

of Fe, the fast diffusion behavior of this species should be noted. It has been observed that the release of Fe from the amorphous precipitates occurs early in the amorphous transformation and is usually linked with the occurrence of $\langle c \rangle$ type dislocation loops. Both phenomena are connected to a sharp increase in growth rate. A link between these observations has been proposed [163] : the loops should be vacancy type loops, with a Burgers' vector $1/6\langle 20\bar{2}3 \rangle$, located in the basal plane. The nucleation and growth of these loops is connected to high concentrations of interstitial impurities such as C, O, Fe or Cr. Therefore, the re-resolution of the alloying elements of the precipitates under irradiation increases the development of $\langle c \rangle$ type dislocation loops and the concomitant accelerated growth.

(ii) For a better understanding of the mechanisms involved, simulated irradiations have been performed using high voltage electron microscopes or heavy ions accelerators [123,165]. It has been shown that amorphous precipitates can be obtained (at much higher damage dose rates) in Zircaloy-2 and -4 without a composition change. These observations have led to the conclusion that the amorphous transformation is not induced by the composition change due to a possible irradiation induced diffusion of alloying elements, but to the high density of point defects induced by neutron damage. This stored energy gives the driving force for a phase transformation from crystalline to amorphous. The chemical potentials of the alloying elements in the amorphous precipitates are not then equal to those in the matrix and re-resolution is necessary to obtain chemical equilibrium [166]. The final situation may be a complete re-resolution of the alloying elements of the initial precipitates in the matrix [164].

In the case of zirconium-niobium alloys, recent work [167] shows that both the α and the β phases appear to be unstable. Some precipitation is observed in the α phase and also a decomposition of the β filaments is reported. However, the Zr-Nb alloys seem to have a microstructure more stable under irradiation than the Zircalloys, as the irradiation induced transformation is observed at a much higher fluence.

In the zirconia layer the effect of irradiation would be very difficult to analyze: recent observations on the microstructure of the oxide layer after corrosion testing without irradiation lead to the conclusion that, during corrosion, the chromium tends to leave the precipitates and also that the precipitates may transform to an amorphous structure once the oxide layer has grown thick enough [140].

Impact upon corrosion kinetics

The crystalline to amorphous transformation of these precipitates and any changes in microstructure under irradiation could have an important impact upon the mechanisms of zirconium alloy corrosion by the coolant. The exact mechanism of precipitate incorporation by the growing oxidation layer under irradiation has not been studied in detail and the exact location and chemical state of Fe, Cr, Ni or Nb in the ZrO_2 is subject to ongoing investigations. A change in the detail of these mechanisms may be expected during the change from crystalline to amorphous or other irradiation induced changes in microstructure.

During the amorphous transformation a strain field develops around the precipitates due to their change in density. The role played by the induced stress field remains to be analyzed, but due to the mismatch in the lattices between Zr and ZrO_2 and the related stress state of the Zr- ZrO_2 interface, a significant effect is expected. If a change in the size and composition of the precipitates alters the corrosion kinetics, as is observed for unirradiated materials, it is expected that the changes induced by irradiation on the microstructure may have a similar effect. In the same way, changes in the matrix composition due to re-solution or irradiation induced precipitation may also be of importance. Attempts to obtain a basic understanding of these effects are strongly recommended.

4.2. LOCAL RADIATION CHEMISTRY

4.2.1. Radiolysis in the bulk water

When water molecules are irradiated with ionizing radiation, the ionizing species interacts with the molecules intermittently along its path way and produces ionized and excited water molecules. The electron ejected in the ionization process loses its energy by further ionization and excitation processes of the water molecules, being thermalized and yielding a hydrated electron if it escapes the geminate recombination process. On the other hand, excited water molecules may dissociate to yield radicals, though there has been no explicit evidence to show that the excited water molecules play an important role. Overall, this leads to the formation of small spherical domains called "spurs" along the path way of ionizing species where radicals and ionic species are distributed in locally high concentrations. This situation is illustrated in Fig.4.2.1. The size of the spurs is inferred to be mostly 1 - 2 nm. The active species diffuse and partly react with each other to give some molecular and radical products as shown below.

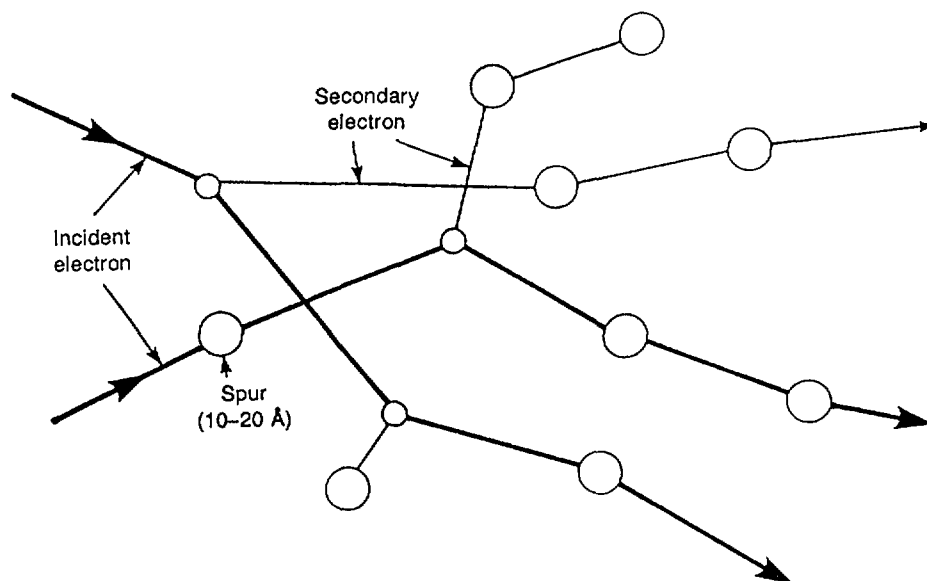
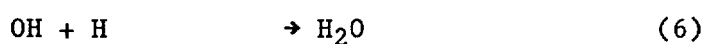
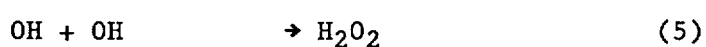
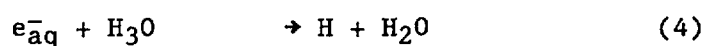
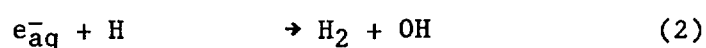
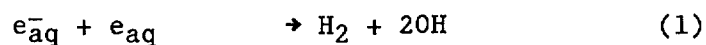
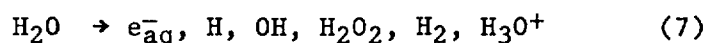


FIG. 4.2.1. Spur formation by high energy electrons.



Thus, the initial process of water radiolysis is expressed for γ -rays or high energy electrons by Eq. (7)



as the result of the intra-spur reactions. The G value, which is usually used in the field of radiation chemistry to give the yield of a radiolysis product, is defined as the number of species produced or consumed per 100 eV of radiation energy absorbed by the medium. In the case of water radiolysis the yields of the primary species shown in Eq.(7) are given as primary G values, which means the G values at the time when the intra-spur reactions are completed. The primary G values for water radiolysis at ambient temperatures by γ -rays or high energy electrons have been measured by many workers and are well established on the basis of the large data base [168].

On the other hand, when water molecules are irradiated with neutrons as in nuclear reactors, neutrons lose their energy mainly by their elastic scattering by hydrogen atoms to yield recoiled protons. The recoiled protons lose their energy again by ionization and excitation of the water molecules. However, the ranges of the recoiled protons are very short in water compared with either high energy electrons or γ -rays because of their larger cross-section for interaction. For instance, a 2 MeV proton has a range of only 70 μ m in water when compared with the 1 cm range of a 2 MeV electron.

High energy heavy particles are usually called "high LET (linear energy transfer) radiation", since they have larger deposition rates of energy along their tracks. It is known that the G values of the primary products are greatly affected by the LET of the radiation, and this phenomenon is called the "LET effect".

In the case of high LET particle irradiation the spurs produced are distributed very closely to each other, leading to the formation of cylindrical spurs or tracks. Consequently, the contribution of the intra-spur reactions is larger for high LET radiation. Therefore, the yields of the radical species such as e_{aq}^- , H and OH are relatively higher for low LET radiation, while the yields of the molecular products increase for high LET radiation. The primary G value data available for fast neutrons are not so abundant at present, and, hence, the reliability of the data is lower than that for γ -rays.

TABLE 4.2.1. G VALUES OF PRIMARY PRODUCTS BY $\beta\gamma$ RADIATION AND FAST NEUTRONS AT AMBIENT TEMPERATURE

Radiation Type	G values						
	e_{aq}^-	H_3O^+	H_2O_2	OH	HO_2	H	H_2
$\beta \gamma$	2.7	2.7	0.72	2.7	0	0.55	0.45
fast neutrons	0.93	0.93	0.99	1.09	0.04	0.50	0.88

In Table 4.2.1 are shown the G values of the primary water radiolysis products by γ -rays at ambient temperatures in comparison with those for radiolysis by fast neutrons from nuclear fissions in reactors. It is to be noted that the G values for fast neutrons depend, in principle, on the energy spectrum of the fast neutrons.

A material balance consideration gives the following relation for low LET radiation,

$$G(-H_2O) = 2G(H_2) + G(H) + G(e_{aq}^-) = 2G(H_2O_2) + G(OH) \quad (8)$$

which gives $G(-H_2O) = 4.2$ at ambient temperatures on the basis of the values in Table 4.2.1.

There has been some controversy over the temperature dependence of these primary G values for water radiolysis. W. G. Burns et al [169,170] reported a marked difference between the G values at ambient temperatures and at high temperatures of 300 to 400°C, indicating decreased yields for e_{aq}^- and H_2O_2 , $G(e_{aq}^-) = 0.4$ and $G(H_2O_2) = 0$, and increased yields for OH and H_2 , $G(OH) = 4.7$ and $G_H = 2.0$. Recently, extensive work has been carried out to measure the G values of the primary products in the high temperature radiolysis of water, and the results obtained are summarized in Table 4.2.2. The values reported by Burns, especially the low yield for e_{aq}^- , are inconsistent with the data reported by other workers [171-177]. It may be said at the moment that there is no established set of G values available for the primary species at high temperature. The experimental results obtained so far seem to indicate a significant increase in $G(e_{aq}^-)$ and G_{OH} with increasing temperature, but some uncertainty still remains with G_H and $G(H_2O_2)$ [178].

TABLE 4.2.2. SUMMARY OF PRIMARY G VALUES MEASURED AT 200°C

Systems	pH	Observed values at 200°C	References
(1) Pulse radiolysis			
pure water	neutral	$G_{e_{aq}^-} \approx 3.5$	[173]
Cd^{2+}	nearly neutral	$G_{e_{aq}^-} \approx 3.5$	[173]
benzotrile (EtOH)	neutral	$G_{e_{aq}^-} \approx 3.4$	[174]
methylviologen (t-BuOH)	nearly neutral	$G_{e_{aq}^-} \approx 3.4$	[177]
H_2	12	$G_{e_{aq}^-} \approx 3.5$	[172]
HCO_2^+ (O_2 -saturated)	4.4-9.2	$G_{e_{aq}^-} \approx G_{OH} \approx 3.4$	[176]
HCO_2^+ (O_2 -saturated)	2	$G_{e_{aq}^-} \approx G_{OH} \approx 2.7$	[176]
(2) Scavengers			
Fricke	strongly acidic	$G_{e_{aq}^-} + G_H \approx 3.9$	[175]
Fricke	strongly acidic	$G_H + G_{e_{aq}^-} = 4.95$	[204]
KBr	neutral	$G_H = 0.44$	[204]
KNO_2	nearly neutral	$G_H = 0.46$	[178]

W.G. Burns et al. also reported [168] that the LET effect in water radiolysis disappears at high temperature and the primary yields by fast neutrons are the same as those by γ -rays at high temperature. A high temperature experiment of fast neutron irradiation of acidic solutions [179], however, seems to show that a LET effect still exists at 200 to 250°C. More data are required in relation to the high temperature G values of the primary products, especially for neutron irradiation.

The primary products shown in Eq (7) react with each other in the bulk of water when the water contains no solutes which are reactive with those products. There are many possible reactions involved as shown in Table 4.2.3. The rate constants of all these reactions at ambient temperatures are well established, based on the abundant data from pulsed radiolysis experiments. The situation, however, is very similar to the case of the high temperature G values, and there have been very limited numbers of data available for the rate constants at high temperatures. Hence, an empirical evaluation is usually made to estimate the high temperature rate constants of the reactions in the absence of experimental data [180,181]. These experimental and evaluated values are compared in Table 4.2.3.

As inferred from Table 4.2.3 the radiolysis process in the bulk of pure water is rather complicated, with many competing reactions. Therefore, computer simulations [181-184] based on the G values of the primary products and the rate constants have been used to analyze the process by solving a set of differential rate equations involving the chemical species shown in Table 4.2.3. The result of a typical calculation is shown for the radiolysis of pure water by γ -rays at high temperature in Fig. 4.2.2. As seen from the figure, continuous irradiation brings the system to a steady state where all the species reach constant concentrations which are determined as a result of the kinetic equilibria, depending on the dose rate.

In Fig. 4.2.3 a calculated result is given showing the effect of a hydrogen addition to a radiolysis system. It is seen that the addition of hydrogen reduces markedly the steady state levels of oxidizing species such

TABLE 4.2.3. RATE CONSTANTS OF REACTIONS INVOLVED IN WATER RADIOLYSIS

Reaction	Rate constant. at 25°C dm ³ mol ⁻¹ s ⁻¹	Rate Constant at 280°C. (l/mol.s)
$e^- + H_2O = H + OH^-$	1.6E + 1	1.65E + 2
$e^- + H^+ = H$	2.3E + 10	2.48E + 11
$e^- + OH = OH^-$	3.0E + 10	3.10E + 11
$e^- + H_2O_2 = OH + OH^-$	1.3E + 10	1.34E + 11
$H + H = H_2$	1.0E + 10	1.03E + 11
$e^- + HO_2 = HO_2^-$	2.0E + 10	2.06E + 11
$e^- + O_2 = O_2^-$	1.9E + 10	1.96E + 11
$2H_2O + e^- + e^- = H_2 + OH^- + OH^-$	5.0E + 9	3.00E + 7
$OH + OH = H_2O_2$	4.5E + 9	4.65E + 10
$OH^- + H = e^- + H_2O$	2.0E + 7	6.63E + 8
$H_2O + e^- + H = H_2 + OH^-$	2.5E + 10	6.22E + 9
$H_2O + e^- + HO_2^- = OH + OH^- + OH^-$	3.5E + 9	8.70E + 8
$H + OH = H_2O$	2.0E + 10	2.06E + 11
$OH + H_2 = H + H_2O$	4.0E + 7	4.00E + 8
$H + H_2O = OH + H_2$	1.04E - 4	8.14E + 2
$H + O_2 = HO_2$	1.9E + 10	1.96E + 11
$H + HO_2 = H_2O_2$	2.0E + 10	2.06E + 11
$H + O_2^- = HO_2^-$	2.0E + 10	2.06E + 11
$H_2O + e^- + O_2^- = HO_2^- + OH^-$	1.3E + 10	1.04E + 10
$H + H_2O_2 = OH + H_2O$	9.0E + 7	1.13E + 9
$OH + H_2O_2 = HO_2 + H_2O$	3.0E + 7	1.00E + 8
$OH + HO_2 = O_2 + H_2O$	1.2E + 10	1.24E + 11
$OH^- + H_2O_2 = HO_2^- + H_2O$	1.8E + 8	5.97E + 9
$HO_2^- + H_2O = OH^- + H_2O_2$	5.7E + 5	1.89E + 7
$H^+ + O_2^- = HO_2$	5.0E + 10	5.16E + 11
$HO_2 = H^+ + O_2^-$	8.0E + 5 [*]	3.40E + 7
$HO_2 + O_2^- = O_2 + HO_2^-$	1.5E + 7	4.97E + 8
$2H_2O + O_2^- + O_2^- = H_2O_2 + O_2 + OH^- + OH^-$	1.7E + 7	3.27E + 5
$HO_2 + HO_2 = H_2O_2 + O_2$	2.7E + 6	8.95E + 7
$H^+ + OH^- = H_2O$	1.4E + 11	1.49E + 12
$H_2O = H^+ + OH^-$	2.6E - 5 [*]	1.33E - 1
$OH + O_2^- = O_2 + OH^-$	1.2E + 10	1.24E + 11
$H_2O_2 = OH + OH$	2.3E - 12 [*]	1.2E - 1 [*]

* First order reaction rate s⁻¹.

as O₂, OH, HO₂, and O₂⁻. A higher concentration of hydrogen is necessary to reduce more significantly the level of hydrogen peroxide. The reduction of O₂ and the other oxidizing radicals is what is expected for hydrogen additions to the primary system in PWR, and also for hydrogen water chemistry in BWR. The situation, however, is rather complicated for radiolysis in nuclear reactors. One factor contributing to the complexity is the boiling of water in the reactor core, which is more vigorous in BWRs. The boiling of water in the core region forces the transfer of hydrogen and oxygen into the steam phase, and consequently, makes the

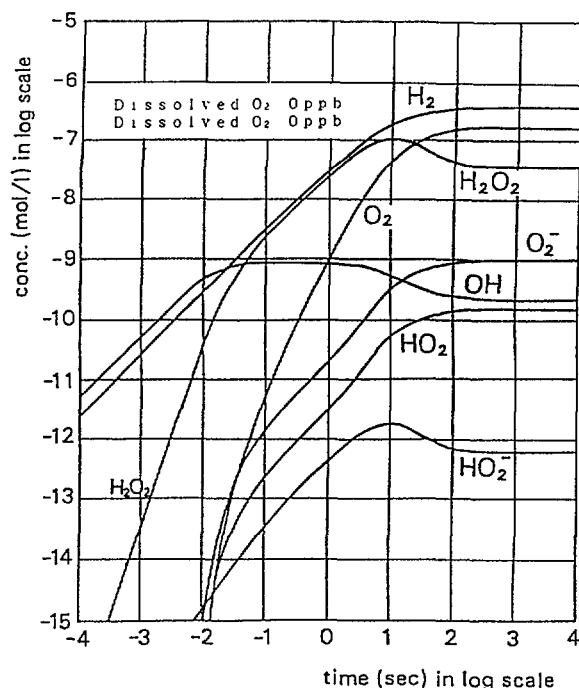


FIG. 4.2.2. A typical result of computer simulation for radiolysis of pure water at 250°C. The primary *G* values used here are Burns' data and the dose rate is 4.5×10^4 R/h.

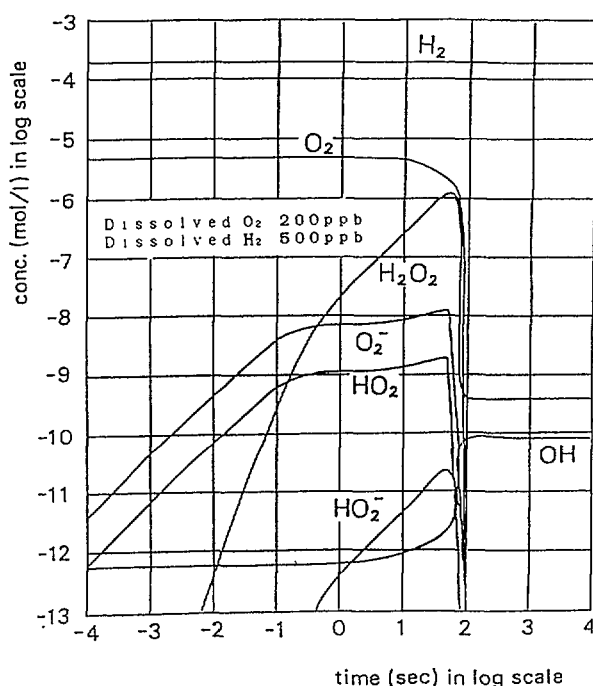


FIG. 4.2.3. A computer simulation result showing the effect of hydrogen addition for water radiolysis at 250°C. The parameters used are the same as in Fig. 4.2.2.

hydrogen additions less effective for reducing the radiolysis in the aqueous phase.

Another important factor is the effect of any impurities which are very reactive with the primary products of water radiolysis and affect the overall scheme of the reactions. In the case of the reactor coolants of LWRs that don't contain reactive additives, impurities at a very low level have the possibility of causing a significant effect. One such impurity in

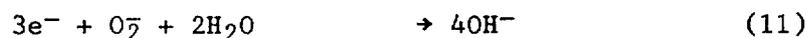
relevant systems is considered to be copper ions released to the coolant by the corrosion process. This may be involved in the reaction scheme as a $\text{Cu}^{2+} - \text{Cu}^+$ redox pair.

4.2.2. Radiolysis near metal surfaces or in the pores surrounded by metal oxides

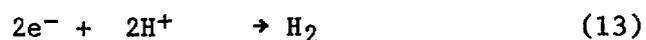
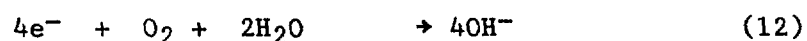
Water radiolysis near metal surfaces or in small pores surrounded by metal oxides such as ZrO_2 may be different from that in the bulk of the water described in the previous section, being affected by the materials in contact with the water. The radiation energy absorbed by water inside the pores surrounded by metal oxides is larger than that absorbed by bulk water, because the flux of the back-scattered electrons arising from substances with high atomic number increases and contributes to the absorbed dose [185-187]. This effect will be more important in small pores than at metal-water interfaces, since the surface to volume (S/V) ratio is larger in the former. The extent of the increase in the absorbed dose depends on the geometry of the pores, the materials surrounding the pores, and the direction of the incident radiation. It may be inferred that an increase of up to 250% or more, relative to the absorbed dose in the bulk water, occurs when this surface effect is taken into account [185]. Thus, the local concentrations of the chemical species produced by radiation may be significantly higher in the pores than in the bulk.

Another important factor will be the significant contributions of surface reactions to the kinetic scheme of the radiolytic reactions in the pores, or at the interface, where the S/V ratio is high. The importance of the surface reactions in systems with high S/V ratios has been pointed out by W.G. Burns et al. [188], who followed the corrosion reactions in sealed stainless steel containers with an S/V ratio of 9.1 dm^{-1} under γ -ray irradiation by measuring the amounts of hydrogen and oxygen evolved. They observed larger radiation-induced accelerations of oxygen removal and of hydrogen formation in the presence of mild steel coupons in the containers, and interpreted these effects on the assumption that the radiolysis products such as e_{aq}^- , OH, HO_2 and H_2O_2 are removed on the surfaces at diffusionaly limited rates. The detailed mechanism of the surface reactions involving the radiolysis products has not been established so far, but it may be possible that the surface reactions rather than the bulk reactions control the overall radiolysis process at interfaces, especially, in pores with a high S/V ratio.

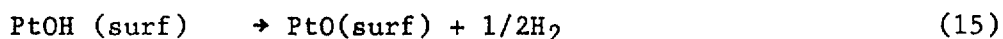
Some species of radiolysis products are significantly oxidizing and have a possibility to be involved in the cathodic reactions which are expressed overall in Eqs (9)-(11).



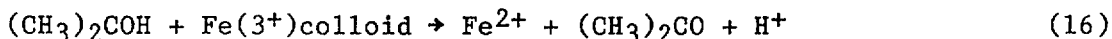
These cathodic reactions may take place under irradiation in addition to the usual ones expressed by Eqs (12) and (13). However, the relative importance of their contributions and the microscopic reaction mechanisms are not well known at the moment.



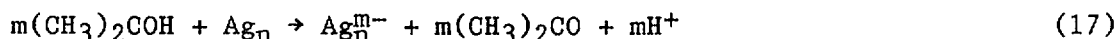
Henglein et al. [189] followed the interaction of OH radicals with the platinum surfaces of a microelectrode by the pulsed radiolysis technique, and directly observed that OH radicals react with the Pt surfaces following Eq. (14), finally yielding platinum oxide.



On the other hand, e_{aq}^- and H are strongly reducing radicals, and are inferred to interact reductively with metal surfaces or metal oxides by analogy with other strongly reducing organic radicals. Colloidal Fe_2O_3 was found by G.W. Buxton et al. [190] to be dissolved rapidly by the propan-2-ol radical produced in aqueous solution by radiolysis through the one-electron reduction reaction shown by Eq. (16).



Henglein et al. [191,192] observed that reducing organic radicals such as the propan-2-ol radical transfer their electrons to colloidal particles of silver or gold as shown by Eq. (17),



and store electrons on them, which are finally discharged by the decomposition of water molecules, yielding hydrogen.

Hydrogen peroxide is one of the key species among the radiolysis products in nuclear reactor cores which is known to have a large effect on the corrosion of some materials. Currently, its behavior in the coolant and the sampling systems has drawn attention, especially with BWRs in relation to hydrogen water chemistry, but has not been well understood because of its instability at high temperatures. It is known that hydrogen peroxide decomposes catalytically on the surfaces of various types of materials at ambient temperatures. Recent work [193-197] shows that oxidized surfaces of stainless steels or Zircaloy catalytically enhance the decomposition of hydrogen peroxide at high temperature. It should be noted that hydrogen peroxide is not stable even in the bulk water at high temperatures and is considered to decompose homogeneously, probably yielding OH radicals.

On the other hand, the reaction route for the catalytic decomposition of hydrogen peroxide on surfaces is believed [198] to be expressed by Eq. (18), giving molecular oxygen but not OH radicals, though no direct experimental evidence has yet been obtained.



It is reported [193,194] that the catalytic hydrogen peroxide decomposition rate is proportional to the area of the surface in contact with the water, and that the surface decomposition predominates over the concomitant bulk decomposition at high temperatures in high S/V regions such as within small diameter pipes and narrow channels or in the crevices and pores surrounded by metal oxides.

In the above discussion the radiolysis of water molecules adsorbed on metal or metal oxide surfaces is not included, though the above mentioned surface reactions of the relevant species are considered to involve adsorption processes on the surfaces. It is known that water adsorbed on some adsorbents such as zeolite or alkali halides is effectively decomposed by radiation at ambient temperatures [199-201], and

it is usually assumed that energy transfer from the adsorbents to the water molecules promotes the decomposition reactions. There are no data available on the radiolysis of water adsorbed on metal oxides at high temperatures. If the amount of water adsorbed on the surfaces is relatively much lower than the amount of the bulk water, it may not contribute significantly to the whole process.

As already mentioned above, the radiolysis of water yields both oxidizing and reducing species, including transient ones, and these species are considered to contribute in several ways via the redox reactions to the electrochemical processes related to the corrosion of the relevant materials, though the detailed mechanisms are not well understood. These processes are represented by changes in the electrochemical potentials of electrodes during irradiation. The total balance of the redox reactions determines the direction of the potential shift, and some additions, or the accumulation of specific species, may change the balance of the redox reactions. For instance, the corrosion potential of stainless steel shows a positive potential shift during γ -ray irradiation at high temperatures

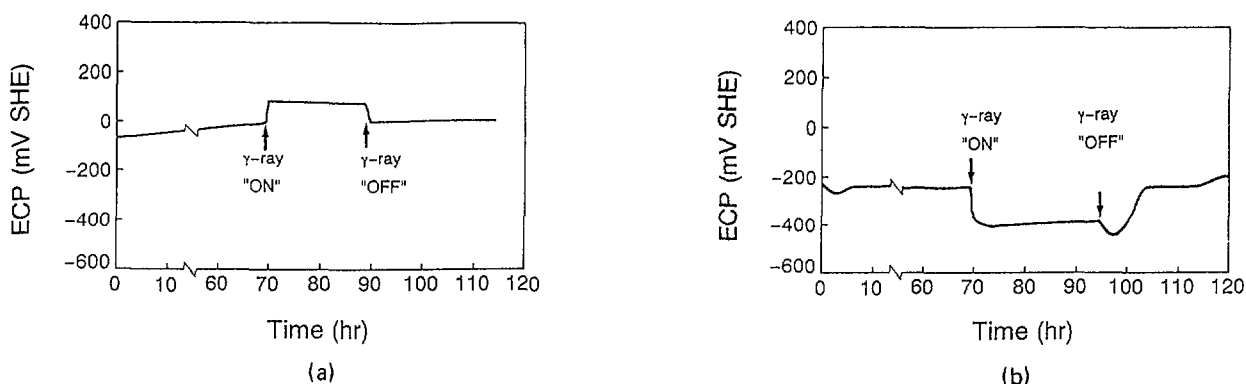


FIG. 4.2.4. Effect of γ rays on ECP (a) under simulated normal water chemistry condition of BWR and (b) under simulated hydrogen water chemistry condition of BWR [202].

under normal water chemistry conditions in BWRs, but gives a negative one, for the same irradiation, under hydrogen water chemistry conditions as shown in Fig.4.2.4 [202]. This is considered to result from the fact that hydrogen additions convert the oxidizing radiolysis products (including oxygen) to reducing species according to the following reactions. These will be discussed in more detail later.



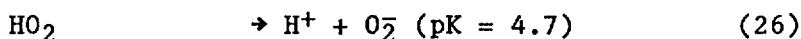
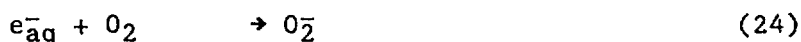
4.2.3. "Thick oxide film effects"

It has been realized [96,97] for more than ten years that there exists a peculiar effect of radiation on the corrosion behavior of Zircaloy in high temperature water under irradiation, which was described already in detail in section 3. This effect was initially explained by the "thick oxide film hypothesis" [109]. This hypothesis is based on in-reactor

experiments on Zircaloy-2 specimens and may be summarized as follows: After the oxide layer on the Zircaloy surface reaches a threshold thickness, the subsequent corrosion rate of the Zircaloy is controlled by water radiolysis in oxide cracks and pores and is independent of the water chemistry outside them [109].

It has been established, generally, that the radiation enhancement of Zircaloy corrosion in the aqueous phase arises from the synergistic interaction of radiation and water chemistry. It has been recognized that in the early stages of Zircaloy corrosion the acceleration by reactor radiation, which is usually observed in oxygenated water, is suppressed in the presence of excess hydrogen in the aqueous phase, but that beyond the threshold oxide thickness Zircaloy specimens exposed to low-oxygen water corrode at accelerated rates under irradiation as if they were immersed in oxygenated water.

The radiolysis of water produces several types of primary species shown in Eq. (7) and described previously. Among these OH and H₂O₂ are oxidizing reagents like oxygen, one of the final products of high temperature water radiolysis, while e_{aq}⁻ and H are strong reducing reagents. Approximately the same numbers of oxidizing and reducing species are produced in the radiolysis of pure water. In oxygenated water e_{aq}⁻ and H are converted very rapidly to O₂⁻ and HO₂, respectively, which are weak oxidizing reagents.



HO₂ and O₂⁻ are less reactive than OH and have relatively longer lives.

The oxidizing species produced by radiolysis may take part in the cathodic reactions in the aqueous corrosion processes of Zircaloy under irradiation, though the detailed mechanism of the cathodic reactions by transient species is not well understood. Thus, this facilitation of the cathodic reactions may make an important contribution to the synergistic interaction and acceleration by radiation in the Zircaloy corrosion under reactor conditions. There is, however, no evidence of the reversibility of the zirconium electrode with respect to these reactions to permit a conclusion on this point.

On the other hand, when excess hydrogen is present the yields of the oxidizing species such as O₂, OH or O₂⁻ are markedly reduced under irradiation as already shown in Fig. 4.2.3, where a steady state is seen to be attained during the continuous irradiation. The most important reaction involved in a hydrogen containing system is reaction (19), converting the oxidizing OH to the reducing H. In hydrogenated systems the consumption of OH, a major reactant to H₂O₂ and e_{aq}⁻, by hydrogen makes the contribution of reactions (20) and (23) relatively more important, and reactions (19) through (23) result in back-reactions reforming water molecules, and reducing the final yields of the oxidizing species. It has been widely accepted that the accelerating effects of radiation on Zircaloy corrosion are greatly reduced by hydrogen additions under PWR conditions, which is not the case in BWRs.

The detailed mechanism of the thick oxide film effect is not well understood at the moment, and some possible mechanisms are discussed here.

One hypothesis is that, when the thickness of the oxide layer is beyond a threshold value, the rate of supply of hydrogen into the pore through diffusion is insufficiently large to maintain the radiolytic suppression effect by hydrogen under irradiation (in the absence of corrosion hydrogen) and, therefore, that the cathodic reactions occurring at the bottom of the pore are facilitated because the radiolytic products escape reaction with hydrogen. Then, the corrosion rate of Zircaloy may be accelerated by this facilitation of the cathodic reactions, when the thickness of the oxide layer is beyond a threshold value. In order for this hypothetical mechanism to occur, excess hydrogen in the cracks or pores has to be consumed by some mechanism. Hydrogen molecules are consumed by reaction (19) under irradiation to yield H atoms if they are present in an excess amount beyond a threshold value. Therefore, if it is assumed that most of the H atoms produced are dissipated or consumed there by some mechanism such as hydrogen pick-up by the metal, then it is possible to show by a simple calculation that when the oxide layers of Zircaloy have deep cracks or pores, the diffusion rates of hydrogen into the cracks or pores is not enough to maintain a hydrogen concentration at the bottoms of the cracks or pores above the threshold value (see Appendix). However, this situation may not occur readily because the recombination reaction (27)



of hydrogen atoms is fast enough to yield hydrogen molecules and the net consumption of hydrogen molecules is not so large.

Another possible mechanism for hydrogen consumption may be boiling of the water inside the cracks or pores. When Zircaloy has very thick oxide layers, it may restrict heat conduction and cause local boiling of water. If the boiling takes place inside the cracks or pores, this would lead to stripping of hydrogen molecules into the vapor phase and thereby reduce its concentration in the cracks or the pores. Again the thick oxide layers may cause a restriction of hydrogen diffusion from the bulk water.

However, it should be noted that, if the cathodic reaction (13) concomitantly occurs at the bottoms of the cracks or pores, then there exists the excess hydrogen arising from the corrosion reactions of Zircaloy. This prevents the above sequence of reactions from occurring. In summary, the thick oxide film effect seems to be a rather complicated phenomenon including surface reactions of chemical species produced by radiation. More research work is necessary for the elucidation of the mechanism.

4.3. CRUD DEPOSITION AND HEAT TRANSFER EFFECTS

4.3.1. PWR crud deposition

(i) Introduction

Deposits on the cladding of corrosion products (CRUD), mainly generated by the release of constitutive elements from all the steel surfaces of power reactors, increase the barrier to heat transfer. Consequently, extensive programs have been carried out in order to investigate the impact of crud deposition on the increase in metal-to-oxide interface temperature, leading to the enhancement of Zircaloy-4 waterside corrosion. The possible inclusion of mineral impurities (Cu, Ca, Mg, Al, Si) which decrease thermal conductivity of the crud eventually aggravates the importance of this process, see Figure 4.3.1 [205,206]. In addition the

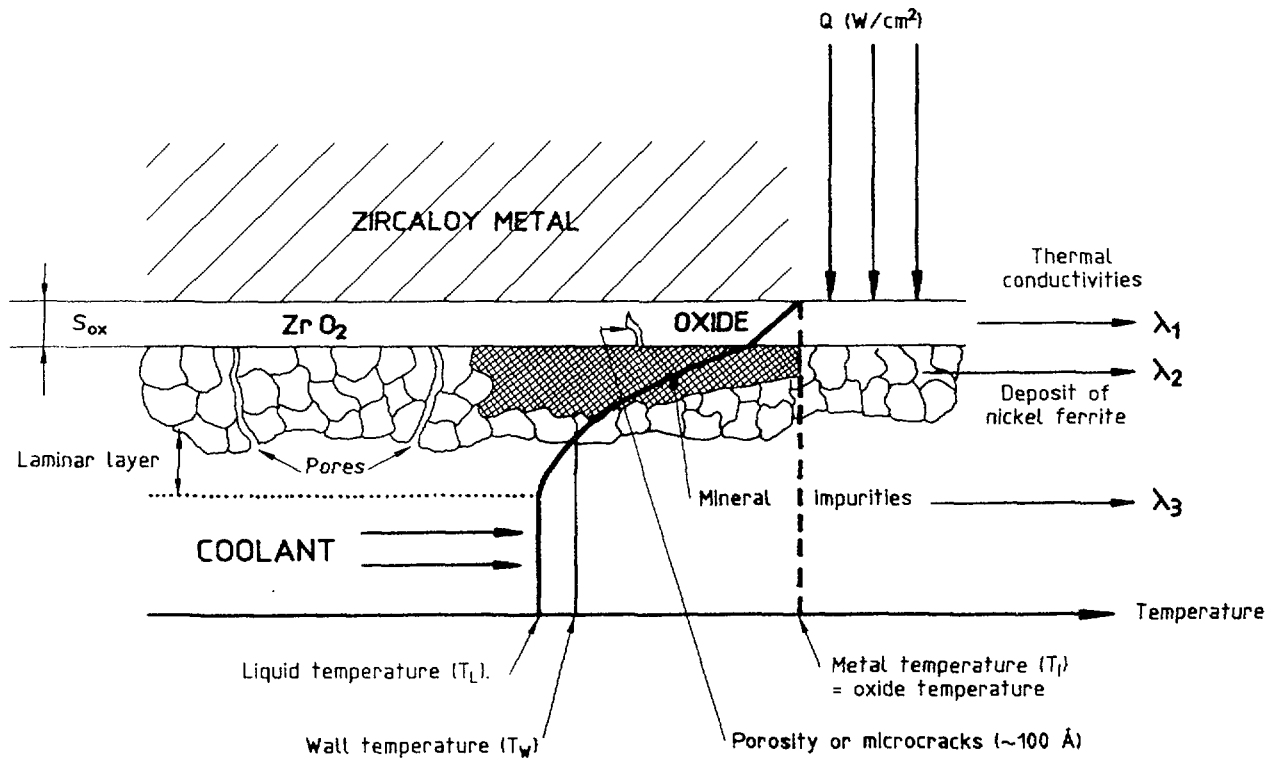


FIG. 4.3.1. Corrosion under a thermal gradient.

crud deposition data from a large program, together with loop test data, has provided clear information concerning appropriate chemistry control required for PWR primary coolant (both Li/B chemistry and impurity control) to minimize the crud deposition on fuel.

Chemistry Control during Power Operation: for a PWR during normal operation the boron concentration at the start of the cycle is up to 2000 ppm and is reduced to about zero at the end of the cycle. This sequence is carried out to adjust the nuclear reactivity of the system. An alkalisng agent (that most often used is lithium hydroxide, LiOH) is added in order to raise the pH together with hydrogen, in order to suppress the radiolytic formation of oxygen and other oxidising species. These additives, which determine the system pH and redox potential, are controlled by the chemical plant (see Specification on Table 4.3.1).

Corrosion: the minimum concentrations of additives were originally specified by the vendors. Operational experience has shown that these specifications were very adequate for maintaining the general corrosion rate of materials of the PWR primary circuit at a very low value. As long as lithium is greater than 0.2 ppm and hydrogen greater than 15 cm³/kg (NTP), the integrity of the various components is ensured for the whole life of the PWR. Upper concentration limits are also specified:

- for impurities such as chloride, fluoride and sulphate in order to prevent the stress corrosion cracking (SCC) and inter-granular attack (IGA) of the austenitic materials (Inconel, SS) (see Table 4.3.1).

- for lithium concentration in order to minimize the corrosion of the fuel cladding. As highlighted later there is evidence that at "higher" lithium concentrations (> 35 ppm, a value that results from out-of-pile loop tests), the rate of Zircaloy corrosion accelerates, but it is also believed that higher lithium levels and higher hydrogen concentrations promote Inconel 600 SCC [207].

TABLE 4.3.1. POWER OPERATION: PRIMARY COOLANT CHEMISTRY SPECIFICATIONS

	W	KWU	EDF	EPRI
LiOH (ppm Li)	0.7-2.2 ^a	1-2 >0.2 ^b	0.7-22	^a
Boric acid (ppm B)	0-1200	0-1200	0-1200	See Fig. 4.3.2
pH ₂₅	5.4-10.5 ^a	5.4-10.5 ^a	5.0-8.5 ^a	—
pH ₃₀₀ (M+F)	6.0-7.9 ^a	—	See Fig. 4.3.3 ^c	6.9-7.4
Dissolved H ₂ (STP/kg)	25-50		25-50	25-50
(ppm)	2.2-4.5	2-4		
Chloride (ppm)	<0.15	<0.2	<0.15	<0.15
Sulphate (ppm)	<0.15	—	—	<0.10
Fluoride (ppm)	<0.15	—	<0.15	<0.15
Dissolved O ₂ (ppm)	<0.1	<0.005	<0.1	<0.01
Suspended solids (ppm)	<0.35	—	—	<0.35
Silica SiO ₂ (ppm)	—	—	<0.2	—
Calcium (ppm)	—	—	<0.1	—
Magnesium (ppm)	—	—	<0.1	—
Aluminium (ppm)	—	—	<0.1	—
Conductivity at 25°C (μS/cm)	—	<30	—	—

^a Dependent on Li/B co-ordination policy.

^b At end of cycle with boron concentration < 10 ppm.

^c A new specification with chemistry to maintain the pH₃₀₀ at 7.1 is being applied successfully in six EDF units.

(ii) Surface potential effects: transport and deposition mechanisms

- During the corrosion process, at the same time that oxidation takes place in situ, metal ions are dissolved at corroding metal surfaces and carried out through the oxide pores, the sublaminar layer and finally the bulk coolant.
- These ions are transported by the circulating pumps around the circuit. Because of the temperature gradient which exists around the circuit, it is natural to consider (when steady-state conditions are reached) that precipitation will take place at some location, depending on chemistry and solubility laws.
- This precipitation leads to the formation of fine particles of oxide which coalesce and grow to a size limit imposed by the turbulence of the fluid.
- These particles are also transported from the bulk coolant to the wall (mass transfer).
- The adhesion forces between the particles themselves and with the wall (deposit or oxide) are assumed to be of magnetic origin.

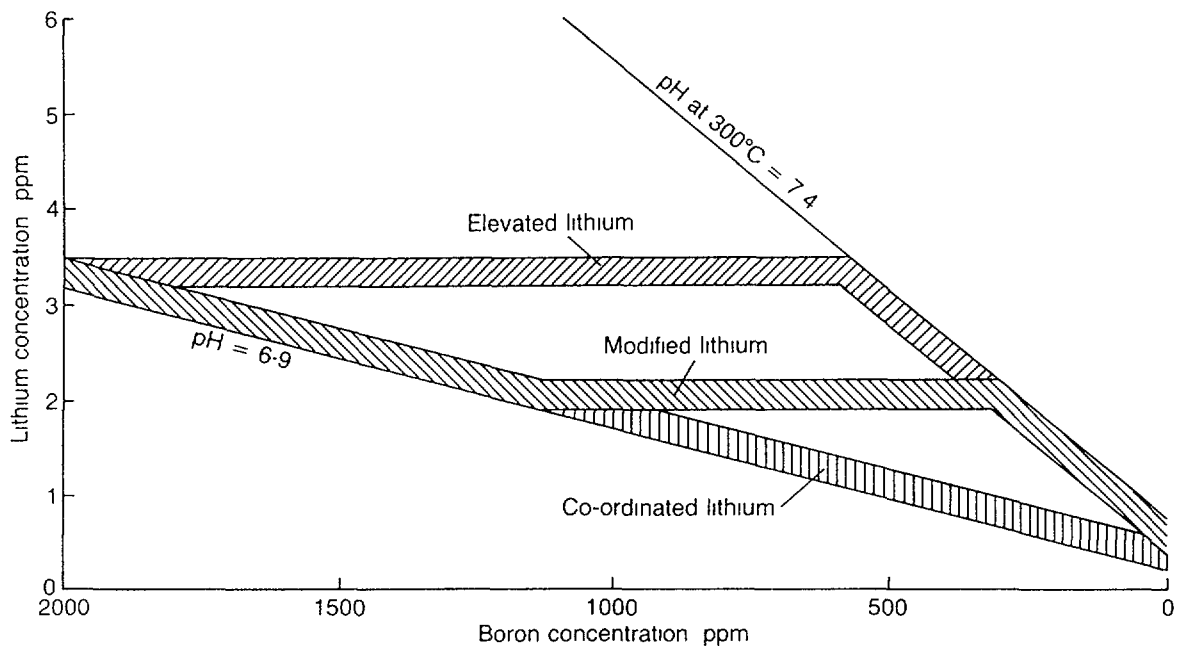


FIG. 4.3.2. Various lithium–boron modes of operation in PWRs (from WOOD, C., *Approaching consensus on the optimum pH for PWRs*, Nucl. Eng. Int., August 1990, p.28).

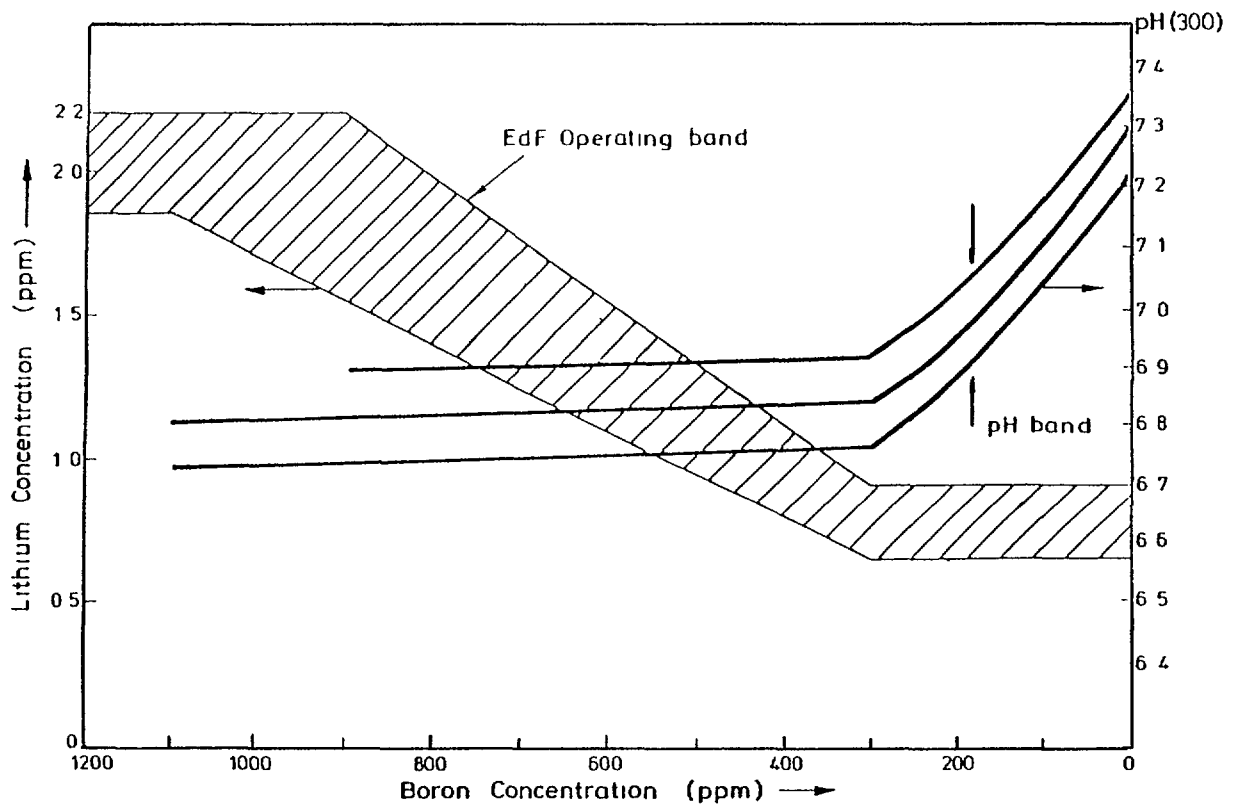


FIG. 4.3.3. EdF lithium–boron co-ordinated chemistry and calculated pH (300) (Note: pH (300°C) values calculated using MBS K_w) (redrawn from Berthet, 1985).

- If, at the location of deposit, the fluid is saturated in the main elements, no dissolution will take place. Particles will reach the wall and the thickness of crud will then increase. But if the particles, which reach the wall, are not totally included within the sub laminar layer, eddies will remove some of the particles. "Erosion" will then take place and can limit the thickness of the

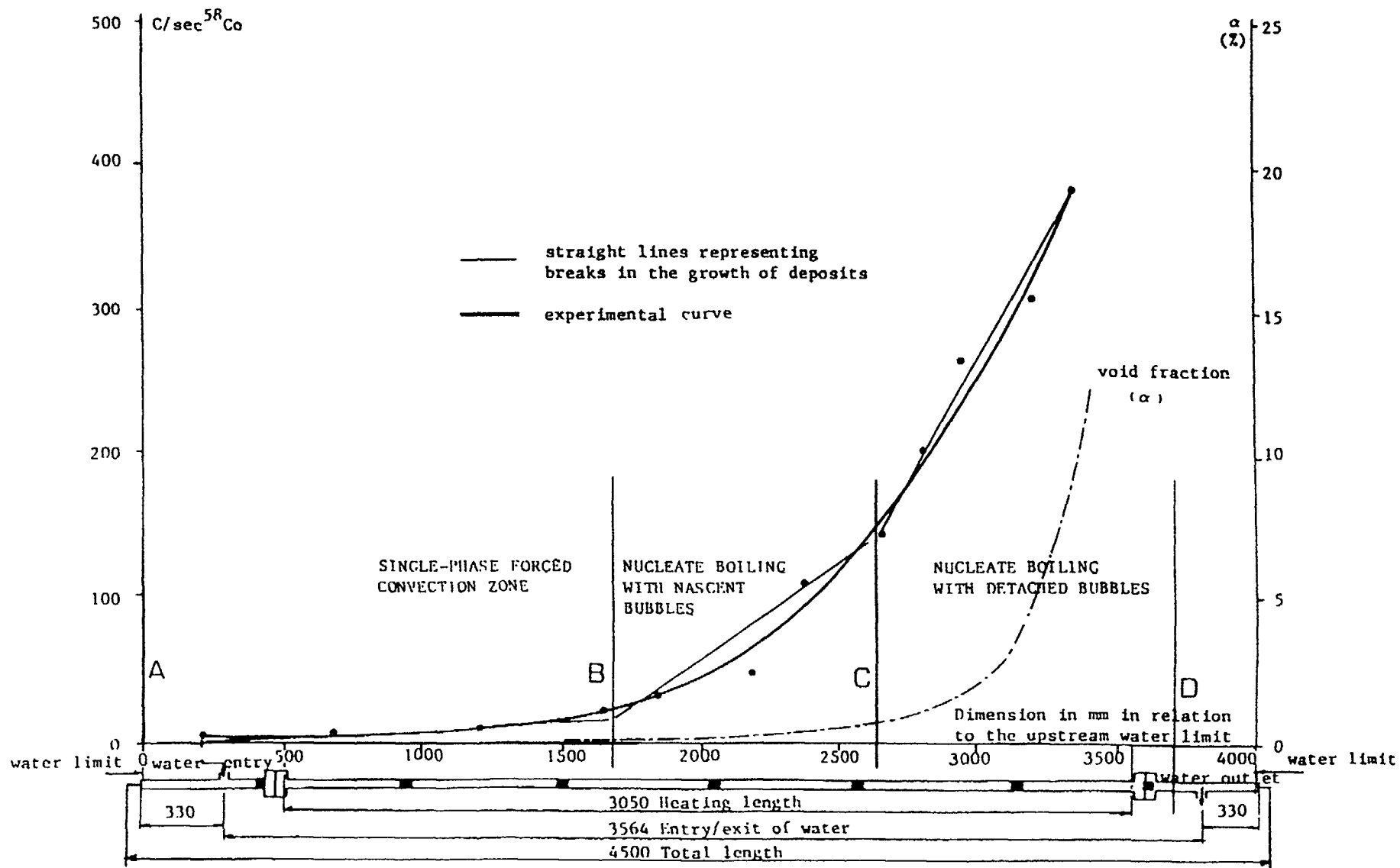


FIG. 4.3.4. Effects of the hydraulic conditions on deposits of corrosion products.

deposit. The erosion forces applied to the deposited crud are the same as those applied to the roughness of the wall. These deposits may be dissolved if their concentrations in the coolant are less than the equilibrium concentrations given by the thermo chemistry of the system. This can lead to a limit in the thickness of the deposits. Indeed, dissolution of deposits will contribute to the transfer of ions into the coolant and the dissolution process will be in competition with the corrosion processes for saturation of the solution. In the same manner, the erosion process will contribute to the amount of circulating particles. Consequently, strong erosion somewhere in the circuit can increase the deposition rate elsewhere.

From this brief description of the main phenomena, it is understandable that the first specifications that were expected to limit the general corrosion rates in reactors might not have been sufficient for the vendors to minimize crud build-up rates. (In addition a reduction of deposits is strongly related to a decrease in the radioactive contamination of the circuit). This is the reason why specific experiments were undertaken in the Cirene out-of-pile loop. The Cirene out-of-pile loop has been used extensively to study the effects of crud deposition and of traces of mineral impurities on cladding corrosion under single-phase and nucleate boiling heat transfer conditions [208]. In general, and as in an actual reactor, corrosion products are generated by the loop wall depending on the specific chemistry of each test. Furthermore, thicker crud can be obtained through the injection of crud pre cursors. These consists of soluble forms of Fe^{++} and Ni^{++} in deoxygenated solution percolated into an anion exchanger at the moment of injection.

Typical axial variations of the thermalhydraulic parameters can lead to three successive regions with specific heat transfer characteristics (see Figure 4.3.4):

- (1) Single phase convection,
- (2) Subnucleate boiling,
- (3) Detached boiling.

The void fraction, α , is defined as the ratio of the volume of vapour to the total volume across a section. The experimental procedure includes qualitative and quantitative analysis of the crud deposit, examination of the zirconium oxide layer and examination of the clad metal. In the boiling experiments it is possible to assign to crud build-up an increasing slope in the three successive thermalhydraulics regions, as shown in Figure 4.3.4. A sharp increase in deposition appears in the detached boiling zone ($\alpha \sim 1$ or 2%). The maximum crud level was approximately 30 mg/dm².

Over the pH range recommended for PWR coolant operation, the influence of pH on core crud fouling was found to be negligible. Indeed, this parameter, which is dependent on solubilities is probably masked by local concentration effects and increases in mass transfer in the nucleate boiling mode.

In another experiment, crud precursors were injected to develop a crud layer in the 20 μ m region on the rods. The axial crud distribution is indicated in Figure 4.3.5, as measured by eddy-current. On one rod, after 368 Effective Full Power Days (EFPD), an axial decrease of crud in the boiling zone was encountered. This decrease corresponds to the appearance of flakes as shown on Figure 4.3.6. At the same time, crud under boiling became more dense with the appearance of chimneys as shown on

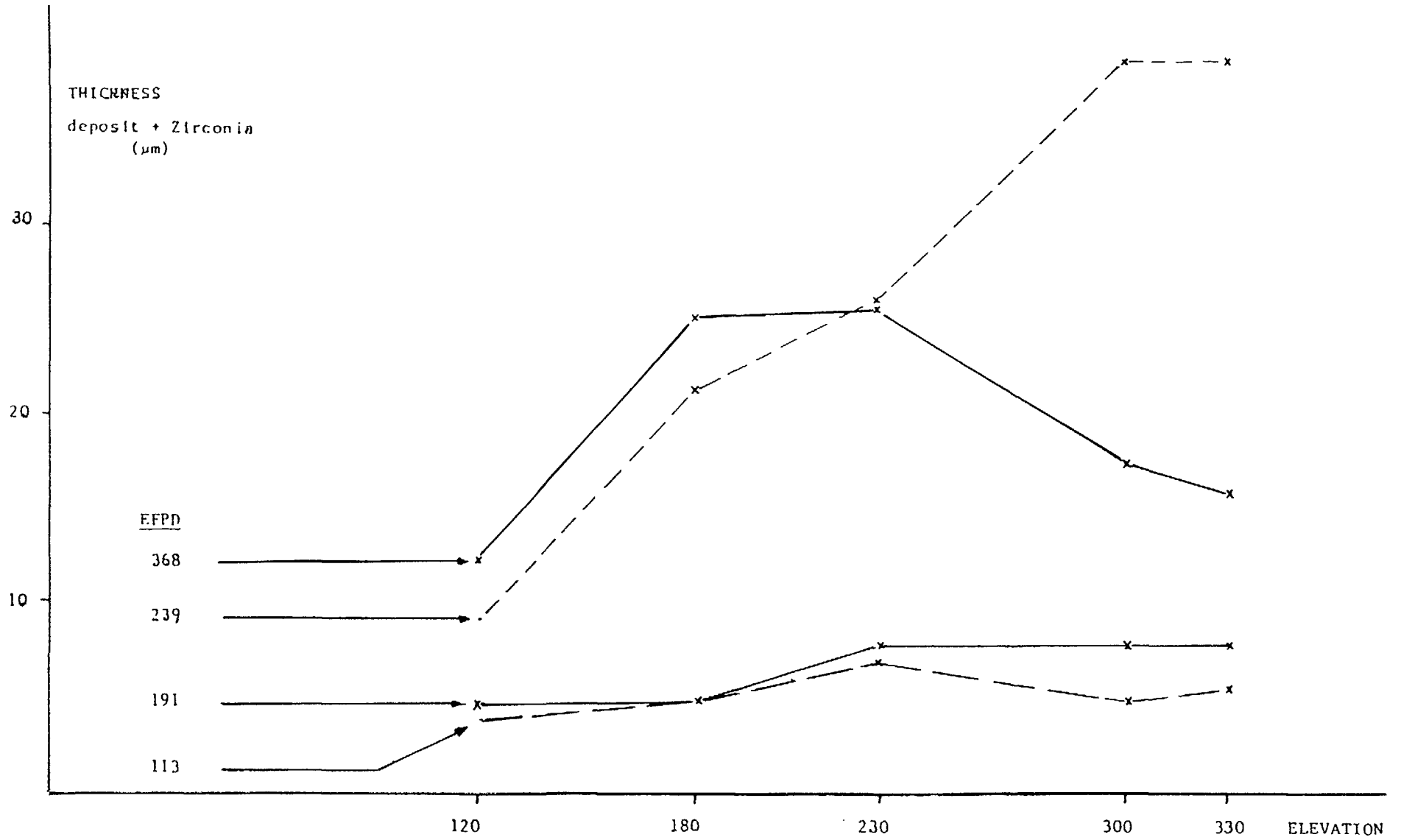


FIG. 4.3.5. Axial crud distribution.

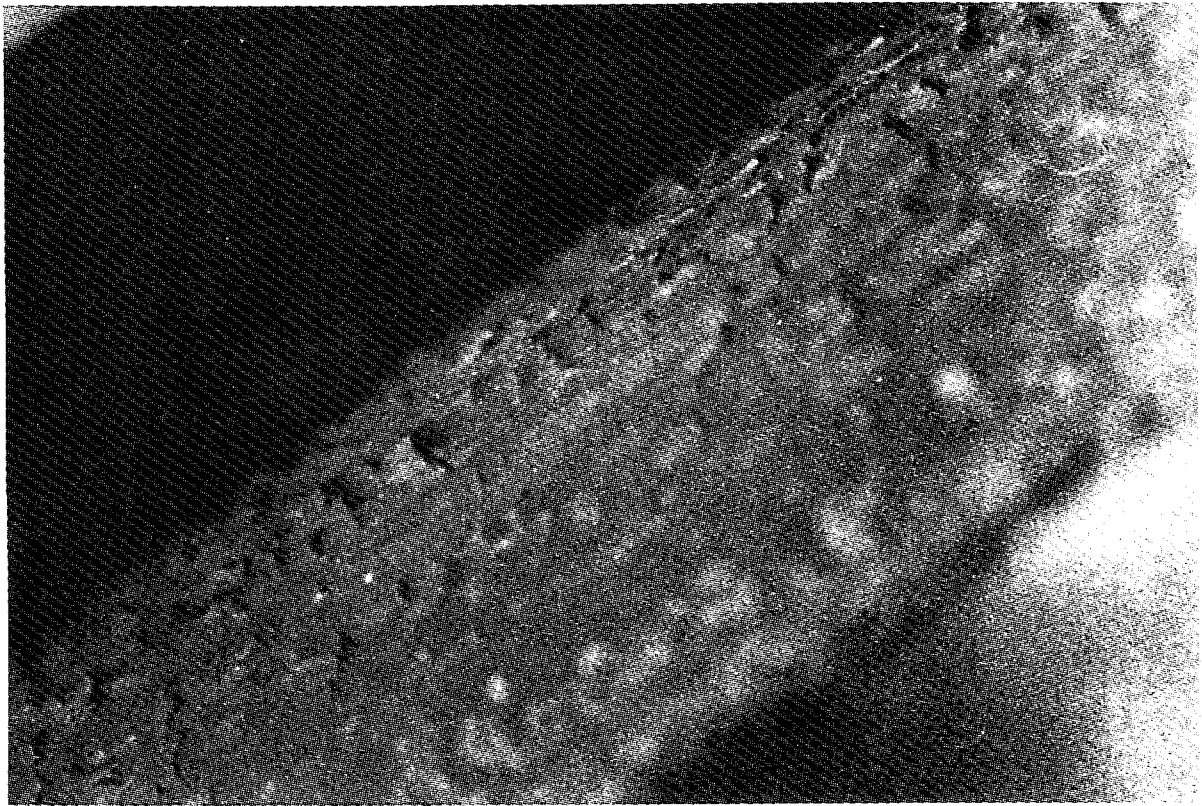


FIG. 4.3.6. Appearance of flakes.

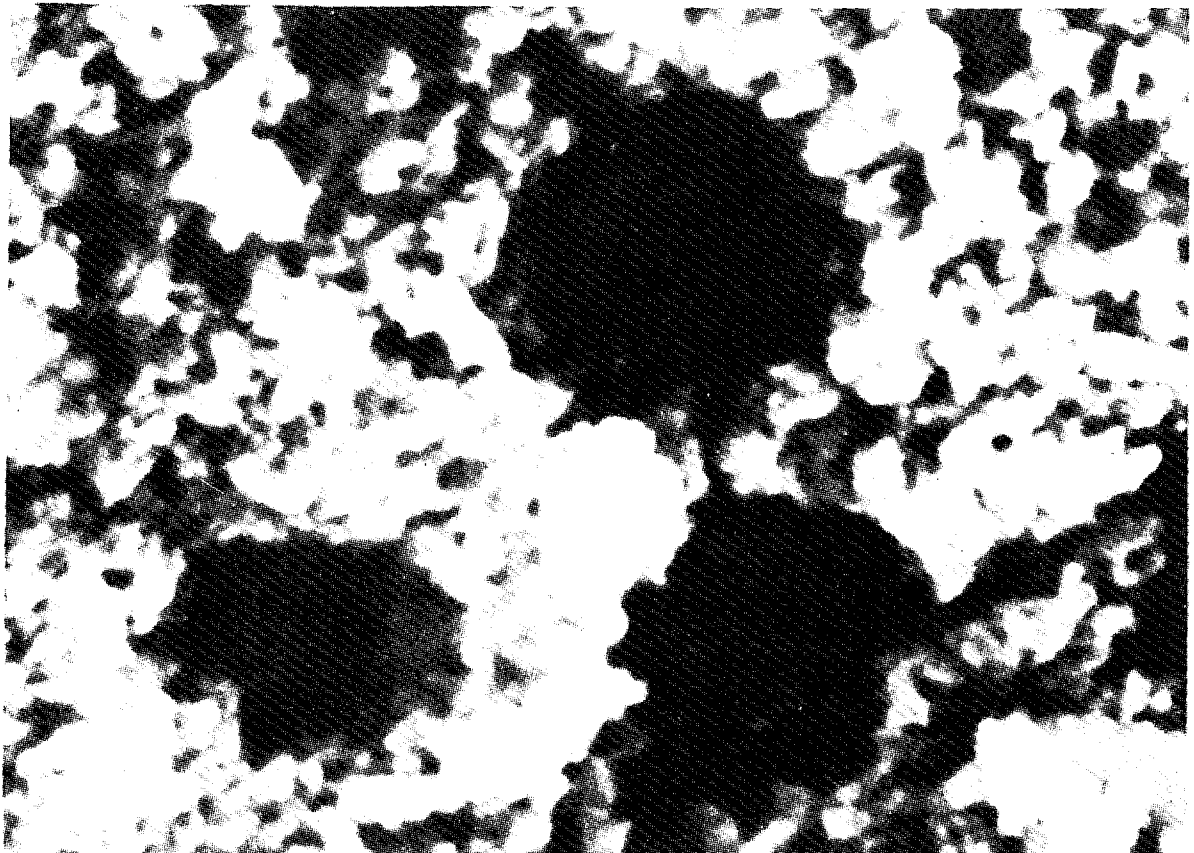


FIG. 4.3.7. Chimneys in crud.

1 μ m

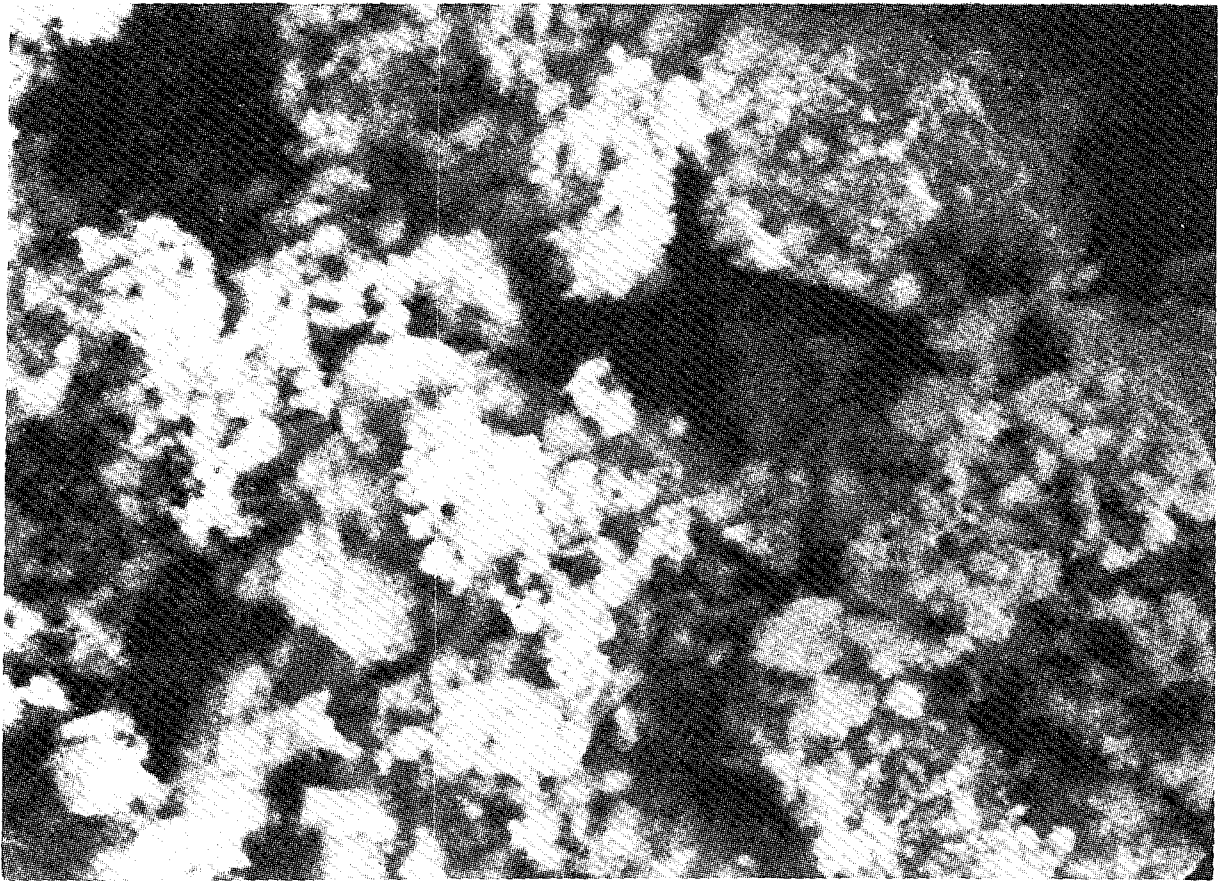


FIG. 4.3.8. Loose texture of the crud.

10 μm

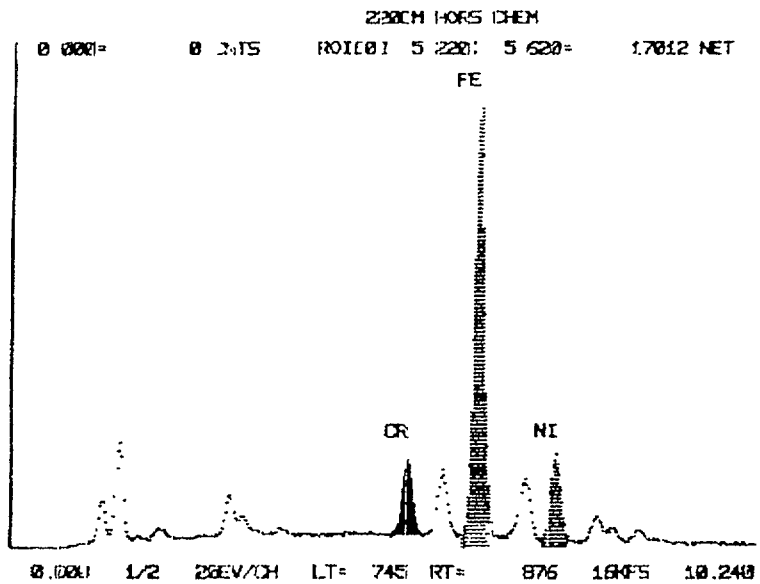
Figure 4.3.7. Crud as freshly deposited on the same boiling zone has a loose texture represented on Figure 4.3.8.

The morphology of the crud deposit results from the nucleation and growth of vapor bubbles at preferred sites on the metal/coolant interface. These sites remain crud free, but mass transfer associated with boiling produces deposition of particulates around the sites, and chimneys are formed. Deposits consisted of particles $\sim 1 \mu\text{m}$ in size; the diameters of the chimneys were about 1–5 μm . The crud layers are the result of an equilibrium between the rates of particle deposition from boiling and crud dissolution and erosion. The rate of crud build-up is proportional to the eddy diffusivities for fully developed turbulent bubble flow. The momentum transfer can be subdivided into two components, one due to the inherent liquid turbulence independent of the relative motion of the bubbles and additional turbulence caused by bubble agitation.

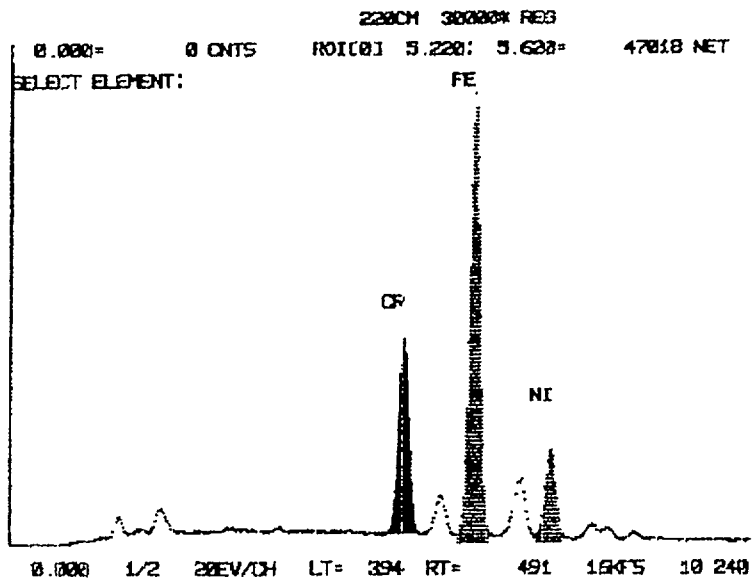
The composition of the crud measured by X-ray dispersive analysis, is given on Figure 4.3.9 for samples with no chimneys (A: non-boiling zone) and samples with chimneys (B: outside a chimney and C: very close or in a chimney). The iron to nickel ratio is constant, but a consistent enrichment in chromium is observed in the zones with chimneys. Thus, the crud deposited consisted of a $(\text{Fe,Ni,Cr})_3\text{O}_4$ spinel, while zeolite-forming impurities with extraneous impurities (Ca, Mg, Al, Si) were negligible.

Then, tests were carried-out with daily replacement of 10% of the loop water volume (feed-and-bleed) by injection from a feedwater tank. Mineral impurities (calcium, magnesium, aluminium and silica) were introduced in concentrations representative of current specifications. In this case, with light deposits (1–2 μm), magnesium and calcium vs. iron

A : Deposit in no Boiling Zone



B : Deposit in Boiling Zone : Outside a Chimney



C : Deposit in Boiling Zone : Very Close or Inside a Chimney

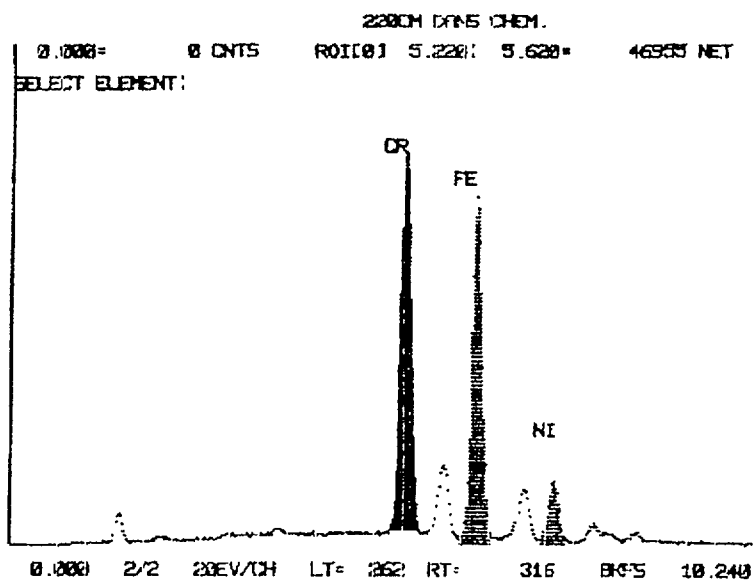


FIG. 4.3.9. X ray dispersive analysis.

TABLE 4.3.2. NICKEL-FERRITE COMPOSITION AND MINERAL IMPURITIES ENRICHMENT

Elevation cm	Ca/Fe x 10 ²		Mg/Fe x 10 ²		Ni/Fe	
	run 1	run 2	run 1	run 2	run 1	run 2
69-73	4.6	1.3	0.9	1.5	0.18	0.12
154-158	2.2	2	0.4	1.5	0.16	0.21
194-198	5.5	4.4	1.2	3	0.47	0.20
264-268	4.1	5.3	0.9	5.7	0.35	0.30
289-293	9.5	7	2.0	8.5	0.25	0.32
343-347	124	17	8.1	15	0.32	0.34

ratios are shown in Table 4.3.2 at different axial elevations. According to these data, enrichment starts in the two-phase zone for a void fraction of 1.5 to 2%. The axial position (A) where zeolite enrichment was initiated is marked on Figure 4.3.10 in comparison with the thermalhydraulics. In one case, accidental calcium contamination (up to 40 ppb measured in the loop water) formed white spots identified as a zeolite in the detached boiling zone. Dramatically increased clad-corrosion was then encountered after 120 EFPD. Photographs of this unique event including X-ray dispersive analysis are displayed on Figure 4.3.11.

In the case of heavy crud deposition, the appearance of a flaky texture is indicative of a strong concentration of zeolites underneath the flakes. As shown on Figure 4.3.12, part of the white deposit could not be separated from the zirconia film by scraping with a scalpel blade.

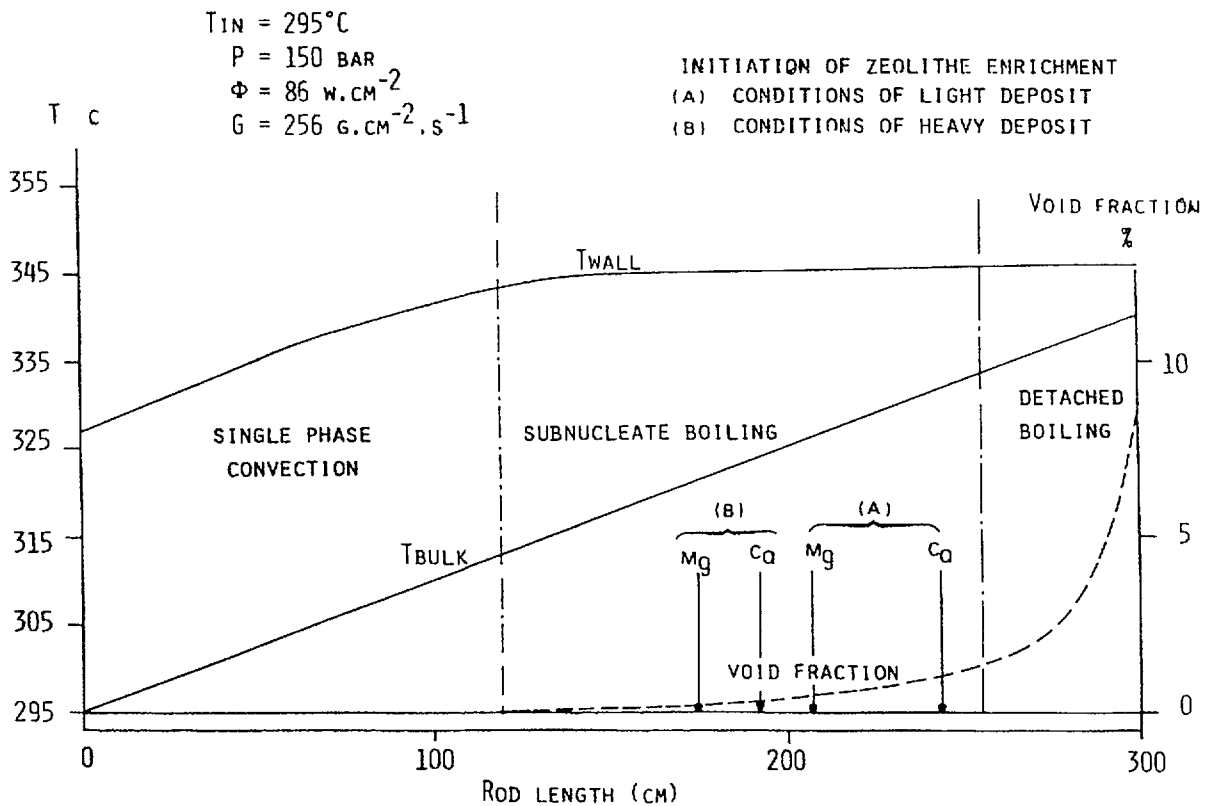
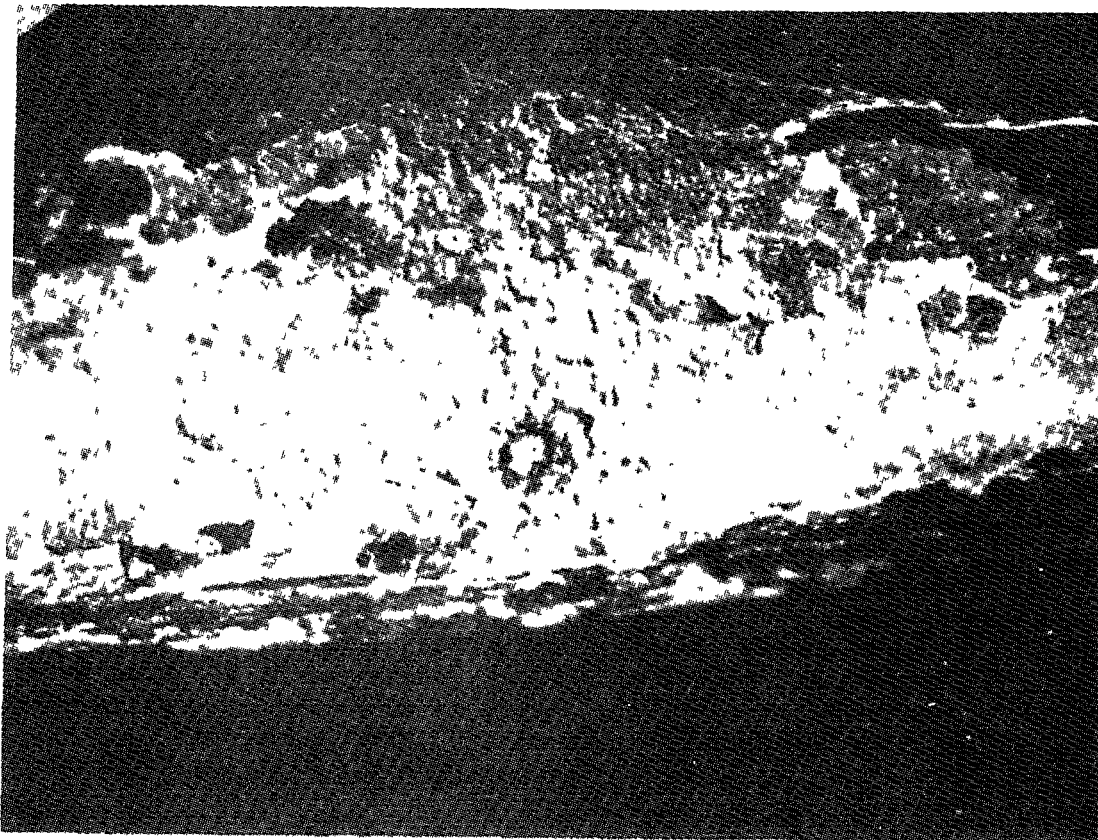
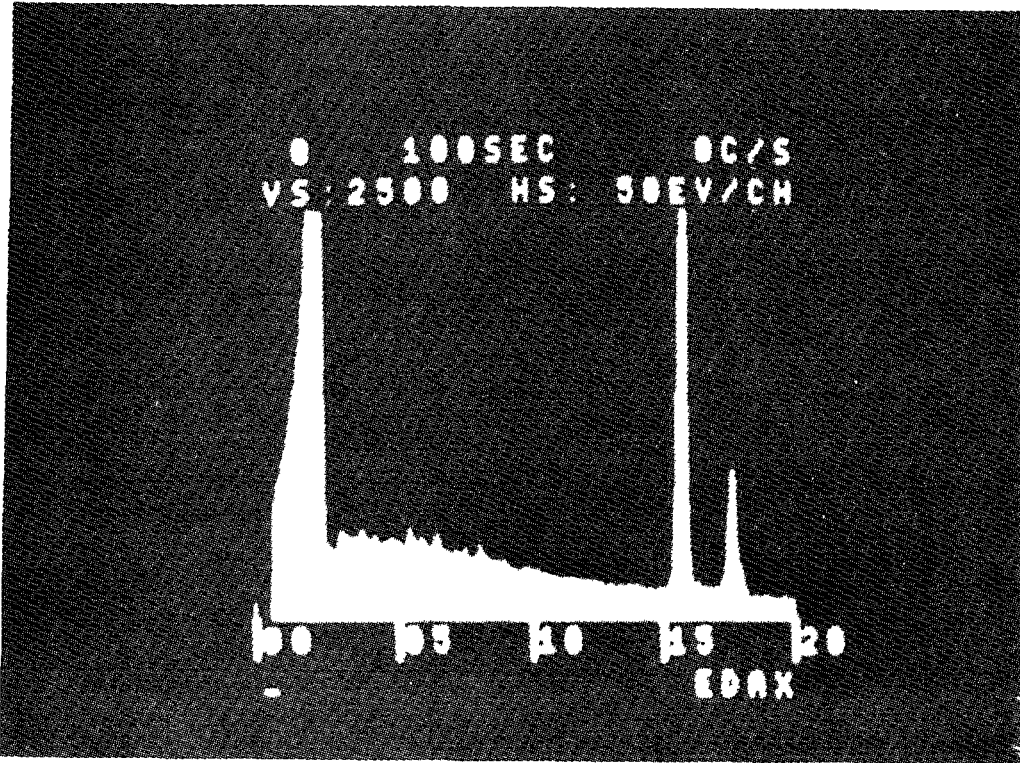


FIG. 4.3.10. Thermohydraulic of Cirene.



Zr(L)

Zr(K)

FIG. 4.3.11. Accidental external corrosion.

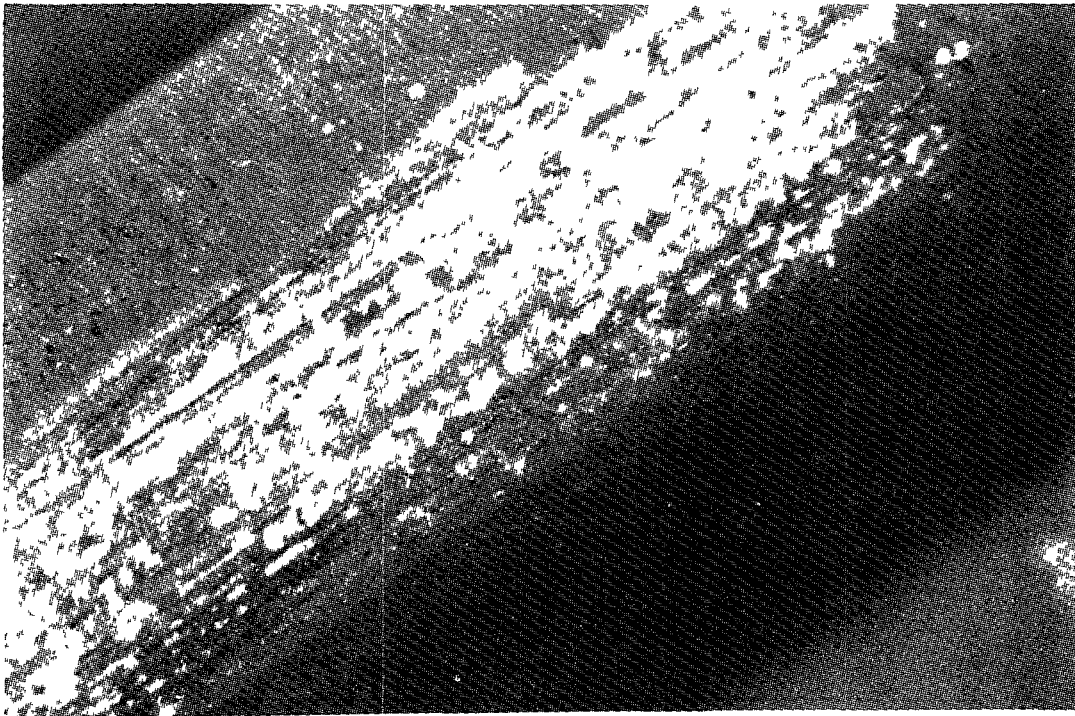


FIG. 4.3.12. Scraping with white deposit.

Figure 4.3.13 shows a SEM view of a flake turned upside-down. Crystallization in the shape of needles is characteristic of magnesia. Chimneys running through the crud flake are also easily identified.

(iii) Thermal conduction effects

The cladding of rods has been subjected to oxide thickness measurements after the following times of operation, under nucleate boiling conditions:

- 1) 174 days, light deposit (rod number 1),
- 2) 270 days, heavy deposit (rod number 2),
- 3) 456 days, heavy deposit (rod number 3).

In areas under "single phase convection" and partially under "developed nucleate boiling" (void fraction less than 1-1.5%), the corrosion kinetics were in agreement with theoretical thermal models, that take into account the heat transfer through the oxide and the crud layers. In the areas with "detached boiling" (void fraction more than 2%), there was evidence of accelerated corrosion. The axial evolution of the corrosion film is shown in Figure 4.3.14 for rod No. 3 after 456 EFPD. Starting at the 160 cm elevation on the rod, the water/oxide interface (wall) temperature is constant (343°C). As the sub-saturation of the bulk water decreases, a greater fraction of the energy is spent on vaporisation (axial power on the rods of Cirene loop is constant). For this constant temperature, the zirconia thickness increased from 6 to 16 μm . The increase in the void fraction is also quoted.

The acceleration of corrosion in boiling zones was by a factor of approximately two with respect to regions under single-phase heat transfer at the same temperature. The acceleration of clad corrosion in the boiling mode cannot be readily explained by a temperature increase at the metal/oxide interface due to the heat transfer barriers through the oxide film and the crud or by a decrease of thermal conductivity of the zirconia

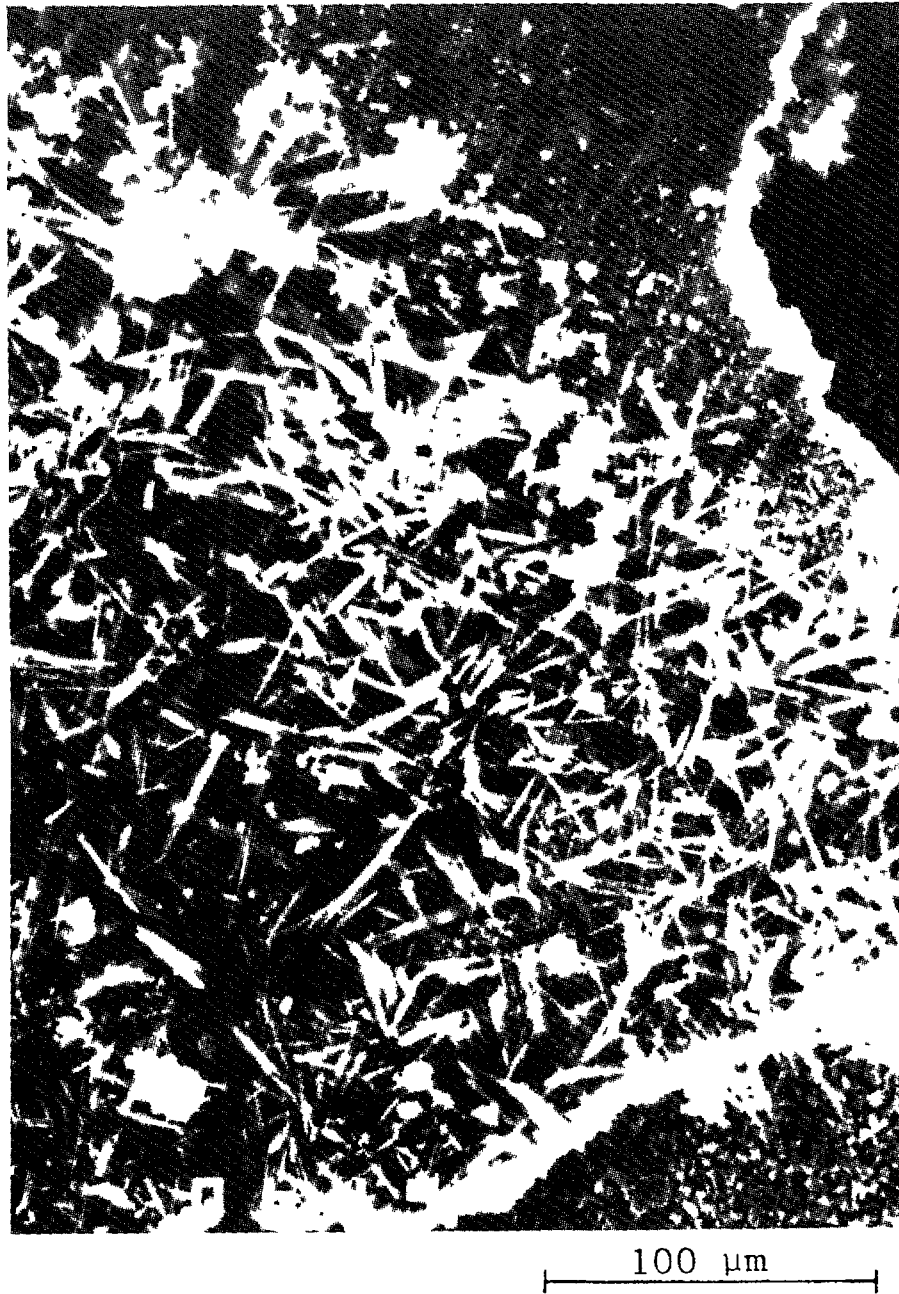


FIG. 4.3.13. SEM view of a flake turned upside down.

or the crud. In our tests, the situation did not appear consistently worse on the rods with heavy deposits (~ 10 to 20μ) than on those with light deposits. Only a slight increase in temperature at the metal/oxide interface was observed as a result of an accelerated rate of crud build-up. (The thermal conductivity of the crud was assessed to be about $0.1 \text{ W/cm}^\circ\text{C}$). However it has been demonstrated that the intrinsic corrosion properties of Zircaloy are affected when lithium is incorporated in the lattice of the oxide [209] or, in micro-cracks in the post-transition film [210].

Furthermore, in a dense deposit the flakes with chimneys can act as vapor-concentrating sites, as they probably originated from effusion of the steam bubbles. A higher concentration of chromium near to and in the chimney holes, and the observation of important mineral crystallization could be indicative of a high concentration factor on these sites. Then lithium enrichment is promoted by boiling conditions leading to a local

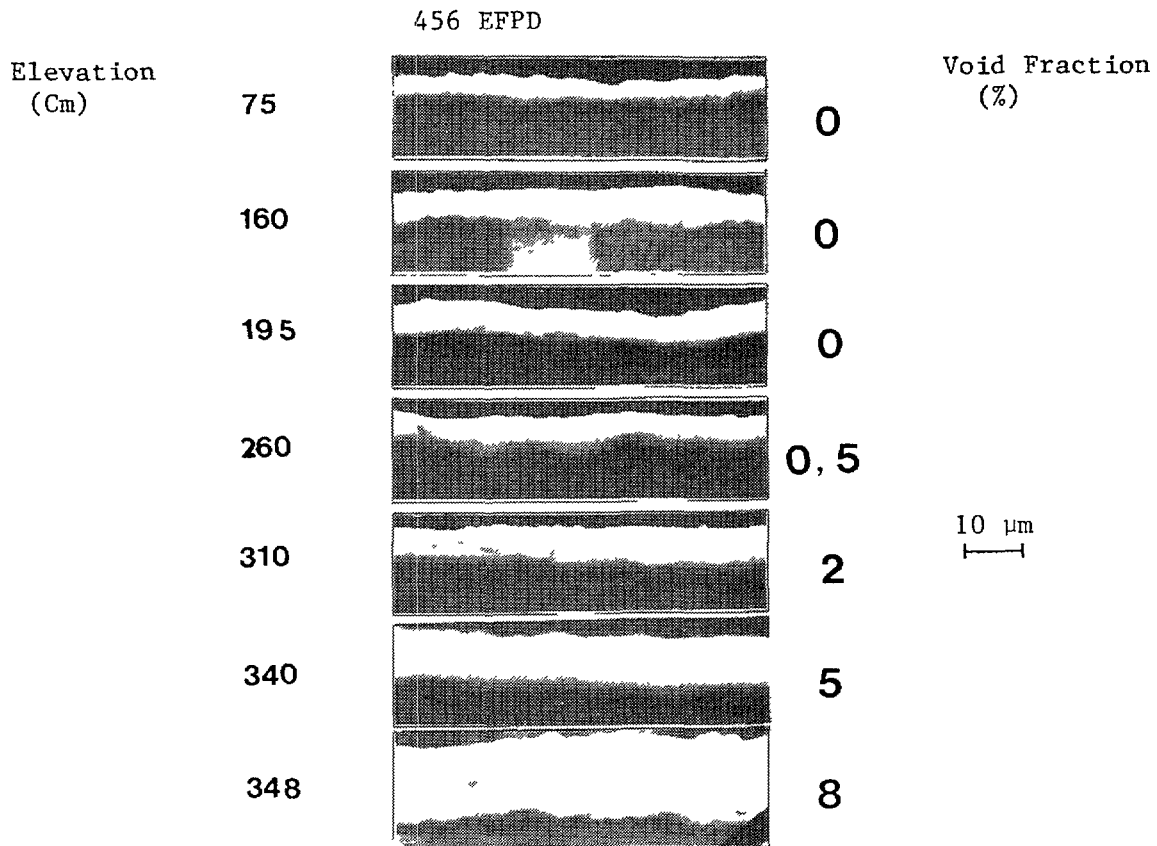


FIG. 4.3.14. Metallography of fuel rod number 3.

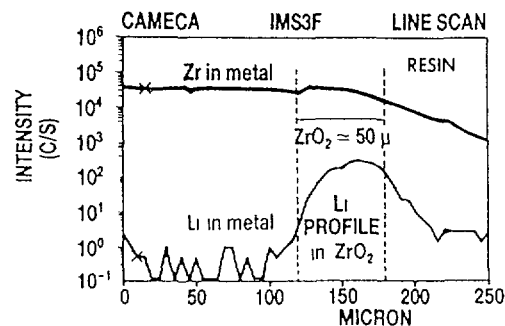


FIG. 4.3.15. Lithium concentration profile in the oxide film.

over concentration of lithium at the wall of the cladding and in the pores of the crud deposit and of the oxide films. These assumptions were confirmed by the detection of lithium ions incorporated in the deposits and in the zirconia layers [211]. Figure 4.3.15 shows a lithium profile (SIMS) across an oxide layer which has undergone an acceleration of the oxidation process. Concentration profiles using the SIMS technique cannot be given in this case because of the lack of calibrated standards (specimens implanted with lithium at known concentrations).

The same observations were made on fuel rods from PWRs. Generally, crud deposition on fuel rod of power reactors is very light or non-existent. Crud scraping campaigns, visual examinations or activity build-up measurements have been performed in several reactors and the "coordinated Li/Boron ratio" seems to be efficient [212,213]. The typical maximum zirconium oxide layer thickness is 20 to 30 microns on three cycle rods. Nevertheless, some examples of tenacious crud were found to have developed as a result of "bad" chemistry control of the primary coolant of reactors such as the Saxton reactor. Coolant permeating through the crud

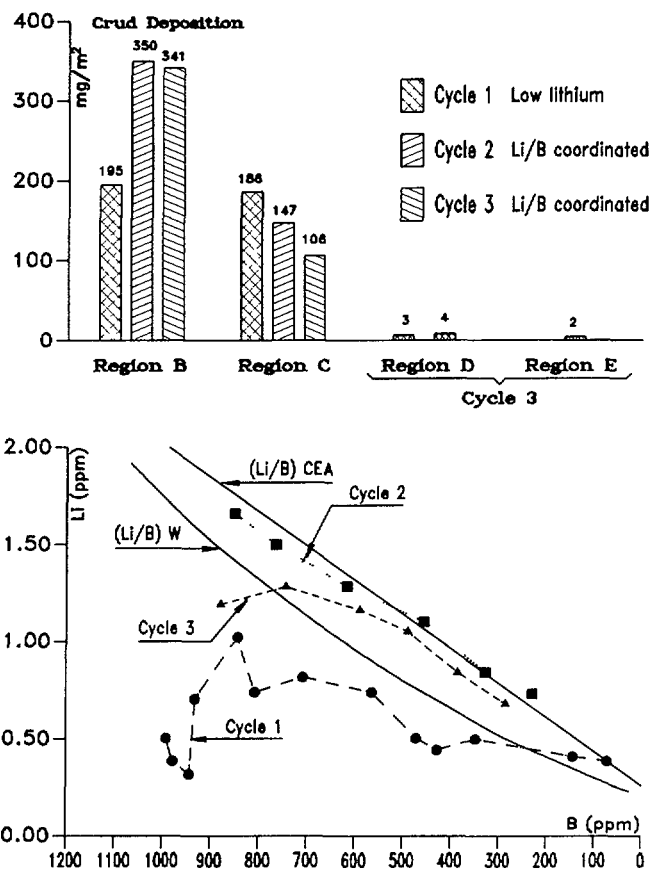


FIG. 4.3.16. Crud buildup of span 7 of Trojan cycle 1, 2 and 3 fuel assemblies during the first three cycles with the chemistry given below.

and containing dissolved lithium, is believed to vaporize in the chimneys of this type of crud (which allows for ready evaporation to steam), resulting in an excessive concentration of lithium at the base of the chimney. Local coolant pH levels in excess of about 11.0 can readily develop by this mechanism (due to lithium concentration), and cause subsequent excessive corrosion of the Zircaloy cladding. The failures observed in the Saxton reactor were believed to have been initiated by this mechanism. Direct image mass analysis (DIMA) of the heavy waterside corrosion films on the Saxton rods confirmed the presence of high levels of lithium in the oxide, adding further support to the believed mechanism. As the oxide thickened, because of the high heat fluxes, the temperature at the oxide-metal interface increased rapidly causing thermal corrosion to accelerate. Thus by a mechanism of accelerated corrosion due initially to lithium hide out, and later due to thermally activated corrosion, failures developed rapidly under thick tenacious crud layers in the Saxton test rods.

In modern PWRs excessive crud build-up in the core can usually be avoided with a well adapted carefully operated coolant chemistry. Optimization of the lithium/pH/hydrogen treatment combines the objectives of reducing the sources of radiation fields and crud buildup. These requirements can be served together (since crud deposits in the core are the origin of this activation, leading to high dose rates) by maintaining the pH in the desired range so as to maintain a positive temperature coefficient of solubility for nickel ferrite in the core, and at the same time by maintaining a zeta potential which prevents the attraction of colloid species to the cladding surface [214]. It was demonstrated [215-217] that a pH_{300} above 6.8-6.9 is sufficient to avoid the presence of a thick deposit in the hot part of the fuel. This is illustrated on the

Figure 4.3.16, and has been confirmed by the observations on French reactors [216].

In contrast, a low pH corresponding to a low lithium concentration (below 0.2 ppm when boron is below 10 ppm) is responsible for the formation of thick in core deposits. The same effect may be observed with an hydrogen concentration below the limit required to suppress the radiolysis, or more generally, with the presence of oxygen in the primary coolant [217]. Either of these conditions is sufficient to produce spectacular effects, due to the presence of heavy deposits on the fuel rods, which can be summarized as follows :

- An increase in pressure drop leading to reduced flow of the primary coolant,
- A thermal barrier between the water and the cladding increasing the temperature of the cladding and subsequently the temperature of the uranium dioxide with a change of the power coefficient (Doppler effect),
- Variations of local coolant density leading to reactivity effects.

The optimum pH value at reactor temperatures was computed by the CEA to be 7.1 [218]. EPRI [219] recommends that the lithium and boron chemistry should be coordinated to achieve a constant or increasing pH in the range 6.9 to 7.4 (Areas B, C, D of Figure 4.3.17). Operation at a pH below 6.9 (Area A) is not recommended. The optimum pH range has yet to be established, but for the present it is recommended that the pH should be as high as is allowed by the vendor specification. In practice the maximum lithium concentration in the current specifications does not allow pH 7.4 to be achieved at the start of a cycle. However, lithium concentrations can be held constant early in the cycle until the desired pH is reached and then coordinated with the boric acid to keep the pH constant for the

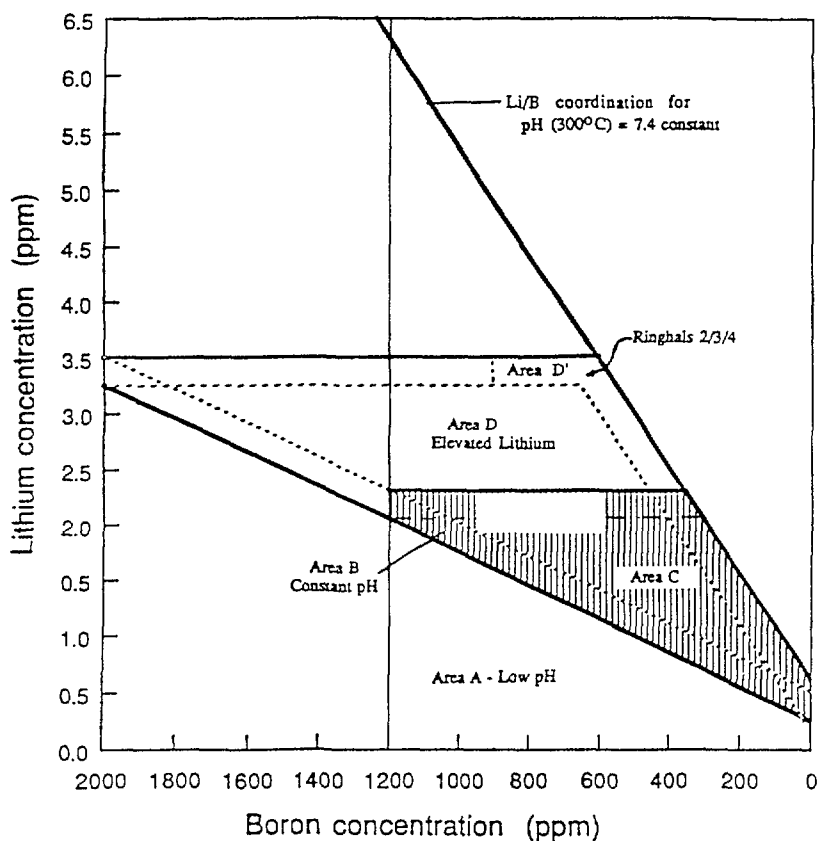


FIG. 4.3.17. Lithium-boron operating regions.

remainder of the cycle. This approach is given by Area D'. The efficiency of the so called "coordinated chemistry" (constant pH) for clean core operation and for decreasing dose rates on out of core surfaces has now been demonstrated [220,221]. Thus, the option for a high pH for the coolant is nowadays preferred to a low pH.

A consensus seems to have developed concerning the operating value of the coolant pH, i.e.: $\text{pH}_{300} = 7.1$ if calculated with the Mesmer K_w value (or $\text{pH}_{300} = 7.2$ if calculated with the Marshall and Franck coefficient). Plant operators are reluctant to use a higher pH due to the potential for an assumed effect of high lithium on both the Zircaloy oxidation and Inconel 600 SCC. Anyway we can conclude that any conditioning with a $\text{pH}_{300} > 6.9$ is good for avoiding additional problems from deposits on the fuel.

4.3.2. WWER crud deposition

The WWER-440 reactors are provided with horizontal steam generators with straight stainless steel tubing, while most other PWRs have vertical steam generators with U-shaped tubes made of Inconel 600 or Incoloy 800. The fuel element cladding of the WWER-440 is made of zirconium-niobium alloy H-1 containing 1% niobium while the fuel elements of the other reactors are clad mainly with Zircaloy-4. The temperature and pressure as well as the heat flux are lower in the case of the WWER-440 reactors than for other PWRs. WWER-440 type reactors use KOH and NH_3 to alkalize the reactor water (Table 4.3.3). The water quality specifications for WWER reactors permit only rather small variations in reactor water pH values, through a correlation between the concentration of the alkali and the boric acid in order to maintain the specified pH. No information is available to assess the WWER fuel surface crud levels. Nevertheless, due to the low coolant and wall temperature, the reduced heat flux and the appropriate chemistry applied, the thickness of the deposited crud layers is expected to be low.

4.3.3. BWR crud deposition

(i) BWR feed water chemistry specifications

A specific feature of BWR water chemistry is that water radiolysis in the core is not suppressed. Unlike PWRs, water radiolysis suppression by maintaining certain H_2 concentrations is difficult because the hydrogen added is removed continuously with the steam from the core. Reactor operation at a given capacity leads to water radiolysis at a constant level. In most cases the O_2 level in the recirculating coolant due to radiolysis is between 0.1 and 0.3 ppm, and the O_2 level in the steam produced ranges between 15 and 30 ppm. It is known that even small amounts of oxygen in the coolant induce deleterious effects on the intergranular corrosion of the recirculation piping. It has turned out that the addition of hydrogen reduces the oxygen level in the recirculation lines through the radiolytic recombination reaction in the downcomer. Therefore, hydrogen injection to the feed water system of BWRs has been proposed as a remedy to piping corrosion. This water chemistry regime is called: "hydrogen water chemistry" and, its demonstration is now being conducted successfully in several power plants [222].

In BWR coolant pH cannot be controlled even with the non-volatile KOH or LiOH because of the danger of local increase in the concentration of these alkalis in the core. Under these circumstances, the minimization of the circuit corrosion processes in the BWR requires both the use of highly

TABLE 4.3.3. SPECIFICATIONS OF REACTOR WATER QUALITY FOR PWR TYPE WWER-440

Indicator (with reactor "on-load")	Value
pH (25°C).....	> 6.0
pH (260°C).....	7.1 - 7.3
KOH as K ⁺ depending on H ₃ BO ₃ concentration mg/kg.....	2.0 - 16.5
NH ₃ , mg/kg.....	5
Hydrogen, ml/kg.....	30 - 60
Chlorides, ug/kg.....	< 100
H ₃ BO ₃ , g/kg.....	0 - 8.0
Oxygen, ug/kg.....	< 10

corrosion-resistant construction materials and of high-purity water throughout the cycle.

The corrosion products released from the large surface areas of the materials must be continuously removed. Condensate demineralizers installed after the turbine condenser and before the flow re-enters the reactor vessel are used for this purpose. However, the corrosion products released downstream of the condensate demineralizer are not removed. The oxygen concentration is very important for minimizing the corrosion product release to the feedwatersystem. Therefore the oxygen level must be controlled in the feedwater. In this way fuel surface deposits are minimized and flow and radioactivation problems reduced. The reactor water is also highly demineralized, the amounts of the respective impurities being in ranges such as to guarantee the reliable operation of the fuel elements and the stainless-steel equipment and pipes as well as adequate purity of the steam produced. The specifications generally allow for a maximum of 100 or 200 ppb chloride, while the critical concentration is 350 ppb. The silica concentrations are specified primarily to avoid deposits on the heat exchange surfaces in the core. A silica concentration of 1000 ppb is sufficiently low to avoid this. However, in the case of the demineralized make-up of water (specific conductivity about 0.1 $\mu\text{S}/\text{cm}$) the maximum silica concentration is usually between 20 and 30 ppb. Thus, silica from make-up water is rarely the source of high coolant levels of SiO₂.

(ii) Water reactor fuel surface crudding levels

The thickness and composition of the deposited crud layers contribute not only to the problem of radioactivation but also to the extent of interference with core heat transfer and pressure drop. Porous magnetite deposits on simulated fuel rods do not cause large increases in cladding temperature. Laboratory tests on open-textured magnetite of less than 100 μm thickness at a heat flux of 100 $\text{W}\cdot\text{cm}^{-2}$ showed less than a 10°C alteration of cladding temperature under BWR conditions; however, a similar deposit but impregnated with the salts normally associated with hard water showed a cladding temperature increase of up to 92°C. The surface friction factor for a crudded rod in these tests exceeded that of a

clean rod by a factor of 3.3. Both of these observations have parallels in early BWR experience when crud levels on fuel surfaces were high. In the first year of SGHWR experience, for example, copper infilling of the Fe₂O₃-based deposit occurred leading in some cases to fuel cladding failures due to steam blanketing and overheating. Subsequent operation of SGHWR with considerably reduced Cu and Ni levels in feedwater and lower overall crud input rates have led to no further fuel cladding failures, although the fuel crud thickness peaks at about 25 µm corresponding to 1.5 to 2.0 mg.cm⁻² of deposit. The porous deposits now formed have been found to assist heat transfer by what has been termed "the wick boiling mechanism".

In second-generation BWRs with reduced iron levels in the feedwater (<10 ppb) and with little or no use of non-ferrous alloys, few fuel defects have occurred due to crud. Deposition levels still vary considerably depending on design, materials and operating factors, e.g. the type of feedwater purification plant and its location or the addition of oxygen to the feedwater. An indication of the improvement in deposition levels in the more recently commissioned BWRs is illustrated by comparing data from SGHWR and the Swedish reactors. A summary of fuel crud deposition levels for various BWRs is given below :

BWR Reactor	Typical Fuel Crud Deposition Levels, mg.cm ⁻²
SGHWR	1 to 2
Swedish BWRs	0.1 to 0.5
US BWRs	<1 to 10
German BWRs	0.5 to 7.6
Japanese BWRs	0.5 to 3

4.3.4 Effects of heat transfer

Because of the strong temperature dependence of the Zircaloy corrosion process, precise description of the thermalhydraulic conditions are required [223,224]. Figure 4.3.18 gives post-transition corrosion behaviour as a function of reciprocal temperature. Results based on long-time exposure in isothermal conditions show that an approximately linear law is followed.

In power reactors or in out-of-pile loops, the heat fluxes are high enough to generate a temperature gradient from the oxide/water interface to the metal/oxide interface. In these conditions, the corrosion rates are largely influenced by the metal/oxide interface temperature according to $T_i = T_w + (\Phi S) / \lambda$ where :

T_i	: metal/oxide interface temperature
T_w	: temperature at the wall
Φ	: heat flux
S	: oxide thickness
λ	: oxide thermal conductivity.

Table 4.3.4 [225] shows the results of investigations concerning the measurement of the thermal conductivity of the oxide film. A large spread in the conductivity values is assumed to be due to a temperature dependence of the thermal conductivity.

The comparison of calculated and measured corrosion rates for claddings from PWR fuel assemblies shows that the calculation of the cladding temperature is sufficiently precise in most cases to explain the

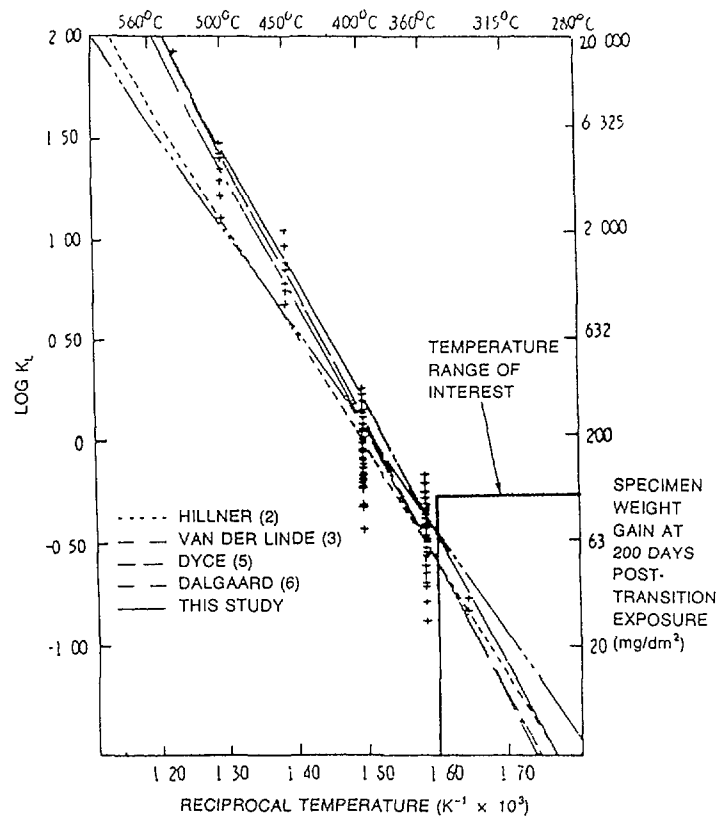


FIG. 4.3.18. Comparison of post-transition corrosion models with data.

axial and circumferential distribution of the zirconia thicknesses [211]. Nevertheless, the more corrosive chemical environment enhanced by two-phase flow conditions at the cladding wall can explain the large azimuthal variations in corrosion data observed on some PWR fuel rods. To account for these variations, corrosion models include a fitting factor F , introduced to account for reactor effects on the corrosion rate. From KWU assessment [224], typical values of F range from 0.8 to 2.8. The large scatter from reactor to reactor and from cycle to cycle could be attributed to specific physico-chemical or thermalhydraulic conditions existing in reactors such as :variations in zirconium oxide thermal conductivity, existence of additional thermal barriers due to crud, variable power histories, occurrence of nucleate boiling heat transfer and eventual irradiation effects.

Nevertheless corrosion data obtained from autoclave and out-of-pile loop tests (see Figure 4.3.19) demonstrate a marked influence of heat flux on the acceleration of the oxidation rates which does not depend entirely on the increase in the metal/oxide temperature. Based on the results obtained from the autoclave tests conducted at 360°C, the isothermal corrosion kinetics were evaluated at the mean metal/oxide interface temperature determined for materials that were subjected to the effect of heat flux in the Cirene out-of-pile loop (see Figure 4.3.20). In the same manner, in an out-of-pile loop, the isothermal area subjected to the primary coolant temperature at the coolant outlet plenum level ($T_1 = T_{sat} = 346^\circ\text{C}$), are comparable to the areas under heat flux and at an equivalent mean interface temperature (approx. 346°C), (see zones A and B in Figure 4.3.21), all other chemical conditions being equal with $[\text{Li}] = 5$ ppm and the concentrations of mineral impurities and corrosion products as specified for the primary coolant of PWRs. The corrosion rates obtained under heat flux reveal the same corrosion acceleration phenomena presented in the loop-autoclave comparison. This comparison resulted from

TABLE 4.3.4. ZIRCONIUM OXIDE THERMAL CONDUCTIVITY DATA

Manner of oxide formation	Oxide thickness (μm)	Thermal conductivity (W/cm·K)		Experimental method
		25–120°C	260–400°C	
ZrO ₂ stabilized with CaO 35.5–87.7% TD	—	0.0167	0.0176	
Oxidized in 360°C water	1–2	0.014 ^{+0.029} _{-0.011}	—	Calorimetry
Zr ₂ oxidized in 400°C steam	1.7–11.6	0.021 ^{+0.017} _{-0.013}	—	
Oxidized in 300°C water 1.25 mol/kg LiOH solution	19	0.0076	—	Calorimetry
Oxidized in 450°C steam	54	0.0088	0.063	
	19	0.0070	0.0545	
Oxidized in 450°C air	53	0.0107	0.0627	
	34	0.0120	0.0400	
Not given except done in steam at high temperature	135	0.013	0.009	Diffusivity
	20	0.003	0.0015	
	22		0.0093	
Stabilized with 5% CaO (5.2 g/cm ³)	—	—	0.027	—
ZrO ₂ sprayed onto tungsten	<700	—	0.006	Calorimetry
ZrO ₂ (5.35 g/cm ³)	—	—	0.019	—

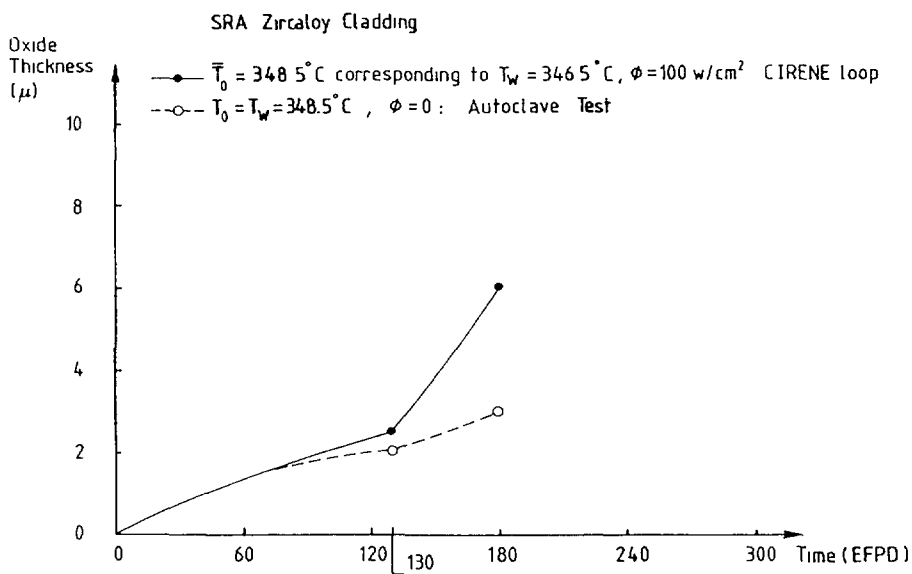


FIG. 4.3.19. Comparison of the corrosion kinetics of Zircaloy assessed in autoclave and in Cirene loop at the same average metal/oxide temperature.

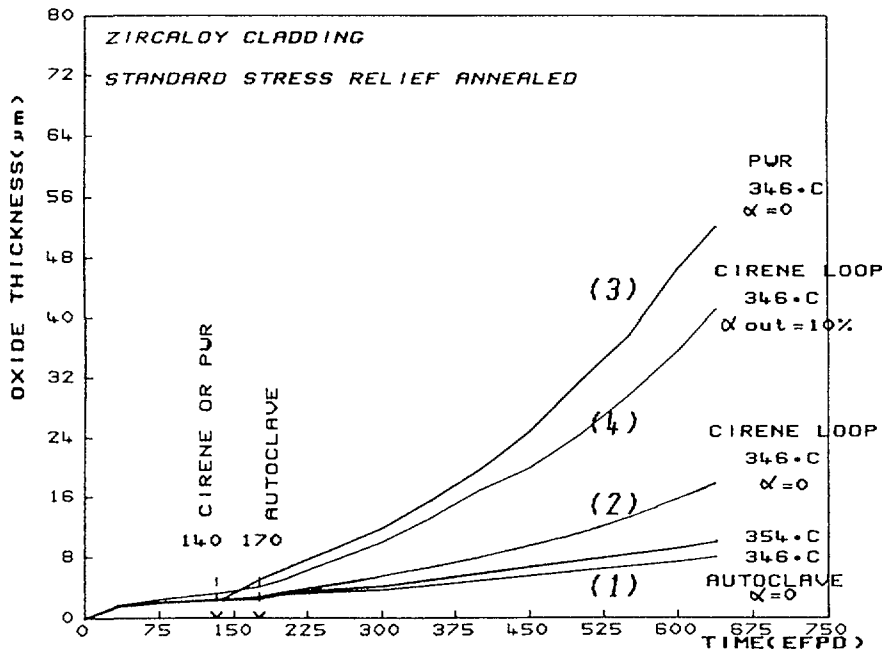


FIG. 4.3.20. Corrosion kinetics - comparison of facilities.

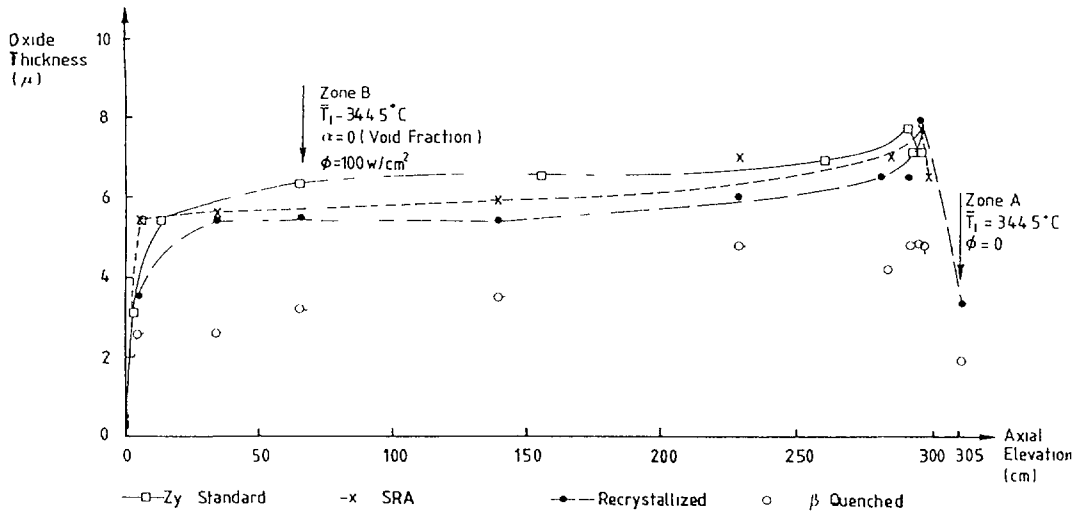


FIG. 4.3.21. Corrosion profile in out-of-pile loop.

metallographic examinations of specimens corroded in out-of-pile loops or in autoclaves.

Thus it appears that there is an apparent acceleration of Zircaloy corrosion under heat flux (Φ). Heat flux apparently acts as an additional driving force in the vacancy diffusion causing the acceleration of the corrosion kinetics with respect to those obtained in isothermal conditions [226]. This thermal gradient effect is predominant in the acceleration process of the oxidation kinetics in the presence of "high" lithium concentration in the primary coolant. This effect was observed from "short" (60 EFPD) corrosion tests with $[\text{Li}] \approx 70$ ppm. Once again, the effect of the heat flux is not limited to the temperature rise alone in the metal/oxide interface. A synergistic effect between heat flux and LiOH concentration at the water/oxide interface is observed.

An increase in the lithium concentration at the wall of the cladding can be due to boiling conditions. Then, under two-phase flow heat

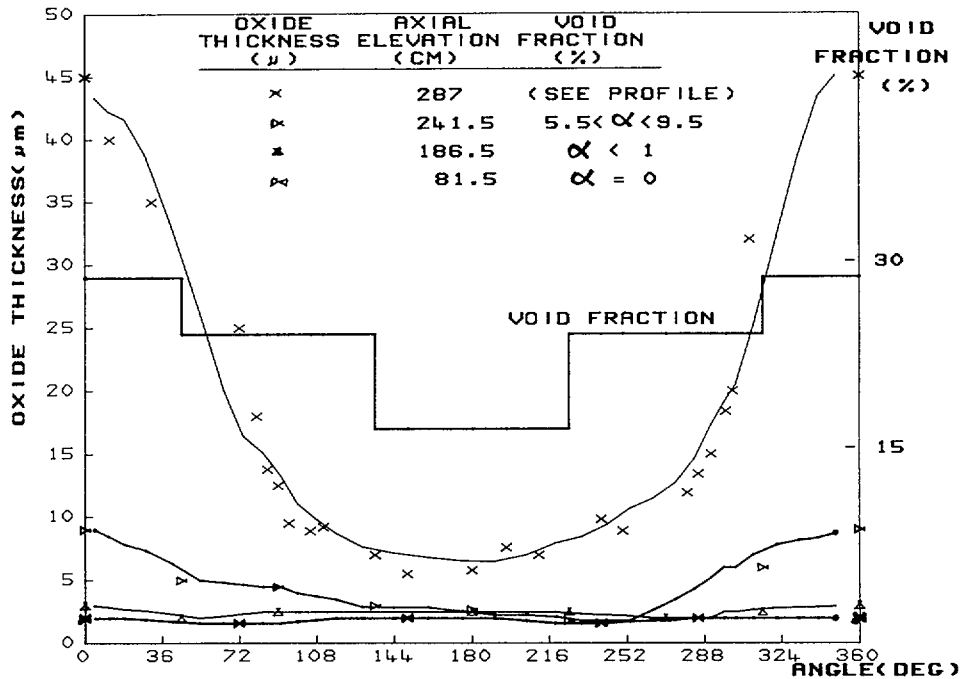


FIG. 4.3.22. Azimuthal corrosion profile in the Cirene loop.

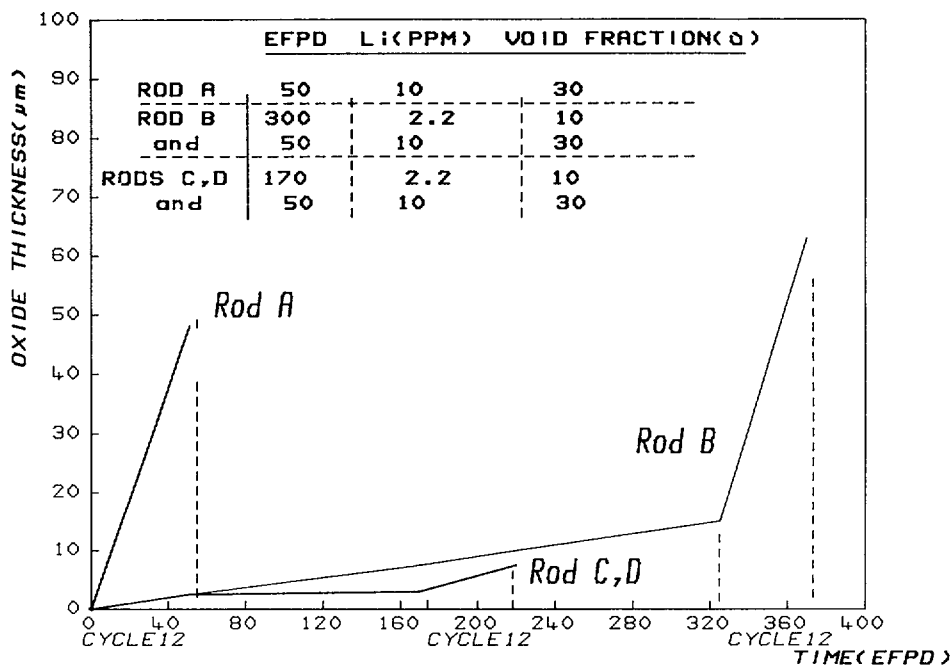


FIG. 4.3.23. Corrosion kinetics - effects of additives.

transfer, heat flux and Li-enrichment at the water/oxide interface constitute a potential acceleration mechanism. Consequently, the Zircaloy claddings subjected to local boiling present higher corrosion rates (see Figures 4.3.20 and 4.3.21).

In particular, the circumferential variations in oxide thickness were related to the void fraction azimuthal distribution along the rod sections (due to hydraulic diameter variations as illustrated in Figure 4.3.22).

In addition, Zircaloy cladding subjected at the beginning of life to boiling conditions undergoes shorter transition times and, subsequently,

faster post-transition corrosion kinetics. The oxidation kinetics increase with the increase in the void fraction. The absence of a pretransition state, with an oxide film of higher porosity, may occur in the case of high void fractions ($\alpha = 30\%$) and can be attributed to the alkalinity and high lithium level at the metal/coolant interface due to the vapor phase ($[\text{Li}] > 10$ ppm), see Figure 4.3.23. Nevertheless, the oxide layers formed under PWR conditions ($[\text{Li}] < 2.2$ ppm) up to thicknesses of $3 \mu\text{m}$ (pretransition state), significantly protect the cladding from a boiling-induced acceleration of corrosion kinetics. Beyond the data at 3 to $5 \mu\text{m}$ as shown in Figure 4.3.23, this protective effect tends to disappear when the zirconia layers become thicker and grow in the post-transition state. The increase in zirconia porosity up to the metal/oxide interface after the transition is the cause of the increased incorporation of lithium and the acceleration of corrosion kinetics.

4.4. METALLURGICAL AND CHEMICAL VARIABLES

4.4.1. Fabrication variables

The primary metallurgical factors that affect the corrosion resistance of the Zircalloys are the size and distribution of the second phase particles, and the amount of residual strain in the α -Zr lattice [227]. The components of these particles (Fe, Cr, Ni) have solubilities in α -Zr that are less than or comparable to, the common impurity levels (especially for Fe) found in unalloyed zirconium. Therefore, the major fraction of these alloying elements is always present as precipitates, and the possibility of maintaining them in solid solution by quenching, as opposed to forming submicroscopic precipitate nuclei, requires quenching rates of the order of 1500 K.s^{-1} (i.e. much higher than in any commercial process). Laboratory testing has not shown any large variations in corrosion resistance over the range of fabrication treatments commonly used to produce fuel cladding. However, early work showed that slow cooling through the ($\alpha + \beta$) phase field led to gross segregation of the transition metals to grain boundaries and triple points because of the preferentially high solubility of these elements in β -Zr and their very low solubilities in α -Zr. Such treatments were detrimental to the corrosion resistance below a critical cooling rate through the ($\alpha + \beta$) phase field [10]. β -quenching to homogenize the alloy at the ingot or billet stage has long been known to be generally advantageous from the corrosion point of view. However, the observation that nodules did not nucleate on welds or heat-affected zones in either fuel channels or cladding in BWRs [228] led to the investigation of ($\alpha + \beta$) or β -quenching at a late stage in the fabrication procedure as a method for significantly reducing nodular corrosion problems in BWRs.

Such β -quenched or $\alpha + \beta$ quenched cladding is now the commonly recommended metallurgical form for BWR cladding. The implication that β -quenched cladding might also offer advantages in PWRs proved to be incorrect, such cladding generally shows the worst behaviour of any fuel cladding under these water chemistry conditions (Figure 4.4.1)[229]. In other metallurgical conditions with various degrees of stress relief, up to and including complete recrystallisation, intermediate behaviour is observed. Although the data are plotted in Figure 4.4.1 versus intermetallic size, it is not established that this is the only important factor controlling this behaviour. Lattice strain is another factor that varies considerably over the range of commonly used fabrication variables, and that may be as important as precipitate size and separation in affecting the corrosion behaviour.

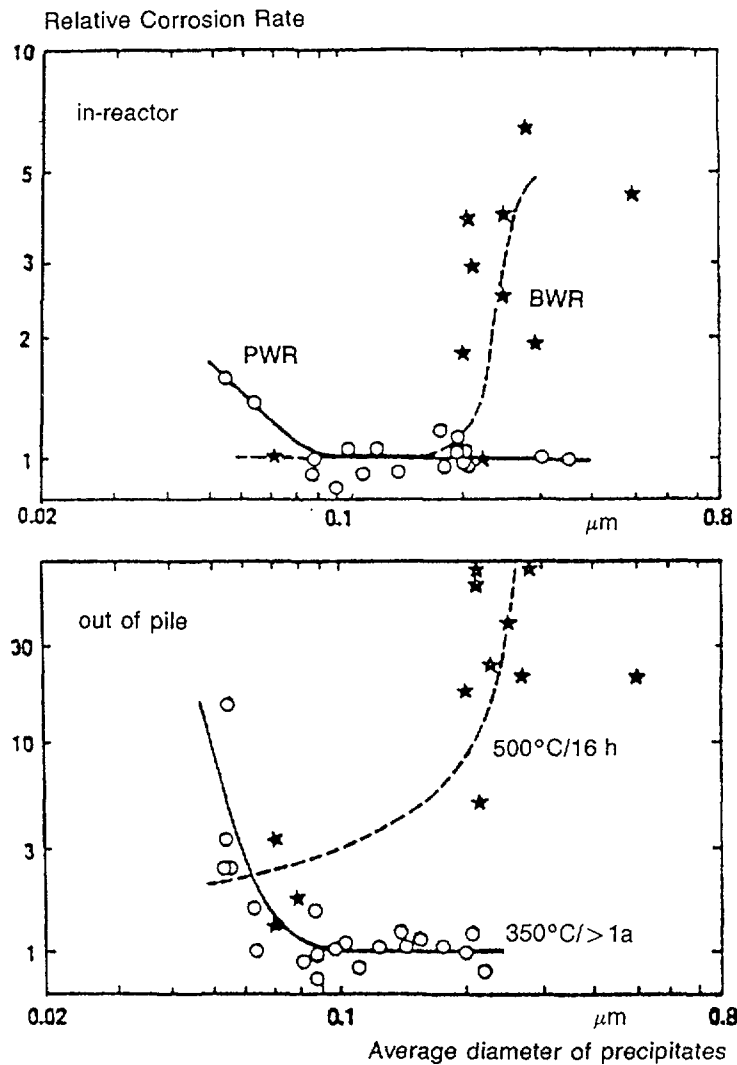
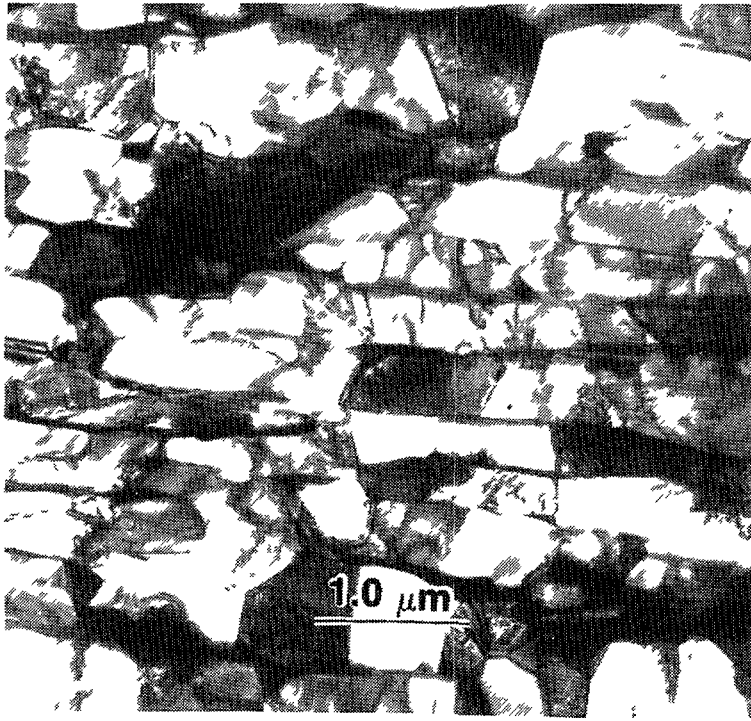


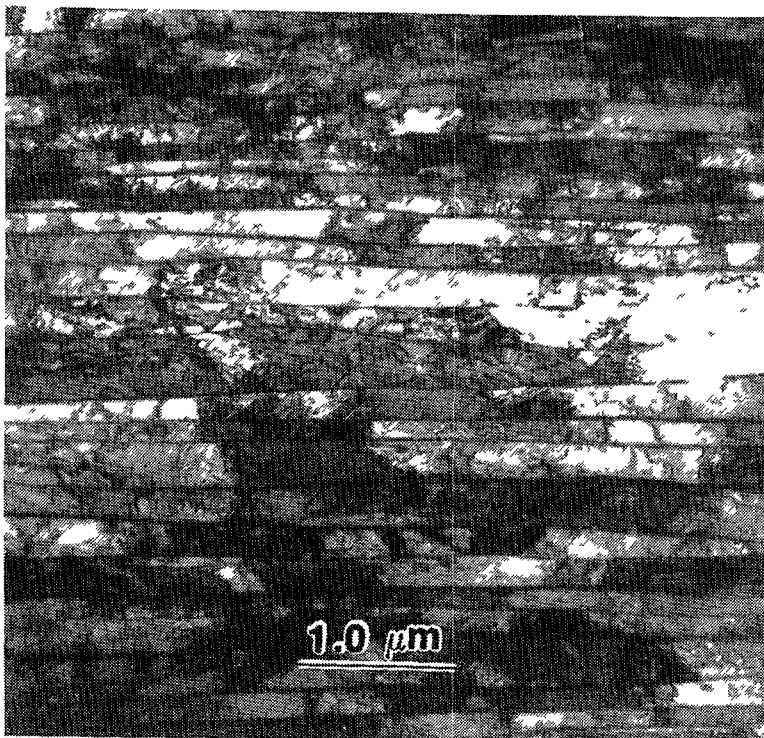
FIG. 4.4.1. Corrosion of Zircaloy versus size of intermetallic precipitates. In general, β quenched material lies to the left of this distribution, and recrystallized material is on the right [221].

The question of whether nodular corrosion in BWRs nucleates at intermetallic particles, between intermetallic particles, or as a collective property of a group of grains, has yet to be resolved [45,46]. The resolution of this question will have a big effect on our understanding of the response to changing metallurgical variables of the corrosion resistance of the Zircaloys, since final annealing can change factors such as lattice strain without significantly changing the particle size and distribution. However, up to the temperatures used in tubing fabrication, it results in only small effects on the texture, which is the cumulative product of the various sinking and wall thinning operations performed in the earlier stages of fabrication. Thus a knowledge of the initiation mechanism, for nodular corrosion is essential if changes in fabrication routes are to be made on a rational basis.

In the case of Zr-2.5 Nb pressure tubes the fabrication variables affect primarily the size, distribution and phase composition of the residual β -phase [230]. In the cold-worked (C.W.) condition the corrosion and hydrogen uptake properties in CANDU water chemistry appear to be better than for the heat-treated (H.T.) alloy (usually an $(\alpha + \beta)$ quench, followed by cold-reduction and a final age at $\sim 500^\circ\text{C}$) [33]. The reason for this appears to be the continuous film of β -Zr(Nb), left along α -Zr grain boundaries following extrusion, that is not decomposed by the C.W. treatment followed by the usual 400°C stress relief (Fig. 4.4.2).



(a) as extruded the elongated α grains contain few dislocation networks



(b) extruded and cold worked 25%. The elongated α grains with a high dislocation density

FIG. 4.4.2. Typical microstructures of Zr-2.5 Nb pressure tubes showing the α grains elongated in the axial direction.

This structure should be compared with the discrete β -Nb precipitates produced in the H.T. alloy. Ageing in reactor results first in the breaking-up of this continuous β -Zr phase, and ultimately in its decomposition to β -Nb [231]. This ageing process reduces the short-term corrosion and no effect on the long-term corrosion properties has yet become evident [231]. Re-exposure of irradiated samples has confirmed that both thermal and irradiation ageing have equivalent effects on the corrosion process.

4.4.2. Behaviour of alloying additions

(a) Incorporation in the oxide film

It is generally believed that both the segregation and the uniform incorporation of alloying additions that has been observed for various different species in the laboratory will persist unchanged in reactor. Virtually no work has been done to support this contention.

(b) Effect of distribution

The distribution of the alloying additions, particularly in the form of intermetallic precipitates, is of great importance in the corrosion behaviour of zirconium alloys such as the Zircalloys. In the laboratory, heat treatments that redistribute and cause Ostwald ripening (growth of large precipitates at the expense of small ones) of the intermetallic particles have a major effect on the corrosion resistance [232]. In particular, slow cooling through the ($\alpha + \beta$) phase region causes segregation to the residual β regions along α grain boundaries, and results in poor corrosion resistance. By comparison, homogenising the additions by a β -quench is good for the corrosion resistance if performed at the ingot or billet stage [233], but is not necessarily good when performed at a later stage in the fabrication, as we have seen in the previous section. Thus, such β quenched material has the best nodular corrosion resistance in BWR conditions, but the worst uniform corrosion resistance in PWR conditions. Other, metallurgical treatments giving a range of stress relief through to full recrystallization show intermediate behaviour, with full recrystallisation being the worst condition in BWRs, with more or less opposite behaviour in PWRs [229]. These differences seem to be related to a combination of precipitate size, distribution, texture and lattice strain effects.

If prolonged irradiation causes dissolution of small precipitates and loss of Fe preferentially over Cr from larger precipitates (with amorphisation of the residual precipitates [126,143,171,172], then highly irradiated cladding may have a different intrinsic corrosion resistance to as-received cladding. Since in-reactor corrosion rates are always compared with laboratory results on as-received material any differences observed cannot be ascribed to a direct instantaneous effect of irradiation, but may incorporate effects resulting from the redistribution of the alloying elements by irradiation. This concern has yet to be addressed by post-irradiation laboratory testing of highly irradiated material. Early results showing no post-irradiation effect on the corrosion of irradiated but unoxidized Zircaloy specimens was based on lightly irradiated material not irradiated highly enough to cause precipitate amorphisation and dissolution [234]. Post-irradiation corrosion of samples from irradiated LWR cladding [223] showed an increasing duration for the memory-effect with increasing oxide thickness formed under irradiation (Figure 4.4.3). Only the highest irradiated sample did not return to the expected out-reactor rate after long post-irradiation exposure, and the remaining increment over the expected rate for an unirradiated specimen may be the result of changes to the precipitate structure in the matrix.

In the case of Zr-2.5 Nb alloy material in the commonly used cold-worked condition, the residual β -Zr phase is metastable, and ageing occurs even in the laboratory at temperatures down to $\sim 300^\circ\text{C}$, albeit slowly at $\leq 400^\circ\text{C}$ [231]. Irradiation enhances this ageing, which comprises diffusion of Zr out of the β -Zr(Nb) phase to leave precipitates of β -Nb, and this has been argued to be the cause of the often observed

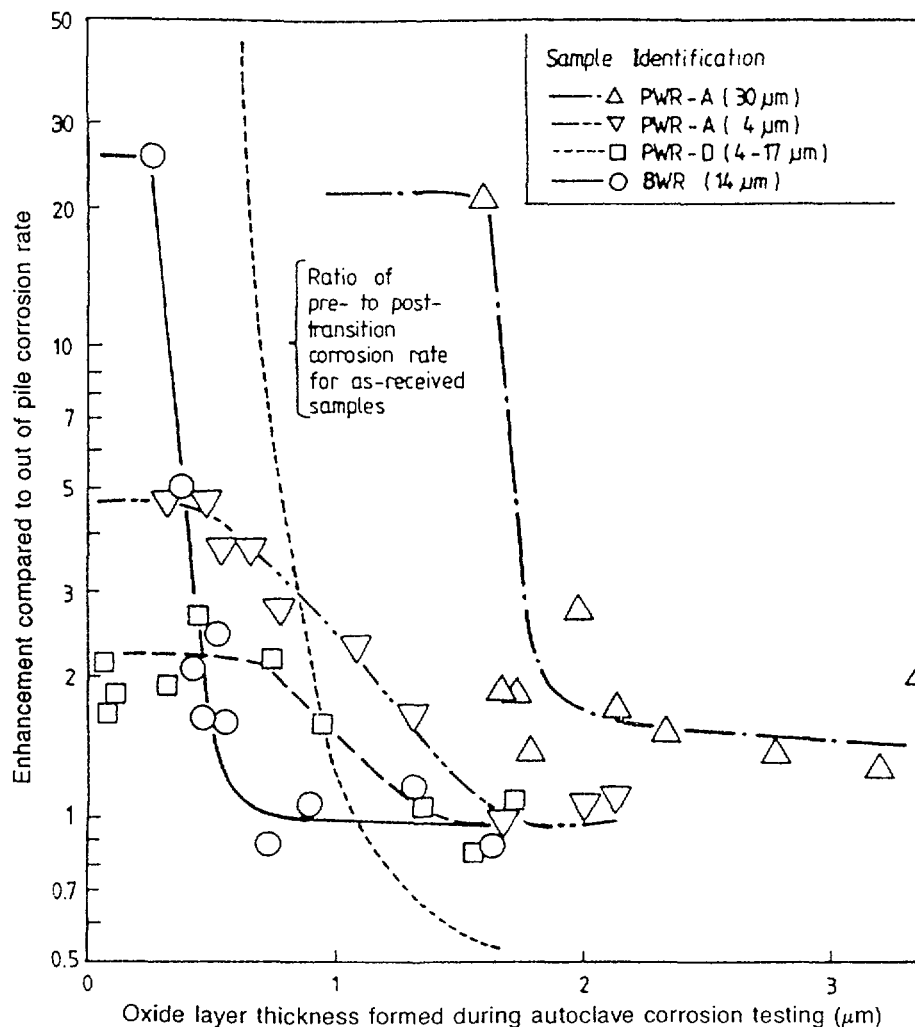
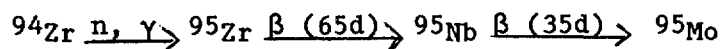


FIG. 4.4.3. Summary of post-irradiation autoclave corrosion tests [223].

better corrosion resistance of Zr-Nb in reactor than in laboratory autoclave tests [96]. Corrosion resistance is observed to increase with prolonged low temperature ageing in the laboratory [235]. Testing of pre-irradiated Zr-Nb specimens in the laboratory has confirmed the validity of this hypothesis [236].

(c) Transmutation effects

Prolonged irradiation, even of low neutron capture cross section elements, can produce significant quantities of new impurities by transmutation of the pre-existing components of the system. Irradiation of zirconium results in small quantities of niobium and molybdenum being produced, and irradiation of Zr-2.5 Nb alloy specimens produces enough molybdenum during the lifetime of a pressure tube for the alloy to become a Zr-2.4 Nb-0.2 Mo alloy. It is not known at present whether such end of life effects can have a significant impact on the corrosion resistance of the alloy, but there is sufficient concern for investigation of such effects to be in progress. None of the possible transmutations of alloying additions in Zircaloy ($^{54}\text{Cr} \rightarrow ^{55}\text{Mn}$; $^{58}\text{Fe} \rightarrow ^{59}\text{Co}$; $^{58}\text{Ni} \rightarrow ^{58}\text{Co}$; $^{62}\text{Ni} \rightarrow ^{63}\text{Cu}$; or $^{120}\text{Sn} \rightarrow ^{121}\text{Sb}$) will produce enough product to be of concern. Transmutation of zirconium to molybdenum by the sequence: -



may reach 0.2 Mo in a Zr-2.5 Nb alloy pressure tube after 20 years

($\sim 1.3 \times 26 \text{ n.m}^{-2}$). Experiments to look for effects from such transmutation are in progress.

4.4.3. Electrochemical effects

The electrochemistry of zirconium alloys in high temperature water (or dilute solutions) has not been extensively studied. Thus, it is not known whether and to what extent polarisation affects the corrosion rate, nor do we know anything about the electrochemical surface reactions that participate in the overall oxidation process. Since they do not appear to be rate limiting, studies of these reactions are notable for their absence, although some early room temperature electrochemical studies were performed. Polarization experiments in fused nitrate melts in the laboratory at 300°C [28] show little effect of either anodic or cathodic polarization on the oxidation rate, confirming the supposition that it is largely controlled by processes within the pre-transition oxide layer (Fig. 4.4.4).

With this experience in the absence of irradiation, it has been surprising to find that repeated examples of electrochemical and galvanic effects on corrosion rates in BWR conditions are appearing. These examples (already cited and referenced in Section 2) comprise:

- The appearance of "shadows" of the control blade handles in the nodular corrosion distribution on the adjacent fuel channels.
- The preferential formation of nodules on fuel cladding under the stainless steel spacer grids used in some fuel bundles. The same effect is not seen under zirconium alloy grids.
- The formation of ridges of thick oxide on the pressure tube adjacent to the stainless steel grids of the fuel cladding in SGHWR and RBMK reactors.

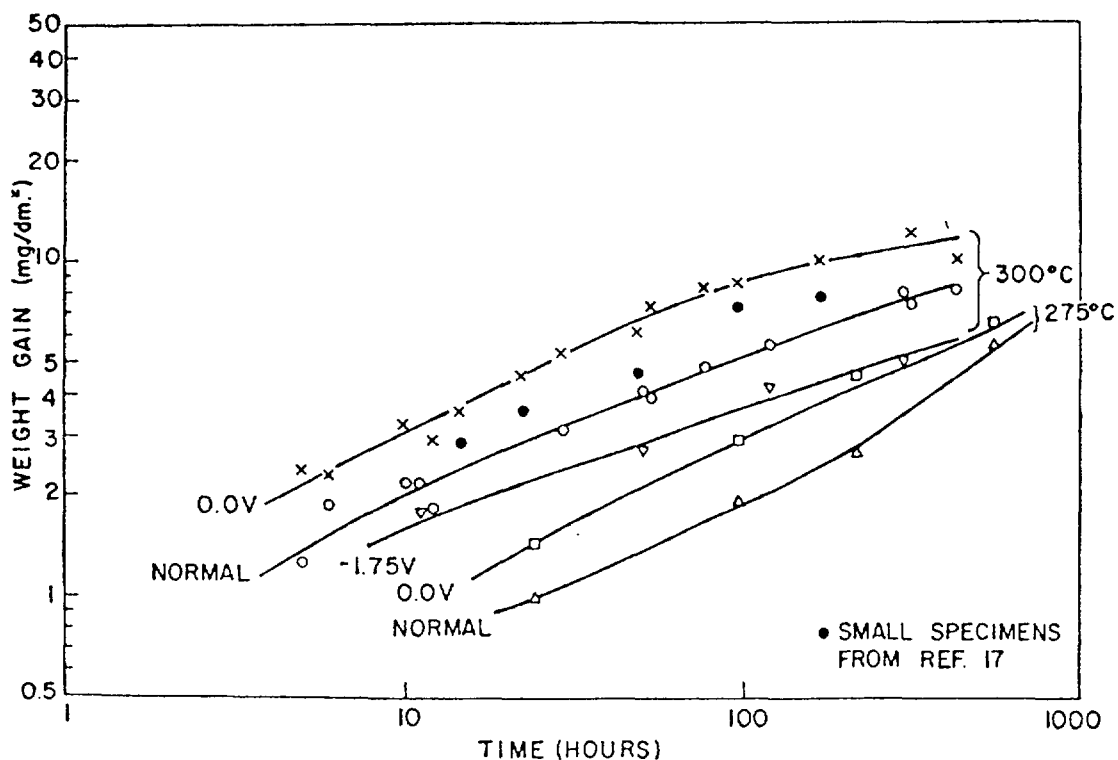


FIG. 4.4.4. Weight gain versus time curves for zirconium specimens biased during oxidation in fused salt at 275 and 300°C [28].

TABLE 4.4.1. POTENTIALS MEASURED IN BWR COOLANTS

Reactor	Location	Electrode	Potential of electrode (V-SHE) for Hydrogen Addition (ppm)				
			0	0.4	0.8	1.2	1.6
NMP-1	Recirc. Line	304 SS	0.06	0.01	-0.08	-0.23	-0.52
PB-3	"	"	-	-	-	-0.32	-0.36
Hatch	"	"	0.13	0.08	-0.03	-0.36	-0.37
Pilgrim	"	"	0.10	-0.02	-0.25	-0.52	-0.59
Nuclenor	"	"	0.01	-0.43	-0.47	-0.48	-0.49
Fitzpatrick	"	"	0.02	-0.52	-0.55	-0.57	-0.58
Duane Arnold	"	"	0.07	-0.58	-0.60	-0.62	-0.63
NMP-1	*LPRM (middle)	"	0.18	-	-	-	-
NMP-1	" (top)	"	0.21	-	-	-	-
NMP-1	" (middle)	Pt	0.15	-	-	-	-
NMP-1	" (top)	"	0.23	-	-	-	-
Duane Arnold	" (bottom)	304 SS (vs Ag/AgCl-1)	0.26	0.18	-0.05	-0.24	-0.32
Duane Arnold	" (top)	" (vs Ag/AgCl-1)	0.28	0.22	0.09	-0.05	-0.12
Duane Arnold	" (top)	" (vs Ag/AgCl-2)	-	0.19	0.13	0.06	0.02
Duane Arnold	" (bottom)	Pt	0.26	-0.26	-0.32	-0.38	-0.42
Duane Arnold	" (top)	"	0.18	-0.10	-0.22	-0.29	-0.32
Fugen [242]	Autoclave (inlet header)	304 SS	-0.03	-	-0.13	-	-0.15
Fugen [242]	"	Pt	-0.20	-	-0.48	-	-0.50

* In-core measurements in local power range monitor (LPRM) housings.

- The local spots of thick white oxide at points of contact with the Inconel springs in Zircaloy spacer grids.
- The thicker oxide on plena of segmented rods in the high flux region compared with the fuelled region of the same rod.

All of these phenomena can be fitted into a single mechanistic framework if these effects are related to local electrochemical (redox potential) or galvanic conditions. However, no supporting evidence or experimentation is available at present. The various effects that might be involved will be discussed separately.

(a) Redox potential of aqueous systems

The redox potential of an aqueous system in a laboratory test is determined primarily by the hydrogen to oxygen ratio derived from overpressures of these species, in the absence of dissolved variable valence (or easily reducible) ions. In a BWR, where these effects seem to appear primarily, the equivalent redox potential of the water is also affected by the radiolytic production of species with different oxidizing or reducing properties, and by the partitioning of volatile molecular species into the steam phase. The net effect is that the equivalent redox potential of the reactor water can be expected to vary along the length of the core from inlet to outlet, and to be different again in the downcomer and external piping where recombination of radiolytic species can be expected. Thus, we might expect electrochemical effects to show as peaks in nodular corrosion that follow the calculated peaks in concentration of some of the prominent radiolytic species.

The difficulties of inserting stable electrodes into a system operating in high temperature water at 300°C, let alone into the high flux region of a reactor, has meant that few such measurements have been reported. Some measurements in the downcomer and recirculation piping of BWRs do show significant variations with location (Table 4.4.1) and from plant to plant together with the expected effect of hydrogen additions (HWC). However, measurements in-core show that the effectiveness of HWC may not extend throughout the core region of the reactor [237].

(b) Irradiation induced currents

When considering the local potential of the Zircaloy cladding and other adjacent components we should not ignore the induced currents caused by the irradiation fluxes. In many ways a reactor fuel pin is like a large self-powered flux detector. The UO_2 is the emitter and the cladding is the collector. However, to the extent that charged particles (β and primary knock-on particles) pass through the cladding or its protective oxide film from either side they represent an electrical current that must be factored into the overall polarisation currents experienced by the oxide film. In addition to this primary flux of charged particles induced by the fast neutron flux flowing outward from the centre of the fuel rod, there are several sources of secondary current. Recoiling protons from the water provide a significant flux through the thin oxide films (proton energies can be up to ~ 3 Mev), and, although the quantity of hydrogen injected as a fraction of the total hydrogen absorbed from the corrosion reaction is negligible, the current represented by this flux cannot be immediately dismissed as negligible. A further source of polarizing current is the flux of Compton electrons resulting from γ -ray absorption in the Zircaloy, the oxide film and the adjacent water. Because of the different densities, and absorption cross-sections, of the phases, these fluxes will not be equal

and there will probably be a net flux of electrons out of the cladding surface which would be equivalent to an effective anodic polarizing current.

Although we cannot accurately assess the magnitude, or even the direction, of the overall polarizing current on the basis of present evidence, we can conclude in a qualitative manner that the current will vary with the local flux spectrum. Thus, changes in the balance between β , γ and neutron fluxes as for instance over a plenum, or over Gd/UO₂ pellets compared with over UO₂ pellets, would be expected to cause small differences in the surface potential of the oxide at these locations. This offers a possible explanation for the observed differences in nodular corrosion coverage and thickness that occur at the various locations cited above (e.g. high nodular coverage of plena in high flux positions compared with the adjacent fuelled region).

(c) Effect of intermetallics

Although nucleation of nodules at a subset of the intermetallic particles present in the cladding surface has been postulated, other sites for nodule initiation have been proposed, and there is no evidence that currently distinguishes these possibilities in any unequivocal fashion. However, the absence of nodular corrosion of alloys, such as Zr-2.5 Nb, that are free from Zr₂Fe precipitates, (when iron impurity levels are low), and the appearance of nodular corrosion where iron is deliberately added, strongly suggests nucleation at intermetallics. This is only circumstantial evidence, however, and work to resolve the question is in progress. If this work should conclude that nodular corrosion nucleates at intermetallics, we would still need to establish a mechanism by which this might occur, and selection rules to predict why only a small fraction of intermetallics nucleate nodules in conventional stress-relief annealed (SRA) tubing, and why no intermetallics are capable of nucleating nodules in β -quenched tubing.

The most probable selection rule would relate the extent of the local cathodic potential shift at the intermetallic to its size, composition and the thickness and nature of the oxide formed on it. Work in this area could be very fruitful. A preliminary experiment in which two lengths of chemically polished fuel cladding (one SRA and one β -quenched) were coupled to a platinum electrode in a dilute CuSO₄ solution at room temperature showed that on the SRA sample a small number of surface sites were sufficiently cathodic to reduce cupric ion to copper and deposit it on the surface; no such sites were observed on the β -quenched sample. A similar process occurring in high temperature water, before a thick oxide formed on the intermetallic site, could provide a permanent local cathode on the surface that could depolarize the anodic process locally and permit enhanced local oxide growth to form a nodule. Such an hypothesis would satisfactorily explain other features of nodular corrosion, for instance, the apparent nucleation of nodules only during a short period immediately after the start of exposure in-reactor, and the tendency for a greater frequency of nodule nucleation on similar batches of cladding in high Cu plants (high Cu concentration in the reactor water) when compared with low Cu plants.

(d) Galvanic effects

A number of phenomena that may be ascribed to galvanic contact with dissimilar metals have been seen in BWRs. In general the extent of good electrical contact between the various components of the system is not known, since the degree of insulation provided by oxide films on the

contacting surfaces is difficult to predict in the high radiation fields that are present. However, if we assume that oxide films become tolerably good conductors under these conditions, and that even high purity water has a reasonable conductivity in-reactor (thought to be close to that of a pH5 solution). The observations that can plausibly be ascribed to galvanic contact, combined with a short current path through the water have already been noted in the introduction to this subsection.

Taken together these observations indicate a major effect of galvanic coupling on the corrosion rate, even though no actual measurements of potentials, or polarization by stainless steel have been made in reactor. In BWRs where nodule nucleation may be occurring during the first one hundred days (or less) of in-reactor exposure the use of an autoclaved cladding surface may provide an initially oxidised surface that is less susceptible to local effects (e.g. of water chemistry) if the operating conditions depart significantly from the norm at the start of a reactor cycle. The abandoning of pre-autoclaving as a routine surface preparation may, therefore, leave fuel cladding more susceptible to water chemistry transients at the start of a cycle, until a normal oxide film has grown in-reactor. Oxide film resistivity measurements on oxidised Zircaloy-2 specimens [238] suggest that an average oxide thickness of $\sim 1 \mu\text{m}$ must be reached before the intermetallics are oxidised enough to give resistivity greater than $10^6 \Omega\cdot\text{cm}$. While this thickness is close to that reached during a pre-autoclaving at 400°C , it would take >100 days to reach the same oxide thickness on a freshly pickled surface at 280°C [18]. Thus susceptibility to nodular corrosion could last for a hundred days or more because of this much slower formation of the protective oxide at 280°C than at 400°C (the usual autoclaving temperature).

4.4.4. Effects of surface treatment of zirconium alloy components

Chemical polishing (in mixed nitric/hydrofluoric acids) of zirconium alloy surfaces was introduced early in the development of these alloys as a means of obtaining reproducibly good corrosion behaviour. However, consistent care with neutralising (stop bath) and washing after pickling are needed to prevent enhanced oxidation from "pickle staining" if residual fluoride were to be left on the surface. There has, therefore, been a desire to avoid this costly and risky operation.

Over the years a change has progressively been made by many fuel vendors from the standard chemically polished and autoclaved (400°C steam) initial surface for fuel cladding, firstly by eliminating the autoclaving treatment, and subsequently by substituting belt-ground surfaces for chemically polished ones. Although tests in high pH solutions in the laboratory suggest that such changes might lead to significant changes in the corrosion of the surfaces, no significant differences have been reported in pH10 (at RT) solutions in laboratory autoclave tests. The assumption has been made therefore, that such changes in surface preparation cause no deleterious effect on the long-term corrosion of the cladding. Other effects such as variability between batches of cladding may have obscured any effects that are present, but it cannot be assumed on present evidence that such effects will be absent. Surprisingly variable results for belt-ground surfaces in laboratory autoclave tests have been reported [239], and lead to the suspicion that perhaps these surfaces are more susceptible to contamination during preparation than pickled surfaces.

Investigation of the effect of surface preparation on the results of 500°C high pressure steam tests [240] has shown little difference between ground and pickled surfaces. Preoxidation by autoclaving at $300\text{--}400^\circ\text{C}$ or

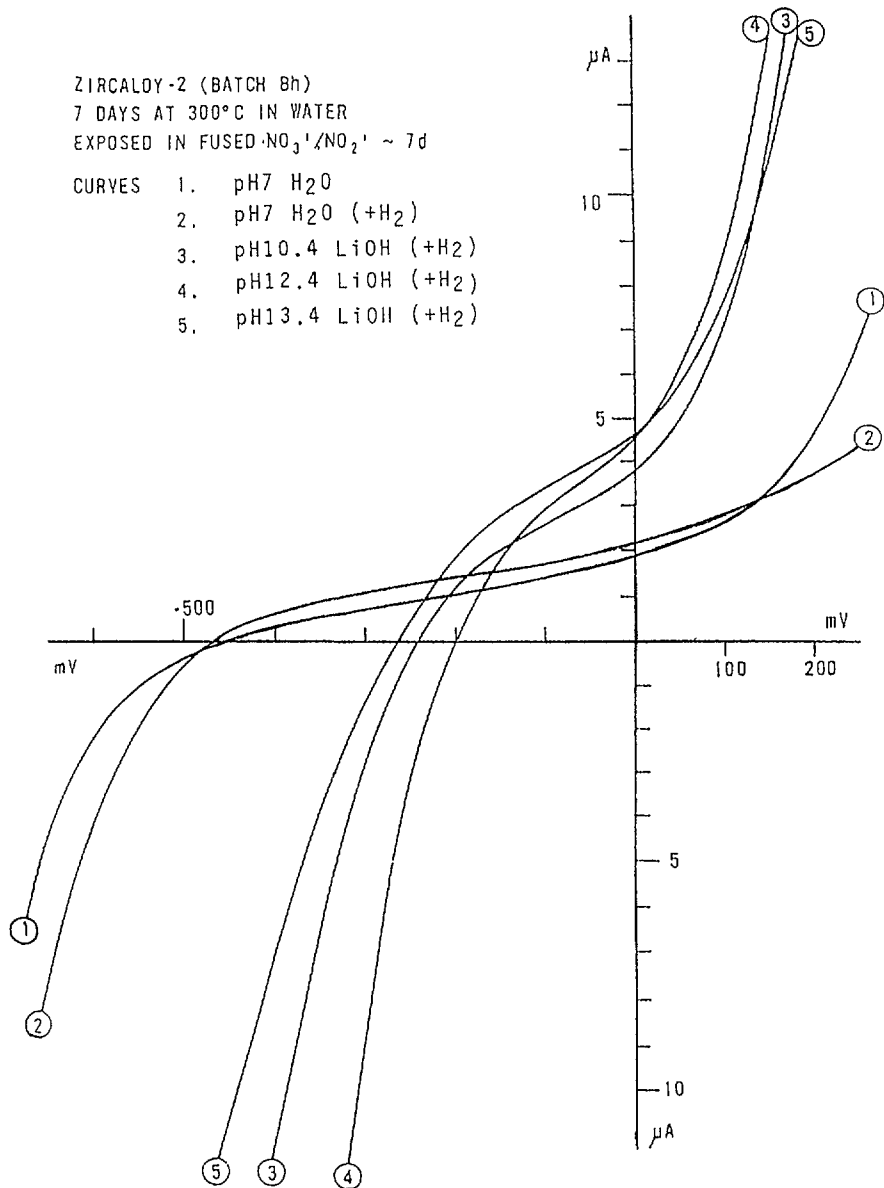


FIG. 4.4.5. Polarization curves in fused salt at 300°C measured on oxide films formed in water or LiOH [241].

by anodic oxidation delayed the nodular attack significantly, but did not prevent it. The delay in nodule nucleation was dependent on oxide thickness rather than mode of formation.

Despite the absence of any apparent differences between corrosion weight gains in pH7 and pH10–12 (at RT) solutions at 300°C, studies of the polarisation curves (measured in fused salt at 300°C) of specimens oxidised in these LiOH solutions show differences (Figure 4.4.5). These results show that (at a point where the specimen weight gains were all essentially equal), the oxides formed in Li⁺ containing solutions were all much more electronically conducting than oxides formed in neutral water. Thus, lithium incorporation in thin oxide films can apparently affect their electrical properties under conditions where it has not yet caused accelerated weight gains (Figure 4.4.6)[241].

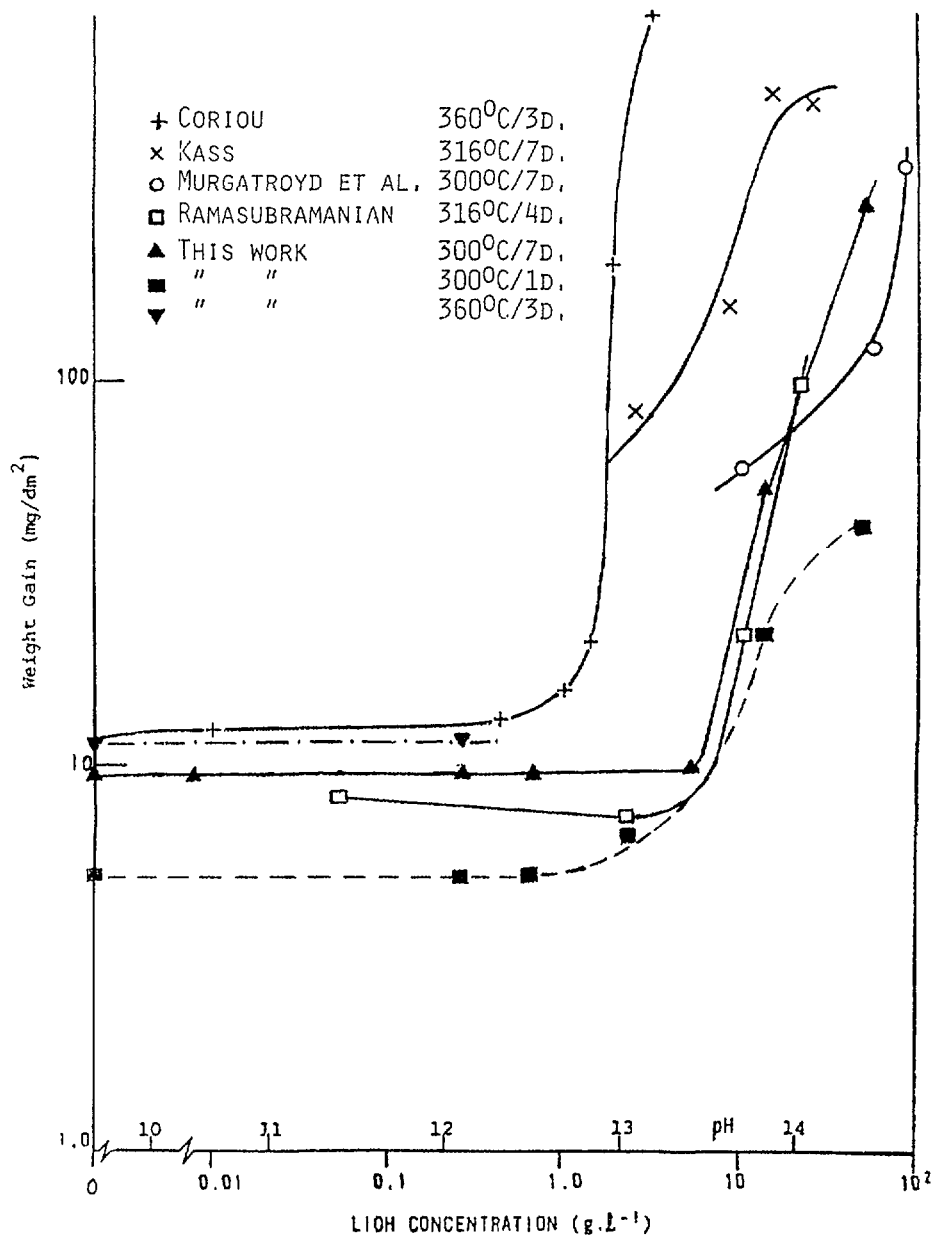


FIG. 4.4.6. Weight gains of Zircaloy specimens oxidized in LiOH at various concentrations and temperatures [241].

5. PRESENT STATUS OF THE MECHANISTIC UNDERSTANDING OF THE EFFECTS OF IRRADIATION

The extent of our understanding of behaviour under irradiation is still limited by the unknown factors that influence oxidation and hydrogen absorption in the laboratory. Before discussing the irradiation behaviour, therefore, it is appropriate to summarise the status of the mechanistic understanding of behaviour in the laboratory.

5.1. CURRENT UNDERSTANDING OF THE OUT-REACTOR OXIDATION MECHANISM

5.1.1. Mobile species

It is generally accepted that oxygen is the most mobile species in the zirconium oxide film formed on commercial alloys [243], and that at low temperatures diffusion of oxygen along crystallite boundaries predominates over lattice diffusion [11,12]. It is usually assumed that O^{2-} is the diffusing species, and evidence for the mobility of OH^- is presently lacking. The evolution of the oxide microstructure, described in the next section, clearly requires that there be some mobility of the zirconium ions. However, no successful measurement of this quantity has been reported [244], and it is presumed, therefore, to be very low.

The mobility of hydrogen in the zirconia lattice is now, generally, conceded to be very low [245]. Early reports claiming high diffusion coefficients for hydrogen in zirconia films almost certainly studied migration through major flaws or cracks in the oxide that were induced by the experimental techniques. Recent work using nuclear reaction techniques [92], and implanted hydrogen, confirm the low diffusion coefficients for hydrogen in zirconia that have been deduced from hydrogen uptake rates. This low diffusivity of hydrogen in zirconia is supported further by the low jump frequencies shown in nuclear magnetic resonance (NMR) studies of oxide films formed in steam [246].

The nature of the mobile hydrogen species in zirconia remains to be established, but proton hopping between OH^- groups appears to be the most probable. Early arguments for H^- and other possible species can probably be discounted because of the basic methodological flaws in this early work [75,247]. Nevertheless, if hopping between OH^- groups is the mechanism then the concentration of such species must be very low since attempts to identify OH^- frequencies in the infra-red spectrum have not been successful [248], even with the most recent Fourier transform infra-red (FTIR) techniques. This implies a very low OH^- concentration in zirconia films which is in conflict with the high H or D concentrations that have sometimes been measured in such oxides by (SIMS) Secondary-ion mass spectrometry or nuclear reaction analysis (NRA) techniques [249,250]. These latter techniques, however, do not demonstrate that the hydrogen measured in the oxide is capable of diffusing into the metal, or that it is other than surface OH^- groups on the walls of pores or cracks in the oxide. If it were merely the latter, however, the stability of T in ZrO_2 against exchange with the atmosphere is surprising [245]. There is still much scope, therefore, to improve our understanding of the form and mobility of hydrogen isotopes in zirconia films. Not the least of our areas of ignorance is whether hydrogen migrates generally through the oxide film, or locally at intermetallic sites. The absence of intermetallic particles from cold-worked Zr-2.5 Nb alloy material (with a low Fe impurity level) has been argued to be one reason for the very low hydrogen uptake rates observed during the aqueous corrosion of this alloy [36].

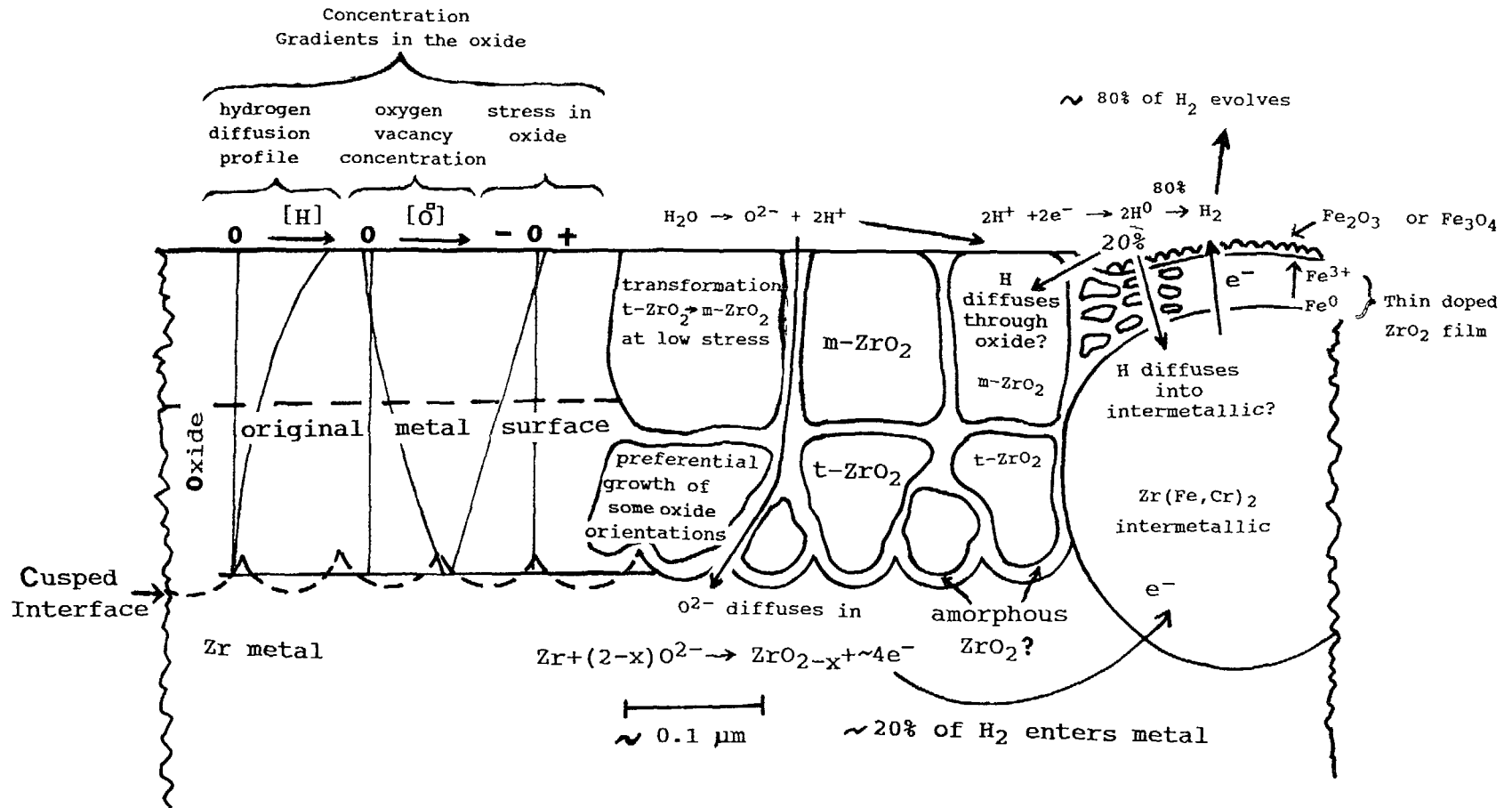


FIG. 5.1. Simplified diagram of growth processes in thin oxide films formed on Zircaloy-4 in an aqueous environment.

The mobility of electronic defects (electrons and holes) is also important to the oxidation process because of the high intrinsic electrical resistivity of zirconia [26,27]. The cathodic current during oxidation has been shown to flow principally at the sites of the intermetallic particles in the Zircalloys [251]. Bulk hypostoichiometric zirconia has been shown to be an n-type semiconductor [252]). However, there is a little evidence that the overlayers of the zirconia may become hyperstoichiometric in highly oxidising environments [253], resulting in a thin surface layer with p-type conductivity. Evidence for both electron and hole conduction in zirconia has been found, especially when layers of iron oxides are present on the surface [27]. A similar situation might be expected in the oxides formed over the intermetallics in the Zircalloys, which are very different from the bulk oxide film because of the high concentrations of Fe, Cr and Ni present in the intermetallics.

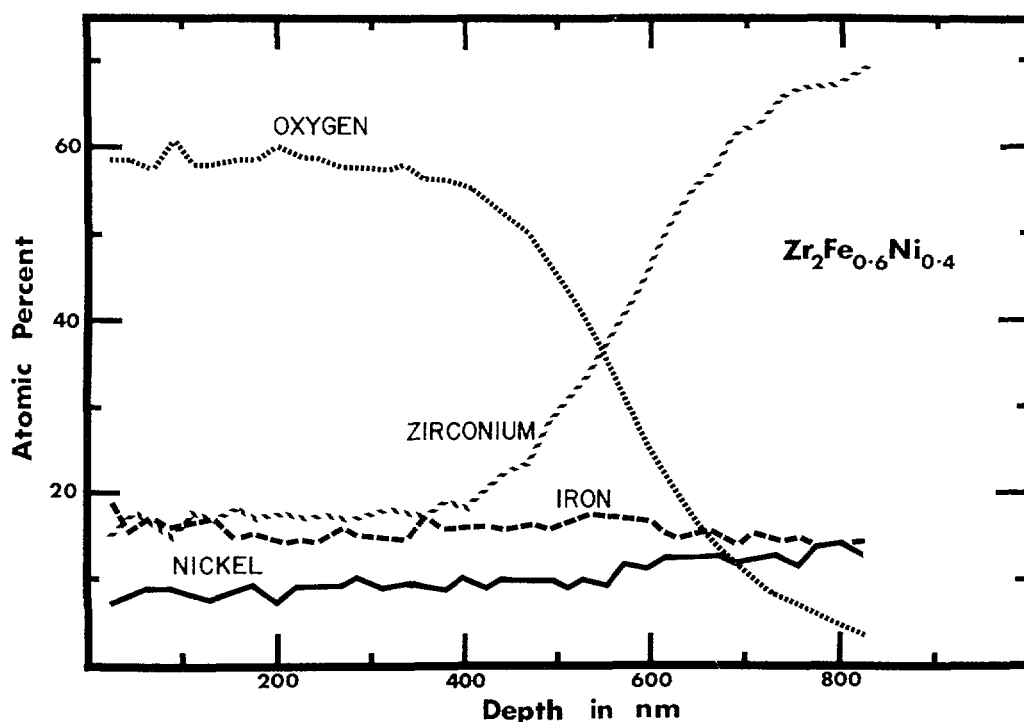


FIG. 5.2. Thin oxide on amorphous $Zr_2(Fe/Ni)$ showing that although Fe appears to be oxidized, nickel appears to be unoxidized in the oxide [29].

Since the oxide over the intermetallics is the primary conduction path for the cathodic component of the oxidation current, and since the proton discharge reaction on the surface of this oxide provides the primary source for hydrogen that ultimately finds its way into the metal, the conditions within and at the interfaces of these oxides on intermetallics are clearly of great importance (Figure 5.1). At present, however, we have virtually no knowledge of the precise nature of these oxides, although this area is slowly being explored (Figure 5.2) [29,254]. Oxide films on intermetallics typically show more, and larger pores in electron microscope replica studies than the oxide on the alloy matrix (Figure 5.3), only at prior metal grain boundaries are similar large pores typically seen [22].

5.1.2. Evolution of oxide morphology

Zirconium specimens initially carry a thin air-formed oxide film that is usually 2-3 nm thick [225,256]. Electron microscopy of these air formed films initially suggested that a large fraction of this film was

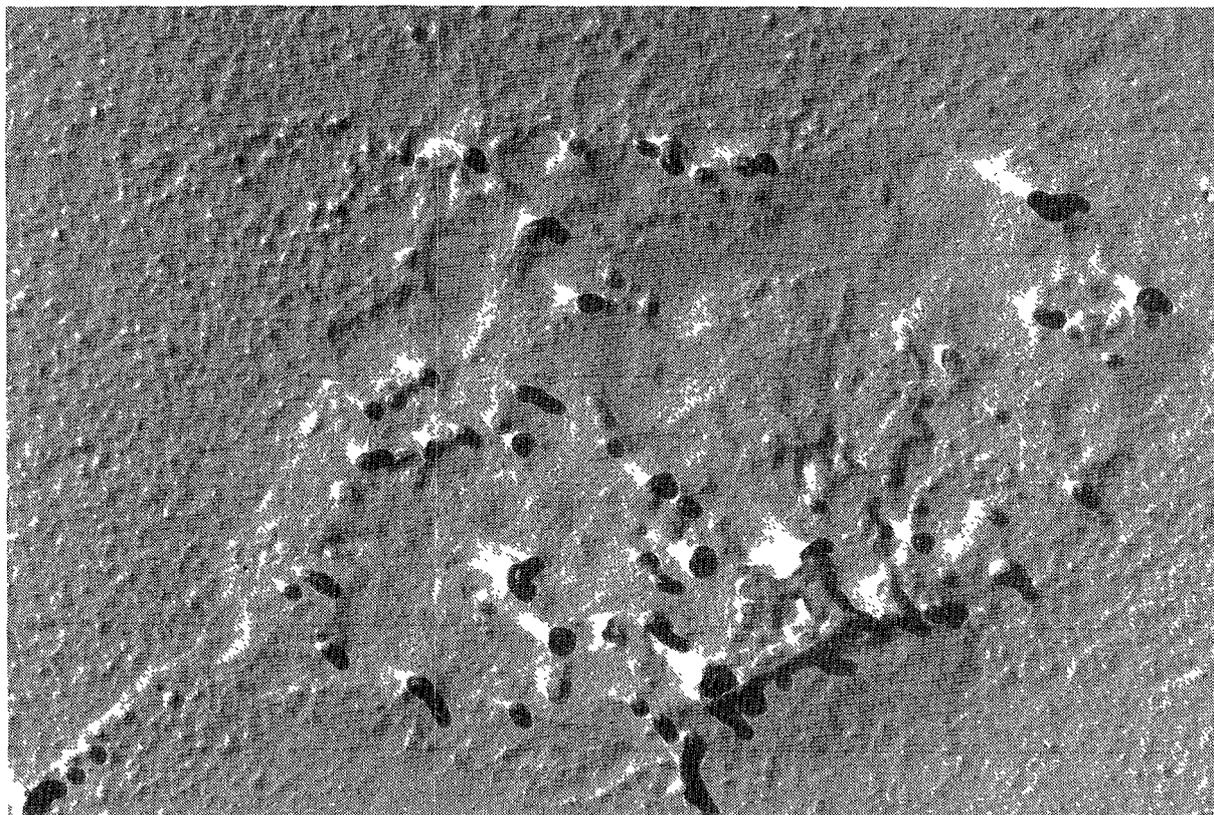


FIG. 5.3. Concentration of large pores in the oxide on an intermetallic in a 10 μm oxide on Zircaloy-2 (Ac 486, 360°C water, Δw 156 mg/dm²) (50 000 \times) [22].

amorphous, however, opinion now generally [257] supports the idea that it is microcrystalline with crystallites near the resolution limit of the transmission electron microscope (i.e. about 2–3 nm diameter for the diffraction conditions in such a film). Early reports of essentially amorphous films and completely ring-type diffraction patterns were probably the result of the surface preparation techniques that were used [258].

When thermally activated oxide growth ensues, the new oxide is formed below the air formed film by inward migration of oxygen. In the thickness range 10–100 nm the oxide appears to be almost fully crystalline when formed thermally in oxygen or steam and the average crystallite size increases with increasing oxide thickness [13]. Although the oxide crystallites are not equiaxed during this period, there is probably only a single layer of crystallites present. The question of whether this film forms by the preferential growth of some orientations of crystallite from the air formed film or whether a new layer of crystallites nucleates under the air formed film has not been completely resolved. However, the evidence favours the latter as signs of the persistence of an unmodified air formed film on top of the main oxide have been found [259].

Above about 100 nm additional layers of oxide crystallites grow as evidence of Moiré fringes becomes more common when the oxides are viewed in transmission in the TEM (Figure 5.4). With further thickening successive layers of crystallites develop even in the pre-transition oxidation period for unalloyed zirconium. Deliberate fracturing of these pretransition films (at about the transition point) can reveal a number of these layers of oxide crystallites (Figure 5.5) [259], although it is not thought that lateral cracks were present between these layers prior to the fracturing of the film [24]. With the successive layers of crystallites formed in these

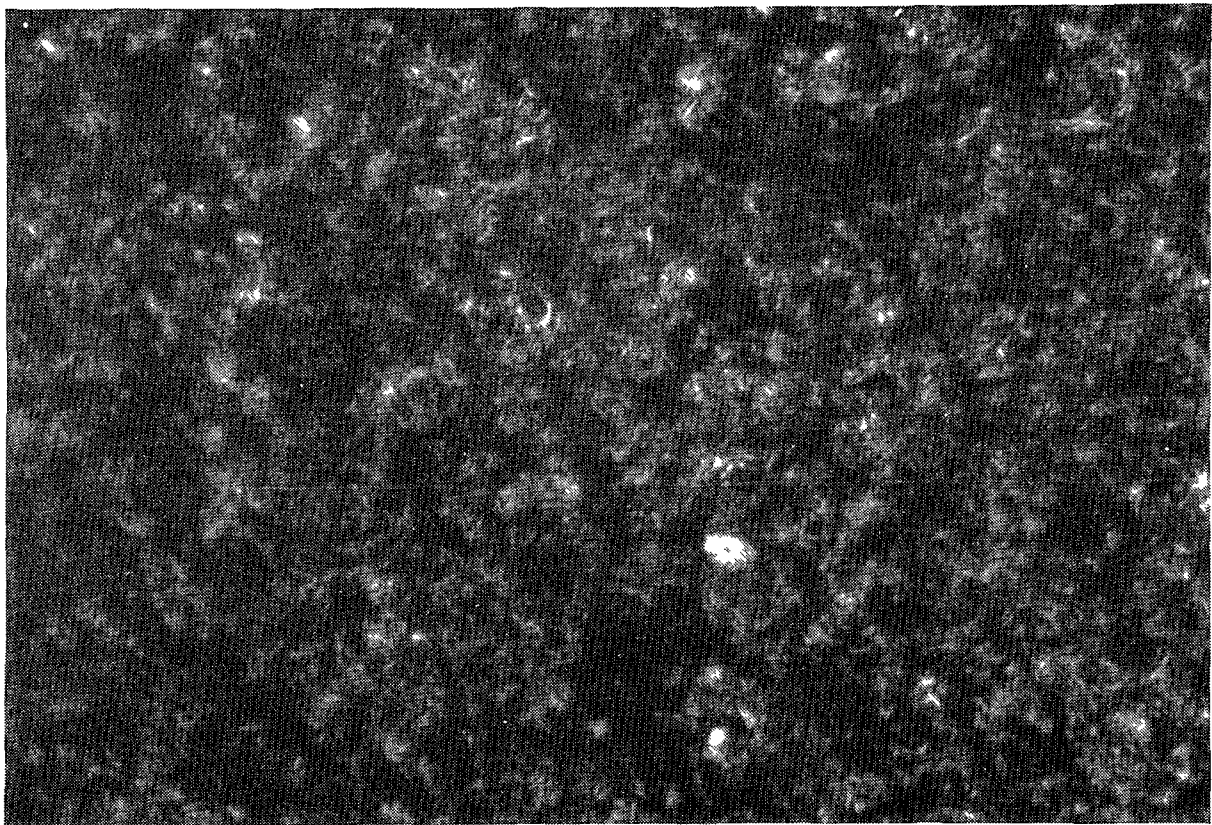


FIG. 5.4. Moiré fringes in thin oxide film formed on Zircaloy-2 (200 000 \times).

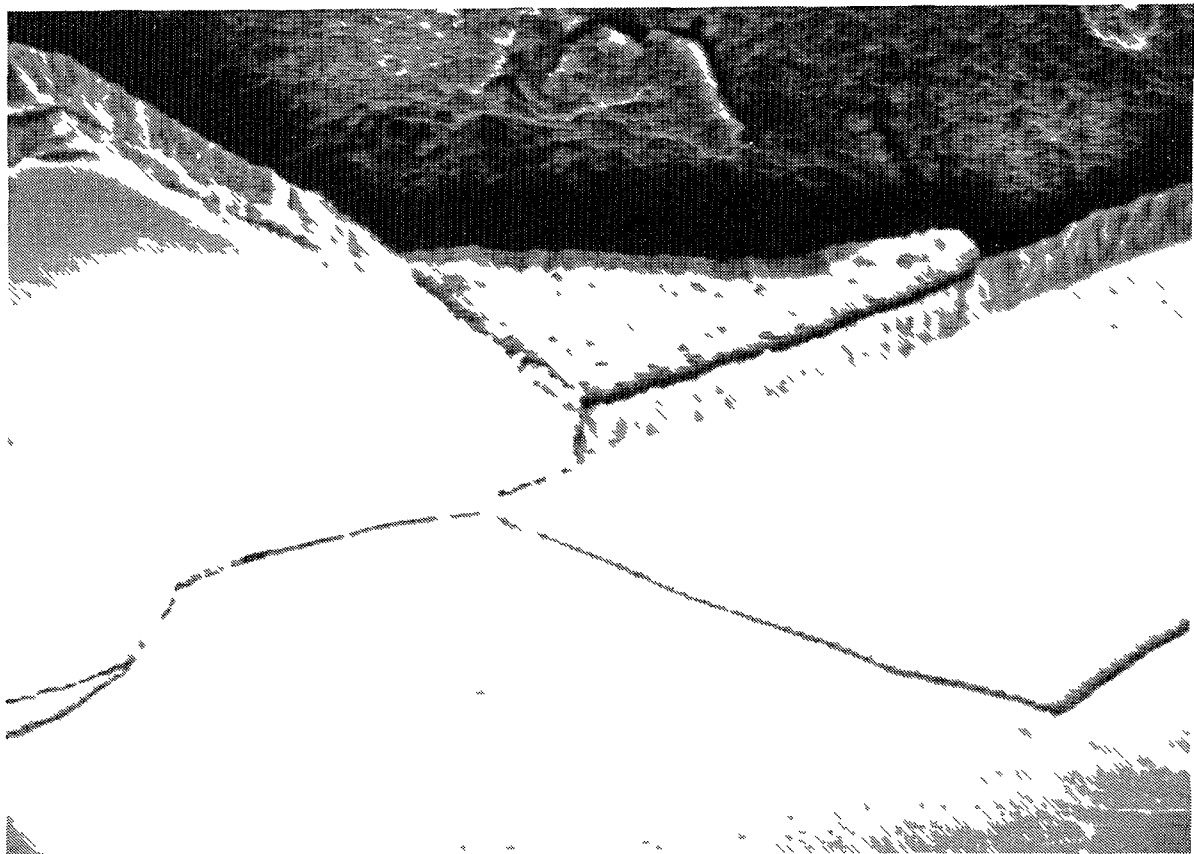


FIG. 5.5. Multiple layers in post-transition oxide on zirconium revealed by fracturing the oxide [259].

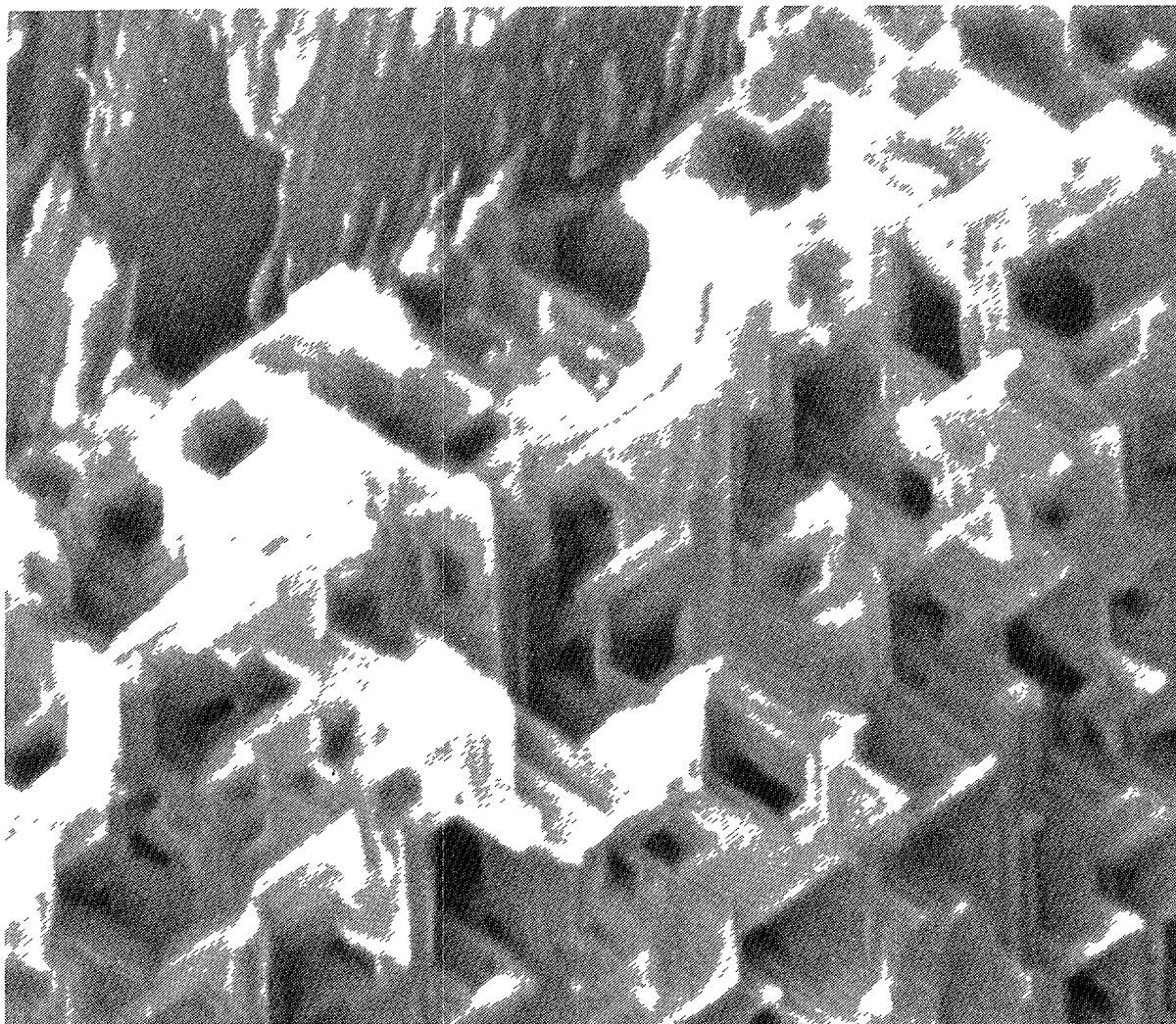


FIG. 5.6. Highly crystalline porous structure in the inner layers of a post-transition oxide on zirconium. Revealed by fracturing off the overlying layers [259].

films the mean crystallite size, and the degree of crystallinity appear to increase, and this results in some highly crystallographic features within the oxide [259]. These features do not necessarily represent individual large crystallites (see later). Also present are highly crystallographic pores that have been shown to be voids by comparing the fractography of both sides of a fractured layer of oxide (Figure 5.6). Such observations clearly have relevance to the onset of breakdown in oxide films, since these crystallographic voids appear to have been present before any surface signs of breakdown were apparent.

During the early stages of growth (up to about 200 nm) the oxide remains parallel sided and uniform over any metal grain, as shown by the uniform interference colours on any grain. The oxide thickness on grains of different orientation differs at any time for thermal oxides, although it does not for anodically formed oxides. The smoothness of the interfaces and the uniformity of thickness indicates that the electric field is important in this period of oxidation. At ~200 nm a mottling of the interference colours spreads across individual grains and eventually the whole surface. It usually starts at a grain boundary and is caused by the development of roughness at the oxide-metal interface (Figure 5.7) [8]. In mottled areas the film soon becomes grey and then black and the interference colours

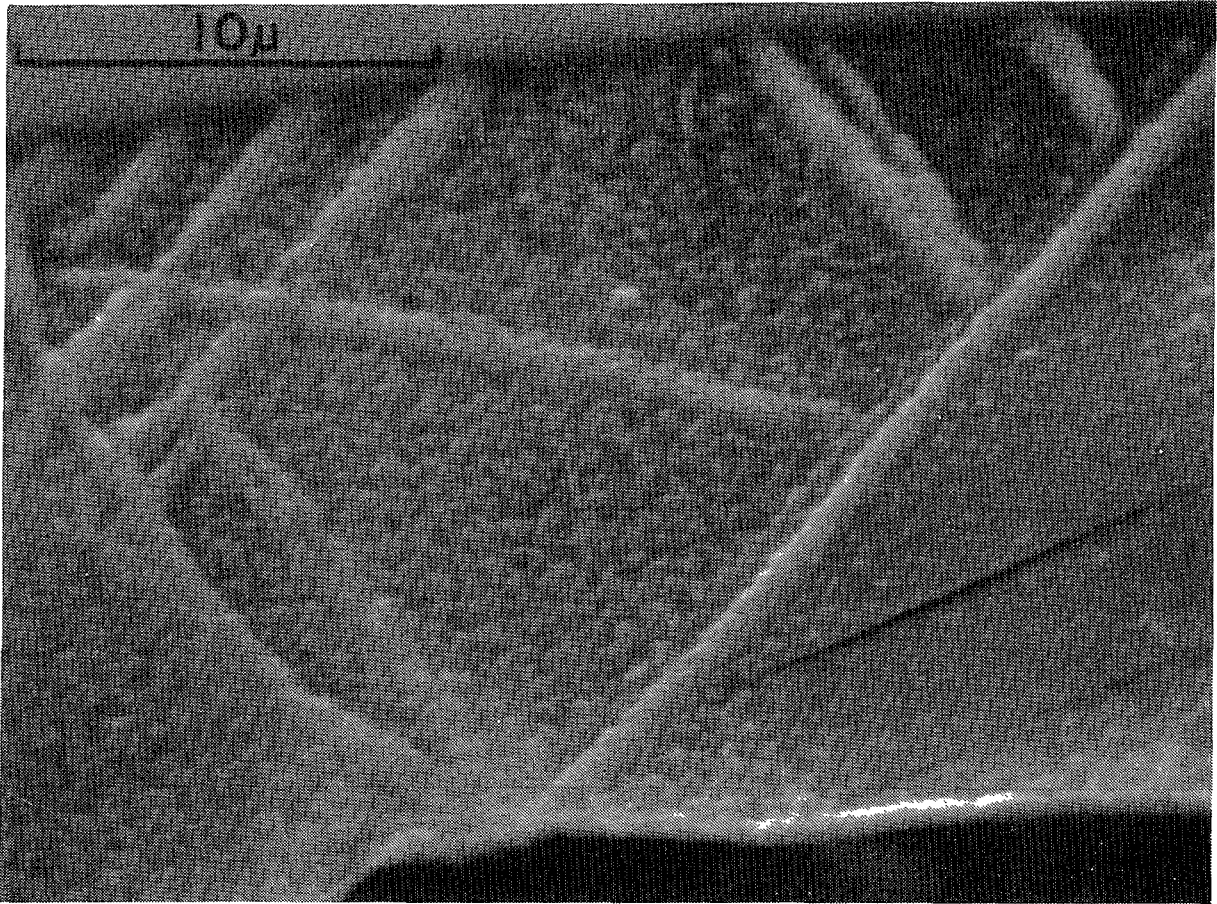


FIG. 5.7. Inner interface of a thin oxide film ($\sim 1500 \text{ \AA}$) showing roughness spreading across the prior metal grain. The straight ridges of thick oxide are along twins and the curved ones along grain boundaries. Mean oxide thickness: $0.4 \text{ }\mu\text{m}$ [8].

disappear at a much lower thickness than for anodic oxides which remain much more transparent. This effect is thought to indicate the development of the vacancy concentration gradient in the oxide, as it is the vacancies acting as colour centres that render the oxide opaque in visible light. The thinnest oxides on slow growing grains can remain transparent and uniform in interference colour even when most of the surface has become black [81]. A small inflection in the oxidation kinetics marks this change in oxide appearance and indicates the change from an electric field controlled growth process to vacancy diffusion control [18]. Beyond this point the cusping of the oxide/metal interface becomes more pronounced and may be related to the interfacial oxide crystallite size, although this has not been confirmed [8].

With increasing oxide thickness beyond about $2 \text{ }\mu\text{m}$ we are usually in the realm of the post-transition oxide, except for the high temperature oxidation of unalloyed zirconium in oxygen. However, whether or not the thick films are porous, both on zirconium and its alloys a strong texture develops in the oxide by the preferential growth of some oxide orientations [14,260]. This texture is a fibre texture (i.e. the preferred orientations are always perpendicular to the free surface (Figure 5.8) irrespective of the metal grain orientation) and commonly in unalloyed zirconium and sometimes in the Zircalloys leads to the formation of large columnar features in the oxide [261-263]. These columnar features appear to be single crystal based on the similarity in size between the columnar features seen in the replicas of oxides formed on Zr at 650°C and those

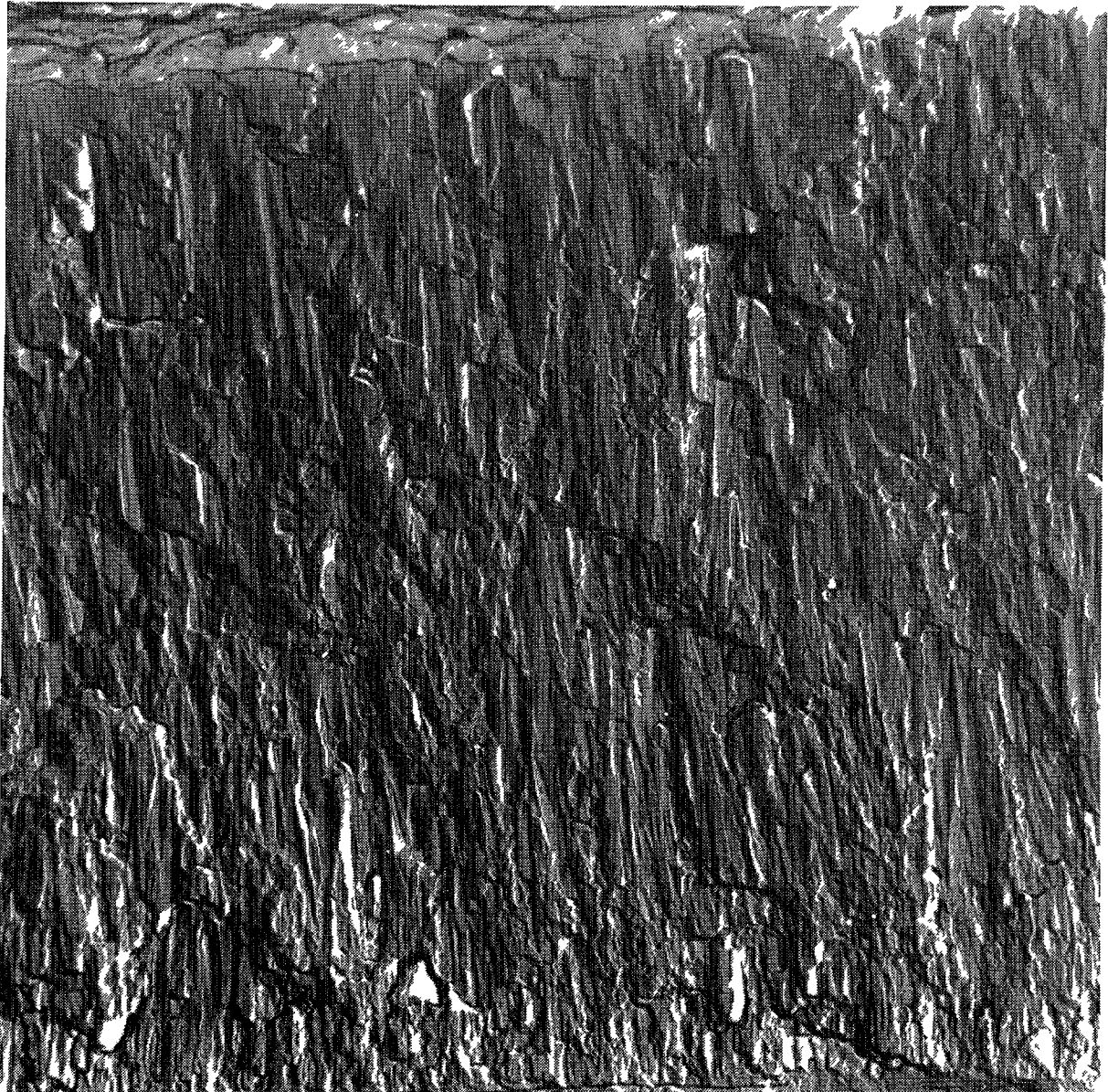


FIG. 5.8. Columnar oxide structure in thick oxide formed on zirconium in air at 650°C. Revealed by fracturing oxide [261].

seen in transmission in oxide sections (Figure 5.9) from oxides formed on Zircaloy at 600°C. The large columnar crystallites can be typically $>10 \mu\text{m}$ long \times $0.2 \mu\text{m}$ diameter when formed at high temperatures such as 600°C, but are not commonly seen in oxides formed in water at 300–360°C. Thus, the dimensions of these columns are a function of the oxidation temperature for zirconium increasing in size with temperature. For the Zircalloys they are not prominent at reactor temperatures, are not always seen at 600°C (compare refs. 261,262), but become very evident (Figure 5.10) during oxidation at high temperatures (e.g. above the α/β transition temperature) that are relevant to LOCA conditions [264]. At these temperatures all the intermetallic particles are in solution, which suggests that one factor limiting the formation of columnar oxides on the Zircalloys at lower temperatures may be a modification in the local oxide morphology resulting from the presence of the intermetallic particles.

The orientations of crystallites that preferentially form the fibre texture seem to be those that are best adapted to minimize the compressive

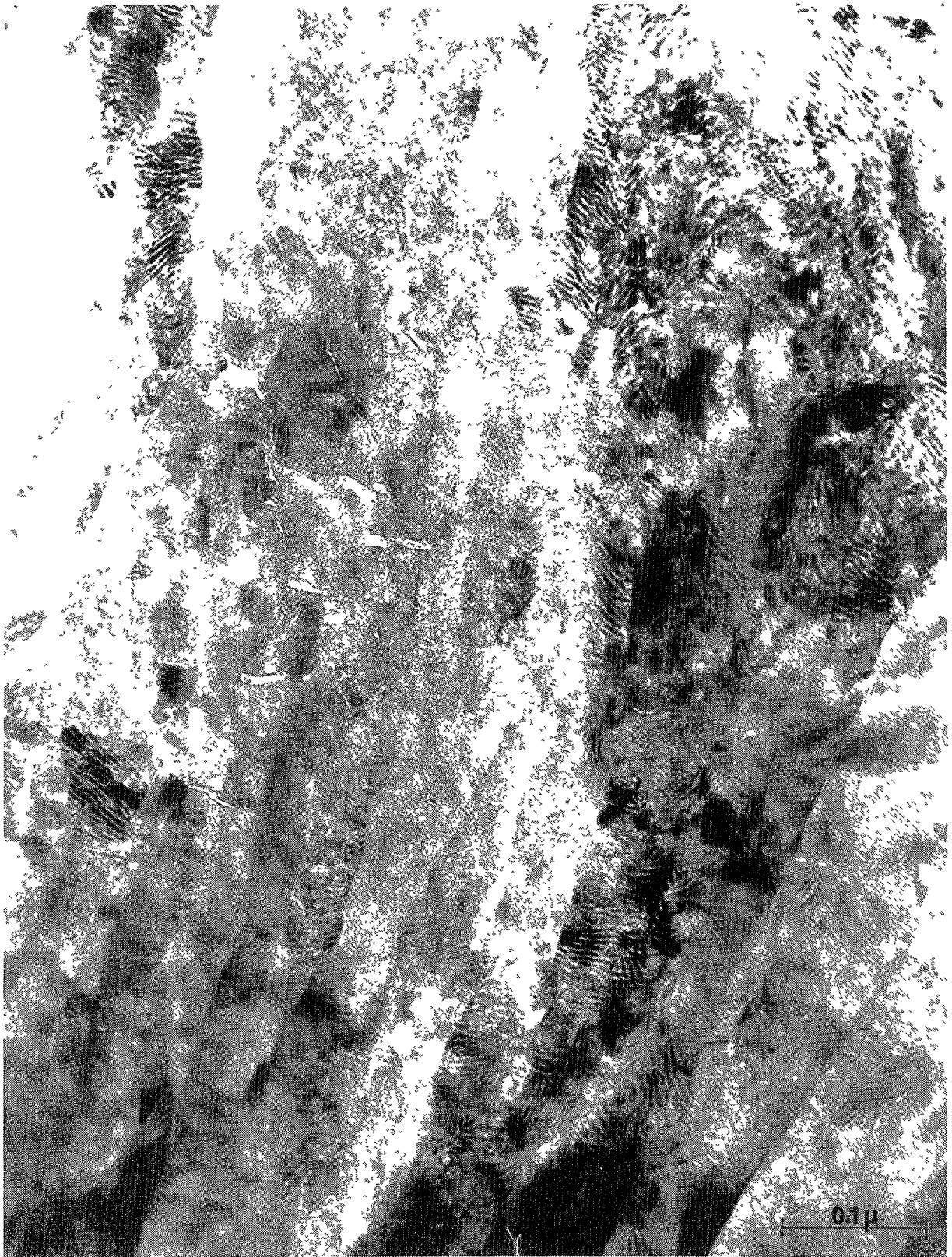


FIG. 5.9. Thin section of columnar oxide formed on Zircaloy-2 at 600°C in air.

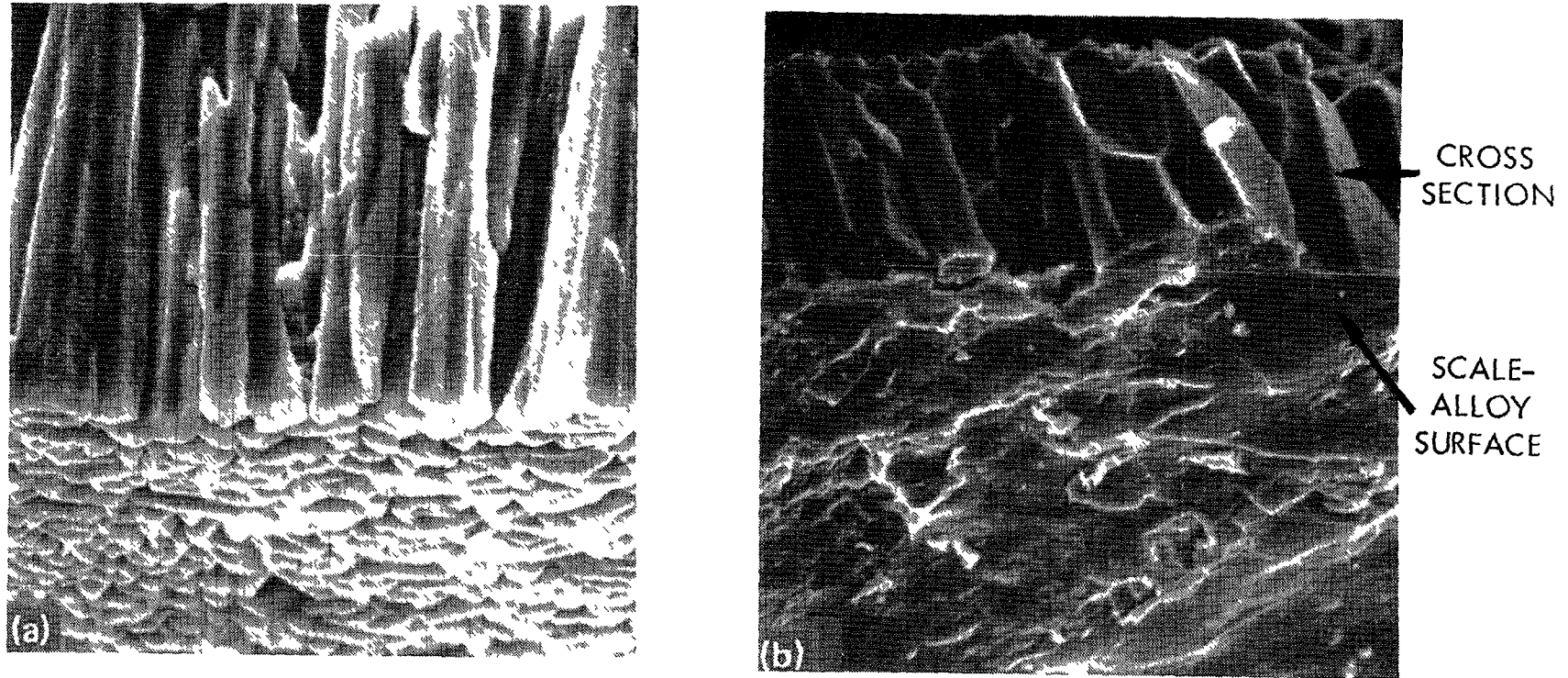


FIG. 5.10. Differences in column dimensions between oxides formed (a) on Zircaloy-4 (2000 \times) and (b) on zirconium (1000 \times) during oxidation in the β phase field (1303 $^{\circ}$ C) in steam [264].

stresses in the plane of the specimen surface [14,266]. From this it is deduced that the driving force for the development of this fibre texture is the compressive stress that has already been generated during the growth of thin films [265,266].

5.1.3. The development and nature of oxide porosity

At the transition in the oxidation kinetics for the Zircalloys the oxide film becomes demonstrably porous. After this transition it is possible to demonstrate the capillary rise of aqueous electrolytes into the previously impervious oxide [267-269] and to force mercury into the same features under pressure [31]. Electron microscopy reveals a variety of features on the oxide surface that can be correlated with the other forms of measurements. The porosity nucleates at a limited number of sites and spreads laterally over the surface. For Zr-2.5 Nb alloy specimens that follow a parabolic oxidation curve (without a distinct increase in oxidation rate [36] corresponding to a transition point) it is similarly possible to identify the presence of porosity from an early stage in the oxidation.

The above techniques identify two primary types of defect that appear in the oxide film. Firstly, cracks which have a high aspect ratio and show up clearly in electron microscope replicas; and secondly, pores having a nearly equiaxed cross section and a range of effective diameters that show up most clearly in the mercury porosimeter traces, but, except for the larger pores, are difficult to image clearly in electron microscope replicas (Figure 5.11). Evidence suggests that both types are usually

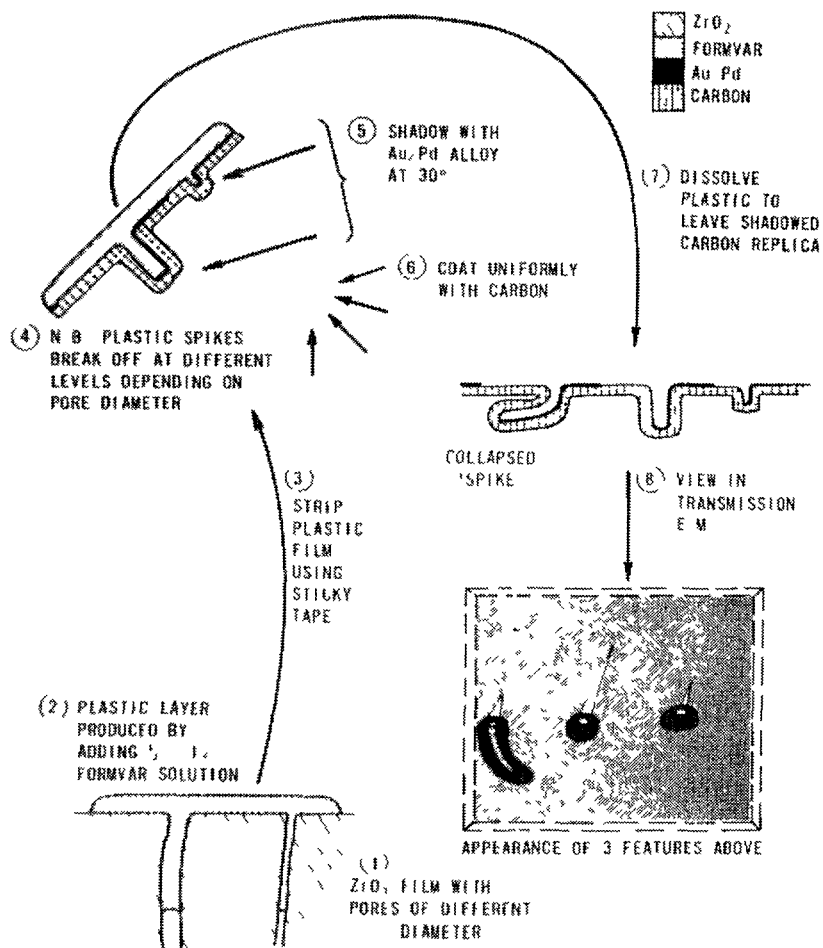


FIG. 5.11. Appearance of pores in an oxide film after replication [36].

present, but that the relative proportions of each are dependent upon the oxidation conditions. Thus, in water or steam at $\leq 400^{\circ}\text{C}$, where the post-transition kinetic curves are highly cyclic in nature, the replica studies show that cracks are very common, but porosimetry shows that small pores are also present in considerable numbers. In steam at high temperature and low pressure, where the kinetic transition is smooth, with no abrupt discontinuities, cracks in the oxide are few and small, whereas the porosimeter showed a wide spectrum of pore sizes [22,31]. It has been concluded, therefore, that the discontinuous cyclic post-transition curves result from repeated episodes of extensive oxide cracking that short-circuit the more regularly developed pore structure of the post-transition oxide films, and that at low pressures of oxidant the pore structure develops, but without the succession of cracking episodes. There is no unequivocal evidence for reformation of a thick barrier oxide layer once the pore structure has developed in oxide films on Zircalloys. The barrier layer on Zr-2.5 Nb alloy surfaces appears to be significantly thicker than on the Zircalloys [36].

It is noteworthy that the low pressure studies often result from continuous oxidation measurements using microbalances, whereas the discontinuous curves typically arise in autoclave testing which is by nature discontinuous and involves repeated thermal cycling. This has led to the supposition that the episodes of cracking may arise from thermal stresses induced during autoclave shutdowns. If this were the case then the shapes of the kinetic curves that are measured would, to some extent be artefacts of the oxidation techniques used. No published study of these effects is available. However, measurements of the change in stress resulting from the cooling of a specimen show that this results in an increment of tensile stress being applied to the oxide that is linearly dependent on the temperature change [23]. Scatter in the data on the thermal expansion coefficients of pure monoclinic ZrO_2 and the anisotropic expansion of the Zircalloys prevents any useful conclusion being reached by calculation alone.

The information obtained from porosimetry and electron microscopy does not permit us to establish the extent of interconnection of the pores that are formed. Some BET surface area measurements have permitted estimates of the extent of porosity [257,258] and give values 1-3% pore volume for thick oxides. However, the discrepancy between metallographic oxide thickness and that calculated from the weight gain can be $>5\%$ for thick oxides formed in 360°C water or 400°C steam. Mercury porosimetry can also measure pore volumes, but the maximum pressure of commercial porosimeters of this type is insufficient to fill the smallest pores believed to be present in zirconia films. Only by using a porosimeter that measures oxide impedance as a function of pressure can the closeness of approach of the pores to the oxide-metal interface be established [31]. Oxide impedance measurements using the capillary rise of an electrolyte, even if done in vacuo, cannot give this information because of the interfering effects of the double-layer impedances of the pore walls, and associated alternative conduction paths (Figure 5.12). A resolution of this question is vital to an acceptance of the nature of the "barrier layer" at the oxide/metal interface. The simplest definition of this barrier layer would be "that layer of impervious oxide remaining at the oxide-metal interface when the closest approach and the spacing of the crack/pore network to this interface are considered". Such a layer is unlikely to be uniform in thickness, but could be described either by an average thickness or by a minimum thickness. It is a dynamic phenomenon. By virtue of the inward migration of oxygen that determines the oxide growth rate, today's barrier layer is part of tomorrow's porous outer oxide.

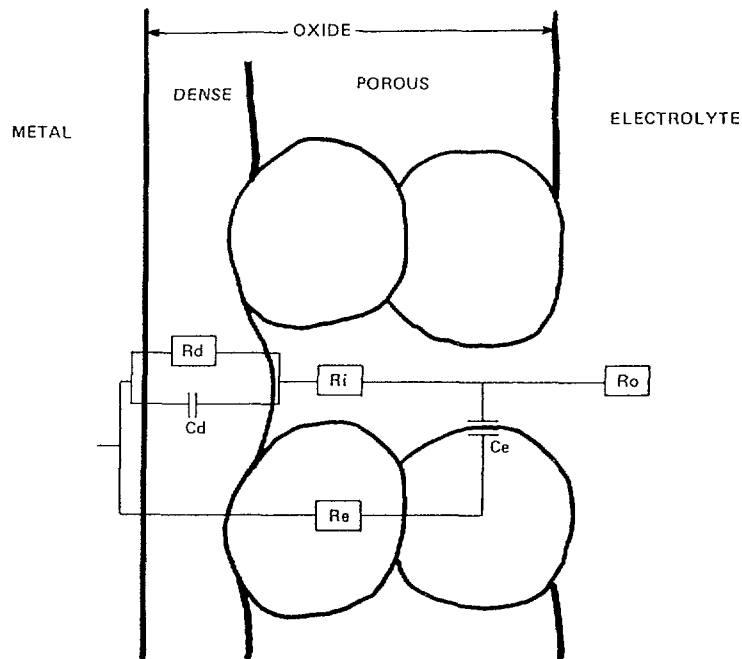


FIG. 5.12. Equivalent electrical circuit for an oxide with a dense and porous sublayer used in analysis of impedance data [223].

Our lack of understanding of the processes creating the pores and cracks in the oxide film is reflected in the number of hypotheses that are still unresolved. These hypotheses can be grouped into three classes according to whether the cracks and pores are thought to originate from the outside, from within, or from the inside of the oxide film:-

Initiation at the outside of the oxide is considered because the compressive stress within the oxide is a maximum at the oxide/metal interface and decreases as one moves out through the oxide, possibly becoming tensile at the outer oxide surface. This has led to two of the three hypotheses below:-

- (1) Rapid crack growth initiating at the outer surface as a result of tensile stresses at this location, accentuated by thermal stresses during cooling [1].
- (2) Slow development of small cracks at oxide triple points, once there is a tensile stress there, which propagate inwards as the stresses in the oxide readjust to the presence of surface cracks [267].
- (3) Localised dissolution and reprecipitation of ZrO_2 starting at the surface (as in thick anodic alumina films) may initiate (or enlarge preexisting) pores [141].

Initiation within the oxide may be demonstrated by the observation of the crystallographic voids already mentioned. There are at least two mechanisms by which this could occur:-

- (4) Preferential growth of some crystallite orientations leads to the formation of crystallographic voids in the inner layers of the oxide which become interlinked and propagate to the surface [259].
- (5) The observation that the restricted set of monoclinic ZrO_2 orientations present in oxide films is that which would be expected if the

crystallites formed first as cubic or tetragonal ZrO_2 leads to a mechanism by which cubic/tetr. ZrO_2 is stabilised by the high compressive growth stresses and transforms to monoclinic, initiating small cracks that interlink, once the crystallites have moved far enough from the oxide-metal interface that the compressive stress is no longer high enough to stabilise the high symmetry phase [35].

Initiation from below the oxide has been observed in high temperature oxidation where a deep, brittle, oxygen diffusion zone is formed [271]. Thermal stresses may then initiate cracks in this layer that will run outwards through the oxide to the specimen surface. This would be hypothesis 6.

At present there is insufficient evidence to distinguish among these hypotheses. Effects of discontinuous weighing techniques and thermal cycles on the kinetics would argue for hypothesis 1 at least as the mechanism for forming the high aspect ratio cracks in the oxide. The observation of crystallographic voids in oxides on unalloyed zirconium may argue for hypothesis 4 as the mechanism for forming an interconnected pore network. Nevertheless, more work needs to be done before an understanding of oxide breakdown can be achieved. As a first step the detection (or otherwise) of porosity within the pretransition oxide films that was not connected to the surface would help to eliminate some of the possibilities.

5.1.4. Oxide barrier layers

Post-transition oxidation rates on zirconium alloys are often similar to the pre-transition rate at an oxide thickness of about $1 \mu m$, leading to the impression that a post-transition barrier layer of about this thickness is present [39,81,270]. This argument has been justified by pointing to impedance measurements on the post-transition oxide (by the capillary rise technique) that seem to confirm this thickness. However, the impedance measurements have seldom been carried out in vacuo, so that the air trapped in the pores limited the depth of penetration of the electrolyte, and no correction was made for the double layer impedance at the surfaces of the pores that is in series with the barrier layer impedance. In addition the argument that matches post-transition rates with a selected tangent to the pretransition curve is flawed because the fractional area of the surface accessible to the oxidant at the bottoms of the pores in the post-transition oxides is very much less than the area through which oxygen transport occurs during pre-transition oxidation. Thus, the effective barrier layer thickness must always be much less than is indicated by merely matching the slopes of the pre- and post-transition kinetic curves. We need to know how much thinner than this the barrier layer is.

A mercury porosimeter designed to resolve this question by measuring the impedance of the oxide during impregnation with mercury confirmed that the minimum thicknesses of barrier layers present in post-transition oxides on the Zircalloys are in fact much thinner than the above comparison indicates [31]. The conclusion reached from these measurements was that the residual impervious oxide layer at the bottom of the pore appeared to be no thicker than the air formed oxide on a fresh surface [267]. The fact that the post-transition oxidation rate of the specimen was so much less than the initial oxidation rate of a freshly pickled specimen arises then from the small cross-sectional area of pores that approach this close to the oxide metal interface. It is of course impossible to measure the fractional area of the pores by determining the initial oxidation rate and comparing this with the post-transition rate, since the initial rate could only be

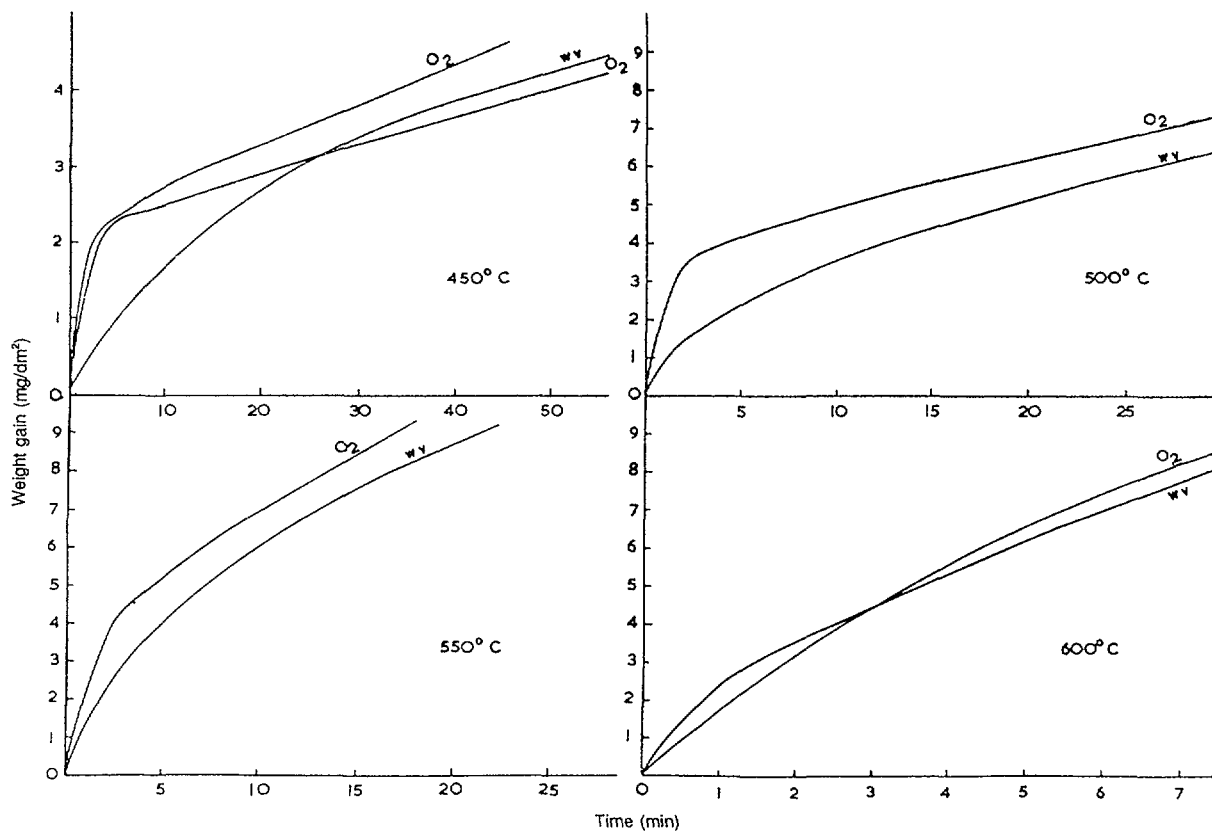


FIG. 5.13. Initial Zircaloy-2 oxidation rates in oxygen and water vapour [88].

TABLE 5.1. INITIAL AND POST-TRANSITION OXIDATION RATES FOR ZIRCALOY-2 (batch Z8006) [88]

Temperature °C	Initial rate (from microbalance curve) mg.dm ⁻² .day ⁻¹	Post-transition rate (in 1atm. steam) mg.dm ⁻² .day ⁻¹	Ratio
450	3.03×10^2	8.01	2.7×10^{-2}
500	1.27×10^3	32.2	2.5×10^{-2}
550	2.10×10^3	115	5.5×10^{-2}
600	4.68×10^3	360	7.7×10^{-2}

determined by extrapolation of short term kinetics to the origin, and theoretical fits to such kinetics will extrapolate to infinite rate at zero time. It is possible to bring specimens up to temperature and measure an initial rate very quickly in a microbalance. Measurements of the initial oxidation rates (as performed above) (Figure 5.13), when compared with post-transition rates under the same conditions (Table 5.1) permit an estimate of the fractional area of the pores. If the minimum barrier layer thickness at the bottom of a pore is the same as the initial air-formed oxide thickness then at their points of nearest approach to the oxide/metal interface (at the lowest temperatures represented in Table 5.1) the pores represent about 2-3% of the interfacial area [88]. This is comparable to what would be expected from the ~5% porosity that seems to be present in thick post-transition oxide films, based on the discrepancy between metallographic and weight-gain thicknesses, and suggests that most

of the pores approach the oxide-metal interface closely. The apparent increase in pore volume with increasing temperature seen in the data in Table 5.1 is thought to be more probably a result of increasing errors in measuring initial oxidation rates, as the temperature increases, than of a real increase in porosity. Other data [223,262] tend to indicate a lower porosity for specimens oxidised at high temperatures.

The barrier layer, however, must be a residual entity of very variable thickness, and the local situation must change continually as fresh oxide forms, pores continue to grow, and occasional cracks propagate right up to the interface. That a small number of cracks in the oxide do initially penetrate right to the interface (although their tips must immediately repassivate by the formation of fresh oxide) was shown at an early date by Pemsler [272], who replaced the oxidant at the end of his experiments with HCl gas (to remove zirconium as a volatile halide), and hence decorated the bottoms of any cracks which at that moment penetrated to the oxide-metal interface. His experiments showed that, at any point in time, only a few such cracks were present, thus confirming the dynamic nature of the situation near the oxide-metal interface. This also supports the concept that the oxide barrier-layer can only be a time averaged phenomenon with some bare metal possibly present at any instant in time, and any subsequent measurement of the barrier layer thickness at room temperature giving a minimum value equal to the air-formed oxide thickness (since any such bare spots would have repassivated before a measurement could be made).

Measurements of the average barrier layer oxide thicknesses on the Zircalloys and Zr-2.5 Nb alloy confirm that the latter shows a much thicker mean barrier layer than the former [36]. This, may be understandable since the Zr-Nb alloy tends to obey para-linear kinetics, which would suggest that the porosity starts to develop at the outside of these oxides, and at an early stage of oxide growth. This difference may also mean that during the oxidation of Zr-Nb specimens there is no point in time when cracks or pores approach close to the oxide/metal interface. This effect, coupled with the low diffusivity of hydrogen in zirconia could be the primary reason for the very low hydrogen uptake rates shown by Zr-Nb specimens.

Attempts to observe the situation at the oxide-metal interface by the examination in the TEM of slices of oxide taken through the interface have had limited success [273]. They suggest that even in thick films the oxide becomes crystalline close to the interface, but so far have failed to establish the distance of closest approach of pores to the interface. SEM studies that show evidence for pores emerging at the inside surface of films stripped from Zircaloy-2 specimens [36], confirm the closeness of approach of the pores to the interface, but cannot give an unequivocal measure of this, since it is known that a small amount of oxide dissolves in the mixed nitric-hydrofluoric acids used to remove these oxide films. Nevertheless, such observations tend to support the above argument that some pores approach very close to the oxide-metal interface during post-transition corrosion.

5.1.5. Effect of some variables on the oxide structure

Oxide films on zirconium alloys are typically relatively parallel sided (apart from the roughness that develops at the oxide/metal interface), and oxidation rates are generally similar in oxygen, air, water, steam, CO₂ and oxygen containing sodium at the same temperature [243]. Thus, the oxidation is usually regarded as being controlled entirely by processes within the oxide film. Nevertheless, there are some situations

where significant differences from this situation occur. We will consider here the more severe of these effects, namely nodular corrosion in high-temperature, high-pressure steam, accelerated corrosion in concentrated LiOH, and irradiation corrosion. In each instance only observations of the oxide morphology will be discussed.

(a) Nodular corrosion in high temperature steam

Above $\sim 450^{\circ}\text{C}$ in high pressure steam the oxide films on the Zircalloys cease to be approximately parallel sided and develop roughly circular nodules of thick oxide [41]. These nodules continue to grow in diameter and thickness until they coalesce. At an early stage of their growth they can be seen to be heavily cracked, with the cracks often concentric with the nodule [53]. The nature of this cracking can be explained largely by the geometry of the nodule and the stresses generated by its growth.

The process that triggers nodule nucleation is still argued [45]; the effects of this on the oxide morphology are not well characterised. Attempts to look at sections of these nodules [274], or electron or x-ray diffraction through them [50], have not produced consistent results. The question of whether the oxide is more or less amorphous than the uniform oxide is unresolved as in reactor water the additional possibility of a dissolution and reprecipitation of ZrO_2 must be considered [141]. Such a process could lead to the precipitation of hydrous zirconia in rapidly growing porous oxide, such as the nodules, and this would appear as amorphous zirconia when sections through nodular oxides, or X-ray or electron-diffraction analyses of them were made.

(b) Accelerated corrosion in LiOH

The accelerating effects of concentrated LiOH on the corrosion of the Zircalloys (Figure 5.14) have been known for many years [39,275-278]. It results in thick porous oxide films from an early period of corrosion. Above about pH 13 (at room temperature) the pretransition kinetic period disappears, and linear oxidation with the formation of porous oxides proceeds from the start of the experiment. X-ray diffraction studies have sometimes indicated the presence of lithium zirconate in the oxide, but this is not universally accepted. Recent work [39] suggests that much of the Li^+ in the oxide is leachable, and that it is mainly contained within the interconnected porosity.

No extensive studies of the morphology of these thick porous oxide films have been reported [210], but they are thought to be much more porous than the normal post-transition oxides. A dissolution of the ZrO_2 in the pores by the formation of Li_2O from Zr-O-Li groups is thought to be occurring, with reprecipitation of any zirconium oxide that is dissolved. This should lead to large amounts of amorphous ZrO_2 in these films compared with normal post-transition oxide films, but such studies have yet to be performed. Even when x-ray diffraction measurements on oxides grown in concentrated LiOH solutions have been made the authors have concentrated on identifying the crystalline phases and have not studied the extent of the diffuse scattering. However, the evidence should be available if these authors [39,278] re-examined their X-ray diffraction patterns.

(c) Accelerated corrosion in-reactor

Examination of irradiated oxide films have been limited. Spitznagel et al. [279] could find no differences between oxide films bombarded with protons and unirradiated oxide films. X-ray evidence shows no signs of the formation of irradiation induced cubic ZrO_2 [5]. Garzarolli et al. [223]

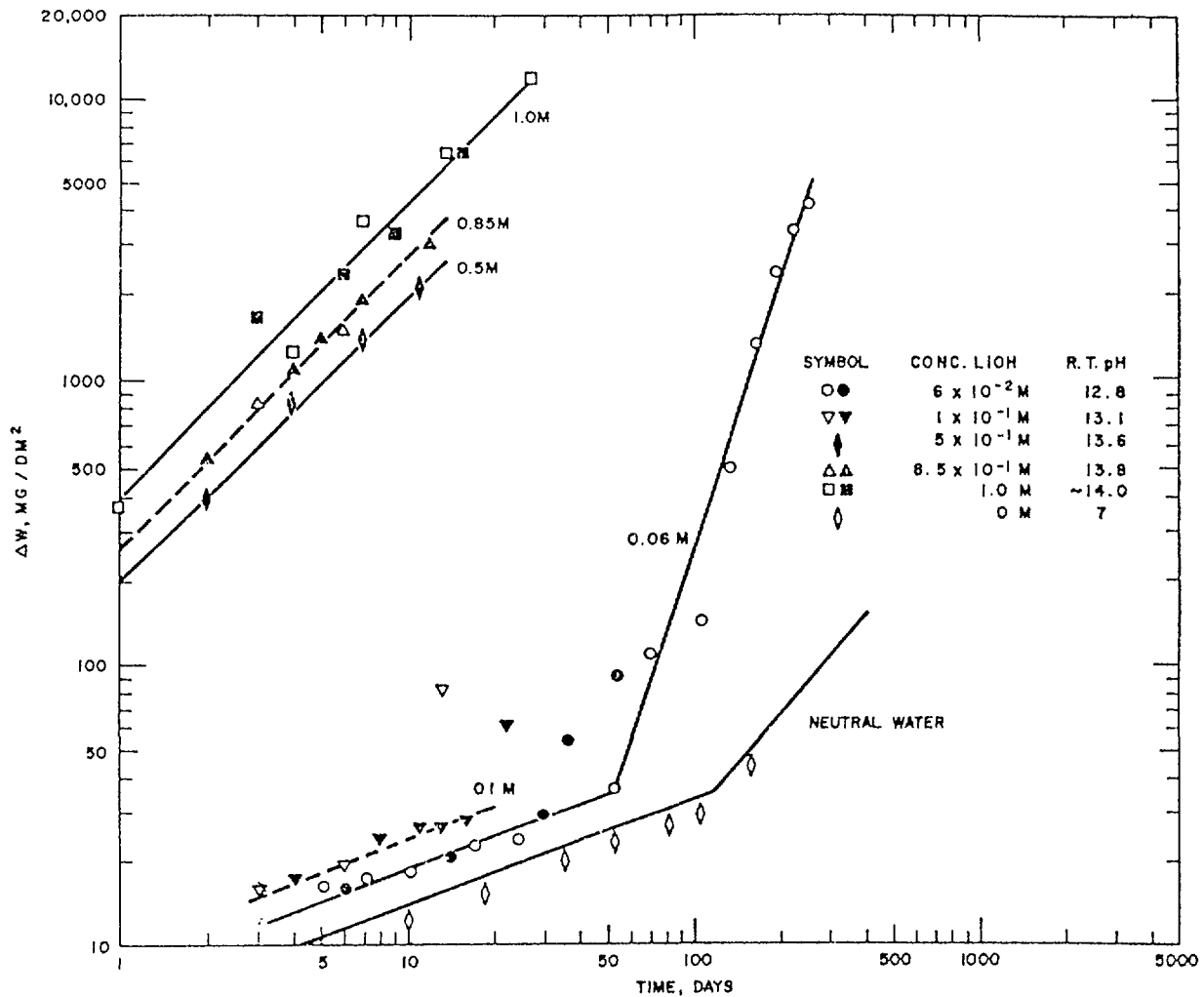


FIG. 5.14. Zircaloy weight gain in concentrated lithium hydroxide solutions (680 F) - static autoclaves [276].

examined oxide films from irradiated fuel cladding in the scanning electron microscope. Although there was considerable variability in both the morphology of the oxide/metal interface and fractures of these oxides no clear distinction between irradiated and unirradiated oxides was evident. A similar conclusion was reached by Cox [36] based on SEM examinations of the oxide/metal interface of irradiated and unirradiated oxides. Garzarolli's conclusions [223] that oxide films that had shown large in-reactor enhancements of corrosion rate were more crystalline in the oxide/metal interface region than comparable thickness unirradiated oxides [the latter often showed an apparently diffuse layer near to the oxide/metal interface] were based on judgements of the morphology seen in the SEM studies. Since this appearance at the edges of oxide samples can be affected in a major way by the imaging conditions, and in particular by local surface charging, these conclusions should be treated with caution. Until we have some TEM images of the oxide/metal interface region we will not be able to reach any firm conclusions on the degree of crystallinity of this region in irradiated oxide films.

The task of studying the oxide-metal interface in the transmission electron microscope is a difficult and thankless task. Even on unirradiated specimens the results are very difficult to interpret [262], and so limited evidence on irradiated specimens is only now becoming available. Nevertheless, evidence of this nature is vital to any understanding of the

effects of irradiation on corrosion, and despite its technical difficulty investigators should be encouraged to tackle this problem. It will be important that both bright and dark field studies be undertaken and the epitaxial relationships as well as the crystallinity of the oxide at the interface be examined.

5.2. EMPIRICAL CORRELATIONS OF EFFECTS OF IRRADIATION

Early in the study of the corrosion of zirconium alloys in aqueous reactor systems an example of grossly enhanced corrosion was observed during the development of the Homogenous Aqueous Reactor [280]. The primary cause of this rapid corrosion was the high energy deposition rate from the fissioning of the aqueous uranyl sulphate solution. The micromechanism by which this enhancement took place was not satisfactorily established, and the question of whether it resulted from enhanced solid state transport processes within the zirconium oxide, or enhanced dissolution and reprecipitation of that oxide appeared to favour the former as clear evidence for the latter was not found [281].

At much the same time evidence in PWRs suggested little or no enhancement of corrosion for the relatively short exposure times for which data were available [282], whereas early results in BWRs did show a significant increase in the corrosion rate [283]. In the latter instance, it was suggested that the poor metallurgical condition of the Zircaloy was an important factor, and subsequent improvements in behaviour have resulted largely from improvements in the physical metallurgy of the alloy. These have revolved around the production of material with a very small uniformly distributed second-phase precipitate population [45,46]. Mechanistic arguments supporting these fabrication changes have been based on observations made in ~500°C high pressure steam, and have been largely corroborated by the improved behaviour observed in BWRs [45,46].

In-reactor experimentation designed to provide accurate measurements of the solid state effects of irradiation on the corrosion process were mainly carried out in CO₂ [284], steam [285] or fog [286] rather than in aqueous systems and confirmed that increases in the oxidation rates of zirconium alloys did occur during the growth of barrier-type (pre-transition) oxide films (Figure 5.15). Despite some argument as to whether the surface temperature of the specimens was known and well controlled in the experiments in gas atmospheres, the similarity in the sizes of the effects seen in fog (where there were no specimen cooling problems) and the CO₂ and dry steam experiments suggests that these results are believable. However, the actual increases in rate under irradiation (as established by weight gain measurements) were small, and no evidence for very large effects was found in such experiments. Large effects seemed to be restricted to specific water chemistry conditions in aqueous systems. Estimates of oxidation rates in aqueous systems are often made from metallographic measurements of oxide thickness (a technique that is not very accurate for thin oxides), and such measurements in PWR chemistry showed little or no effect in the pre-transition period, with a significant increase in in-reactor corrosion rate after transition (Figure 5.16) [287]. Where measurements have been made after short exposures in aqueous systems by weight gain the results have often given lower values than expected from the out-reactor corrosion curve, or from the visual appearance of the oxide [141,288]. An example of the results from such a test is given in Table 5.2. Because the weights of the irradiated specimens have often been obtained on a different balance from that on which the initial weighing was done there has been a strong

TABLE 5.2. LOW WEIGHT GAINS OBSERVED IN SHORT IN-REACTOR LOOP TESTS
(second materials test bundle — U2500 phase II)

Material:	(See column headings)	Specimen Preparation:	Pickled
Specimen Size:	30 x 15 x 1 mm	Time:	25 days
Conditions:	pH 10 LiOH + H ₂ , ~260°C	Neutron Flux (>1 MeV):	1.9 x 10 ¹³ n _f v

	Zircaloy-2 (Ac)		Ni-free Zircaloy-2 (M)		Zr-2.5% Nb (T)		Zr-2.5% Nb -0.5% Cu (Am)		Zr-2.5% Nb-0.2% Fe-0.1% Cr (A)			
	ΔW (mg/dm ²)	ΔH (mg/dm ²)	ΔW (mg/dm ²)	ΔH (mg/dm ²)	ΔW (mg/dm ²)	ΔH (mg/dm ²)	ΔW (mg/dm ²)	ΔH (mg/dm ²)	ΔW (mg/dm ²)	ΔH (mg/dm ²)		
In-flux specimens	-9	1.367	4	0.343	(2.377)	(-22)	0.606	2	1.696	0	0.946	
	2	0.960	6	1.022	0.245	6	0.797	-9	(4.420)	2	(3.778)	
	-6	0.757	-4	8	(3.475)	0.678	2	1.563	0	1.545	(25)	0.718
	9	0.511	(22)	4	0.453	(4.853)	4	(14.0)	8	1.644	4	0.629
	4	0.873	2	2	(2.840)	0.790	0	0.558	11	(9.670)	2	0.496
	4	1.276	0	4	0.480	0.671	0	0.814	0	1.923	2	0.875
	(-30)	0.696	6	3	0.415	0.279	2	0.757	9	1.756	-4	(3.076)
	2	(3.671)	(16)	2	0.645	0.698	4	0.575	7	1.878	4	(77.0)
Means	0.85	0.918	2.8	0.561		2.6	0.808	3.5	1.74	1.4	0.733	
Appearance	Shiny black oxide		Shiny black oxide		Dark oxide showing pink interference colours		Black oxide		Black oxide			
Est. from film thickness	~15 mg/dm ² non-uniform		≥10 mg/dm ²		6-8 mg/dm ² non-uniform		≥10 mg/dm ²		≥10 mg/dm ²			
Lab. Autoclave	9-11 mg/dm ²		9-11 mg/dm ²		10-11 mg/dm ²		8-10 mg/dm ²		15-17 mg/dm ²			

NB: Figures in brackets have been omitted in calculating means

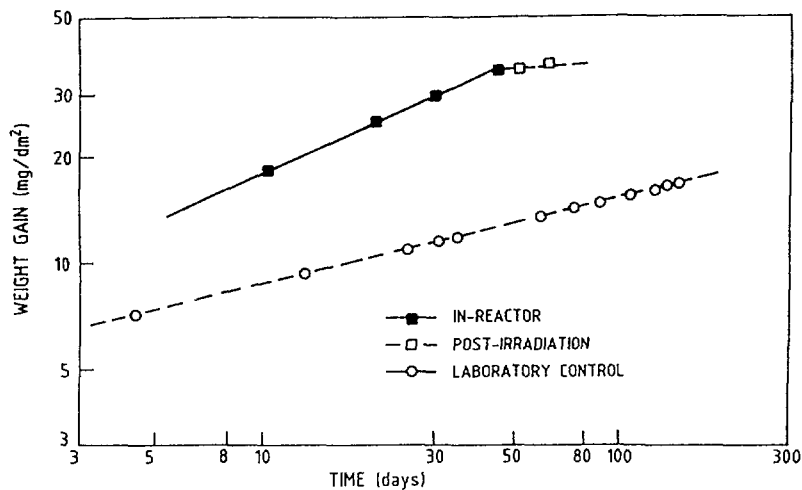


FIG. 5.15. Effect of irradiation on pretransition oxidation. The solid line refers to in-flux exposure, the dashed line to out-of-pile exposure [286].

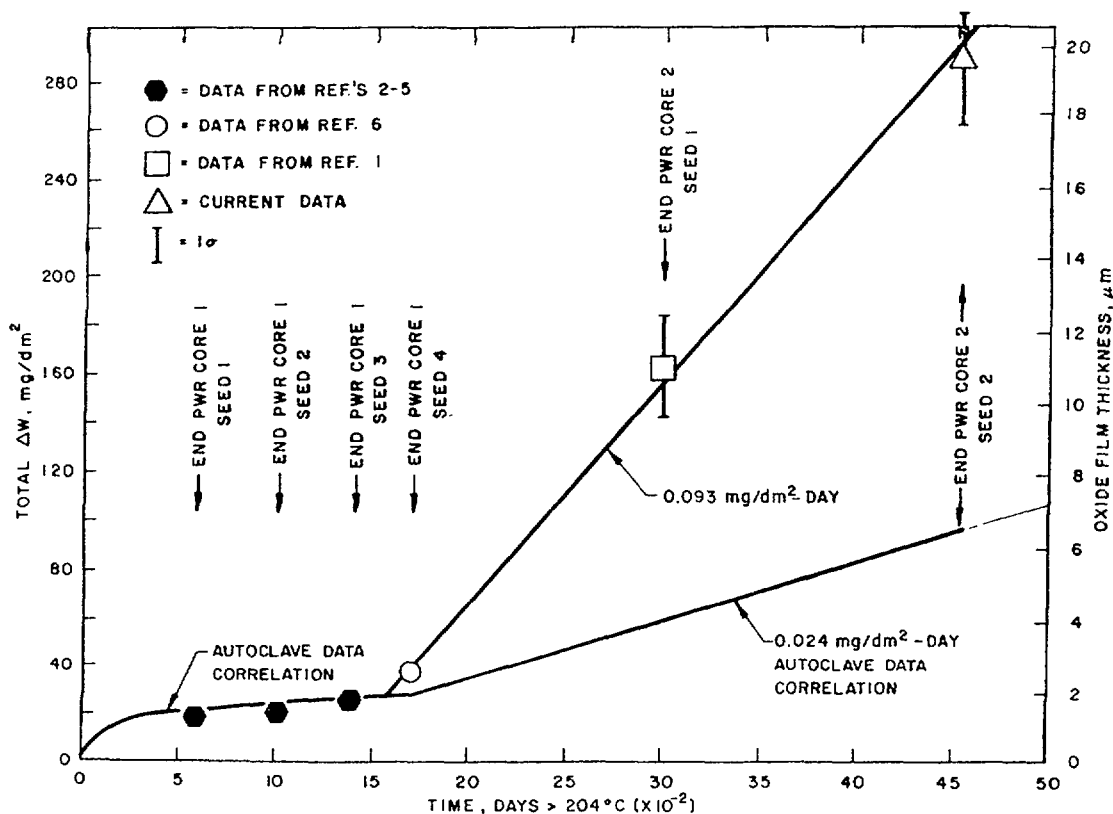


FIG. 5.16. Total weight gain as a function of exposure time for region 2 of rod 11 from bundle 0120 (references refer to the original figure in Ref. [287]).

temptation to dismiss these low weight gains as experimental error, and to concentrate on cases of clearly observed increased corrosion. Perhaps we have missed important clues to the material behaviour by so doing, since loss of ZrO_2 in this thin film region is difficult to explain except by a dissolution process.

5.2.1. Development of irradiation corrosion models

The enhanced corrosion in BWR-type water chemistries was shown to require both a high fast neutron flux and the presence of radiolysis

products in the water for its observation. As a result of this an hypothesis was proposed claiming that in order to see large increases in corrosion rate in-reactor both the ionic diffusion processes and the electronic transport processes in the oxide had to be accelerated. The acceleration of only one of these processes was insufficient, since the other one would then become rate limiting [5]. This hypothesis predicts certain shifts in the electrochemical polarisation curves of Zircaloy specimens undergoing enhanced corrosion that were not observed when experiments were set up to measure such effects using an accelerator as a radiation source [289]. Errors introduced in the polarisation curves by the 20 μ A proton beam current, while not entirely negligible, did not affect the overall conclusion that increases in ionic conductivity (and oxidation rate) were influenced primarily by the oxygen content of the coolant [289]. In the light of these results and subsequent evidence showing that enhanced corrosion seemed to be primarily a phenomenon of post-transition Zircaloy corrosion and was associated with the porosity of the oxide and processes going on in the pores, the above hypothesis was abandoned [290].

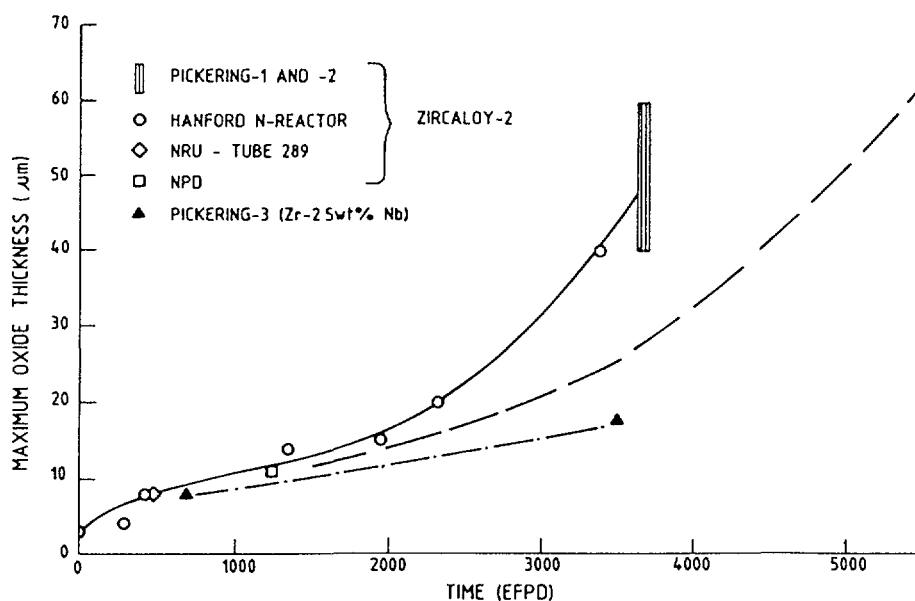


FIG. 5.17. Corrosion of zirconium alloy pressure tubes in reactor [108].

The observations [33,291] of accelerating corrosion rates with increasing oxide thickness above ~10 microns on both PHWR [Figure 5.17] pressure tubes (with no heat flux), and on PWR cladding (Figure 5.18), drew attention to Johnson's [109] earlier observations that changing the water chemistry from oxygenated to hydrogenated conditions produced no reduction in the corrosion rate of Zircaloy specimens already carrying oxide films thicker than a critical value. This "thick-film" hypothesis postulates that oxidation rates in-reactor increase above the critical thickness and continue to increase with increasing oxide thickness in PWR chemistry conditions because the chemistry inside the porous post-transition oxide progressively deviates from that in the bulk water as the oxide thickens. Chemistry conditions inside thick oxides are, thus, assumed to become more like a BWR chemistry.

While this hypothesis does not address the critical question of precisely what aspect of the BWR chemistry induces accelerated corrosion, and how this acceleration is achieved, it does qualitatively explain many of the observations of enhanced corrosion in PWR-type water chemistry. In particular it explains the similarity in the behaviour of Zircaloy-2

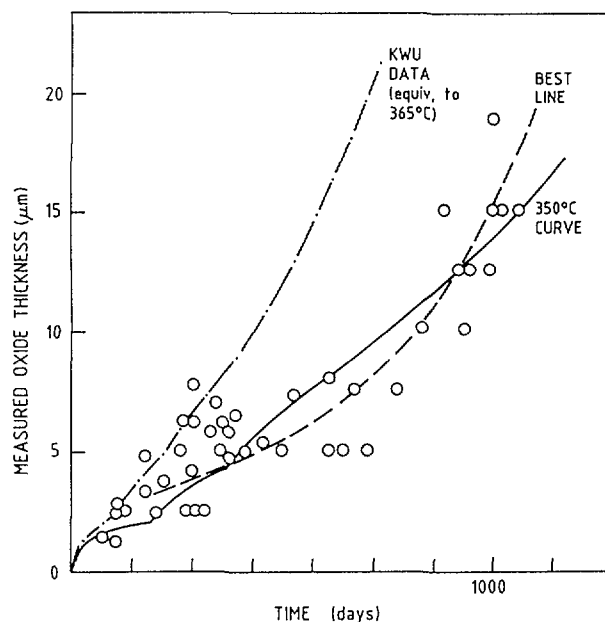


FIG. 5.18. Measured versus predicted oxide thickness in Westinghouse reactors with forced convective heat transfer, converted to an effective time scale [291].

pressure tubes in both N-reactor [111] and Pickering [33] despite the difference in chemistry. The N-reactor used NH_4OH for pH control while Pickering uses LiOH . However, the "thick-film" hypothesis depends upon an inability to replenish hydrogen within the porous oxide structure to permit the postulated change in water chemistry within the pores, and this is its fatal flaw. Firstly, in an initially hydrogenated aqueous system, hydrogen is not used up in suppressing water radiolysis, so that restricted diffusion down narrow pores is not an important factor. Secondly, after the development of porous post-transition films on the Zircalloys both the anodic and cathodic components of the oxidation process should be occurring at the outside of any residual barrier oxide layer and at the bottom of the pore network. Thus, provided that less than 100% of the hydrogen released by the cathodic part of the oxidation process is absorbed by the metal, enough hydrogen would be released into the pore network to provide a completely hydrogen environment if diffusion into the pores was not fast. In the presence of LiOH , since the corrosion reaction removes the water from the solution in the pores, a progressively concentrating LiOH solution will be present, again depending upon the extent of interdiffusion between the bulk water and that in the pores. Since hydrogen uptakes for Zircaloy-4 are usually less than ~20%, and seldom exceed 50-60% for Zircaloy-2 under irradiation it should be impossible to deplete the hydrogen in solution in the water in the porous oxide.

A simple calculation, for a 10 μm oxide film containing 10% porosity by volume (very much higher than measurements indicating $\leq 1\%$ porosity [223]), for conditions where the oxidation rate is 0.1 $\mu\text{m}/\text{day}$, and 50% of the corrosion hydrogen is absorbed by the metal, shows that enough hydrogen to fill the pores with 100 atm hydrogen gas is released every 10 hours, and that the water content of the pores is converted to new zirconium oxide and hydrogen approximately every 3 days. Thus the precise conditions within the pore network will depend critically on pore size and interconnection and the effect that these will have on the degree to which the contents of the pores can mix with the bulk water. Under heat flux conditions in fuel cladding the pores may be filled with steam rather than water. Nevertheless, whatever the contents of the pores it seems unlikely that they can ever be other than highly hydrogenated and significant LiOH

concentration in the pores is clearly feasible, even in the absence of a heat flux.

Until we have a clear idea of just how the porosity develops in ZrO_2 films and how major factors such as LiOH affect it, we are in a poor position to understand irradiation effects. KWU studies [223] show only minor differences between irradiated and unirradiated oxide films, but do suggest that oxides on samples showing increased corrosion are more crystalline than others, leading to a suggestion that irradiation enhances recrystallisation of the oxide. However, as we have no clear demonstration of just how oxide recrystallisation processes and oxide porosity are linked, and as the results cited [223] were based on a technique that does not unequivocally measure crystallite size, this hypothesis remains largely speculative.

There have been prolonged arguments about the extent to which the corrosion rates of PWR cladding can be explained purely on the basis of out-reactor corrosion data and the thermal hydraulics of the system [111], or whether an additional enhancement factor is needed [292]. Furthermore, whether such an enhancement factor is an irradiation effect [292], results from LiOH concentration effects [211], or arises from some other phenomenon is not yet resolved. At present it appears that, since LiOH concentration can occur whether or not a heat flux is present, most observations of enhanced corrosion in LiOH solutions could be explained by such a concentration effect. The differences in the behaviour of different batches of cladding could be explained by variations in the porosity of the oxide, and, hence, in the extent of mixing of the solution in the pores with bulk water. The effect of LiOH concentration is well established in the laboratory, however, testing of cladding batches at low to intermediate Li^+ concentrations, and examination of the pore structure of post-transition oxide films would seem to be an area where more work is warranted. The mathematical correlations on which these arguments were based contain enough constants of uncertain value that it seems unlikely that universal agreement in this area will ever be reached. However, the abilities of these largely thermal-hydraulic models to correctly estimate both the maximum intergrid oxide thickness and the minimum thickness at grid positions is still a severe test that most models fail. The micromechanistic content of them is small anyway.

Although we seem to be able to qualitatively explain effects in LiOH solutions by concentrations in the porous oxide, possible effects of boric acid are a confounding factor. Tice et al [293] have claimed that boric acid suppressed the accelerating effects of LiOH on unirradiated specimens in mixtures of the two. However, this study lacked adequate control specimens and a sounder study of effects in LiOH/ H_3BO_3 mixtures is badly needed because of its importance to PWR operation, where suggestions to raise the Li^+ content of the water continue to be made. A potential for increased corrosion in high water temperature plants at high burnup would seem to exist if such increases are put into practice. Furthermore, if boric acid functions to mitigate the effects of LiOH concentration on zirconium oxidation in the same manner as it appears to inhibit denting on the secondary side of steam generators (namely by physically plugging pores in oxide films by depositing insoluble borates) then it may be rendered ineffective at high burnups because most of the ^{10}B sequestered in the pores in the oxide will be rapidly transmuted to 7Li . Thus after long times it may actually serve to enhance lithium concentration in the oxide. However, the final location of such lithium is uncertain as recoil of 7Li during transmutation may inject it into the oxide lattice.

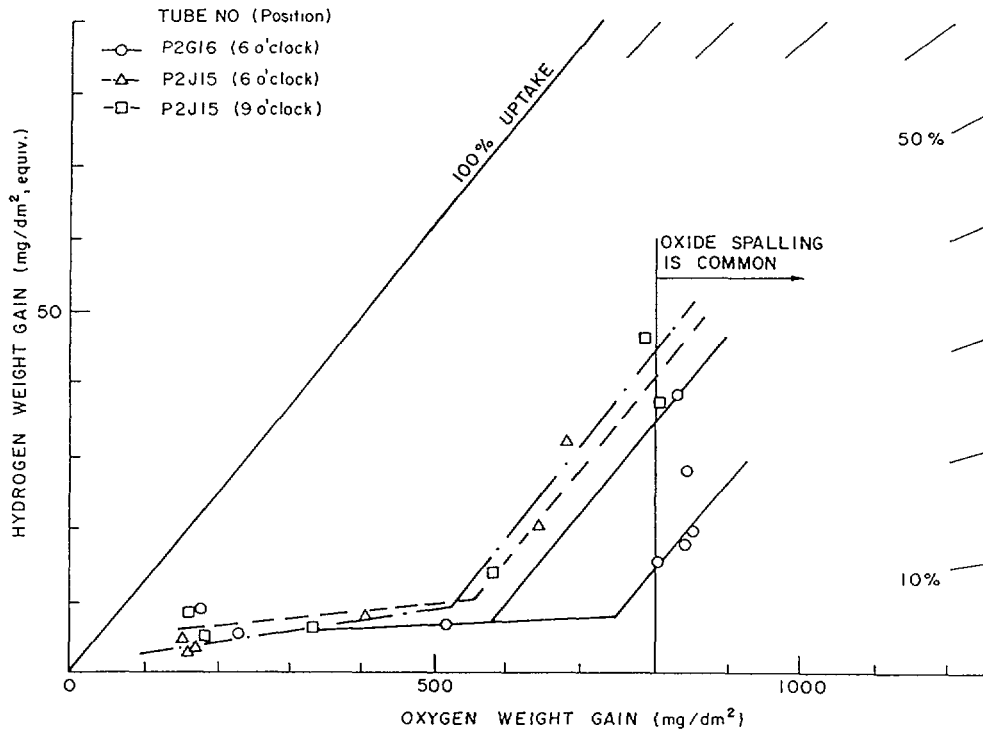


FIG. 5.19. Change in fractional uptake rate for oxide films on Zircaloy-2 $>30 \mu\text{m}$ (from B. Cox, AECL-9180, 1986).

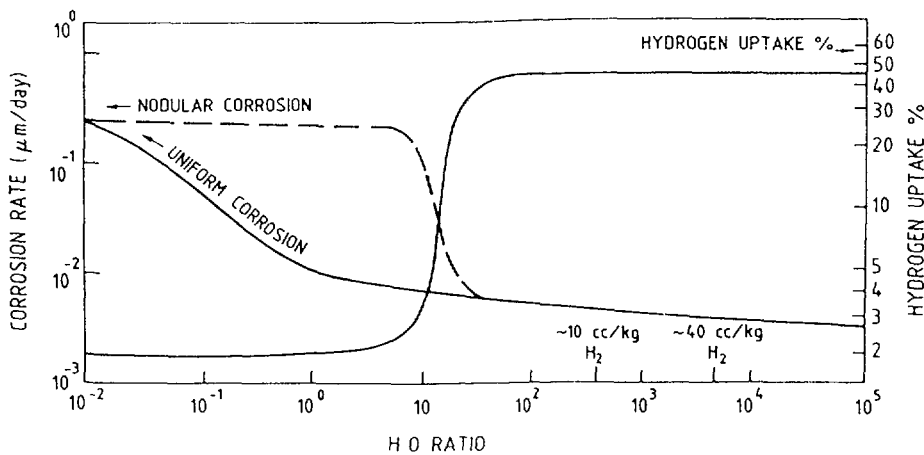


FIG. 5.20. Effect of H:O ratio in water on corrosion and hydrogen uptake in-reactor [294].

A further area in which Li^+ concentration effects are better able to explain the observations than the thick film hypothesis is that of enhanced hydrogen uptake percentages accompanying the enhanced corrosion of PHWR pressure tubes (Figure 5.19) [33]. If the enhanced corrosion arises from a BWR like water chemistry in the oxide film, then the hydrogen uptake percentage should go down (Figure 5.20) [294], although increases in hydrogen uptake were observed for Johnson's specimens with thick oxide films when hydrogen was added to the system [109], even though no reduction in oxidation rate was observed (Figure 5.21). While the uptake percentage did apparently rise to 100% following the acceleration of the oxidation of the Zircaloy-2 pressure tubes in Pickering, and would, therefore, have permitted a shift to oxidising conditions within the porous oxide, this must have been an effect and not a cause of the accelerated oxidation, since the oxidation rate increased before the hydrogen uptake rate [33]. That some of this deuterium may have been absorbed from the gas annulus

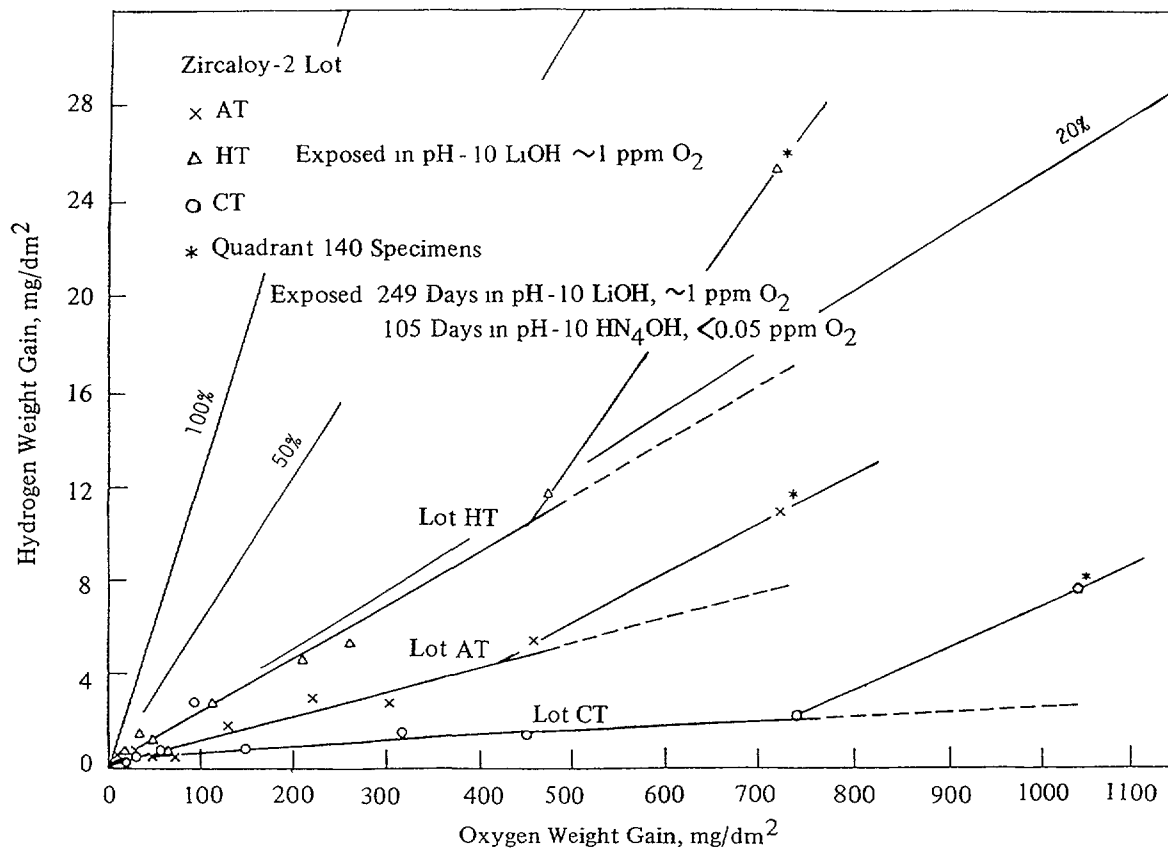


FIG. 5.21. In-flux hydrogen weight gain as a function of in-flux oxygen weight gain [109].

side of these pressure tubes is an additional confounding factor in attempts to understand these observations.

Johnson observed identical effects in both NH₄OH and LiOH in the ETR loop tests; and the similarities between N-reactor (NH₄OH) [107] and Pickering (LiOH) [33] pressure tube oxidation have been alluded to previously. Since NH₄OH concentration in the laboratory has no effect on the corrosion of the Zircaloys, these similarities are a major problem for any hypothesis explaining in-reactor effects on the basis of LiOH concentration. Occam's Razor tells us that we should prefer the simplest hypothesis that explains the most observations; this is clearly the thick-film hypothesis, but this hypothesis seems to be fatally flawed based on our present understanding of the post-transition corrosion mechanism for the Zircaloys. Do we then need a completely new hypothesis or is there an irradiation effect on the chemistry of concentrated NH₄OH that can cause a similar effect on Zircaloy oxidation to the laboratory effect of LiOH. This seems to be an area where no work has been done.

Before finishing it should be pointed out that the hypothesis that explains nodular corrosion in BWRs as an effect of oxidising species in the water produced by radiolysis is equally flawed. While such an hypothesis may describe the initiation of nodules (we have no agreed site for their initiation), once formed, a nodule is merely another area of porous zirconium oxide, hydrogen uptakes are very low, and therefore any water or steam in the pores of this oxide must be highly hydrogenated. Even in the presence of hard crud layers a steam filled crack is necessary, either in the crud or the oxide, to permit temperatures at the oxide/metal interface to come anywhere near to those of the 500°C steam test that in the laboratory shows such similar nodular corrosion to the in-reactor behaviour. Are we again missing some vital step in the mechanism that can

get us to this situation? Obviously the proposed CILC mechanisms [295,296] function logically once conditions in the oxide become similar to a 500°C steam test, and a radiolytic species hypothesis may satisfy the conditions for nodule initiation, although it lacks a detailed micromechanism for relating the radiolytic species to nodule initiation. The overall hypothesis breaks down in bridging the gap between nodule initiation and the onset of gross CILC failure. If an embryonic nodular oxide becomes filled with hydrogenated water immediately after initiation, when the oxide is still thin and temperatures at the oxide-metal interface are still close to 300°C then it should not develop into a visible nodule and the whole subsequent development should be stifled. Clearly there is some component of the process that is not being considered.

The factor that is least often considered mechanistically, although its effects are well known practically in reactor operations, is the chemistry or electrochemistry of other species in the water. Of these the one that appears most prominently to affect the corrosion is the copper content of the water [297]. While copper was recognised early [295] as a major factor in the formation of the hard crud layers leading to the grosser forms of CILC failure, its importance in the early nodule nucleation and growth stages is not well documented. Nevertheless, it appears to be equally important at this stage of nodule growth, even at low concentration (Figure 5.22). Since copper is close to its redox potential in 300°C water, the initial state of the copper (soluble or insoluble) and small changes in water chemistry that can change this state would appear to be important. The only other commonly occurring transition metal that is easily reducible in 300°C water is nickel. Additionally, the reduction of soluble cupric or nickelous ions to metallic copper or nickel at some intermetallic sites on the Zircalloys may provide a permanent cathode for the zirconium oxidation process that could locally enhance the anodic process (i.e. oxide growth) and might maintain the proton reduction reaction on the surface of a porous film, thus preventing the water in the pores from becoming highly hydrogenated. Features that might be described as embryonic nodules were seen to start at flaws (second-phase particles?) in zirconium samples that were short-circuited during oxidation (Figure 5.23), but not in normally oxidised specimens [28]. Perhaps one contribution of irradiation to such initiation steps is to effectively short-circuit the oxide by producing large numbers of electron-hole pairs.

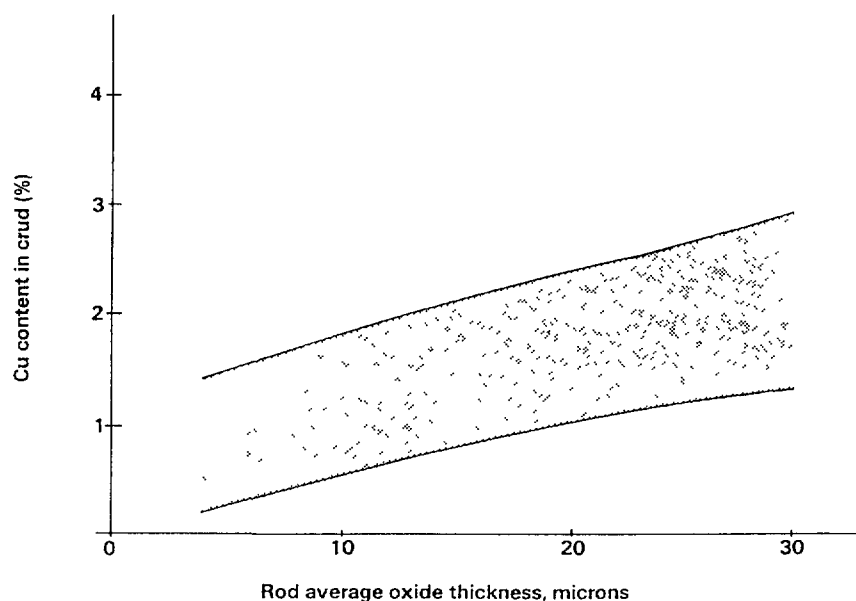


FIG. 5.22. Correlation between Cu content in the crud and oxide thickness in Barsebeck 1 [297].

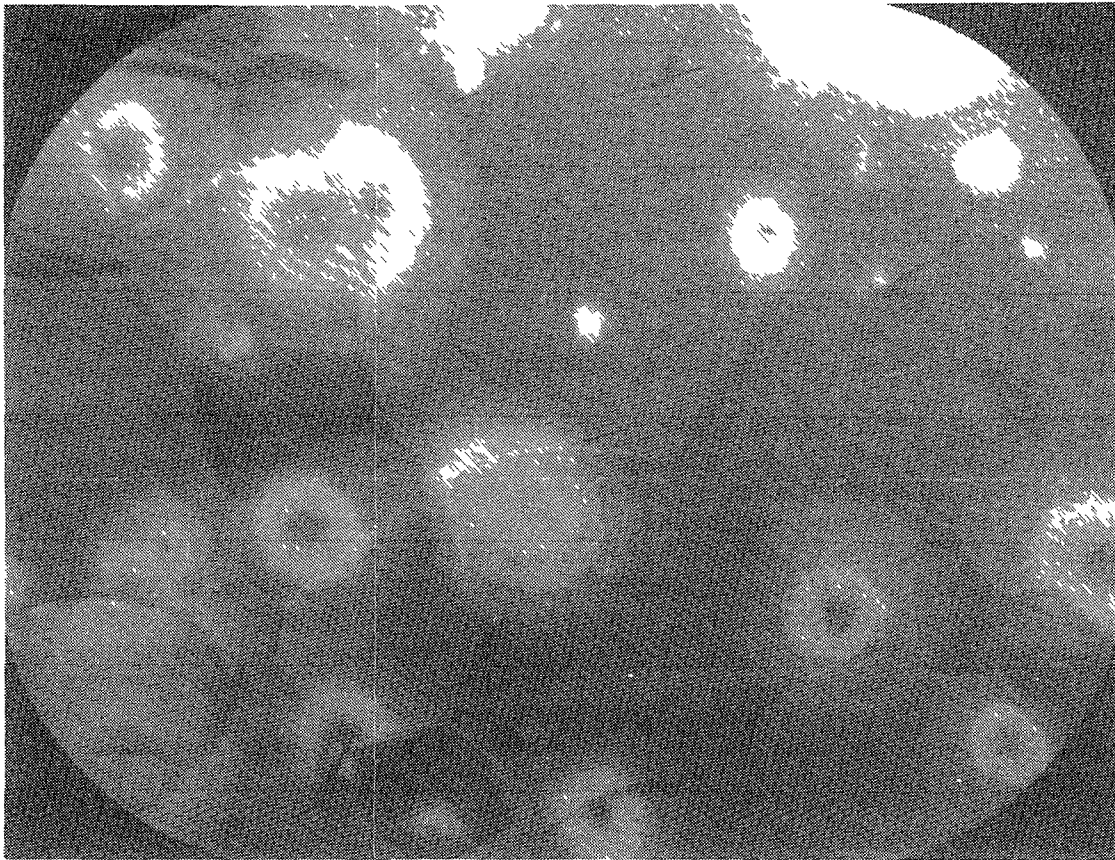


FIG. 5.23. Localized oxidation at second phase particles resulting from short-circuiting the oxide film.

This is clearly speculative at present and represents an area of investigation that has not been addressed. Perhaps such studies could provide a micromechanism that could bridge the gap between nodule initiation in 300°C water and the later stage of CILC failures where conditions in the oxide become more like a 500°C steam test. There is certainly evidence for copper deposition within cracks in the zirconia film during CILC failures [296], but the chemical form of it is unknown, as is its role as either cause or effect of the cladding degradation.

5.2.2. Micromechanisms for in-reactor corrosion

At present the development of our understanding of the in-reactor corrosion of zirconium alloys is restricted by our lack of well authenticated micromechanisms for the basic processes accompanying the development of porous oxide films

(i) We do not know whether the porosity that develops at the rate transition originates at the outer surface of the oxide and grows in towards the metal-oxide interface, or whether it initiates randomly within the oxide and links up to finally form a network connected with the outside surface [35].

(ii) The development of oxide porosity in reactor is closely linked to observations of enhanced corrosion. Recent evidence [141] suggests that it may originate much earlier than would be expected from the laboratory observations. Does this arise by an acceleration of the laboratory process, or is a new process (dissolution and reprecipitation?) participating in the effect under irradiation? Quantities of zirconia appear at a variety of locations in a reactor system, however, it has always appeared to be

impossible to establish whether they arrive there as species in solution or as particles of oxide that could be released from the alloy surface by fretting or spalling. In some situations it appears that only transport in solution could explain the observations, however, careful study of these circumstances has not been possible, and so, it remains impossible to say whether or not an in-reactor solution and reprecipitation of ZrO_2 is a realistic micro-mechanism.

(iii) We still know virtually nothing about the electrochemistry of zirconium alloys in 300°C water, and in particular about variations in surface electrochemical potential at intermetallic sites, and the extent to which local redox potentials vary with small changes in water chemistry. Until we understand this aspect of the process more clearly we will be unable to factor-in the galvanic effects that seem to be visibly involved in the in-reactor corrosion process in BWRs.

5.2.3. Present status of mechanistic studies

After many years of studying in-reactor corrosion of zirconium alloys we are still without any scientifically sound hypothesis that explains what is going on. Progress in our understanding of the processes, and improvements in the future performance of zirconium alloys in reactor, clearly need sound micromechanistic hypotheses whose predictions can be tested. At present we seem to be doing little experimentation that will resolve this, and recent advances in the performance of fuel cladding have usually resulted from an "ad hoc" engineering development approach.

5.2.4. Recommendations for future work

Throughout the above discussion, gaps in our knowledge that should be considered for future investigation have been identified. On considering the field as a whole it is our opinion that the following areas are most in need of concerted experimental efforts to resolve them:-

(a) Studies of the local electrochemistry of oxidized Zircaloy surfaces at elevated temperature, and preferably either in-reactor or in a high γ -radiation field. Techniques should be capable of resolving the local electrochemical potential at intermetallic particles (or their oxidized products) in the surface of the specimen.

(b) Polarisation studies, of the type performed by Norfolk et al [289] using proton irradiation, should be carried out in-reactor (or an in-reactor loop) in conditions typical of a BWR.

(c) A detailed study of radiation chemistry, and the behaviour of impurity species in porous zirconia systems should be initiated.

(d) A concerted effort is needed to understand the nature of the porosity in zirconium oxide films and the mechanisms that generate it.

6. CONCLUSIONS

The performance of zirconium alloy clad fuel in water-cooled reactors has been generally excellent. Instances where fuel behaviour has been less satisfactory than expected are few, but significant, as they indicate that the limits of acceptable behaviour of the cladding are being reached. As a result of pressure to maximise the value obtained from the fuel, by going to as high a burnup as possible, an increase in occurrences of unsatisfactory end-of-life behaviour is expected. Although it has been common in the past to alleviate such problems by the adoption of an "ad hoc" engineering approach to their solution, the present situation requires an improved fundamental understanding of the micromechanisms involved if any solution is to be founded on a sound scientific base.

Because of the pressure to develop improved fuel cladding alloys for very high burnup applications, a resurgence of research interest in the area of the irradiation corrosion behaviour of zirconium alloys is evident. As a result of this, previous hypotheses explaining the phenomena have been found wanting, and many new hypotheses are being proposed, but have not yet become established. In this rapidly evolving state of the research very different views of the causative factors are being proposed. Although the members of the group responsible for the preparation of this document were in general agreement on the phenomena being observed, and the extent of the gaps in our knowledge of the mechanisms, it is hardly surprising, in the present state of flux in our scientific understanding, that not all the arguments presented herein should be accepted by all of the participants.

The conclusions in this document should be viewed, in the light of the rapidly evolving development of the mechanistic understanding of the phenomena, as an attempt to present a series of snapshots of current ideas in specific areas of study that are relevant to the whole problem. An attempt to present an agreed micromechanistic hypothesis that explains the overall phenomena must await further investigations. Throughout the text the authors have endeavoured to indicate where critical gaps in our basic knowledge lie. It is hoped that, thereby, further investigation in these areas will be stimulated.

In describing the situation in-reactor, a clear distinction was seen between "Corrosion under irradiation" and "Irradiation induced corrosion". The former was perceived to describe a situation wherein corrosion rates under irradiation differ from those predicted from laboratory data based only on the temperature dependence of these data; any local changes in water chemistry; and a thermal hydraulic calculation of the oxide-metal interface temperature. The latter describes a change in corrosion rate arising from a direct effect of some component of the radiation field on a rate controlling step in the corrosion process, wherever this step may be. In such a case the effect could not be simulated without the use of irradiation.

Most work that assesses the in-reactor behaviour of zirconium alloys finds a small factorial difference that cannot be predicted purely from laboratory data and thermal hydraulics. There is, however, no agreement as to whether this difference results from a direct effect of irradiation, or whether some other factor (e.g. Li^+ concentration in PWRs, or Cu deposition in BWRs, etc.) can explain the observed differences.

In order to provide an improved understanding of the phenomena, a close interaction is needed between those workers involved in studies in-reactor of those factors influencing the corrosion behaviour of both

current and potential future cladding alloys, and those workers performing experiments to study the micromechanistic processes. With the limited potential to conduct such research in any one country, co-operative research projects are to be encouraged. In achieving this, periodic meetings to exchange information and discuss the state of the field are particularly valuable, if organized in a Workshop format. The recently sponsored IAEA Technical Committee Meeting in Portland, Oregon (September 1989) was an example of such a meeting. The organization of collaborative research programmes in this area, such as the Nuclear Fuel Industry Research (NFIR) group sponsored by the Electric Power Research Institute, is another example of a organization that brings together active workers in the field to discuss specific problems and sponsor research in specific areas. Further collaborative efforts along these lines are to be encouraged.

In evaluating the results of experiments on irradiation corrosion at various locations it is evident that comparability is often lost either through too great a divergence between the experimental conditions, or a failure to measure or report critical parameters of the experiments. It is particularly important to document all the conditions of an experiment in the current state of our mechanistic knowledge, because it is still far from clear how important some of these factors are. Thus, some agreed standardisation of experimental conditions, or of the reporting of specific parameters for all experiments would aid in the comparison of experiment and theory. If by pointing out the above shortcomings in the present state of the field, we can aid in its future understanding, then the efforts of this group will have been justified.

APPENDIX

It is assumed that a deep crack or pore with a constant area of cross section (S) is under irradiation in a thick oxide layer on Zircaloy, and that hydrogen is sufficiently supplied outside the pore (concentration Y_0) and diffuses inside the pore where it is depleted by reaction (14). Attention is paid only to the OH radical as a reactive transient species for the simplicity. Mass balance equations are expressed as follows, assuming one-dimensional diffusion:

$$Sdx \frac{\partial Y}{\partial t} = -SD_Y \frac{\partial Y}{\partial x} + g_Y Sdx + SD_Y \left[\frac{\partial Y}{\partial x} + \left(\frac{\partial^2 Y}{\partial x^2} \right) dx \right] - kZY Sdx \quad (A1)$$

$$Sdx \frac{\partial Z}{\partial t} = -SD_Z \frac{\partial Z}{\partial x} + g_Z Sdx + SD_Z \left[\frac{\partial Z}{\partial x} + \left(\frac{\partial^2 Z}{\partial x^2} \right) dx \right] - k'Z^2 Sdx - kYZ Sdx \quad (A2)$$

Where Y and Z refer to the concentrations of H_2 and OH at a distance x from the inlet of the pore, respectively, D_Y and D_Z are diffusion constants for H_2 and OH, g_Y and g_Z are the production rates of H_2 and OH by radiolysis, and k and k' are the rate constants of reaction (19) and the second order decay constant of OH, respectively. In this treatment the surface reactions in which OH radical may be involved and the hydrogen formation in the course of the corrosion process (reaction 13) are neglected.

In the steady state Eqs (A1) and (A2) are reduced to Eqs (A3) and (A4).

$$d^2 Y / dx^2 - (k/D_Y)ZY + g_Y/D_Y = 0 \quad (A3)$$

$$d^2 Z / dx^2 - (k'/D_Z)Z^2 - (k/D_Z)YZ = g_Z/D_Z = 0 \quad (A4)$$

A very simple approximation is introduced here to derive a rough concentration profile for hydrogen in the pore.

Now, if the concentration of OH, (Z), is assumed to be constant and independent of distance x, taking an average value Z_{av} , then Eq. (A3) may be solved straightforwardly. The boundary conditions and the final solution are given below:

$$x = 0 \quad Y = Y_0$$

$$x = \infty \quad dY/dx = 0$$

$$Y = (Y_0 - g_Y/kZ_{av}) \exp(-\sqrt{kZ_{av}/D_Y} x) + g_Y/kZ_{av} \quad (A5)$$

The value of Y_0 is estimated to be $1 \times 10^{-3} \text{ mol.dm}^{-3}$ (corresponding to PWR conditions and g_Y is calculated to be approximately $2 \times 10^{-3} \text{ mol.dm}^{-3} \cdot \text{s}^{-1}$ (assuming an average primary G value of 0.65 for H_2 and an average dose rate of $4.3 \times 10^4 \text{ Gy/s}$ in the core) [192]. The rate constant of reaction (19), k, and the diffusion constant of H_2 , D_Y , in water, at 300°C are estimated to be $1.3 \times 10^9 \text{ dm}^{-3} \cdot \text{mol}^{-1} \cdot \text{s}^{-1}$ [193,194] and $5.7 \times 10^{-6} \text{ dm}^2 \cdot \text{s}^{-1}$ [178] respectively, assuming an activation energy of 12.5 kJ/mol for the

TABLE A.1. CALCULATED PROFILES OF HYDROGEN CONCENTRATION IN PORE

Distance $x/10^{-6}$ m	$[H_2]$ $[H_2]_0$ $[OH]_{av} = 1 \times 10^{-7} \text{ mol dm}^{-3}$	$[H_2]/[H_2]_0$ $[OH]_{av} = 1 \times 10^{-6} \text{ mol dm}^{-3}$
0	1.0	1.0
1	0.95	0.86
5	0.79	0.46
10	0.62	0.21
15	0.49	0.098
20	0.39	0.046
25	0.30	0.021

latter. The value of Z_{av} is taken to be a parameter, and the ratios Y/Y_0 ($[H_2]/[H_2]_0$) calculated using the above estimated values are shown as a function of distance x in Table A.1 for two values of Z_{av} , 1×10^{-7} and $1 \times 10^{-6} \text{ mol.dm}^{-3}$. As seen from the Table, the ratio $[H_2]/[H_2]_0$ is largely dependent on parameter Z_{av} . The values used here are very close to these estimated in a computer simulation of a BWR core [192].

The Table shows that the concentration of hydrogen is reduced two order of magnitude at the distance of $25 \mu\text{m}$ from the inlet of the pore, if Z_{av} is assumed to be $1 \times 10^{-6} \text{ mol.dm}^{-3}$, and it is too low to maintain the suppression effect of hydrogen on Zircaloy corrosion there.

REFERENCES

- [1] Outlook on Materials, Special Report to the Readers of Nucleonics Week, Jan.4 (1990) 12.
- [2] NECHAEV, A., "Trends in the nuclear fuel cycle: Development in the 1990s and international co-operation", Nuclear Fuel Cycle in the 1990s and Beyond the Century: Some Trends and Foreseeable Problems, Technical Reports Series No. 305, IAEA, Vienna (1989) 1-15.
- [3] NECHAEV, A., SKJOELDEBRAND, R., "IAEA programme on water chemistry in nuclear power plants: status and tendencies", Water Chemistry in Nuclear Power Plants (Proc. Int. Conf. Tokyo, 1988), JAIF, 1 (1988) 42-48.
- [4] KOMAREK, K.L., SILVER, M., "Thermodynamic properties of zirconium–oxygen, titanium–oxygen and hafnium–oxygen alloys", Thermodynamics of Nuclear Materials (Proc. Int. Conf. Vienna, 1962), IAEA, Vienna (1962) 749–774.
- [5] COX, B., "Oxidation of zirconium and its alloys", Advances in Corrosion Science and Technology, Vol. V (FONTANA, M. G., STAEHLE, R.W., Eds), Plenum Press, New York (1976) 173.
- [6] DOERFFLER, W.W., A Contribution to the Mechanism of Dissolution and Diffusion of Oxygen in Zirconium, Rep. EIR-82, Würenlingen (1965).
- [7] WANKLYN, J.N., Corrosion of Zirconium Alloys, ASTM-STP-368, American Society for Testing and Materials, Philadelphia, PA (1964) 66.
- [8] COX, B., The zirconium–zirconia interface, J. Aust. Inst. Met. 14 (1969) 123.
- [9] LUSTMAN, B., KERZE, F., Metallurgy of Zirconium, McGraw Hill, New York (1955).
- [10] KASS, S., The Development of the Zircalloys, ASTM-STP-368, American Society for Testing and Materials, Philadelphia, PA (1964) 3.
- [11] COX, B., ROY, C., Transport of oxygen in oxide films on zirconium determined by the nuclear reaction $O^{17}(\text{He}^3, \alpha)O^{16}$, Electrochem. Technol. 4 (1966) 121.
- [12] COX, B., PEMSLER, J.P., Diffusion of oxygen in growing zirconia films, J. Nucl. Mater. 28 (1968) 73.
- [13] PLOC, R.A., Transmission of electron microscopy of thin (<2000 Å) thermally formed ZrO_2 films, J. Nucl. Mater. 28 (1968) 48.
- [14] DAVID, G., GESCHIER, R., ROY, C., Etude de la croissance de l'oxyde sur le zirconium et le Zircaloy-2, J. Nucl. Mater. 38 (1971) 329.
- [15] PLOC, R.A., Electron Diffraction Analysis of ZrO_2 on α -Zr (1120), J. Nucl. Mater. 113 (1983) 75.
- [16] PLOC, R.A., A Theoretical Treatment of Zr/ ZrO_2 Epitaxy, Rep. AECL 2751, Atomic Energy of Canada Ltd, Chalk River Nuclear Laboratories (1967).
- [17] DONALDSON, A.T., EVANS, H.E., Oxidation-Induced Creep in Zircaloy-2, Pts I-III, Reports RD/T/N4855, 4952 and 4976, Central Electricity Generating Board, Berkeley Nuclear Laboratories (1980).
- [18] COX, B., Low temperature (<300°C) oxidation of Zircaloy-2 in water, J. Nucl. Mater. 25 (1968) 310.
- [19] PETERS, H.R., Improved Characterisation of Aqueous Corrosion Kinetics of Zircaloy-4, ASTM-STP-824, American Society for Testing and Materials, Philadelphia, PA (1984) 507.
- [20] DAWSON, J.K., LONG, G., SEDDON, W.E., WHITE, J.F., The kinetics and mechanism of the oxidation of Zircaloy-2 at 350–500°C, J. Nucl. Mater. 25 (1968) 179.
- [21] GRIGGS, B., MAFFEI, H.P., SHANNON, D.W., Multiple rate transitions in the aqueous corrosion of Zircaloy, J. Electrochem. Soc. 109 (1962) 665.
- [22] COX, B., Processes occurring during the breakdown of oxide films on zirconium alloys, J. Nucl. Mater. 29 (1969) 50.
- [23] BRADHURST, D.H., HEUER, P.M., The influence of oxide stress on the breakaway oxidation of Zircaloy-2, J. Nucl. Mater. 37 (1970) 35.
- [24] COX, B., Comments on the Paper, The influence of oxide stress on the breakaway oxidation of Zircaloy-2, J. Nucl. Mater. 41 (1971) 96.
- [25] CORIOU, H., GRALL, L., WILLERMOZ, H., Influence du Cyclage Thermique sur la Corrosion due Zircaloy-2 dans l'Eau ou la Vapeur à 360°C et sur l'Absorption de

- l'Hydrogène par le Métal", Rep. DM 1005, Commissariat à l'Energie Atomique, Saclay (1961).
- [26] SHIRVINGTON, P.J., COX, B., A study of charge transport processes during the oxidation of zirconium alloys, *J. Nucl. Mater.* **35** (1970) 211.
- [27] SHIRVINGTON, P.J., Electron conduction through oxide films on Zircaloy-2, *J. Nucl. Mater.* **37** (1970) 177.
- [28] COX, B., Rate controlling processes during the pre-transition oxidation of zirconium alloys, *J. Nucl. Mater.* **31** (1969) 48.
- [29] PLOC, R.A., Oxidation Kinetics and Auger Microprobe Analysis of Some Oxidised Zirconium Alloys, ASTM-STP-1023, American Society for Testing and Materials, Philadelphia, PA (1989) 498.
- [30] SAWICKI, J.A., MAREST, G., COX, B., JULIEN, S.R., Mossbauer spectroscopy of iron implanted and doped in ZrO₂, *Nucl. Instrum. Methods* **B32** (1988) 79.
- [31] COX, B., A porosimeter for determining the sizes of flaws in zirconia or other insulating films 'in situ', *J. Nucl. Mater.* **27** (1968) 1.
- [32] KASS, S., Corrosion of prefilmed Zircaloy, *Corrosion* **23** (1967) 374.
- [33] URBANIC, V.F., COX, B., FIELD, G.J., Long-Term Corrosion and Deuterium Uptake in CANDU-PHW Pressure Tubes, ASTM-STP-939, American Society for Testing and Materials, Philadelphia, PA (1987) 189.
- [34] PLOC, R.A., "Existence of cubic ZrO₂ at 300°C on bulk zirconium" (Proc. 27th Ann. EMSA Conf., St. Paul, MN), Electron Microscopical Society of America (1969) 166.
- [35] COX, B., "Are Zirconia Corrosion Films a Form of Partially Stabilised Zirconia (PSZ)?" , Rep. AECL 9382, Atomic Energy of Canada Ltd, Chalk River Nuclear Laboratories (1987).
- [36] COX, B., Pore structure in oxide films on irradiated and unirradiated zirconium alloys, *J. Nucl. Mater.* **148** (1987) 332.
- [37] FIDLERIS, V., The irradiation creep and growth phenomena, *J. Nucl. Mater.* **159** (1988) 22.
- [38] BUTLER, E.P., BONANOS, N., The characterisation of ZrO₂ engineering ceramics by A.C. impedance, *Mater. Sci. Eng.* **71** (1985) 49.
- [39] RAMASUBRAMANIAN, N., PREOCANIN, N., LING, V.C., Lithium Uptake and the Accelerated Corrosion of Zirconium Alloys, ASTM-STP-1023, American Society for Testing and Materials, Philadelphia, PA (1989) 187.
- [40] COX, B., "Factors controlling the corrosion behaviour of zirconium alloys under irradiation", *Reactor Materials Science* (Proc. Int. Conf., Alushta, Crimea) Vol. 5, Atominform, Moscow (1978) 90.
- [41] URQUHART, A.W., VERMILYEA, D.A., A preliminary correlation between the accelerated corrosion of Zircaloy in BWR's and in high temperature high pressure steam, *J. Nucl. Mater.* **62** (1976) 111.
- [42] CHENG, B., ADAMSON, R.B., US Patent 4440862, 3 April 1984.
- [43] RUDLING, P., MACHIELS, A.J., Corrosion Performance Ranking of Zircaloy-2 for BWR Applications, ASTM-STP-1023, American Society for Testing and Materials, Philadelphia, PA (1989) 315.
- [44] URQUHART, A.W., VERMILYEA, D.A., ROCCO, W.A., A mechanism for the effect of heat treatment on the accelerated corrosion of Zircaloy-4 in high temperature, high pressure steam, *J. Electrochem. Soc.* **125** (1978) 199.
- [45] "Papers on Nodular Corrosion", presented at 7th Int. Symp. on Zirconium in the Nuclear Industry, Strasbourg, 1985, ASTM-STP-939, American Society for Testing and Materials, Philadelphia, PA (1987).
- [46] "Papers on Nodular Corrosion", presented at 8th Int. Symp. on Zirconium in the Nuclear Industry, San Diego, 1988, ASTM-STP-1023, American Society for Testing and Materials, Philadelphia, PA (1989).
- [47] CHARQUET, D., "Corrosion nodulaire du Zircaloy-4 en vapeur d'eau à 500°C (Proc. 8^e Congrès européen de corrosion, Nice 1985), Vol. 2, Société de chimie industrielle and Centre français de la corrosion, Paris, P10-1-6.
- [48] SABOL, G., McDONALD, S.G., NURMINEN, J.I., JACOBSEN, W.A., Laser-Beam Beta Heat Treatment of Zircaloy, ASTM-STP-939, American Society for Testing and Materials, Philadelphia, PA (1987) 168.

- [49] DEMARS, H., GIVORD, J.P., ARMAND, M., Influence de la structure du Zircaloy-2 sur sa résistance à la corrosion par la vapeur d'eau, *Mem. Sci. Rev. Metall.* **62** (1965) 269.
- [50] BENTLEY, M.J., Out-of-Reactor Studies of the Nodular Oxidation of Zirconium Alloys, Rep. TRG-3001(S), United Kingdom Atomic Energy Authority, Reactor Fuel Element Laboratory, Springfield (1977).
- [51] BROWN, A., HARDIE, D., The effect of dissolved oxygen on the terminal solubility of hydrogen in alpha zirconium, *J. Nucl. Mater.* **4** (1961) 110.
- [52] ROY, C., Hydrogen Distribution in Oxidized Zirconium Alloys by Autoradiography, Rep. AECL-2085, Atomic Energy of Canada Ltd, Chalk River Nuclear Laboratories (1964).
- [53] RAMASUBRAMANIAN, N., Out-reactor nodular corrosion behaviour of Zircalloys, *J. Nucl. Mater.* **119** (1983) 208.
- [54] KUWAE, R., SATO, K., HIGASHINAKAGAWA, E., KAWASHIMA, E., NAKAMURA, S., Mechanism of Zircaloy nodular corrosion, *J. Nucl. Mater.* **119** (1983) 229.
- [55] GARZAROLLI, F., STEHLE, H., STEINBERG, E., WEIDINGER, H., Progress in the Knowledge of Nodular Corrosion, ASTM-STP-939, American Society for Testing and Materials, Philadelphia, PA (1987) 417.
- [56] SUMERLING, R., GARLICK, A., STUTTARD, A., HARTOG, J.M., TROWSE, F.W., SIMS, P., Further Evidence of Zircaloy Corrosion in Fuel Elements Irradiated in a Steam Generating Heavy Water Reactor, ASTM-STP-681, American Society for Testing and Materials, Philadelphia, PA (1979) 107.
- [57] ADAMSON, R.B., CHENG, B., LEVIN, H.A., TUCKER, R.P., "Zircaloy corrosion in GE plants", Zircaloy Corrosion (Proc. EPRI Workshop, Charlotte, NC), Electric Power Research Institute, Palo Alto (1986).
- [58] FERRETT, D.J., BLACK, W.S.A., BLACKMAN, T.E., "Winfrith SGHWR operations experience", Nuclear Power Plant Thermal Hydraulics and Operations (Proc. 2nd Int. Topical Mtg, Tokyo), American Nuclear Society (1986) 5-87.
- [59] PLATONOV, P.A., EPERIN, A.P., IVANOV, A.N., FROLOV, I.A., RODCHENKO, B.S., VAROVIN, I.A., "Some results of investigating the deformation behaviour of Zr-2.5 wt% Nb pressure tubes in the MR reactor and the operating RBMK units", paper presented at 8th Int. Symp. on Zirconium in the Nuclear Industry, San Diego, CA, 1988.
- [60] GARLICK, A., SUMERLING, R., SHIRES, G.L., Crud-induced overheating defects in water reactor fuel pins, *J. Br. Nucl. Energy Soc.* **16** (1977) 77.
- [61] MARLOWE, M.O., ARMIJO, J.S., CHENG, B., ADAMSON, R.B., "Nuclear fuel cladding localized corrosion", Light-Water Reactor Fuel Performance (Proc. ANS Topical Mtg, Orlando, FL), Vol. 1, American Nuclear Society (1985) 3-73.
- [62] BURNS, W.G., MOORE, P.B., "Radiation enhancement of Zircaloy corrosion in boiling water systems: A study of simulated radiation chemical kinetics", Water Chemistry of Nuclear Reactor Systems (Proc. BNES Conf. Bournemouth), British Nuclear Energy Society, London (1977) 281.
- [63] COX, B., Atomic Energy of Canada Ltd, Chalk River Nuclear Laboratories, unpublished results.
- [64] NELSON, H.G., WACHOB, H.F., Stress Corrosion Cracking of Zircaloy, Rep. EPRI-NP-717, Section 6, Electric Power Research Institute, Palo Alto, CA (1978).
- [65] COLEMAN, C.E., COX, B., Cracking of Zirconium Alloys in Hydrogen, ASTM-STP-824, American Society for Testing and Materials, Philadelphia, PA (1984) 675.
- [66] COLEMAN, C.E., AMBLER, J.F.R., Delayed hydrogen cracking in Zr-2.5 wt% Nb Alloys, *Revs. of Coatings and Corrosion* **3** (1979) 105 (YAHALOM, J., Ed.) Freund, Tel Aviv (1979).
- [67] SHANNON, D.W., Role of oxidation rate on the hydriding of zirconium alloys in gas atmospheres containing hydrogen, *Corrosion* **67** (1963), 414T.
- [68] COX, B., Some effects of pressure on the oxidation of Zircaloy-2 in steam and oxygen, *J. Less-Common Met.* **5** (1963) 325.
- [69] BOYLE, R.F., KISIEL, T.J., Hydrogen Permeation of Zircaloy-2 Corrosion Films, *Bettis Tech. Rev.*, Rep. WAPD-BT-10, Bettis Atomic Power Lab., W. Mifflin, PA (1958) 31.
- [70] UNE, K., Kinetics of Reaction of Zirconium Alloy with Hydrogen, *J. Less-Common Met.* **57** (1978) 93.

- [71] ARONSON, S., Some Experiments on the Permeation of Hydrogen Through Oxide Films on Zirconium, Bettis Technical Rev., Rep. WAPD-BT-19, Bettis Atomic Power Lab., W. Mifflin, PA (1960) 75.
- [72] GULBRANSEN, E.A., ANDREW, K.F., Mechanism of the reaction of hydrogen with Zircaloy, 1. Role of oxide films, pretreatments and occluded gases, *J. Electrochem. Soc.* **101** (1954) 348.
- [73] GULBRANSEN, E.A., ANDREW, K.F., Reaction of hydrogen with preoxidized Zircaloy-2 at 300° to 400°C, *J. Electrochem. Soc.* **104** (1957) 709.
- [74] SMITH, T., Mechanism of hydrogen permeation of oxide films on zirconium, *J. Electrochem. Soc.* **112** (1965) 560.
- [75] SMITH, T., Kinetics and mechanism of hydrogen permeation of oxide films on zirconium, *J. Nucl. Mater.* **18** (1966) 323.
- [76] COX, B., ROY, C., The Use of Tritium as a Tracer in Studies of Hydrogen Uptake by Zirconium Alloys, Rep. AECL-2519, Atomic Energy of Canada Ltd, Chalk River Nuclear Laboratories (1965).
- [77] ELLEMAN, T.S., VERGHESE, K., Surface effects on tritium diffusion in niobium, zirconium and stainless steel, *J. Nucl. Mater.* **53** (1974) 299.
- [78] AUSTIN, J.H., ELLEMAN, T.S., VERGHESE, K., Tritium diffusion in Zircaloy-2 in the temperature range -78 to 204°C, *J. Nucl. Mater.* **51** (1974) 321.
- [79] COX, B., Oxide breakdown on arc-melted sponge zirconium, *Corrosion* **16** (1960) 306.
- [80] COX, B., McINTOSH, A.B., The Oxide Topography on Crystal- Bar and Reactor Grade Sponge Zirconium", Rep. AECL-3223, Atomic Energy of Canada Ltd, Chalk River Nuclear Laboratories (1968).
- [81] WANKLYN, J.N., BRITTON, C.F., SILVESTER, D.R., WILKINS, N.J.M., The corrosion of zirconium and its alloys, Part III. The influence of the environment on oxidation, *J. Electrochem. Soc.* **110** (1963) 856, and Rep. AERE-4130, UK Atomic Energy Authority, AERE Harwell (1962).
- [82] COX, B., Examination of Oxidized Zirconium Alloys with the Photo-Emission and Scanning Electron Microscopes, Rep. PR-CMa-9, Atomic Energy of Canada Ltd, Chalk River Nuclear Laboratories (1969) 76.
- [83] PEMSLER, J.P., Diffusion of oxygen in zirconium and its relation to oxidation and corrosion, *J. Electrochem. Soc.* **105** (1958) 315.
- [84] PEMSLER, J.P., Studies of Oxygen Gradients in Corroding Zirconium Alloys. *J. Nucl. Mater.* **7** (1962) 16.
- [85] HILLNER, E., "Hydrogen absorption in Zircaloy during aqueous corrosion", Effect of Environment, Rep. WAPD-TM-411, Bettis Atomic Power Lab., W. Mifflin, PA (1964).
- [86] RAMASUBRAMANIAN, N., Localized electron transport in corroding zirconium alloys, *J. Nucl. Mater.* **55** (1975) 134.
- [87] KASS, S., KIRK, W.W., Corrosion and hydrogen absorption properties of nickel-free Zircaloy-2 and Zircaloy-4, *ASM Trans. Quart.* **56** (1962) 77.
- [88] COX, B., Some Factors Which Affect the Rate of Oxidation and Hydrogen Absorption of Zircaloy-2 in Steam, Rep. AERE-R4348, UK Atomic Energy Authority, Atomic Energy Research Est., Harwell (1963).
- [89] PLOC, R.A., DAVIDSON, R.D., "Auger Electron Analysis of Oxides Grown on Dilute Zirconium Alloys", *Microstructural Science*, Vol. 13 (SHIELS, S.A., BAGNALL, C., WITKOWSKI, R.E., VANDERVOORT, G.F., Eds), International Metallographic Society, Columbus, OH (1985) 131-141.
- [90] MAEKAWA, T., TERADA, M., Infra-red spectra study on the oxidation film of zirconium, *Trans. Jpn. Inst. Met.* **4** (1963) 47.
- [91] WARR, B.D., RASILE, E.M., BRENNENSTUHL, A.M., "Electron microscopical analyses of oxides in Zr-2.5 wt% Nb", *Fundamental Aspects of Corrosion on Zirconium Base Alloys in Water Reactor Environments* (Proc. Tech. Comm. Mtg Portland, OR, 1989), IWGFPT/34, IAEA, Vienna (1990) 124.
- [92] KHATAMIAN, D., MANCHESTER, F.D., An ion beam study of h diffusion in oxides of Zr and Zr-Nb (2.5 wt%), *J. Nucl. Mater.* **166** (1989) 300.

- [93] WARR, B.D., ELMOSELI, M.B., NEWCOMBE, S.B., McINTYRE, N.S., LICHTENBERGER, P.C., "Oxide characteristics and their relationships to hydrogen uptake in zirconium alloys", Zirconium in the Nuclear Industry (Proc. 9th Int. Symp. Kobe, Japan, 1990), ASTM-STP- (to be published).
- [94] PERRYMAN, E.C.W., "Pickering Pressure Tube Cracking Experience", Nucl. Energy 17 (1978) 95.
- [95] JOHNSON, A.B., Jr., "Aqueous corrosion and hydriding of zirconium alloys in nuclear reactor environments", Metallic Corrosion (Proc. 4th Int. Cong. Amsterdam), National Association of Corrosion Engineers, Houston (1972).
- [96] JOHNSON, A.B., Jr., LeSURF, J.E., PROEBSTLE, R.A., Study of Zirconium Alloy Corrosion Parameters in the Advanced Test Reactor, ASTM-STP-551, American Society for Testing and Materials, Philadelphia, PA (1974) 495.
- [97] JOHNSON, A.B., Jr., A review of corrosion phenomena on zirconium alloys, niobium, titanium, inconel, stainless steel and nickel plate under irradiation, Revs. on Coatings and Corrosion 4 (YAHALOM, J. Ed.) Freund, Tel Aviv (1975) 299.
- [98] URBANIC, V.F., Observations of Accelerated Hydriding in Zirconium Alloys, ASTM-STP-824, American Society for Testing and Materials, Philadelphia, PA (1984) 554.
- [99] AMBARTSUMYAN, et al., "Peaceful Uses of Atomic Energy", Proceedings of the Second International Conference, Geneva, Vol. 5 (1958) 12.
- [100] CHEADLE, B.A., HOLT, R.A., FIDLERIS, V., CAUSEY, A.R., URBANIC, V.F., "High-strength, creep-resistant EXCEL pressure tubes", Zirconium in the Nuclear Industry: Fifth Conference, ASTM-STP-754 (FRANKLIN, D.G. Ed.), American Society for Testing and Materials (1982) 193-207.
- [101] TYZACK, C., et al., SCANUK: A collaborative programme to develop new zirconium cladding alloys, J. Nucl. Mater. 66 (1977) 163.
- [102] SABOL, G.P., KILP, G.R., BALFOUR, M.G., ROBERTS, E.R., "Development of a cladding alloy for high burnup", Zirconium in the Nuclear Industry: Eighth International Symposium, ASTM-STP-1023 (VAN SWAM, L.F.P., EUCKEN, C.M., Eds), American Society for Testing and Materials (1989) 227-244.
- [103] DALGAARD S.B., "Long-term corrosion and hydriding of Zircaloy-4 fuel clad in commercial pressurized water reactors with forced corrective heat transfer", paper presented at the 149th meeting of the Electrochemical Society, Washington, D.C., 1976.
- [104] TSYKANOV, V.K., et al., Material behavior investigations of the VK-50 reactor, Translated from Atomnaya Energiya 56 (1984) 131-134.
- [105] PLANMAN, T., VAITTINEN, M., MOISIO, J., "Corrosion behavior and oxide characterization of surface treated Zr-1% Nb fuel cladding tubes", Fundamental Aspects of Corrosion on Zirconium Base Alloys in Water Reactor Environments (Proc. Tech.Comm. Mtg Portland, OR, 1989), IWGFPT/34, IAEA, Vienna (1990) 249.
- [106] STEHLE, H., GARZAROLLI, F., GARDE, A.M., SMERD, P.G., "Characterization of ZrO₂ films formed in-reactor and ex-reactor to study the factors contributing to the in-reactor waterside corrosion of Zircaloy", Zirconium in the Nuclear Industry: Sixth International Symposium, ASTM-STP-824 (FRANKLIN, D.G., ADAMSON, R.B., Eds), American Society for Testing and Materials (1984) 483-506.
- [107] LANNING, D.D., JOHNSON, A.B., JR., TRIMBLE, D.J., BOYD, S.M., "Corrosion and hydriding of N reactor pressure tubes", Zirconium in the Nuclear Industry: Eighth International Symposium, ASTM-STP-1023 (VAN SWAM, L.F.P., EUCKEN, C.M., Eds), American Society for Testing and Materials (1989) 153-164.
- [108] URBANIC, V.F., COX, B., Long-term corrosion and deuteriding behaviour of Zircaloy-2 under irradiation, Can. Metall. Quart. 24 (1985) 189-196.
- [109] JOHNSON, A.B., Jr., Zirconium Alloy Oxidation and Hydriding Under Irradiation: Review of Pacific Northwest Laboratory's Test Program Results, Rep. EPRI-NP-5132, Electric Power Research Institute, Palo Alto, CA (1987).
- [110] COX, B., Effects of irradiation on the oxidation of zirconium alloys in high temperature aqueous environments (A Review), J. Nucl. Mat. 28 (1968) 1-47.
- [111] KAISER, R.S., MILLER, R.S., MOON, J.E., PISANO, N.A., "Westinghouse high burnup

- experience at Farley 1 and Point Beach 2", LWR Fuel Performance (Proc. Topical Mtg Williamsburg, VA, 1988), American Nuclear Society (1988) 119-124.
- [112] JOHNSON, A.B., JR., LEVY, I.S., LANNING, D.D., GERBER, F.S., TRIMBLE, D.J., "A laboratory method to predict hydriding properties of zirconium alloys under irradiation", Zirconium in the Nuclear Industry: Eighth International Symposium, ASTM- STP-1023 (VAN SWAM, L.F.P., EUCKEN, C.M., Eds), American Society for Testing and Materials (1989) 153-164.
- [113] URBANIC, V.F., LESURF, J.E., JOHNSON, A.B., JR., Effect of ageing and irradiation on the corrosion of Zr-2.5 wt% Nb, *Corrosion* **31** (1973) 15-20.
- [114] LUNDE, L., Special features of external corrosion of fuel cladding in boiling water reactors, *Nuclear Engineering and Design* **33** (1975) 178-195.
- [115] MISHIMA, Y., et al., Proving Test on the Reliability for Nuclear Fuel Assemblies Test on Fuel Assemblies (translation of excerpt, summary report of proving tests on the reliability for nuclear power plant - 1987, Nuclear Power Engineering Test Center, Tokyo, Japan).
- [116] SHEPPARD, M.F., TYZACK, C., "Corrosion monitoring of steam generating heavy water reactor pressure tubes", Zirconium in the Nuclear Industry, ASTM-STP-633 (LOWE, A.L., Jr., PARRY, G.W., Eds), American Society for Testing and Materials (1977) 258-280.
- [117] URBANIC, V.F., GRAY, R., LISTER, D.H., Review of In-Reactor Zircaloy Corrosion and Crud Deposition Experience at AECL, Rep. EPRI NP-1254, Electric Power Research Institute, Palo Alto, CA (1979).
- [118] MEGERTH, F.H., RUIZ, C.P., WOLFF, U.E., Zircaloy-Clad UO₂ Fuel Rod Evaluation Program, Final Report, November 1967 to June 1971, USAEC Rep. GEAP 10371, General Electric Company, San Jose, CA (1971).
- [119] JOHNSON, A.B., Jr., Corrosion and failure characteristics of zirconium alloys in high-pressure steam in the temperature range 400 to 500°C, Applications-Related Phenomena for Zirconium and Its Alloys, ASTM-STP-458, American Society for Testing and Materials, Philadelphia, PA (1969) 271-285.
- [120] LANDAU, L.A., LIFSHITZ, E.M., *Mécanique*, Moscow, Les Editions MIR (1969), 243.
- [121] OEN, O.S., Cross Section for Atomic Displacements In Solids by Fast Electrons, Rep. ORNL 4897, Oak Ridge National Laboratory, TN (1973).
- [122] GRIFFITHS, M., Displacement energies for Zr measured in a HVEM, *J. Nucl. Mater.* **165** (1989) 315.
- [123] MOTTA, A., "Electron irradiation induced amorphization of precipitates in Zircaloy-2", 14th ASTM Meeting on the Effect of Irradiation on Materials, Andover, MS, 1988.
- [124] ROBINSON, M.T., The Influence of the Scattering Law on the Radiation Damage Displacement Cascade, I: *Phil. Mag.* **12** (1965) 741.
- [125] ZIELER, J.F., BIRSACK, J.P., LITTMARK, U., *The Stopping and Range of Ions in Solids*, Pergamon Press, New York (1985).
- [126] GRIFFITHS, M., GILBERT, R.W., CARPENTER, G.J.C., Phase instability, decomposition and redistribution of intermetallic precipitates in Zircaloy 2 and 4 during neutron irradiation, *J. Nucl. Mater.* **150** (1987) 53.
- [127] LEFEBVRE, F., "Thesis: Etude des Effets d'Irradiation sur la Microstructure du Zircaloy-4", Grenoble, France (1989).
- [128] GOLDBERG, M.D., MUGHABGHAB, S.F., MARGURNO, B.A., MAY, V.M., Neutron Cross Sections, Vol. II-A: Z=21 to 40, Rep. BNL325, Brookhaven National Laboratory (1966).
- [129] JOHNSON, W.G., MOGRO-CAMPERO, A., WALTER, J.L., BAKHRU, H., Crystalline to amorphous phase transformation by ion bombardment of the alloy Fe₇₅B₂₅, *Mat. Sci. Eng.* **55** (1982) 121.
- [130] HOWE, L.M., RAINVILLE, M.H., A study of the irradiation behaviour of Zr₃Al, *J. Nucl. Mater.* **68** (1977) 215, and The nature of irradiation produced damaged regions in ordered Zr₃Al, *Phil. Mag.* **A39** (1979) 195.
- [131] SHARPE, J.V., RUMBSY, D., Electron irradiation damage in magnesium oxide, *Rad. Effects* **17** (1973) 65.
- [132] SOULLARD, J., ALAMO, A., Etude du ralentissement des ions dans une cible diatomique, II: Calcul du nombre d'atomes déplacés, *Rad. Effects* **38** (1978) 133.

- [133] CLINARD, F.W., JR., HOBBS, L.W., *Physics of Radiation Effects in Crystals* (JOHNSON, R.A., ORLOV, A.N., Eds) Elsevier Science Pub. B.V. (1986) 387.
- [134] TOULEMONDE, M., BALANZAT, E., BOUFFARD, S., JOUSSET, J.C., Structural modifications induced by electronic energy deposition during the slowing down of heavy ions in matter, *Nucl. Instrum. Methods Phys. Res.* **B39** (1989) 1.
- [135] YUANXUN, Q., GRIFFITH, J.E., TOMBRELLO, T.A., Sputtering of Al₂O₃ and LiNbO₃ in the electronic stopping region, *Rad. Effects* **64** (1982) 111.
- [136] VARLEY, J.H.O., Radiation damage in covalent and ionic solids, *Prog. Nucl. Energy* **5** (1956) 672.
- [137] CLINARD, F.W., JR., ROHR, D.L., RANKEN, W.A., Neutron irradiation damage in stabilized ZrO₂, *J. Amer. Ceram. Soc.* **60** (1977) 287.
- [138] WITTELS, M.C., SHERRILL, F.A., Irradiation Induced Phase Transformation in Zirconia, *J. Appl. Phys.* **27** (1956) 643.
- [139] ADAM, J., COX, B., Neutron and fission fragment damage in zirconia, *Phys. Rev. Letters* **3** (1959) 543.
- [140] BRADLEY, E.R., PERKINS, R.A., "Characterisation of Zircaloy corrosion films by analytical transmission electron microscopy", *Fundamental Aspects of Corrosion on Zirconium Base Alloys in Water Reactor Environments* (Proc. Tech. Comm. Mtg Portland, OR, 1989), IWGFPT/34, IAEA, Vienna (1990) 101.
- [141] COX, B., FIDLERIS, V., "Enhanced low temperature oxidation of Zr alloys under irradiation", 8th Int. Symposium on Zirconium in the Nuclear Industry, San Diego, 1988, ASTM-STP-1023, American Society for Testing and Materials, Philadelphia, PA (1990) 245.
- [142] BAIG, M.R., MESSOLORAS, S., STEWART, R.J., Absence of voids in fast neutron irradiated zirconium by small angle neutron scattering, *Rad. Effects and Defects in Sol.* **108** (1989) 355.
- [143] GRIFFITHS, M., A review of microstructure evolution in zirconium alloys during irradiation, *J. Nucl. Mater.* **159** (1988) 190.
- [144] NORTHWOOD, D.O., Irradiation damage in zirconium and its alloys, *Atomic Energy Rev.* **15** (1977) 547.
- [145] NORTHWOOD, D.O., et al., Characterisation of neutron irradiation damage in zirconium alloys - An international "round-robin" experiment, *J. Nucl. Mater.* **79** (1979) 379.
- [146] HELLIO, C., de NOVION, C.H., BOULANGER, L., Influence of alloying elements on the dislocation loops created by Zr⁺ or by electron irradiation in α-zirconium, *J. Nucl. Mater.* **159** (1988) 368.
- [147] BUCKLEY, S. N., BULLOUGH, R., HAYNS, M.R., The direct observation of irradiation damage in zirconium and its alloys, *J. Nucl. Mater.* **89** (1980) 283.
- [148] GRIFFITHS, M., GILBERT, R. W., The formation of c-component defects in zirconium alloys during neutron irradiation, *J. Nucl. Mater.* **150** (1987) 169.
- [149] HOLT, R.A., GRIFFITHS, M., GILBERT, R. W., c-component dislocations of Zr-2.5 wt% Nb alloys, *J. Nucl. Mater.* **149** (1987) 51.
- [150] McEWEN, S.R., FABER, J., TURNER, A.P.L., The use of time of flight neutron diffraction to study grain interaction stresses, *Acta. Metall.* **5** (1983) 657.
- [151] HOLT, R.A., Mechanisms of irradiation growth of alpha-zirconium alloys, *J. Nucl. Mater.* **159** (1988) 310.
- [152] HOLT, R.A., CAUSEY, A.R., The effects of intergranular constraints on irradiation growth of Zircaloy-2 at 320 K, *J. Nucl. Mater.* **150** (1987) 306.
- [153] VERSACI, R.A., IPOHORSKI, M., Composition of Zr(Cr,Fe)₂-type precipitates in Zircaloy-2 and -4, *J. Nucl. Mater.* **116** (1983) 321.
- [154] VITIKAINEN, E., NENONEN, P., Transmission electron microscopy studies on intermetallics in some zirconium alloys, *J. Nucl. Mater.* **78** (1978) 362.
- [155] MENG, X.Y., NORTHWOOD, D.O., Intermetallic precipitates in Zircaloy-4, *J. Nucl. Mater.* **132** (1985) 80.
- [156] BANGARU, N.V., An investigation of the microstructure of heat treated Zircaloy-4, *J. Nucl. Mater.* **131** (1985) 280.
- [157] CHARQUET, D., ALHERITIERE, E., "Second phase particles and matrix properties on

- Zircalloys", Specialists Workshop, Erlangen, 1985, Kerntechnische Gesellschaft, Bonn, 1987; and 8th Int. Symposium on Zirconium in the Nuclear Industry, San Diego, 1988, ASTM-STP-1023, American Society for Testing and Materials, Philadelphia, PA (1990) 405.
- [158] STRASSER, A.A., ANDREWS, M.G., "Relationship of precipitates, their composition, heat treatment and irradiation to corrosion resistance of Zircalloys", Fundamental Aspects of Corrosion on Zirconium Base Alloys in Water Reactor Environments (Proc. Tech. Comm. Mtg Portland, OR, 1989), IWGFPT/34, IAEA, Vienna (1990) 88.
- [159] KUBO, T., WAKASHIMA, Y., IMAHASHI, H., NAGAI, M., Distribution of intermetallic particles and its effects on SCC of zirconium alloys, *J. Nucl. Mater.* **138** (1986) 256.
- [160] SCHEMEL, J.J., CHARQUET, D., WADIER, J.F., "Influence of the manufacturing process on the corrosion resistance of Zircaloy-4 cladding", 8th Int. Symposium on Zirconium in the Nuclear Industry, San Diego, 1988, ASTM-STP-1023, American Society for Testing and Materials, Philadelphia, PA (1990) 141.
- [161] GILBERT, R.W., GRIFFITHS, M., CARPENTER, G.J.C., Amorphous intermetallics in neutron irradiated Zircalloys after high fluences, *J. Nucl. Mater.* **135** (1985) 265.
- [162] YANG, W.J.S., TUCKER, R.P., CHENG, B., ADAMSON, R.B., Precipitates in Zircaloy: Identification and effect of irradiation and heat treatment, *J. Nucl. Mater.* **138** (1986) 185.
- [163] GRIFFITHS, M., GILBERT, R.W., FIDLERIS, V., TUCKER, R.P., ADAMSON, R.B., Neutron damage in zirconium alloys during neutron irradiation, *J. Nucl. Mater.* **150** (1987) 159.
- [164] YANG, W.J.S., Precipitate stability in neutron-irradiated Zircaloy-4, *J. Nucl. Mater.* **158** (1988) 71–80.
- [165] LEFEBVRE, F., LEMAIGNAN, C., Heavy ion induced amorphisation of Zr(Fe,Cr)₂ precipitates in Zircaloy-4, *J. Nucl. Mater.* **165** (1989) 122.
- [166] LEFEBVRE, F., LEMAIGNAN, C., "Effect of irradiation on the microstructure of Zr4: Amorphous transformation and alloying element resolution", Fundamental Aspects of Corrosion on Zirconium Base Alloys in Water Reactor Environments (Proc. Tech. Comm. Mtg Portland, OR, 1989), IWGFPT/34, IAEA, Vienna (1990) 80.
- [167] URBANIC, V.F., GILBERT, R. W., "Effect of microstructure on the corrosion of Zr-2.5 Nb Alloy", Fundamental Aspects of Corrosion on Zirconium Base Alloys in Water Reactor Environments (Proc. Tech. Comm. Mtg Portland, OR, 1989), IWGFPT/34, IAEA, Vienna (1990) 262.
- [168] BUXTON, G.V., "Radiation chemistry of the liquid state. Water and homogeneous aqueous solutions", Radiation Chemistry. Principle and Applications (RODGERS, M.A.J., Ed.), VCH Publishers Inc., New York (1987) 312–350.
- [169] BURNS, W.G., MARSH, W.R., Radiation chemistry of high temperature water (300–410°C). Part. 1. Reducing products from gamma radiolysis, *J. Chem. Soc. Faraday Trans. I* **77** (1981) 197–215.
- [170] BURNS, W.G., Water Chemistry of Nuclear Reactor Systems, 2, BNES, London (1981) 373.
- [171] JHA, K.N., RYAN, T.G., FREEMAN, G.R., Radiolysis of H₂O and D₂O between 0 and 300°C, *J. Phys. Chem.* **79** (1975) 868–870.
- [172] CHRISTENSEN, H., SEHESTED, K., Hydrated electron and its reactions at high temperatures, *J. Phys. Chem.* **90** (1986) 186–190.
- [173] SHIRAISHI, H., KATSUMURA, Y., HIROISHI, D., ISHIGURE, K., WASHIO, M., Pulse-radiolysis study on the yield of hydrated electrons at elevated temperatures, *J. Phys. Chem.* **92** (1988) 3011–3017.
- [174] SHIRAISHI, H., KATSUMURA, H., ISHIGURE, K., On the yield of hydrated electrons at elevated temperatures, *Radiat. Phys. Chem.* **34** (1989) 705–710.
- [175] KATSUMURA, Y., TAKEUCHI, Y., ISHIGURE, K., Radiation chemistry of high temperature water – 1. Degradation products in acid by gamma radiation, *J. Phys. Chem.* **32** (1988) 259–263.
- [176] BUXTON, G.V., WOOD, N.D., DYSTER, S., Ionisation constants of radical OH and HO₂ radical in aqueous solutions up to 200°C. A pulse radiolysis study, *J. Chem. Soc., Faraday Trans. I* **84** (1988) 1113–1121.
- [177] SHIRAISHI, H., BUXTON, G.V., WOOD, N.O., Temperature dependence of the absorption

- spectrum of the methyl viologen cation radical and use of methyl viologen as a scavenger for estimating yields of the primary radicals in the radiolysis of high-temperature water, *Radiat. Phys. Chem.* **33** (1989) 519–522.
- [178] ELLIOT, A.J., CHENIER, M.P., QUELLETTE, D.C., g-values for gamma-irradiated water as a function of temperature, *Can. J. Chem.* **68** (1990) 712–718.
- [179] KATSUMURA, Y., TAKEUCHI, Y., HIROISHI, D., ISHIGURE, K., Fast neutron radiolysis of acid water at elevated temperatures, *Radiat. Phys. Chem.* **33** (1988) 299–306.
- [180] JENKS, G.H., Effects of Reactor Operation on HFIR Coolant, ORNL-3848, Oak Ridge National Laboratory (1965).
- [181] BURNS, W.G., MOORE, P.B., Water radiolysis and its effect upon in-reactor Zircaloy corrosion, *Radiat. Effects* **30** (1976) 233–242.
- [182] ISHIGURE, K., TAKAGI, J., KATO, I., SHIGETO, T., FUJITA, N., "Computer Simulation of Reactor Water Chemistry in a BWR", *Water Chemistry and Corrosion Problems in Nuclear Power Plants (Proc. Symp. Vienna, 1982)*, IAEA, Vienna (1983) 181.
- [183] ISHIGURE, K., TAKAGI, J., SHIRAIISHI, H., Hydrogen injection in BWR and related radiation chemistry, *Radiat. Phys. Chem.* **29** (1987) 195–199.
- [184] IBE, E., UCHIDA, S., Evaluation of the yields from the radiolysis of water in boiling water reactors by neutron and gamma radiation, *Nucl. Sci. Eng.* **85** (1983) 339–349.
- [185] SPIERS, F.W., The influence of energy absorption and electron range in irradiated bone, *Br. J. Radiol.* **22** (1951) 521–533.
- [186] DUTRIEX, J., BERNARD, M., Dosimetry at interfaces for high energy X and gamma rays, *Br. J. Radiol.* **39** (1966) 205–210.
- [187] AIREY, P.L., The effect of radiation on electrode processes, *Radiat. Res. Rev.* **5** (1973) 341.
- [188] BURNS, W.G., MARSH, W.R., WALTERS, W.S., The gamma irradiation-enhanced corrosion of stainless and mild steels by water in the presence of air, argon and hydrogen, *Radiat. Phys. Chem.* **21** (1983) 259–279.
- [189] HENGLEIN, A., LINDIG, B., WESTERHAUSEN, J., Radiation-electrochemistry of the colloidal platinum electrode. Reactions of oxidizing free radicals, *Radiat. Phys. Chem.* **23** (1984) 199.
- [190] BUXTON, G.V., RHODES, T., SELLERS, R.M., Radiation induced dissolution of colloidal haematite, *Nature* **295** (1982) 583–585.
- [191] HENGLEIN, A., LILLIE, J., Storage of electrons in aqueous solution: the rates of chemical charging and discharging in colloidal silver electrode, *J. Am. Chem. Soc.* **103** (1989) 1059–1066.
- [192] WESTERHAUSEN, J., HENGLEIN, A., LILLIE, J., Radiation-electrochemistry of the colloidal gold micro-electrode hydrogen formation by organic free radicals, *Ber. Bunsenges. Phys. Chem.* **85** (1981) 182–189.
- [193] TAKAGI, J., ISHIGURE, K., Thermal decomposition of hydrogen peroxide and its effect on reactor water monitoring of boiling water reactors, *Nucl. Sci. Eng.* **89** (1985) 177–186.
- [194] HIROISHI, D., ISHIGURE, K., "Homogeneous and heterogeneous decomposition of hydrogen peroxide in high temperature water", *Water Chemistry of Nuclear Reactor Systems 5 (Proc. Int. Conf. 1989) Vol. 1*, British Nuclear Energy Society, London (1989) 311–312.
- [195] ULLBERG, M., ROTH, T., PERSSON, B., "Hydrogen peroxide in BWRs", *Water Chemistry of Nuclear Reactor Systems 4 (Proc. Int. Conf. 1986) Vol. 2*, British Nuclear Energy Society, London (1986) 67–73.
- [196] LIN, C.L., SMITH, F.R., ICHIKAWA, N., BABA, T., ITOW, M., "Decomposition of hydrogen peroxide in aqueous solutions at elevated temperatures", *Water Chemistry of Nuclear Reactor Systems 5, Vol. 1*, British Nuclear Energy Society, London (1989) 145–151.
- [197] REBENDORFF, B., WIKMARK, G., "Decomposition of hydrogen peroxide in high temperature waters: A laboratory study", *ibid.*, 153–158.
- [198] GERISCHER, R., GERISCHER, H., Über die katalytische Zersetzung von Wasserstoffsperoxyd an metallischem Platin, *Z. Phys. Chem., Neue Folge* **6(S)** (1956) 178–200.
- [199] AOKI, M., NAKAZATO, C., MASUDA, T., "Radiation of water absorbed on zeolite", *Radiation Research (Proc. 8th. Int. Congress Edinburgh, 1989)* (FIELDEN, E. M., FOWLER, J.F., HENDRY, J. H., SCOTT, D., Eds), Taylor and Francis, London (1987) 28.

- [200] ALEXANDROV, A.B., NECHAEV, A.F., *J. Phys. Chem. (Sov.)* **58** (1984) 1108.
- [201] NECHAEV, A.F., "Radiation induced processes on solid surfaces: General approach and outlook", *Radiat. Phys. Chem.* **28** (1986) 433-436.
- [202] TAKAGI, J., ICHIKAWA, N., HEMMI, Y., "Evaluation of corrosion environment in BWR primary circuit by water radiolysis model", *Water Chemistry of Nuclear Power Plants (Proc. Int. Conf. 1988)*, Vol. 2, Japan Atomic Industrial Forum, Tokyo (1988) 517-522.
- [203] CHRISTENSEN, H., SEHESTED, K., "Reaction of hydroxyl radicals with hydrogen at elevated temperatures. Determination of the activation energy", *J. Phys. Chem.* **87** (1983) 118-120.
- [204] RIKAEV, A.K., KABAKCHI, S.A., EGOROV, A.F., "Some radiation chemistry aspects of nuclear engineering", *Radiat. Phys. Chem.* **31** (1988) 789-803.
- [205] NOE, M., FREJAVILLE, G., BESLU, P., *Corrosion of Fuel Assembly Materials*, Note CEA-N 2440, Commissariat à l'Energie Atomique, Cadarache (1985).
- [206] SOLOMON, Y., Paper presented at *Int. Conf. on Decontamination of Nuclear Facilities*, Niagara Falls, Canada, 1982, Electric Power Research Institute, Palo Alto, CA.
- [207] BERGMAN, C.A., "Evaluation of elevated pH coolant chemistry on exposure rates", *Water Chemistry of Nuclear Reactor Systems*, Vol. 1, BNES, Bournemouth (1989).
- [208] EDF/CEA/FRAMATOME/WESTINGHOUSE, Joint Venture: PWS1-4 Final Report 2-9 (1984).
- [209] HILLNER, E., "Corrosion of zirconium alloys - An overview", *Zirconium in the Nuclear Industry*, Third International Symposium, Quebec City, Quebec, 1976, ASTM-STP-633, American Society for Testing and Materials, Philadelphia, PA (1977) 211-235.
- [210] SABOL, G.P., McDONALD, S.G., "Structural aspects of oxide film growth on zirconium based alloys", *Stress Effects and the Oxidation of Metals* (CATHCART, J.V., Ed.), AIME (1975) 352.
- [211] BILLOT, P., et al., "Development of a mechanistic model to assess the external corrosion of the Zircaloy claddings in PWRs", *Zirconium in the Nuclear Industry*, Eighth International Symposium, ASTM-STP-1023, American Society for Testing and Materials, Philadelphia, PA (1989) 165.
- [212] BERGE, P., et al., "Expérience française sur le contrôle chimique de l'eau et le contrôle des produits de corrosion des réacteurs à eau sous pression" (Proc. Symp.), IAEA, Vienna (1982).
- [213] THOMAZET, J., et al., "Power reactor experience and experimental program to control crud build-up on fuel", IAEA Specialists Meeting, San Miniato, Italy, 1981.
- [214] SMITH MAGOWAN, D., et al., "Evaluation of the Applicability of Colloid Studies to Cobalt-60 Deposition in LWRs", Rep. EPRI-NP-3773, Electric Power Research Institute, Palo Alto, CA (1984).
- [215] ELECTRIC POWER RESEARCH INSTITUTE, Rep. EPRI-NP-3463 (1984) and Rep. EPRI-NP-4247 (BERGMANN, C.A., et al., *The Role of Coolant Chemistry in PWR Radiation Field Buildup*, 1985), Electric Power Research Institute, Palo Alto, CA.
- [216] BESLU, P., *French experience of PWR chemistry*, *Nuclear Europe* **78** (1989).
- [217] ISHIGURE, K., et al., "Water chemistry experience on nuclear power plants in Japan", *J. Nucl. Sci. and Technol.* **26** (1989) 145.
- [218] BESLU, P., LALET, A., Paper presented at the *International Conference on Water Chemistry in Nuclear Power Plants*, 1988, JAIF, Tokyo.
- [219] EPRI PWR Primary Water Chemistry Guidelines, Rep. EPRI-NP-5960-SR, Electric Power Research Institute, Palo Alto, CA (1988).
- [220] BERGMANN, C.A., et al., *The Role of Coolant Chemistry in PWR Radiation Field Buildup*, Rep. EPRI-NP-4247, Electric Power Research Institute, Palo Alto, CA (1985).
- [221] MENET, O., BLAIN, M., NAUDIN, O., Paper presented at EPRI Seminar on PWR Water Chemistry and Radiation Field Control, 1986, Electric Power Research Institute, Palo Alto, CA.
- [222] COWAN, R.L., et al., "Experience with hydrogen water chemistry in boiling water reactors", *Water Chemistry for Nuclear Reactor Systems*, BNES, London (1986).
- [223] GARZAROLLI, F., et al., *Waterside Corrosion of Zircaloy Fuel Rods*, Rep. EPRI-NP-2789, Research Project 1250-1, Final Report, Electric Power Research Institute, Palo Alto, CA (1982).

- [224] BILLOT, P., BESLU, P., FREJAVILLE, G., "Justification of in-plant waterside corrosion of Zircaloy clad on the basis of thermal and hydraulic calculations", IAEA Technical Committee Meeting on External Cladding Corrosion in Water Power Reactors, Cadarache, France, Oct. 14-18 (1985).
- [225] GARZAROLLI, F., et al., Review of PWR Fuel Rod Waterside Corrosion Behaviour, EPRI-NP-1472, Research Project 1250-01, Interim Report, Electric Power Research Institute, Palo Alto, CA (1980).
- [226] BILLOT, P., ROBIN, J.C., "Mechanistic understanding of Zircaloy corrosion in pwr's through a corrosion model", Fundamental Aspects of Corrosion on Zirconium Base Alloys in Water Reactor Environments (Proc. Tech. Comm. Mtg Portland, OR, 1989), IWGFPT/34, IAEA, Vienna (1990) 173.
- [227] SCHEMEL, J.H., CHARQUET, D., WADIER, J.F., Influence of the Manufacturing Process on the Corrosion Resistance of Zircaloy-4 Cladding, ASTM-STP-1023, American Society for Testing and Materials, Philadelphia, PA (1989) 141.
- [228] URQUHART, A.W., VERMILYEA, D.A., A preliminary correlation between the accelerated corrosion of Zircaloy in BWR and in high temperature high pressure steam, J. Nucl. Mater. **62** (1976) 111.
- [229] GARZAROLLI, F., STEINBERG, E., WEIDINGER, H.G., Microstructure and Corrosion Studies for Optimized PWR and BWR Zircaloy Cladding, ASTM-STP-1023, American Society for Testing and Materials, Philadelphia, PA (1989) 202.
- [230] MENG, X., NORTHWOOD, D.O., Intermetallic Precipitates in Zirconium-Niobium Alloys, ASTM-STP-1023, American Society for Testing and Materials, Philadelphia, PA (1989) 478.
- [231] URBANIC, V.F., WARR, B.D., MANOLESCU, A., CHOW, C.K., SHANAHAN, M.W., Oxidation and Deuterium Uptake of Zr-2.5Nb Pressure Tubes in CANDU-PHW Reactors, ASTM-STP-1023, American Society for Testing and Materials, Philadelphia, PA (1989) 20.
- [232] MAUSSNER, G., STEINBERG, E., TENCKHOFF, K., Nucleation and Growth of Intermetallic Precipitates in Zircaloy-2 and Zircaloy-4 and Correlation of Nodular Corrosion Behaviour, ASTM-STP-939, American Society for Testing and Materials, Philadelphia, PA (1987) 307.
- [233] SCHEMEL, J.H., β -quenched Zircalloys, Nucleonics **20** (1962) 4.
- [234] COX, B., The Effect of Fission Fragment Irradiation on the Subsequent Corrosion of Two Zirconium Alloys, Rep. AERE-R2875, UK Atomic Energy Authority, AERE Harwell (1959).
- [235] COX, B., REID, J.A., Oxidation of a Zr-2.5Nb Alloy in Steam and Air, Rep. AERE-R4459, UK Atomic Energy Authority, AERE Harwell (1963).
- [236] URBANIC, V.F., GILBERT, R.W., "Effect of microstructure on the corrosion of Zr-2.5 Nb alloy", Fundamental Aspects of Corrosion on Zirconium Base Alloys in Water Reactor Environments (Proc. Tech. Comm. Mtg Portland, OR, 1989), IWGFPT/34, IAEA, Vienna (1990) 262.
- [237] INDIG, M.E., "Recent advances in measuring ECPs in BWR systems", Environmental Degradation of Materials in Nuclear Reactor Systems - Water Reactors (Proc. 4th Int. Symp. Jekyll Island, GA 1989), NACE (1991) 4-111.
- [238] COX, B., SPEIRS, D.L., Rectification by Oxide Films on Zirconium Alloys, Rep. AECL-2690, Atomic Energy of Canada Ltd, Chalk River Nuclear Laboratories (1967).
- [239] PERKINS, R.A., BUSCH, R., "Corrosion of Zircaloy-4 fuel cladding", Environmental Degradation of Materials in Nuclear Reactor Systems - Water Reactors (Proc. 4th Int. Symp. Jekyll Island, GA, 1989), NACE (1991) 10-15.
- [240] LUNDE, L., VIDEM, K., Effect of Materials and Environmental Variables on Localized Corrosion of Zirconium Alloys, ASTM-STP-681, American Society for Testing and Materials, Philadelphia, PA (1979) 40.
- [241] COX, B., "The determination of oxidation rates from in-situ electrical measurements", Paper presented at NACE Canadian Regional Conference, Ottawa, 1979.
- [242] NIIZAWA, T., KITABATA, T., "Effect of hydrogen addition on stress corrosion cracking in the Fugen nuclear power station", Water Chemistry of Nuclear Reactor Systems (Proc. 4th Int. Conf.), Vol. 2, British Nuclear Energy Society, London (1987) 75.
- [243] WOLSEY, I.S., MORRIS, J.R., A study of Zircaloy-2 corrosion in high temperature water using ion beam methods, Corrosion **37** (1981) 575.

- [244] WHITTON, J.L., The measurement of ionic mobilities in the anodic oxides of tantalum and zirconium by a precision sectioning technique, *J. Electrochem. Soc.* **115** (1968) 58.
- [245] COX, B., "Mechanisms of Hydrogen Absorption by Zirconium Alloys", Rep. AECL-8702, Atomic Energy of Canada Ltd, Chalk River Nuclear Laboratories (1985).
- [246] COX, B., HALLIDAY, J.D., Atomic Energy of Canada Ltd, Chalk River Nuclear Laboratories, unpublished results.
- [247] SMITH, T., Diffusion coefficients and anion vacancy concentrations for the zirconium-zirconium dioxide systems, *J. Electrochem. Soc.* **112** (1965) 560.
- [248] BANTER, J.G., Incorporation of ions in anodic oxide films on zirconium and their effect on film behaviour, *J. Electrochem. Soc.* **114** (1967) 508.
- [249] STERN, A., KHATAMIAN, D., LAURSEN, T., WEATHERLY, G.C., PERZ, J.M., Hydrogen and deuterium profiling at the surface of zirconium alloys, I. The effects of surface preparation, *J. Nucl. Mater.* **144** (1987) 35.
- [250] STERN, A., KHATAMIAN, D., LAURSEN, T., WEATHERLY, G.C., PERZ, J.M., Hydrogen and deuterium profiling at the surface of zirconium alloys, II. The effects of oxidation, *J. Nucl. Mater.* **148** (1987) 257.
- [251] RAMASUBRAMANIAN, N., TROTTIER, T., Electrical breakdown in anodic oxide films on Zircaloy-2, *J. Electrochem. Soc.* **118** (1971) 1797.
- [252] RAMASUBRAMANIAN, N., An imaging technique for studying localized electronic conduction in valve metal-oxide systems, *J. Electrochem. Soc.* **116** (1969) 1237.
- [253] RAMASUBRAMANIAN, N., Electrical switching in anodic films on Zircaloy-2, *J. Electrochem. Soc.* **119** (1972) 1375.
- [254] PLOC, R.A., COX, B., "Oxidation of some zirconium-based precipitates", Second Phase Particles in Zircaloys (Proc. Workshop Conf. Erlangen 1985), Kerntechnische Gesellschaft e.V. (KTG) Bonn (1987) 59.
- [255] BARR, T. L., ESCA studies of naturally passivated metal foils, *J. Vac. Sci. and Technol.* **14** (1977) 660.
- [256] SAENZ, J.M., PALACIO, C., CASAS, Y., MARTINEZ-DUART, J.M., An AES study of the oxidation of polycrystalline zirconium at room temperature and low oxygen pressures, *Surface and Interface Anal.* **10** (1987) 177.
- [257] PLOC, R.A., "Physical changes in thin ZrO₂ films with thickening", Proc. 7^e Congrès Int. de Microscopie Electronique, Grenoble (1970) 373.
- [258] DRAPER, P.H.G., The structure of anodic films - I. An electron diffraction examination of the products of anodic oxidation of tantalum, niobium and zirconium, *Acta Metall.* **11** (1963) 873.
- [259] PLOC, R.A., Breakaway oxidation of zirconium at 573 K, *J. Nucl. Mater.* **82** (1979) 411.
- [260] ROY, C., DAVID, G., X-ray diffraction analyses of zirconia films on zirconium and Zircaloy-2, *J. Nucl. Mater.* **37** (1970) 71.
- [261] COX, B., DONNER, A., The morphology of thick oxide films on Zircaloy-2, *J. Nucl. Mater.* **38** (1971) 329.
- [262] URQUHART, A., VERMILYEA, D.A., Characterization of Zircaloy Oxidation Films, ASTM-STP-551, American Society for Testing and Materials, Philadelphia, PA (1974) 463.
- [263] SABOL, G.P., MacDONALD, S.G., AIREY, G.P., Microstructure of the Oxide Films Formed on Zirconium-Based Alloys, ASTM-STP-551, American Society for Testing and Materials, Philadelphia, PA (1974) 435.
- [264] YUREK, G.J., CATHCART, J.V., PAWEL, R.E., Microstructures of the scales formed on Zircaloy-4 in steam at elevated temperatures, *J. Oxid. Metals* **10** (1976) 255.
- [265] PENELLE, R., BOISOT, P., BERANGER, G., LACOMBE, P., Influence de l'orientation des monocristaux de zirconium sur les textures de croissance de la zircone monoclinique, and Discussion de X-ray diffraction analysis of zirconium films on zirconium and Zircaloy-2, *J. Nucl. Mater.* **38** (1971) 340 and 343.
- [266] ROY, C., DAVID, G., Authors' reply to Note by LACOMBE, P., BERANGER, G., BOISOT, P. and PENELLE, R., *J. Nucl. Mater.* **38** (1971) 344.
- [267] WANKLYN, J.N., SILVESTER, D.R., A Study of corrosion films on zirconium and its alloys by impedance measurements, *J. Electrochem. Soc.* **105** (1958) 647.

- [268] COX, B., The Use of Electrical Methods for Investigating the Growth and Breakdown of Oxide Films on Zirconium Alloys, Rep. AECL-2668, Atomic Energy of Canada Ltd, Chalk River Nuclear Laboratories (1967).
- [269] ROSECRANS, P.M., Application of Alternating Current Impedance Measurements to Characterise Zirconium Alloy Oxidation Films, ASTM-STP-824, American Society for Testing and Materials, Philadelphia, PA (1984) 531.
- [270] RAMASUBRAMANIAN, R., Oxidation and polarization measurements on zirconium and Zircaloy-2 in molten nitrite and nitrates in 573 K, J. Electrochem. Soc. **127** (1980) 2566.
- [271] PAWEL, R.E., et al., Diffusion of Oxygen in Beta-Zircaloy and the High Temperature Zircaloy-Steam Reaction, ASTM-STP-633, American Society for Testing and Materials, Philadelphia, PA (1977) 119.
- [272] KNEPPEL, D.S., PEMSLER, J.P., Research on the Mechanism of Zirconium Alloy Corrosion in High-Temperature Steam, Rep. NMI-1251 B, Nuclear Metals Inc., Concord, MA (1961).
- [273] GARZAROLLI, F., GROS, J.P., SEIDEL, H., TRICOT, R., "Oxide growth mechanisms on zirconium alloys", Paper presented at 9th Int. Symp. on Zirconium in the Nuclear Industry, Kobe, Japan, 1990, ASTM-STP- (to be published).
- [274] Proc. 23rd UKAEA Diffraction Analysis Conference, Springfields, 1975, Rep. TRG 2799(S), UK Atomic Energy Authority, Reactor Group (1975).
- [275] CORIOU, H., GRALL, L., MEUNIER, J., PELRAS, M., WILLERMOZ, J., Corrosion du Zircaloy dans divers milieux alcalins à haute température, J. Nucl. Mater. **7** (1962) 320.
- [276] HILLNER, E., CHIRIGOS, J.N., The Effect of Lithium Hydroxide and Related Solutions on the Corrosion Rate of Zircaloy-2 in 680F Water, Rep. WAPD-TM-307, Bettis Atomic Power Laboratory, W. Mifflin, PA (1967).
- [277] MURGATROYD, R.A., WINTON, J., Hydriding Zircaloy-2 in lithium hydroxide solutions, J. Nucl. Mater. **23** (1967) 249.
- [278] McDONALD, S.G., SABOL, G.P., SHEPPARD, K.D., Effect of Lithium Hydroxide on the Corrosion Behaviour of Zircaloy-4, ASTM-STP-824, American Society for Testing and Materials, Philadelphia, PA (1983) 519.
- [279] SPITZNAGEL, J.A., FLEISCHER, L.R., CHOYKE, W.J., "The effect of ion bombardment on the thin film oxidation behaviour of Zircaloy-4 and Zr-1.0Nb", Applications of Ion Beams to Metals (Proc. Int. Conf. Albuquerque) (1973) 87.
- [280] JENKS, G.H., Zircaloy-2 Corrosion In-Pile in Aqueous Homogeneous Reactor Solutions, ASTM-STP-368, American Society for Testing and Materials, Philadelphia, PA (1964) 41.
- [281] ALCOCK, K., COX, B., The Effect of Neutron Irradiation on the Dissolution Rate of ZrO₂, Rep. AERE-R3114, UK Atomic Energy Authority, AERE Harwell (1959).
- [282] RUBIN, B., LYNAM, L., Behaviour of blanket-UO₂ fuel rods in Shippingport PWR core, Nucl. Appl. **2** (1966) 49.
- [283] NAYMARK, S., SPALARIS, C.N., "Oxide fuel fabrication and performance", Peaceful Uses of Atomic Energy (Proc. 3rd Int. Conf. Geneva), Vol. 11, United Nations (1964) 425.
- [284] NICHOLS, R.W., PICKLES, B.W., SHEPPARD, M.R., WOODS, D.S., ASHER, R.C., HESKETH, R., "Irradiation effects in zirconium-alloy pressure tubes", Peaceful Uses of Atomic Energy (Proc. 4th Int. Conf. Geneva), Vol. 10, IAEA, Vienna (1972) 549.
- [285] ASHER, R.C., DAVIES, D., HALL, A., KERSTEIN, T.B.A., MARRIOTT, J.W., WHITE, J.F., Effects of radiation on the oxidation and hydrogen absorption of zirconium alloys in steam, Electrochem. Technol. **4** (1966) 231.
- [286] CERRAI, E., GADDA, F., SCARONI, A., Further Experiments on the Corrosion Rate of Zircaloy-2 in Steam-Water Mixture Under Reactor Radiations, Rep. CISE-R-290, Centro Informazioni Studi Esperienze, Milan (1969).
- [287] HILLNER, E., Long Term In-Reactor Corrosion and Hydriding of Zircaloy-2 Tubing, ASTM-STP-754, American Society for Testing and Materials, Philadelphia, PA (1982) 450.
- [288] COX, B., AECL Experiments on the Corrosion of Zirconium Alloys under Irradiation, Rep. AECL-2257, Atomic Energy of Canada Ltd, Chalk River Nuclear Laboratories (1965).
- [289] NORFOLK, D.J., BURNS, W.G., MARSH, W.R., Zircaloy-2 Oxidation Using 46 MeV Protons to Simulate a Reactor Environment, Rep. RD/B/N4368, Central Electricity Generating Board, Berkeley Nuclear Laboratories (1987).

- [290] COX, B., "Mechanisms of corrosion of zirconium alloys in high temperature water, High Temp. Materials Chem.", Proc. Symp., Electrochem. Soc. N.Y., Vol. 82-1 (1982) 18.
- [291] GARZAROLLI, F., BODMER, R.P., STEHLE, H., TRAPP-PRITSCHING, S., "Progress in understanding PWR fuel rod waterside corrosion", Light Water Reactor Fuel Performance (Proc. Topical Mtg, Orlando), Vol. 1, American Nuclear Society (1985) 3-44.
- [292] HOLZER, R., KNAAB, H., "Recent fuel performance and improved products", LWR Fuel Performance (Proc. Topical Mtg, Williamsburg, VA), American Nuclear Society (1988) 69.
- [293] TICE, D.R., HUDDART, G., BRAMWELL, I.L., "Corrosion of Zircaloy-4 fuel cladding in high concentration lithium and boron conditions simulating extended burnup in PWR", Proc. Conf. Materials for Nuclear Core Applications, British Nuclear Energy Society, London (187) 57.
- [294] COX, B., Effect of Hydrogen Injection on Hydrogen Uptake by BWR Fuel Cladding, Rep. EPRI-NP-3146, Electric Power Research Institute, Palo Alto, CA (1983).
- [295] GARLICK, A., SUMERLING, R., SHIRES, G.L., Crud-induced overheating defects in water reactor fuel pins, *J. Br. Nucl. Energy Soc.* **16** (1977) 77.
- [296] MARLOWE, M.O., ARMIJO, J.S., CHENG, B., ADAMSON, R.B., "Nuclear fuel cladding localised corrosion", Light Water Reactor Fuel Performance (Proc. Topical Mtg, Orlando, FL), Vol. 1, American Nuclear Society (1985) 3-73.
- [297] RUDLING P., MASSIH, A., "Corrosion of Zr-2 cladding tubes in boiling water reactor environment", Proc. EPRI Workshop Zircaloy Corrosion, Charlotte, NC (SANTUCCI, J., Ed.) (1986).

CONTRIBUTORS TO DRAFTING AND REVIEW

Billot, P. Commissariat à l'énergie atomique, Cadarache, France
Cox, B. University of Toronto, Canada
Ishigure, K. University of Tokyo, Japan
Johnson Jr., A.B. Battelle, Pacific Northwest Laboratories, USA
Lemaignan, C. Commissariat à l'énergie atomique, Grenoble, France
Nechaev, A.F. International Atomic Energy Agency
Petrik, N.G. All-Union Institute of Complex Power Technology,
 Russia
Reznichenko, E.A. Kharkov Institute of Technology, Ukraine
Ritchie, I.G. International Atomic Energy Agency
Sukhanov, G.I. International Atomic Energy Agency

HOW TO ORDER IAEA PUBLICATIONS

An exclusive sales agent for IAEA publications, to whom all orders and inquiries should be addressed, has been appointed for the following countries:

CANADA
UNITED STATES OF AMERICA UNIPUB, 4611-F Assembly Drive, Lanham, MD 20706-4391, USA

In the following countries IAEA publications may be purchased from the sales agents or booksellers listed or through major local booksellers. Payment can be made in local currency or with UNESCO coupons.

ARGENTINA Comisión Nacional de Energía Atómica, Avenida del Libertador 8250, RA-1429 Buenos Aires

AUSTRALIA Hunter Publications, 58 A Gipps Street, Collingwood, Victoria 3066

BELGIUM Service Courrier UNESCO, 202, Avenue du Roi, B-1060 Brussels

CHILE Comisión Chilena de Energía Nuclear, Venta de Publicaciones, Amunategui 95, Casilla 188-D, Santiago

CHINA IAEA Publications in Chinese:
China Nuclear Energy Industry Corporation, Translation Section, P.O. Box 2103, Beijing
IAEA Publications other than in Chinese:
China National Publications Import & Export Corporation, Deutsche Abteilung, P.O. Box 88, Beijing

CZECHOSLOVAKIA S N T L, Spálená 51, CS-113 02 Prague 1
Alfa, Publishers, Hurbanovo námestie 3, CS-815 89 Bratislava

FRANCE Office International de Documentation et Librairie, 48, rue Gay-Lussac, F-75240 Paris Cedex 05

HUNGARY Kultura, Hungarian Foreign Trading Company, P.O. Box 149, H-1389 Budapest 62

INDIA Oxford Book and Stationery Co., 17, Park Street, Calcutta-700 016
Oxford Book and Stationery Co., Scindia House, New Delhi-110 001

ISRAEL YOZMOT Literature Ltd., P.O. Box 56055, IL-61560 Tel Aviv

ITALY Libreria Scientifica Dott. Lucio di Biasio "AEIOU", Via Coronelli 6, I-20146 Milan

JAPAN Maruzen Company, Ltd, P.O. Box 5050, 100-31 Tokyo International

PAKISTAN Mirza Book Agency, 65, Shahrah Quaid-e-Azam, P.O. Box 729, Lahore 3

POLAND Ars Polona, Foreign Trade Enterprise, Krakowskie Przedmieście 7, PL-00-068 Warsaw

ROMANIA Ilexim, P.O. Box 136-137, Bucharest

RUSSIAN FEDERATION Mezhdunarodnaya Kniga, Sovinkniga-EA, Dimitrova 39, SU-113 095 Moscow

SOUTH AFRICA Van Schaik Bookstore (Pty) Ltd, P.O. Box 724, Pretoria 0001

SPAIN Díaz de Santos, Lagasca 95, E-28006 Madrid
Díaz de Santos, Balmes 417, E-08022 Barcelona

SWEDEN AB Fritzes Kungl. Hovbokhandel, Fredsgatan 2, P.O. Box 16356, S-103 27 Stockholm

UNITED KINGDOM HMSO, Publications Centre, Agency Section, 51 Nine Elms Lane, London SW8 5DR

YUGOSLAVIA Jugoslovenska Knjiga, Terazije 27, P.O. Box 36, YU-11001 Belgrade

Orders from countries where sales agents have not yet been appointed and requests for information should be addressed directly to:



Division of Publications
International Atomic Energy Agency
Wagramerstrasse 5, P.O. Box 100, A-1400 Vienna, Austria